

**The Influence
of Particle Size, Composition and Transport
on the Distribution of $^{230}\text{Th}_{\text{xs}}$, $^{231}\text{Pa}_{\text{xs}}$, and ^{10}Be
in Marine Sediments**

**Der Einfluss von Korngrößenverteilung,
Partikelzusammensetzung und Sedimenttransport
auf die Verteilung von $^{230}\text{Th}_{\text{xs}}$, $^{231}\text{Pa}_{\text{xs}}$ und ^{10}Be
in Meeressedimenten**

Dissertation zur Erlangung des Doktorgrades
am Fachbereich Geowissenschaften der Universität Bremen

vorgelegt von
Sven Kretschmer
Bremen, im September 2010

Tag des Promotionskolloquiums:

5. November 2010

Gutachter:

Frau Prof. Dr. Gesine Mollenhauer

Herr Prof. Dr. Michael Schlüter

Prüfer:

Frau Prof. Dr. Simone Kasemann

Herr Prof. Dr. Michael Schulz

Zusammenfassung	1
Abstract	5
Chapter 1: Introduction	9
Chapter 2: Manuscript I	23
<i>Grain size effects on $^{230}\text{Th}_{\text{xs}}$ inventories in opal-rich and carbonate-rich marine sediments</i>	
Kretschmer, S., W. Geibert, M. M. Rutgers van der Loeff, G. Mollenhauer	
Chapter 3: Manuscript II	47
<i>The origin of focused marine sediments: an exploration of local vs. remote sediment sources from grain size data, $^{230}\text{Th}_{\text{xs}}$ and clay mineralogy</i>	
Kretschmer, S., W. Geibert, D. Heslop, G. Kuhn, I. Meyer, M. M. Rutgers van der Loeff, G. Mollenhauer	
Chapter 4: Manuscript III	73
<i>Contributions from size fraction-specific $^{230}\text{Th}_{\text{xs}}$ data towards understanding of sediment redistribution processes in the Panama Basin</i>	
Mollenhauer, G., S. Kretschmer, S. Kusch, M. M. Rutgers van der Loeff, A. C. Mix	
Chapter 5: Manuscript IV	87
<i>Fractionation of ^{230}Th, ^{231}Pa, and ^{10}Be induced by particle size and composition within an opal-rich sediment of the Atlantic Southern Ocean</i>	
Kretschmer, S., W. Geibert, M. M. Rutgers van der Loeff, C. Schnabel, S. Xu, G. Mollenhauer	
Chapter 6: Conclusions and Perspectives	103
References	107
Appendix	121
Danksagung	133

Zusammenfassung

Die vorliegende Arbeit befasst sich mit der Korngrößenabhängigen Verteilung von natürlichen Radionukliden im Meeressediment und die Anwendung dieser Radionuklide als Indikatoren für Partikeltransport im Ozean. In den Ozeanen wird ein großer Anteil der absinkenden Partikel sowie der Schwebfracht durch die Advektion von Wassermassen über weite Entfernungen verfrachtet bevor sich das partikuläre Material auf dem Meeresgrund als Sediment ablagert. Zusätzlich kann bereits abgelagertes Sediment durch die Bodenströmung wieder aufgewirbelt werden und als Suspensionsfracht einen weiteren Transport erfahren. Es ist bekannt, dass dieser Lateraltransport von Partikeln im Ozean ein wichtiger Prozess für die Verteilung von organischem Material entlang der Kontinentalränder bis hin zu den Tiefseeebenen darstellt. Um die Rolle zu verstehen, die das organische Material im Ozean als Teil des globalen Kohlenstoff-Kreislaufes einnimmt, ist es notwendig, die verschiedenen Transportprozesse zu unterscheiden. Das Verständnis von Partikeltransport ist essentiell für die Untersuchung der biogeochemischen Kreisläufe der Ozeane. Transportprozesse innerhalb der euphotischen Zone, in der tieferen Wassersäule oder in bodennahen Trübeschichten können mittels natürlich vorkommender Isotope der Uran-Zerfallsreihen (wie zum Beispiel ^{230}Th , ^{234}Th , ^{231}Pa , ^{210}Pb , ^{210}Po) oder aus kosmogenem Ursprung (wie zum Beispiel ^{10}Be , ^{26}Al) nachvollzogen werden. Die Partikel-Reaktivität in Meerwasser ist ein gemeinsames charakteristisches Merkmal und führt zur schnellen Adsorption dieser Isotope an Kolloide oder Partikel welche in der Wassersäule schweben oder absinken. So trägt jedes Partikel im Ozean seine eigene Isotopensignatur abhängig von Herkunft, Transportprozess, Korngröße oder Zusammensetzung des Partikels. Während Erosion, Transport und erneuter Ablagerung von Sedimenten kann es vorkommen, dass einzelne Partikel oder Aggregate unterschiedlicher Größe und Dichte voneinander getrennt werden und dadurch eine Sortierung von Partikeln stattfindet. Der Prozess der Partikelsortierung kann möglicherweise bestimmte Isotopensignaturen, die an verschiedenartige Partikel gebunden sind, physikalisch-räumlich voneinander trennen. Die Isotope, welche als Indikator („Tracer“) für Partikeltransport dienen, sind bezüglich ihrer Geochemie in der Wassersäule bereits gut untersucht. Allerdings ist über die Verteilung dieser Tracer-Isotope in Sedimenten noch recht wenig bekannt, zum einen deshalb, weil das Sediment aus einer Vielzahl verschiedenartiger Partikel zusammengesetzt ist und zum anderen, weil sich, wie oben erwähnt, komplexe Resuspensions- und Transportprozesse abspielen, welche noch nicht ausreichend untersucht wurden. Deshalb befasst sich diese Arbeit mit der partikelspezifischen Verteilung der Tracer-Isotope ^{230}Th , ^{231}Pa und ^{10}Be in Tiefseesedimenten. Die Untersuchungsgebiete sind das Südpolarmeer (Ostatlantischer Sektor), der Südost-Atlantik (Walvis Ridge) und das Panamabecken. In diesen drei Gebieten hat der laterale Sedimenttransport einen großen Einfluss auf die lokalen Ablagerungsprozesse. Die zentrale Frage in der vorliegenden Studie ist, ob die Korngröße und Zusammensetzung eines Partikels zusammen mit dem Prozess des Partikeltransportes zu einer räumlichen Trennung

zwischen hohen und niedrigen Konzentrationen der Partikel-Tracer ^{230}Th , ^{231}Pa und ^{10}Be in den Sedimenten führen kann, und ob ein solcher Sortierungseffekt möglicherweise zu einer fehlerbehafteten Abschätzung von Partikelflussraten führen kann. Für diese Studie wurden an Sedimentproben des Holozäns und des letzten Hochglazials eine Trennung nach Korngröße und -dichte sowie eine anschließende Isotopenanalyse durchgeführt. Die Sedimentfraktionen werden aufgrund ihrer Eigenschaften verschiedenen Transportpfaden im Ozean (vertikal gegenüber lateral) zugeordnet. Untersuchungsstandorte mit sehr hohen Massenakkumulationsraten werden mit solchen niedrigerer Akkumulationsraten verglichen, um den Einfluss von Sedimenttransport und Partikelsortierung auf die Verteilung der korngrößenspezifischen Tracer-Isotope zu bewerten.

Der Anteil des ^{230}Th , welches aus dem Meerwasser an Partikel adsorbiert ist, wird „excess ^{230}Th “ oder auch „ $^{230}\text{Th}_{\text{xs}}$ “ genannt. Mithilfe der weithin bekannten Methode der „ $^{230}\text{Th}_{\text{xs}}$ -Normalisierung“ können vertikale Flussraten von Partikeln aus der Wassersäule ins Sediment berechnet werden. Auch der Eintrag von seitlich durch Bodenströmungen herantransportiertem Sediment kann mit der $^{230}\text{Th}_{\text{xs}}$ -Methode quantifiziert werden („Fokussierungsfaktor“). Die Untersuchungen der Sedimentproben von verschiedenen Standorten und unterschiedlichen Alters in der vorliegenden Studie ergaben einen übereinstimmenden Befund bezüglich der korngrößenspezifischen $^{230}\text{Th}_{\text{xs}}$ -Verteilung: $^{230}\text{Th}_{\text{xs}}$ ist größtenteils in den Feinfraktionen konzentriert. 53-89% des Gesamt- $^{230}\text{Th}_{\text{xs}}$ -Gehaltes sind in der Tonfraktion (d.h. Partikel mit einem Durchmesser kleiner $2\ \mu\text{m}$) enthalten, welche bevorzugt an den Orten verringerter Bodenströmung und hoher Akkumulationsraten abgelagert wird. Die starke Affinität des ^{230}Th für bestimmte Korngrößen impliziert, dass die Vorbedingungen für die Anwendung der $^{230}\text{Th}_{\text{xs}}$ -Methode nicht vollständig erfüllt sind. Unter der Annahme, dass die $^{230}\text{Th}_{\text{xs}}$ -reiche Feinfraktion leichter zu resuspendieren und transportieren ist als die $^{230}\text{Th}_{\text{xs}}$ -arme Grobfraktion, kann eine Partikelsortierung zu einer systematischen Fehlabschätzung der $^{230}\text{Th}_{\text{xs}}$ -normalisierten Flussraten führen. Die vorliegende Arbeit zeigt, wie eine Korngrößenkorrektur auf die $^{230}\text{Th}_{\text{xs}}$ -normalisierten Flussraten angewendet werden kann. An einem Standort hoher Sedimentfokussierung hat die Anwendung einer Korngrößenkorrektur zur Folge, dass die vertikale $^{230}\text{Th}_{\text{xs}}$ -normalisierte Flussrate hin zu einem höheren Wert korrigiert wird, während die Menge des lateral eingetragenen Sediments nach unten korrigiert wird. Die Größenordnung dieses systematischen Fehlers hängt sehr von den Korngrößenverteilungen des Lateral- und Vertikaleintrags ab. Daher wurden für den Untersuchungsstandort im Südpolarmeer die Korngrößenspektren rechnerisch mithilfe einer Hauptkomponentenanalyse in zwei einzelne Korngrößen-Komponenten zerlegt. Die Komponente des groben Kornspektrums ($>300\ \mu\text{m}$) wird der vertikal absinkenden Partikelfraktion zugeordnet, während die Komponente des feinen Kornspektrums ($<300\ \mu\text{m}$) eine Mischung aus vertikal sinkenden und lateral transportierten Partikeln darstellt. Die daraus resultierende Korngrößenkorrektur reduziert den Fokussierungsfaktor am Untersuchungsstandort

des Südpolarmeers zur Zeit des Glazials (z.B. von 5.8 auf 4.4) und erhöht dementsprechend die vertikale Flussrate (z.B. von 1.5 auf 2.0 g cm⁻² ka⁻¹). Auf Grundlage der Korngrößenkorrektur wird der Effekt der Partikelsortierung auf die ²³⁰Th_{xs}-normalisierten Flussraten an diesem Standort als unbedeutend bewertet. Im Gegensatz dazu wirkt sich die Korngrößenkorrektur am Untersuchungsstandort im Panamabecken relativ stark auf die ²³⁰Th_{xs}-normalisierten Flussraten aus. Durch die Korngrößenkorrektur wird dort der Fokussierungsfaktor signifikant reduziert (z.B. von 6.8 auf 3.4), bzw. die vertikale Flussrate signifikant erhöht (z.B. von 1.3 auf 2.7 g cm⁻² ka⁻¹). Die Ergebnisse zu dem Standort im Panamabecken lassen die Schlussfolgerung zu, dass starker Eintrag von Feinmaterial aus lateralem Sedimenttransport mit einer erhöhten vertikalen Flussrate (aufgrund erhöhter Primärproduktion) einhergeht und somit gleichzeitig beide Transportprozesse zu der hohen Akkumulation von Sediment und ²³⁰Th_{xs} im letzten Hochglazial führten.

Neben der Analyse von einzelnen Sedimentproben hat die vorliegende Arbeit außerdem zum Ziel, Aussagen zu Ablagerungs- und Transportprozessen über längere Zeiträume zu treffen. Daher wurde für den Standort im Südpolarmeer der Versuch unternommen, die Variationen der ²³⁰Th_{xs}-Konzentration im Sediment der letzten ~140 000 Jahre anhand von Korngrößen Daten zu modellieren. Es zeigt sich, dass Gesamt-²³⁰Th_{xs}-Konzentrationen im Sediment auf der Grundlage von Korngrößenverteilungen berechnet werden können. Diese Studie verdeutlicht, dass die Akkumulation von ²³⁰Th_{xs} im Sediment weitgehend von der Menge an Ton bestimmt wird, welche an dieser Stelle abgelagert wird. Weiterhin zeigt sich eine Korrelation zwischen dem ²³⁰Th_{xs}-Inventar im Sediment und dem relativen Beitrag des Tonminerals Chlorit, dessen Ursprung mehrere Tausend Kilometer entfernt in der Westantarktis und Patagonien liegt. Die erstaunlich enge Beziehung zwischen den beiden ozeanographischen Tracern legt den Schluss nahe, dass ²³⁰Th_{xs} in partikulärer Form über sehr weite Entfernungen herantransportiert wurde und dass dieser Transport zeitlichen Variationen ausgesetzt ist. Dieser Transport führt im Wechselspiel mit den lokalen Quellen von ²³⁰Th und Tonmineralen letztlich zu den zeitlichen Variationen der ²³⁰Th_{xs}-Akkumulation.

Die Sedimentproben vom Untersuchungsstandort im Südpolarmeer wurden mittels Sinkgeschwindigkeit in Wasser in zwei Dichteklassen aufgetrennt. Die langsam sinkenden Partikel mit geringerer Dichte sind durch einen hohen Anteil an biogenem Opal (SiO₂) gekennzeichnet. Die Analysen in dieser Studie zeigen, dass solche opalreichen Partikel relativ hohe Konzentrationen an adsorbiertem ²³¹Pa und ¹⁰Be tragen, und dass die Adsorption von ²³⁰Th an denselben Partikeln vergleichsweise gering ist. Dieser Unterschied in der Affinität zu Opal äußert sich in erhöhten Isotopenverhältnissen von ²³¹Pa/²³⁰Th (bis zu ~0.5) und ¹⁰Be/²³⁰Th (bis zu ~0.6×10⁹ Atome dpm⁻¹) in den opalreichen Partikeln. Diese Isotopenverhältnisse sind im Vergleich zu den Produktionsraten im Meerwasser (²³¹Pa/²³⁰Th= 0.09 bzw. ¹⁰Be/²³⁰Th= ~0.15×10⁹ Atome dpm⁻¹) relative stark erhöht. Außerdem zeigt ²³¹Pa eine stärkere Affinität

gegenüber den opalreichen Partikeln als ^{10}Be . Die Ergebnisse bestätigen, dass $^{231}\text{Pa}/^{230}\text{Th}$ im Opalgürtel des Südpolarmeers bevorzugt für die Rekonstruktion von Opal-Flussraten verwendet werden sollte. Eine weitere Bestätigung für die Eignung von $^{231}\text{Pa}/^{230}\text{Th}$ oder $^{10}\text{Be}/^{230}\text{Th}$ als Partikel-Tracer ergibt sich aus dem Vergleich zwischen schneller und langsamer Sedimentakkumulation, denn es konnte keine Beeinflussung der Isotopenverhältnisse durch Partikelsortierung gefunden werden. Gegenüber einer Isotopenanalyse, die üblicherweise an einer Gesamt-Sedimentprobe gemacht wird, hat die Untersuchung von partikelspezifischen $^{231}\text{Pa}/^{230}\text{Th}$ - und $^{10}\text{Be}/^{230}\text{Th}$ -Verhältnissen den großen Vorteil, dass Schlussfolgerungen bezüglich der Herkunft dieser Isotopensignaturen gemacht werden können und weiterreichende Erkenntnisse über Transportprozesse von Partikeln im Ozean gewonnen werden.

Abstract

This study focuses on the grain size-dependent distribution of natural radionuclides in marine sediments and their application for tracing particle transport in the ocean. Large proportions of particulate matter experience lateral transport pathways before the ultimate burial in the marine sediments. The lateral displacement of particles includes long distance advection within the water column prior to initial deposition and the transport within deep and bottom waters following resuspension by bottom currents. Lateral transport is widely recognized as an important mode of delivery of organic matter across continental margins and to the abyssal plains of the oceans. Distinguishing between different modes of particle transport is therefore an integral part of those studies that focus on the fate of organic matter within marine reservoirs as part of the global carbon cycle. Biogeochemical cycles in the modern and past oceans can be traced by using different naturally occurring isotopes including cosmogenic isotopes (e.g. ^3He , ^{26}Al , ^{10}Be) and U-series isotopes (e.g. ^{230}Th , ^{234}Th , ^{231}Pa , ^{210}Po , ^{210}Pb) covering a wide range of particle dynamics on different timescales. Most of these isotopes in seawater are characterized by their particle reactivity, a property that leads to the adsorption onto particles. Each particle carries a particular isotope signature according to source, transport, grain size, and composition of this particle. During the lateral displacement of particles in seawater, a physical separation according to their grain size and density may result in a particle sorting at the site of deposition. The particle sorting process bears the potential to result in a spatial decoupling of the isotope signature residing on those advected particles. The tracer isotopes are well studied with respect to their geochemistry in seawater. In sediments, however, the distribution of tracer isotopes depends on the complex particle dynamics prior to the final deposition, an interplay of various processes which is not yet well understood. Therefore, this study addresses the particle-specific distribution of the tracer isotopes ^{230}Th , ^{231}Pa , and ^{10}Be in deep-ocean sediments from areas in the Southern Ocean (East Atlantic Sector), the South East Atlantic (Walvis Ridge) and the Panama Basin where lateral sediment transport processes are of particular importance. This study focuses on the question if particle size and composition combined with the process of particle transport could lead to a decoupling between ^{230}Th , ^{231}Pa , and ^{10}Be in sediments, and to what extent this particle sorting effect could generate a bias to flux calculations based on those tracers. Sediment samples from the Last Glacial Maximum to the Holocene are studied by the separation into particle size and density classes with a subsequent isotope analysis. According to particle size and composition, those particle types are ascribed to the different (vertical vs. lateral) transport modes. Locations of very high mass accumulation rates are compared with those of slower accumulation to assess the influence of sediment focusing on the distribution of the grain size-specific tracer isotopes.

The scavenged ^{230}Th (=excess ^{230}Th or $^{230}\text{Th}_{\text{xs}}$) is widely used as constant flux proxy. By normalizing a sediment component against excess ^{230}Th , the primary vertical flux of this

component can be calculated. In addition, the lateral contribution of sediment by bottom currents can be quantified (“focusing factor”). Results of this study show that grain size-specific ^{230}Th of samples from different locations and ages are consistent with respect to the finding that $^{230}\text{Th}_{\text{xs}}$ generally is highly concentrated within the clay-size fractions. 53-89 % of the total $^{230}\text{Th}_{\text{xs}}$ inventory is concentrated in clay-size material (i.e. particle diameter smaller than $2\ \mu\text{m}$), which is preferentially deposited at the high accumulation sites. The affinity of $^{230}\text{Th}_{\text{xs}}$ to certain particle size classes implies that the assumptions behind the $^{230}\text{Th}_{\text{xs}}$ -method may not be entirely valid. As the fine-grained ^{230}Th -rich sediment fraction is preferentially resuspended and transported, while the coarse-grained ^{230}Th -poor components are hydrodynamically stationary, a grain size-induced bias of ^{230}Th -normalized fluxes is expected. This study shows that one can apply a grain size correction to the ^{230}Th -normalized fluxes. Such a correction procedure reveals that in the case of focused sedimentation the amount of vertical particle fluxes may be underestimated, while the contribution by lateral sediment transport may be overestimated when based on the traditional, uncorrected ^{230}Th -normalization. The magnitude of this grain size bias depends on the grain size distribution of laterally advected particles compared to that of the vertically settling particle fraction. In the case of the Southern Ocean study site, decomposition (principal component analysis) of grain size distributions into two grain size-endmembers suggests that particles larger than $300\ \mu\text{m}$ have been derived solely from vertical settling, while the fraction of particles smaller than $300\ \mu\text{m}$ represents a mixture of vertical settling and lateral advection. The corresponding grain size correction slightly reduces the focusing factor for the Southern Ocean study site (e.g. from 5.8 to 4.4 during the glacial) and accordingly increases the calculated amount of the vertical particle flux (e.g. from 1.5 to $2.0\ \text{g cm}^{-2}\ \text{ka}^{-1}$). Regarding the Southern Ocean study site however, those results imply that the grain size bias is of minor importance to the reconstruction of the past export productivity. The Panama Basin sediment in contrast, reveals a substantial grain size bias in ^{230}Th -normalized particle fluxes. Correcting for this grain size-effect significantly reduces the focusing factor (e.g. from 6.8 to 3.4 during the last glacial) while increasing the vertical flux (e.g. from 1.3 to $2.7\ \text{g cm}^{-2}\ \text{ka}^{-1}$). The results suggest for the Panama Basin that both strong lateral sediment transport and increased vertical fluxes contributed to increased mass accumulation rates during the last glacial.

A modeling approach where bulk- $^{230}\text{Th}_{\text{xs}}$ is calculated based on grain size distributions reveals that $^{230}\text{Th}_{\text{xs}}$ accumulation at the Southern Ocean study site is largely controlled by the clay deposition during the past $\sim 140,000$ years. The close correlation between $^{230}\text{Th}_{\text{xs}}$ -focusing and the relative contribution of the clay mineral chlorite (deriving from several thousand kilometers upstream of the study site) leads to the conclusion that the vast amount of ^{230}Th has been advected over large distances in particulate form prior to the final deposition. This transport from remote sources is variable through time and the interplay with local sources of $^{230}\text{Th}_{\text{xs}}$ and clay minerals (smectite) finally results in the temporal variations of $^{230}\text{Th}_{\text{xs}}$ accumulation.

The fractionation of the Southern Ocean sediment samples into density classes based on settling velocities led to the isolation of a very opal-rich phase. Those opal-rich (slowly settling, lower density) particles contain higher ^{231}Pa and ^{10}Be concentrations than opal-poor (faster settling, higher density) particles. The isotope ratios $^{231}\text{Pa}/^{230}\text{Th}$ (up to ~ 0.5) and $^{10}\text{Be}/^{230}\text{Th}$ (up to $\sim 0.6 \times 10^9$ atoms dpm^{-1}) as found in opal-rich particles strongly exceed their production ratio in seawater ($^{231}\text{Pa}/^{230}\text{Th} = 0.09$, $^{10}\text{Be}/^{230}\text{Th} = \sim 0.15 \times 10^9$ atoms dpm^{-1}). The fractionation of ^{231}Pa and ^{10}Be relative to ^{230}Th induced by the adsorption to opal-rich particles is more pronounced for ^{231}Pa than for ^{10}Be . The results of this study support the application of bulk $^{231}\text{Pa}/^{230}\text{Th}$ as a proxy for past opal fluxes to Southern Ocean sediments. The comparison between the twin cores with rapid and slow accumulation rates reveals that the isotope ratios $^{231}\text{Pa}/^{230}\text{Th}$ and $^{10}\text{Be}/^{230}\text{Th}$ are not influenced by the intensity of sediment focusing (i.e. particle sorting) at these two study sites. The study of compound-specific $^{231}\text{Pa}/^{230}\text{Th}$ and $^{10}\text{Be}/^{230}\text{Th}$, as conducted here, allows a more detailed picture of the origin of the isotopic signatures.

Chapter 1

Introduction

Marine sediments represent a valuable archive of information concerning the ocean and its role in the past carbon cycle. The production of organic matter (OM) in the ocean by marine phytoplankton, its sinking to the deep ocean, and subsequent burial in sediments is termed the “biological pump” [Anderson *et al.*, 2002]. The recognition that variations in the biological pump may be responsible for variations in atmospheric carbon dioxide [Knox and McElroy, 1984; Sarmiento and Toggweiler, 1984] has stimulated research to reconstruct the past history of biological production. The most direct measure of past ocean productivity are the mass accumulation rates of the biogenic phases, i.e. the organic matter (OM), the biogenic silica (bSiO₂, opal), and the calcium carbonate (CaCO₃). In general, the reconstruction of the past ocean productivity from mass accumulation rates is complicated by two difficulties: (i) The poor preservation of reactive biogenic material in marine sediments and (ii) the lateral advection through the water column over long distances between the site of production to the site of the final burial.

Biogenic phases are often poorly preserved in sediments as they are subject to dissolution during settling and early diagenesis [Schlüter *et al.*, 1998; Sayles *et al.*, 2001; Volbers and Henrich, 2002]. The spatial and temporal variability of the preservation of biogenic phases complicates the interpretation of sediment records. Consequently, indirect measures (“proxies”) have been developed to evaluate past changes in ocean productivity such as excess ²³¹Pa/²³⁰Th [Anderson *et al.*, 2009], excess ¹⁰Be/²³⁰Th [Anderson *et al.*, 1998], biogenic barium [Paytan and Griffith, 2007], authigenic uranium [Chase *et al.*, 2001], and nutrient availability such as the Cd/Ca ratio of foraminiferal calcite [Boyle, 1992], the carbon isotopic composition δ¹³C [Kohfeld *et al.*, 2000], and nitrogen isotopic composition δ¹⁵N [Holmes *et al.*, 1999].

In the case of lateral transport, it is of interest to reconstruct the age, source, composition, and quantity of the advected material in order to distinguish between the biological production (vertical source) and the lateral contribution, but also in order to gain information on those environmental parameters of the past ocean that led to lateral particle transport, such as patterns in ocean circulation. For studying modern and past particle fluxes in the ocean, a suite of particle flux tracers is available. Studies on particle fluxes include the application of various naturally occurring radio-isotopes deriving from the uranium-decay series (such as ²³⁰Th, ²³⁴Th, ²³¹Pa, ²¹⁰Pb, ²¹⁰Po) or from cosmogenic production (such as ¹⁰Be, ²⁶Al, ³He). This study focuses on the methodology in the use of ²³⁰Th, ²³¹Pa, and ¹⁰Be as particle flux tracers towards an enhanced understanding of particle dynamics in the ocean.

1.1 Lateral transport of particles

The pathway of organic and inorganic matter is not solely via direct vertical settling from the sea surface to the deep ocean. In fact, large proportions of particulate matter in marine sediments experienced lateral pathways before final burial [Biscaye and Eittrheim, 1977; McCave, 1986]. The lateral displacement of particles includes long distance transport by advection within the water column prior to initial deposition [Mollenhauer et al., 2006] and the “resuspension-transport-deposition-loop” within benthic nepheloid layers (BNL) [Gardner et al., 1985; Rutgers van der Loeff et al., 2002]. Grain size and hydrodynamic properties determine the susceptibility of a particle to lateral transport [Thomsen and Gust, 2000]. Owing to the slow settling velocities, the fine-grained and low-density particles such as clay [Baker and Feely, 1978] or diatoms [Geibert et al., 2005], and organo-mineral aggregates [Ransom et al., 1998] are most susceptible to transport in suspension. In contrast, foraminifers, radiolarians and ice-rafted particles in the size range of sand rapidly sink through the water column as discrete particles with little lateral displacement. Being less susceptible to resuspension following deposition, transport only occurs in traction or saltation as part of the bedload [Gorsline, 1984]. Lateral transport is widely recognized as an important mode of delivery of OM to the deep sea and across continental margins [Freudenthal et al., 2001; Mollenhauer et al., 2005]. The preferential redistribution of fine-grained organo-mineral aggregates [Thomsen and van Weering, 1998] or fine-grained lithogenic components such as clays [Diekmann et al., 1996; Petschick et al., 1996] by advective processes may result in a decoupling of proxy-records between proxies residing in fine, i.e. hydrodynamically mobile sediment compounds and those residing in coarse, i.e. hydrodynamically stationary compounds. Investigations of molecular-level radiocarbon (^{14}C) has supplied evidence for this transport effect, showing that different compounds from the same sediment layer may exhibit a wide spectrum of ^{14}C ages [Eglinton et al., 1997; Pearson et al., 2001]. The coeval deposition of pre-aged advected material (e.g. alkenones from coccolithophorids) with younger freshly produced material (e.g. tests of planktic foraminifers) results in age-offsets between the different sediment compounds up to 10^3 years [Ohkouchi et al., 2002; Mollenhauer et al., 2003; 2005; Mollenhauer and Eglinton, 2007]. The method of molecular-level ^{14}C -ages is a valuable tool for identifying pre-aged OM that has been laterally advected, and it provides insight into the timescales of sediment transport [Mollenhauer et al., 2006; Kusch et al., 2010]. However, changing flow directions and velocities of bottom currents responsible for redistribution of fine-grained sediments modify the relative contribution of lateral sediment supply at the site of sediment focusing. Molecular-level ^{14}C ages are not suitable for supply of quantitative estimates of the relative contributions of pre-aged advected material and autochthonous material [Mollenhauer et al., 2005].

1.2 Quantification of past vertical fluxes

In order to assess ocean productivity, the past autochthonous signals, i.e. the past vertical flux rates must be quantified. Therefore, constant flux proxies (CFP) have been developed. Two isotopes from different sources, ^3He [from cosmogenic origin; *Marcantonio et al.*, 1996] and ^{230}Th [from radioactive decay; *Cochran*, 1992] have been found to form sufficiently constant vertical fluxes to the pelagic ocean sediments. If the sediment component of interest (e.g. biogenic opal) is normalized against the CFP, the flux rates of this component deriving from the sea surface i.e. the vertical pathway, can be calculated [*François et al.*, 2004]. By doing so, the flux of any sedimentary constituent may be estimated. The advantages using a CFP-normalization method is that fluxes of sediment components can be corrected for sediment focusing and fluxes can be evaluated at a higher temporal resolution than by using traditional stratigraphic methods. The temporal resolution is limited by the bioturbation depth and the sediment accumulation rate, only [*Henderson and Anderson*, 2003, and references therein].

In the case of the ^3He -normalization method, progress has been made by *Marcantonio* and co-workers [*Marcantonio et al.*, 1996; 2001; 2009; *Higgins et al.*, 2002]. The advantage of the ^3He -method is its potential for application as a CFP well back into the Mesozoic [*Anderson*, 2004, and references therein]. The application of ^{230}Th -normalization, in contrast, is limited by the half-life of ^{230}Th (75,380 years) to sediments of the past ~300,000 years. The $^{230}\text{Th}_{\text{xs}}$ -normalization method was developed by *Bacon* and co-workers [*Bacon*, 1984; *Suman and Bacon*, 1989; *François et al.*, 1990] and has found widespread use since then. Paleoproductivity studies in the Southern Ocean, where the deep-reaching Antarctic Circumpolar Current causes substantial sediment redistribution, have been particularly dependent on the ^{230}Th -normalization method to obtain flux rates of opal, biogenic barium, organic carbon and other paleoproductivity proxies [*François et al.*, 1997; *Anderson et al.*, 1998; *Frank et al.*, 2000a; *Geibert et al.*, 2005]. Based on ^{230}Th -normalized fluxes, the past changes in the biological productivity of the Southern Ocean from the Last Glacial Maximum to the Holocene have been intensively discussed [*Anderson*, 2004].

However, the abovementioned variability in the extent of preservation of reactive biogenic compounds remains a factor of uncertainty in flux-based studies. The ^{230}Th -normalization cannot get around this problem [*Chase*, 2008]. For instance, most of the biogenic silica produced in surface waters is dissolved during settling through the water column and at the sediment/water interface. In the Southern Ocean (Weddell Sea and ACC), only a minor fraction (0.2 to 24 %) of biogenic silica produced in surface waters is preserved and recorded in the sediments [*Schlüter et al.*, 1998]. Thus, the ^{230}Th -normalization can provide only “preserved vertical fluxes” [*François et al.*, 2004; *Geibert et al.*, 2005] so that reconstructing the past changes in biological productivity of the oceans remains challenging.

Therefore, indirect approaches have been developed, such as the isotope ratios $^{231}\text{Pa}/$

^{230}Th and $^{10}\text{Be}/^{230}\text{Th}$. It has been recognized that $^{231}\text{Pa}/^{230}\text{Th}$ and $^{10}\text{Be}/^{230}\text{Th}$ in particles are correlated to the intensity of the vertical particle fluxes [Lao *et al.*, 1993; Kumar *et al.*, 1995] and that their sedimentary record is insensitive to variable preservation effects [Bourles *et al.*, 1989a; Chase, 2008]. Geochemical proxies such as $^{231}\text{Pa}/^{230}\text{Th}$ and $^{10}\text{Be}/^{230}\text{Th}$ that faithfully record the intensity of particle fluxes are therefore a valuable measure of past changes in biological productivity, and have found widespread application [François *et al.*, 1993; Kumar *et al.*, 1993; 1995; Anderson *et al.*, 1998; 2009; Frank *et al.*, 2000a; Bradtmiller *et al.*, 2009].

1.3 Properties of particle tracers

The common property of Th, Pa, and Be is their particle reactivity in seawater, what makes them suitable for tracing past particle fluxes (**Figure 1.1**). Those trace elements differ in intensity of particle reactivity with $\text{Th} > \text{Pa} > \text{Be}$ ordered from higher to lower reactivity. Accordingly, the differences in oceanic residence times are in the inverse order ($\text{Th} < \text{Pa} < \text{Be}$). This can be employed by applying $^{231}\text{Pa}/^{230}\text{Th}$ and $^{10}\text{Be}/^{230}\text{Th}$ for investigating modern particle fluxes in the water column of the open ocean compared with that of ocean margins [“boundary scavenging”; Anderson *et al.*, 1983a, b; 1990; Lao *et al.*, 1993], and for investigating past particle fluxes by comparing relative changes of isotope ratios in sediment cores for unraveling past changes in ocean productivity [François *et al.*, 1993; Kumar *et al.*, 1995; Anderson *et al.*, 2009; Bradtmiller *et al.*, 2009] or ocean circulation [Yu *et al.*, 1996; McManus *et al.*, 2004]. In the case of the past ocean circulation, the sedimentary $^{231}\text{Pa}/^{230}\text{Th}$ -proxy is still under development and subject to recent investigations [Guihou *et al.*, 2010; Negre *et al.*, accepted]. An important property is the distinctive affinity of each tracer element to preferentially adsorb onto a particular sediment phase. Water column studies and controlled laboratory experiments have shown that thorium preferentially adsorbs onto lithogenics and carbonates, beryllium onto lithogenics and opal, whereas protactinium strongly prefers opal [Lao *et al.*, 1993; Chase *et al.*, 2002; 2003; Guo *et al.*, 2002; Geibert and Usbeck, 2004]. This disparity in adsorption behavior has been regarded to be disadvantageous for particle flux studies [Frank *et al.*, 2000a; Lippold *et al.*, 2009], as it is one additional controlling factor on the tracer flux to the sediment, which may overprint the effect of other controlling factors (such as total particle flux or water mass advection) and complicate the interpretation of the sedimentary tracer records. Within this study it is shown that the distinct adsorption properties of elements in fact may present additional potential for advanced particle flux reconstructions. The following two sections provide a brief introduction to the sources and properties of the particle reactive tracer-isotopes in seawater.

1.3.1 Thorium-230 and Protactinium-231

Thorium-230 and Protactinium-231 are decay products of the Uranium-238 and Uranium-235 decay chains, respectively (**Figure 1.2**). Uranium is supplied from the continents to the oceans by river runoff, aeolian dust, and groundwater discharge [*Henderson and Anderson, 2003*]. Uranium is soluble in oxygenated seawater, and its conservative behavior leads to a residence time [$\sim 400,000$ years; *Henderson and Anderson, 2003*] much longer than the time of the oceanic overturning circulation. Therefore, dissolved uranium is equally distributed throughout the entire water column of the oceans. The uranium isotopes ^{235}U and ^{238}U occur in dissolved form in seawater at a constant activity ratio of $^{238}\text{U}/^{235}\text{U} = 21.77$. Both isotopes are progenitors of several decay products that are particle reactive in seawater (**Figure 1.2**). They adsorb onto particles, sink out of the water column (“scavenging”), and are buried in the sediment. The differing solubility of elements is the property which allows radionuclides to be separated from one another to create disequilibria. The production rates of uranium daughter nuclides are well known and the daughter-progenitor-disequilibria in water column or sediments produced by scavenging provide an insight into oceanic particle fluxes of the past ocean on timescales of days (^{234}Th) to 10^5 years (^{231}Pa and ^{230}Th) [*Rutgers van der Loeff and Geibert, 2008*].

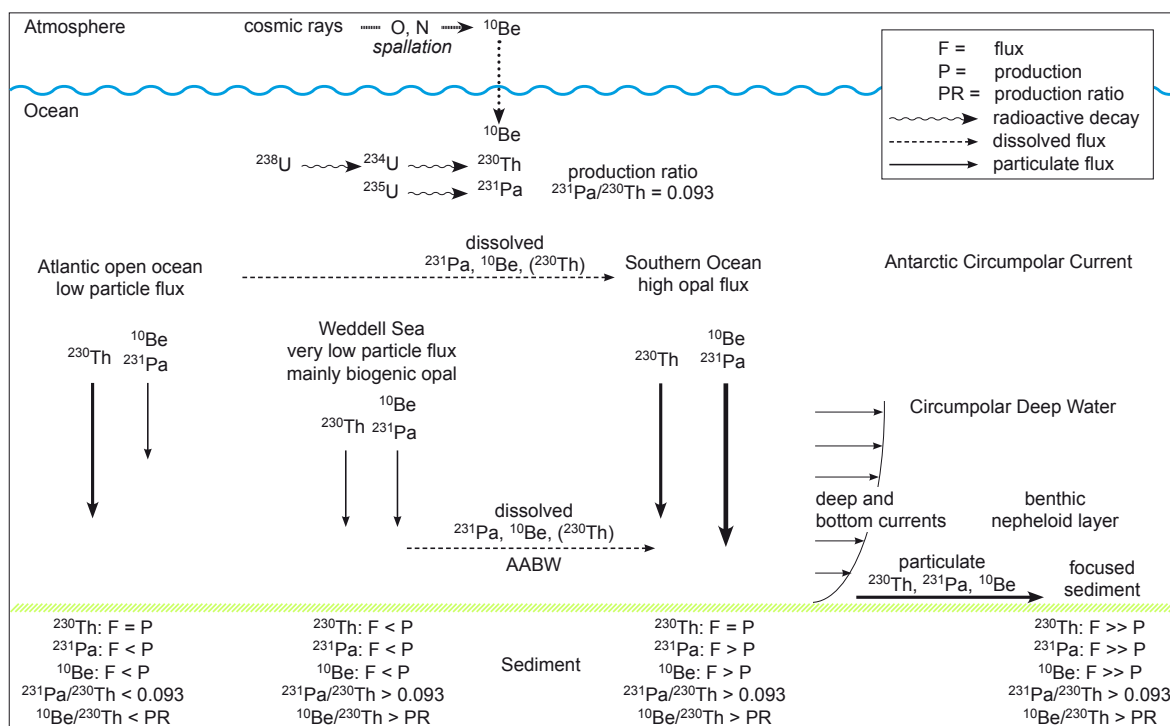


Figure 1.1 ^{231}Pa - ^{10}Be - ^{230}Th fractionation in the oceans, modified after *Henderson and Anderson* [2003]. The length and thickness of the solid arrows represents the intensity of the particulate fluxes (F) of the isotopes illustrating that ^{230}Th is rapidly scavenged everywhere (with notable exception in the Weddell Sea; *Walter et al., 2000*). Dissolved ^{231}Pa and ^{10}Be can be advected from the site of their production (P) to areas of high particle flux resulting in sedimentary isotope ratios that deviate from the production ratio (PR). In areas of strong deep and bottom currents (e.g. Antarctic Circumpolar Current) particles with adsorbed ^{231}Pa , ^{10}Be , and ^{230}Th experience lateral transport contributing to high inventories at places of focused sedimentation.

^{230}Th (half-life 75,380 years) is produced by its progenitor ^{234}U in seawater [$\sim 2910 \text{ dpm m}^{-3}$ at 35 ‰ salinity; *Robinson et al.*, 2004] at a constant rate of $0.0267 \text{ dpm m}^{-3} \text{ a}^{-1}$ [*François et al.*, 2004, cf. **Table 1.1**]. Due to its strong particle reactivity [*Langmuir and Herman*, 1980], ^{230}Th is adsorbed to colloids or suspended particles shortly after its production in seawater [*Moore and Hunter*, 1985; *Moore and Millward*, 1988; *Niven and Moore*, 1993]. Those suspended particles coagulate and aggregate to larger particles and eventually sink to the sea floor [*Rutgers van der Loeff and Geibert*, 2008 and references therein]. The scavenging process for thorium is very efficient so that the rain rate of particulate ^{230}Th to the sea floor is nearly independent from the intensity of particle fluxes, and thus the vertical ^{230}Th flux is spatially and temporally constant and equal [within an uncertainty of $\pm 30\%$; *Henderson et al.*, 1999; *Scholten et al.*, 2001] to its production in the water column. Therefore, the residence time of ^{230}Th in the water column with respect to scavenging is short [10-40 years; *Anderson et al.*, 1983a, b]. Due to its nearly constant vertical flux, the $^{230}\text{Th}_{\text{xs}}$ concentration in sediments is inversely related to the intensity of the vertical particle flux [*Bacon*, 1984; *Suman and Bacon*, 1989].

Table 1.1: Production rates of the tracer isotopes and their concentrations in deep-sea surface sediments

	production rate (*per 1000 m water column) [atoms $\text{cm}^{-2} \text{ a}^{-1}$]	concentration of the scavenged component in surface sediments [g g^{-1}]
^{230}Th	1.5×10^8 (*)	$10^{-11} - 10^{-9}$
^{231}Pa	6.2×10^6 (*)	$10^{-13} - 10^{-11}$
^{10}Be	1.2×10^6	$10^{-15} - 10^{-13}$

The source of ^{231}Pa (half-life 32,760 years) in seawater is the radioactive decay of ^{235}U at a constant rate of $0.0025 \text{ dpm m}^{-3} \text{ a}^{-1}$ (cf. **Table 1.1**). Protactinium is less particle reactive and has a longer scavenging residence time [10^2 years; *Anderson et al.*, 1983a, b)] than thorium. ^{231}Pa is used as particle tracer by normalizing its activity to that of ^{230}Th . The activity ratio of $^{231}\text{Pa}/^{230}\text{Th}$ at the time of production from ^{235}U and ^{234}U is 0.093. The $^{231}\text{Pa}/^{230}\text{Th}$ activity ratios measured in seawater and sediments can deviate from the production ratio as a result from their differences in scavenging behavior. As opposed to ^{230}Th , the distribution of dissolved ^{231}Pa is largely influenced by lateral advection of water masses and its flux to the sediments is controlled by the intensity and composition of particle fluxes [“boundary scavenging”; *Anderson*

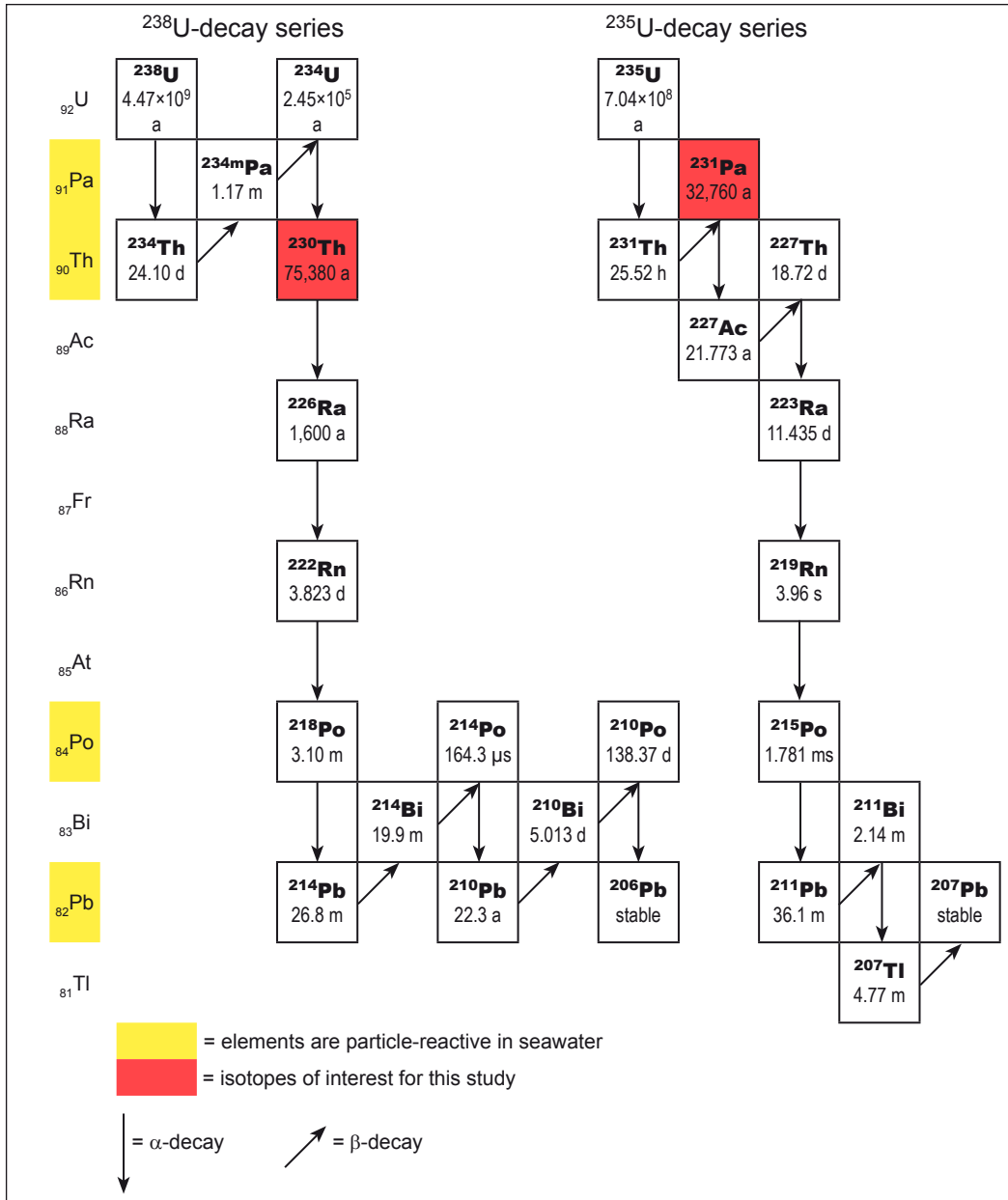


Figure 1.2: ²³⁸U- and ²³⁵U-decay series, modified after Bourdon *et al.* [2003] and Geibert [2008].

et al., 1983a, b; Rutgers van der Loeff and Geibert, 2008, **Figure 1.1**]. It has been recognized that biogenic SiO₂ particles preferentially scavenge protactinium, whereas carbonate and lithogenic particles are efficient thorium scavengers [Luo and Ku, 1999; Chase *et al.*, 2002; Guo *et al.*, 2002; Geibert and Usbeck, 2004].

The scavenging process is the principal source for ²³⁰Th and ²³¹Pa in sediments. Additionally, two further sources contribute variable small amounts to the total ²³⁰Th and ²³¹Pa in sediments: ²³⁰Th and ²³¹Pa that is supported by decaying uranium in lithogenic minerals, and by decaying uranium from authigenic sources. For particle flux studies the scavenged component

of ^{230}Th and ^{231}Pa is of interest only, i.e. the total ^{230}Th and ^{231}Pa measured in sediments must be corrected for the other two components. The scavenged fraction is referred to as “excess” (excess ^{230}Th or $^{230}\text{Th}_{\text{xs}}$ and excess ^{231}Pa or $^{231}\text{Pa}_{\text{xs}}$) and must be decay corrected for the time of deposition, which requires an independent chronology for the sediment core. Chapter 2 in this study provide a brief summary on the calculation of excess ^{230}Th ; [Henderson and Anderson, 2003] provide a more detailed review of this subject.

1.3.2 Beryllium-10

Isotopes of cosmogenic origin such as ^3He , ^{26}Al , ^{14}C and ^{10}Be are of widespread application in geoscience investigation. ^{14}C is incorporated to the global carbon cycle and exchanges between atmosphere, biosphere, and ocean. ^{14}C is an important nuclide for determination of sediment chronologies for the past ~55,000 years. ^3He implanted in micrometeorites by the solar wind, rains down to the Earth’s surface in particulate form and is retained within those particles over at least 10^8 years [Patterson *et al.*, 1998]. Extraterrestrial ^3He is the principal contributor to the total ^3He in pelagic marine sediments [Marcantonio *et al.*, 1996] and is used as a constant flux proxy. Cosmogenic ^{10}Be - and ^{26}Al -atoms in the atmosphere become attached to aerosols which are transported to the Earth’s surface by dry or wet precipitation.

^{10}Be is produced by spallation reactions in the troposphere [high energy fission by cosmic rays; Goel, 1969] on O and N at a globally averaged production rate of 1.2×10^6 atoms $\text{cm}^{-2} \text{a}^{-1}$ at present [Table 1.1, Monaghan *et al.*, 1986]. It has been shown that measurements of ^{10}Be (half-life 1.5×10^6 years) in geophysical reservoirs (such as Antarctic ice or marine sediments) can be used to probe variations in the production rate of cosmogenic nuclides [Raisbeck *et al.*, 1978; 1981b; Beer *et al.*, 1990]. Such variations can be caused by changes in the primary cosmic ray intensity, the geomagnetic field intensity, and solar activity (through the modulating influence of the solar wind). Variations in the geomagnetic field intensity causes latitudinal variations in cosmogenic ^{10}Be production which is largely mixed out during the atmospheric residence time of ~1-2 years [Raisbeck *et al.*, 1981a]. Once introduced to the ocean, ^{10}Be does not re-exchange with the atmosphere [Morris *et al.*, 2002]. Dissolved ^{10}Be is removed from the ocean by scavenging to particles and burial in sediments [Finkel *et al.*, 1977; Kusakabe *et al.*, 1982; Lao *et al.*, 1992; Figure 1.1]. Owing to its residence time of ~500-1000 years, dissolved ^{10}Be is laterally advected in the ocean by different water masses and preferentially scavenged and deposited in regions of high particle flux, similar to ^{231}Pa [“boundary scavenging”; Anderson *et al.*, 1990]. The ^{10}Be flux to marine sediments also vary as a function of lithology [Henken-Mellies *et al.*, 1990; Chase *et al.*, 2003]. Long term records of ^{10}Be in marine sediments serve as a proxy for past variations in cosmic ray intensity and for the past geomagnetic dipole strength [Frank *et al.*, 1997; Frank, 2000; Christl *et al.*, 2007; 2010]. ^{10}Be is also an important tool for sediment chronology [Bourles *et al.*, 1989b; Frank *et al.*, 2008] and for the investigation of water mass

advection [Ku *et al.*, 1990; Frank *et al.*, 2002; Luo and Ku, 2003]. ^{10}Be normalized to the flux of excess ^{230}Th ($^{10}\text{Be}/^{230}\text{Th}_{\text{xs}}$) has been used for the reconstruction of variations in the past ocean productivity [Anderson *et al.*, 1998].

1.4 Influence of particle type and transport on the distribution of particle tracers

The physical decoupling of the proxies in the water column by resuspension and advection of distinct particle types may also affect the distribution of particulate $^{230}\text{Th}_{\text{xs}}$, $^{231}\text{Pa}_{\text{xs}}$, and ^{10}Be in marine sediments. Each particle type may carry a particular isotope signature according to the source and transport pathway of the particle. This has been shown for particles in the water column by numerous studies [e.g. Chase *et al.*, 2002; Scholten *et al.*, 2005]. In addition, several in-vitro scavenging experiments contributed to the understanding of the mechanism of isotope adsorption kinetics [e.g. Geibert and Usbeck, 2004]. On the other hand, studies on particle type-specific isotope distribution in sediments are rare. In case of $^{230}\text{Th}_{\text{xs}}$, it has been shown by Thomson *et al.* [1993] for North-East Atlantic sediments that fine (<5 μm) particles carry the highest $^{230}\text{Th}_{\text{xs}}$ concentrations, and contribute a major proportion to the sedimentary $^{230}\text{Th}_{\text{xs}}$ inventories. Recently, the grain size-specific distribution of both constant flux proxies $^{230}\text{Th}_{\text{xs}}$ and ^3He has been studied by McGee *et al.* [in press] for sediments from the western North Atlantic. They report strong enrichment-factors for $^{230}\text{Th}_{\text{xs}}$ within <4 μm -particles and for ^3He within <20 μm -particles relative to the 4-20 μm - and >20 μm -size fractions, respectively. The role of particle composition on $^{230}\text{Th}_{\text{xs}}$ and $^{231}\text{Pa}_{\text{xs}}$ distribution in sediments was studied by Luo and Ku [1999], but the methods applied by the authors and their conclusions have been questioned by Chase *et al.* [2002]. This dispute shows that compound-specific analysis of scavenged isotopes is still a challenging task. The insight into particle dynamics by compound-specific isotope analysis however, is expected to bear important implication for paleoceanographic studies. For instance, the analysis of beryllium isotopes ($^{10}\text{Be}/\text{Be}$) in a Southern Ocean sediment by a compound-specific measurement on cleansed biogenic silica [Lal *et al.*, 2006] provided information on the past $^{10}\text{Be}/\text{Be}$ ratios of surface waters. Consequently, compound- and grain size-specific analyses of ^{230}Th , ^{231}Pa , and ^{10}Be concentrations and ratios are expected to provide, analogous to the molecular-level ^{14}C ages, insight to the processes of particle transport. **This study, therefore, investigates grain size-specific isotope ($^{230}\text{Th}_{\text{xs}}$, $^{231}\text{Pa}_{\text{xs}}$, ^{10}Be) concentrations, and focuses on the question if particle size and composition combined with the process of particle transport could lead to a decoupling between ^{230}Th , ^{231}Pa , and ^{10}Be in sediments, and to what extent this particle sorting effect could generate a bias to flux calculations based on those tracers.** The grain size distributions in pelagic sediments are closely coupled with the intensity of deep and bottom currents which immediately control the deposition or resuspension of particles [McCave, 1984; McCave and Hall, 2006]. In this study therefore, sediment was fractionated by sieving and settling into various particle types differing in size and density (Figure 1.3).

According to their size, density and composition, those separated particle type classes, together with the associated isotope signatures are attributed to a particular pathway (i.e. vertical vs. lateral fluxes).

The information on particle size-specific isotope signatures allows assessment of whether particle sorting could bias the bulk isotope signature in such a way that the derived variables would lead to a wrong conclusion. *Scholten et al.* [1994] performed grain size-specific $^{230}\text{Th}_{\text{xs}}$ measurements and concluded that a reasonable application of $^{230}\text{Th}_{\text{xs}}$ -normalization is restricted to those investigations where the origin and grain size dependent composition of focused sediment is known. Also other authors [*Frank et al.*, 1996; *François et al.*, 2004; *Geibert et al.*, 2005] mention a particle sorting effect as a potential source of uncertainty for the $^{230}\text{Th}_{\text{xs}}$ method. This uncertainty however, has not yet been quantified and is one major focus of this study. Moreover, this study provides insight into the source of laterally advected particulate material by the combined interpretation of grain size-specific ^{230}Th with data on sedimentology and compound-specific ^{14}C -ages. The flux proxies $^{231}\text{Pa}_{\text{xs}}/^{230}\text{Th}_{\text{xs}}$ and $^{10}\text{Be}/^{230}\text{Th}_{\text{xs}}$ are commonly regarded as being insensitive to post-depositional particle transport, an assumption that also is tested in this study by the particle type-specific measurements.

In general, the goal of obtaining high-resolution records of paleoceanographic processes has led to the selection of coring sites in areas of high sedimentation rates. Often though, high sedimentation rates may result from sediment drifts created by bottom currents. These are the settings where sediment redistribution is maximized and the accumulation history is at its most complicated [*McCave*, 2002; *Ohkouchi et al.* 2002]. Focusing of particles by deep-sea currents may create artifacts in paleoceanographic studies because the primary vertical particle flux is substantially diluted by advected particles from secondary sources. At sites of strong sediment focusing, the lateral contribution of material dominates the sedimentation rates. The proportion of the lateral contribution of sediment can be quantified by the “focusing factor”, which is calculated from downcore records of excess ^{230}Th in sediments [e.g. *François et al.*, 2004]. A focusing factor greater than 1 indicates an accumulation of excess ^{230}Th greater than that expected by production in the water column, i.e. bottom currents have laterally advected particles that contain excess ^{230}Th . Extremely high focusing factors (up to ~10) have been reported for regions of the Southern Ocean [e.g. *Dezileau et al.*, 2000] and the east equatorial Pacific [Panama Basin, *Kienast et al.*, 2007]. This has led to the dispute as to whether or not focusing factors can be regarded as quantitative estimates for sediment focusing in the Panama Basin [*Lyle et al.*, 2005; 2007; *François et al.*, 2007]. By using a combination of both constant flux proxies $^{230}\text{Th}_{\text{xs}}$ and ^3He , *Marcantonio et al.* [2001] and *Higgins et al.* [2002] showed for the Equatorial Pacific that variations in the sediment accumulation are driven by climate-related changes in deep-ocean circulations rather than by changes in the supply of sediment. However, the origin of sediment focusing and $^{230}\text{Th}_{\text{xs}}$ accumulation is not yet readily understood. This study, therefore, seeks to

contribute towards the understanding of focusing processes at three locations where focusing is of particular importance: the Southern Ocean (Eastern Atlantic sector), the Southeastern Atlantic (Walvis Ridge), and the Eastern Equatorial Pacific (Panama Basin).

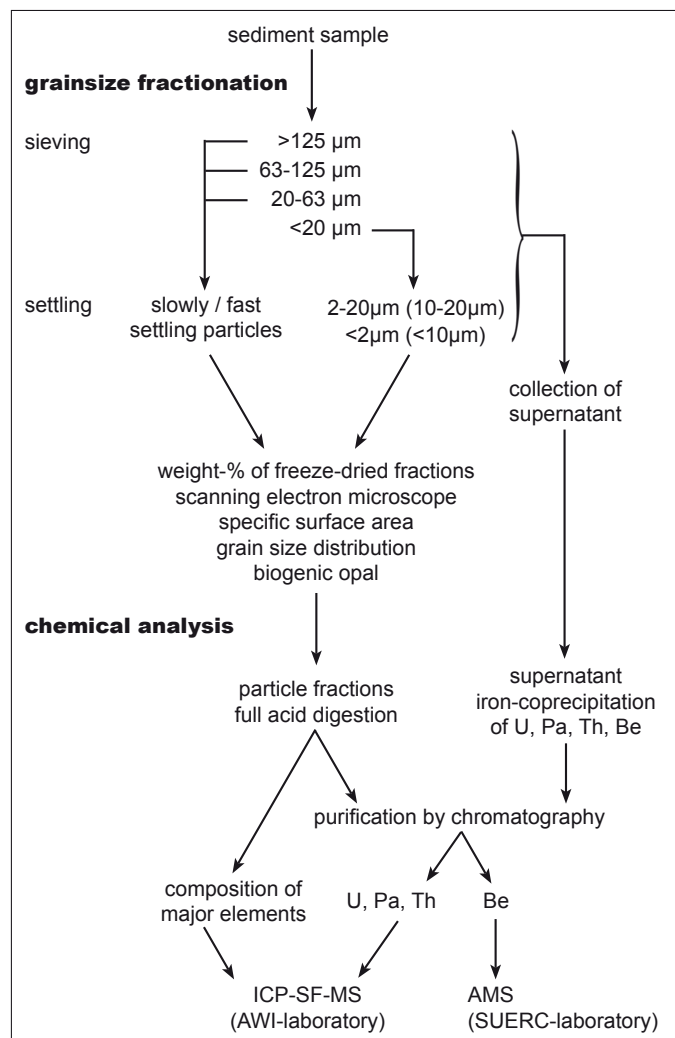


Figure 1.3: Schematic of analyses performed for this study.

1.5 Objectives

At three study locations, the Southern Ocean, the Panama Basin, and the Southeast Atlantic, two neighboring sediment coring sites (“twin cores”) with contrasting mass accumulation rates are investigated. By comparing sites of slow versus rapid sedimentation, the effect of particle advection on tracer accumulation is quantified. In order to study the effect of past climate changes on sediment focusing, sediment samples from time periods between the Last Glacial Maximum to the early Holocene have been selected. Those samples were fractionated into particle classes of different grain sizes and densities by sieving and settling. Isotope analyses have been performed

on those particle classes (**Figure 1.3**). As previously outlined, those data on particle size specific isotopes help in understanding the process of particle redistribution, because distinct particle classes are ascribed to particular sources and transport pathways. The study on particle fractions further provides an estimate of the uncertainty in particle flux studies introduced by particle sorting. The following four manuscripts contribute to the understanding of particle dynamics and to the application of particle flux proxies.

1.5.1 Grain size specific $^{230}\text{Th}_{\text{xs}}$

The first manuscript (Manuscript I: *Grain size effects on $^{230}\text{Th}_{\text{xs}}$ inventories in opal-rich and carbonate-rich marine sediments*) seeks to identify and characterize those particle classes that represent the main carrier for $^{230}\text{Th}_{\text{xs}}$ during the last deglacial period. Samples from the Southern Ocean and the Southeastern Atlantic are analyzed. The twin cores from the Southern Ocean differ in their accumulation rates by a factor of ~ 2 as revealed by subbottom echo sounding (**Figure 1.4**). Using magnetic susceptibility, the slowly accumulated sediment core (PS1769-1) is correlated to the well constrained stratigraphy of the rapidly accumulated core (PS1768-8) (**Figure 1.5**). Two methods of sediment fractionations are tested for their suitability in particle-specific radionuclide analyses. Further, the hypothetical effect of size sorting on the application of $^{230}\text{Th}_{\text{xs}}$ as a constant flux proxy is quantified using a grain size correction method based on the grain size-specific $^{230}\text{Th}_{\text{xs}}$ concentrations. In addition, the lateral advection of organic matter at both study sites is discussed based on the grain size-specific authigenic uranium record.

1.5.2 The origin of focused sediments

The second manuscript (Manuscript II: *The origin of focused marine sediments: an exploration of local vs. remote sediment sources from grain size data, $^{230}\text{Th}_{\text{xs}}$ and clay mineralogy*) shows how grain size specific $^{230}\text{Th}_{\text{xs}}$ data can be applied on an entire sediment core (the Southern Ocean study site) in order to gain new information on the history and mechanism of $^{230}\text{Th}_{\text{xs}}$ accumulation. It investigates whether or not lateral particle advection with subsequent particle sorting could significantly bias the calculations of the past vertical fluxes at this study site. The dataset from the first manuscript is supplemented by additional measurements of grain size-specific $^{230}\text{Th}_{\text{xs}}$. This manuscript discusses whether a generalized statement on the grain size-specific $^{230}\text{Th}_{\text{xs}}$ distribution can be made for the past 140,000 years. Additional measurements of grain size distributions by laser diffraction help identifying the particular grain size fraction which is responsible for the lateral sediment contribution. As the clay mineral assemblages in sediment cores are known to trace deep-water advection and sources of sediment, they are exploited together with $^{230}\text{Th}_{\text{xs}}$ data in order to reveal the pathway of advected particulate $^{230}\text{Th}_{\text{xs}}$.

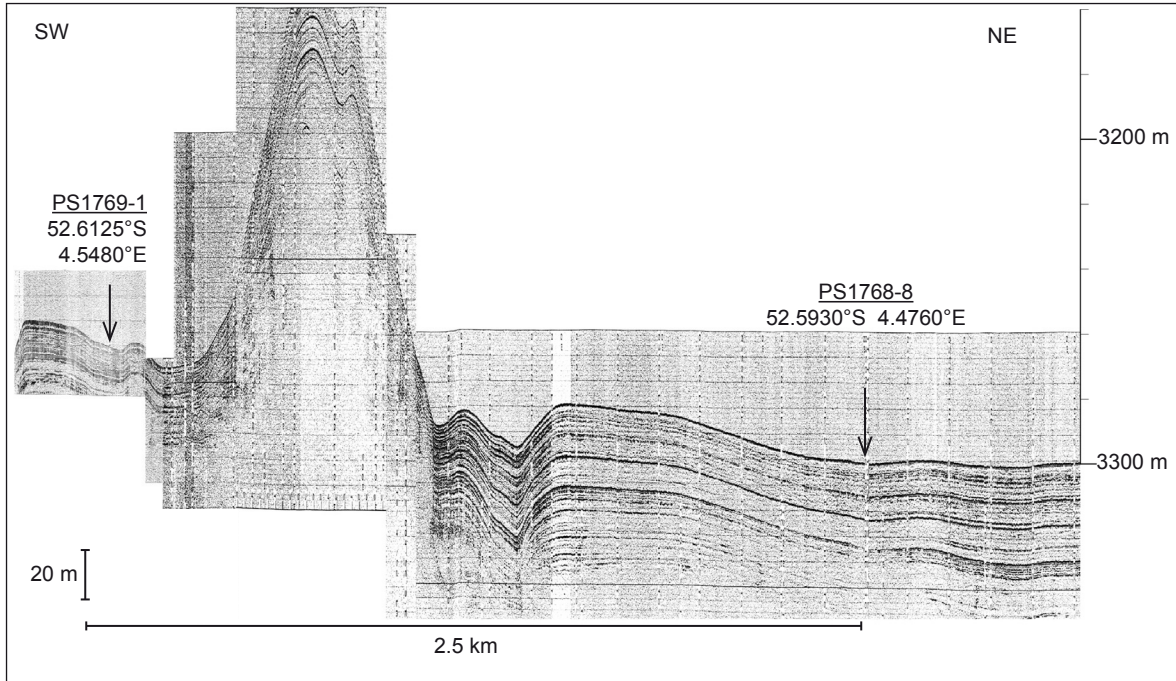


Figure 1.4: Sediment echo sounder profile (PARASOUND) along a cross section at the study site in the Eastern Atlantic Sector of the Southern Ocean. The arrows indicate the coring sites of the sediment cores PS1768-8 and PS1769-1 with a lateral separation of 2.5 km (“twin cores”). The reflector lines reveal that sedimentation at PS1768-8 is two-fold compared with PS1769-1.

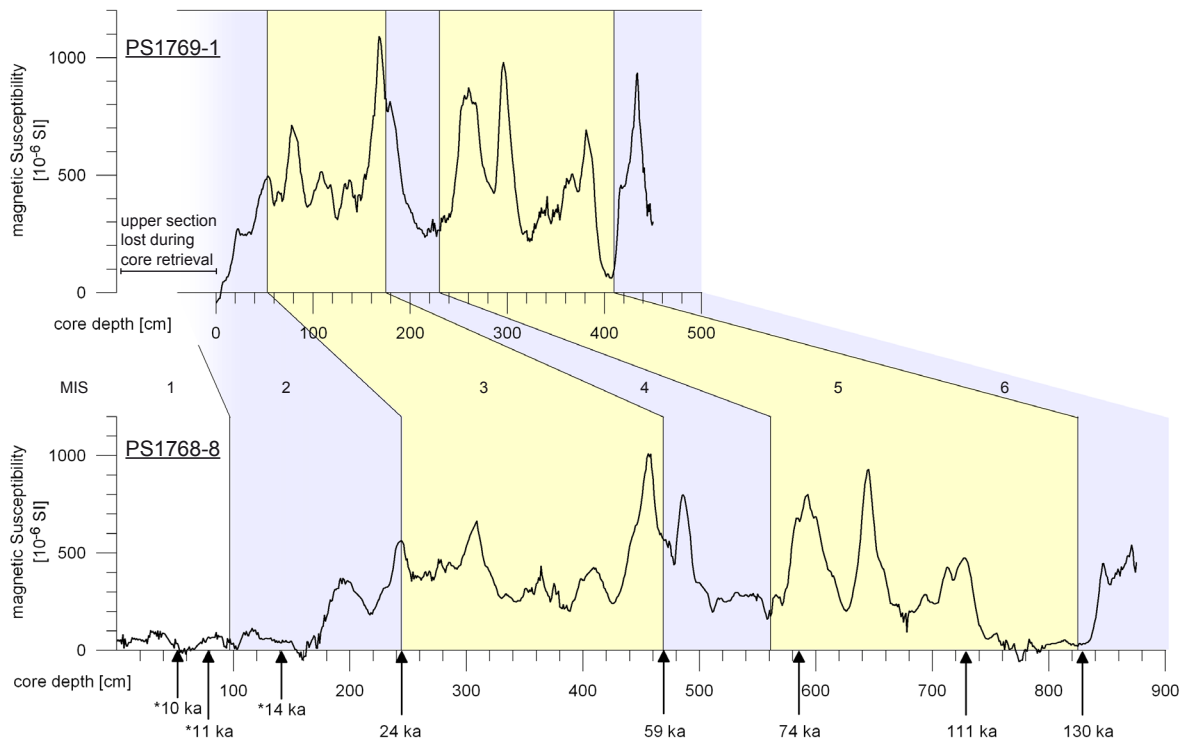


Figure 1.5: Magnetic susceptibility downcore records from sediment cores PS1768-8 and PS1769-1. The age model of core PS1768-8 is constrained by a combination of radiocarbon dating (labeled with *), oxygen isotope stratigraphy, siliceous microfossil biofluctuation stratigraphy, and $^{230}\text{Th}_{\text{ss}}$ dating [Frank et al., 1996]. Age control for core PS1769-1 was obtained by correlating the magnetic susceptibility record to that of the parallel core.

1.5.3 Sediment redistribution in the Panama Basin

Recently, there is an ongoing debate whether $^{230}\text{Th}_{\text{xs}}$ focusing is a quantitative measure for sediment focusing in the Panama Basin. In fact, some investigators suspect that the basic conditions for applying $^{230}\text{Th}_{\text{xs}}$ as a constant flux proxy are not fulfilled in this region, and consequently, that preserved vertical fluxes and redistribution of sediment, both based on $^{230}\text{Th}_{\text{xs}}$ measurements, do not reflect naturally occurring sedimentation processes of the past. The third manuscript (Manuscript III: *Contributions from size fraction-specific $^{230}\text{Th}_{\text{xs}}$ data towards understanding of sediment redistribution processes in the Panama Basin*) focuses on the processes leading to high $^{230}\text{Th}_{\text{xs}}$ accumulation in this region. The method for grain size-specific $^{230}\text{Th}_{\text{xs}}$ as developed in the first manuscript is applied to those sediment samples from the Panama Basin, on which molecular-level ^{14}C ages have been published by *Kusch et al.* [2010]. Based on the compound-specific ^{14}C and $^{230}\text{Th}_{\text{xs}}$ data in concert with findings from the second manuscript and other studies, a scenario for explaining the process of sedimentation in the Panama Basin during the Last Glacial and the Holocene is developed.

1.5.4 Grain size specific $^{231}\text{Pa}_{\text{xs}}$ and ^{10}Be

As abovementioned, the timescale and amount of past sediment redistribution may be quantitatively estimated using compound-specific ^{14}C dating and $^{230}\text{Th}_{\text{xs}}$ measurements, respectively. The application of isotope ratios $^{231}\text{Pa}_{\text{xs}}/^{230}\text{Th}_{\text{xs}}$ and $^{10}\text{Be}/^{230}\text{Th}_{\text{xs}}$ add to this suite of proxies as they record the relative intensity of past vertical particle fluxes. However, ^{231}Pa and ^{10}Be differ in their chemical affinity to particular sediment phases, so that the isotope ratios may be affected by particle sorting during lateral advection, similar to the effect on ^{14}C and $^{230}\text{Th}_{\text{xs}}$. Within the fourth manuscript (Manuscript IV: *Fractionation of ^{230}Th , ^{231}Pa , and ^{10}Be induced by particle size and composition within an opal-rich sediment of the Atlantic Southern Ocean*), therefore, we investigate particle type-specific isotope ratios on those same samples from the Southern Ocean site that have been studied for the first manuscript. The disparity of Pa, Th, and Be in adsorption to particles is discussed and the influences of particle source and transport on isotope ratios are assessed.

Chapter 2

Grain size effects on $^{230}\text{Th}_{\text{xs}}$ inventories in opal-rich and carbonate-rich marine sediments

Sven Kretschmer^{1,2}, Walter Geibert^{3,4}, Michiel M. Rutgers van der Loeff¹, Gesine Mollenhauer^{1,2}

¹Alfred Wegener Institut für Polar- and Meeresforschung, Bremerhaven, Germany

²Fachbereich Geowissenschaften, Universität Bremen, Germany

³School of GeoSciences, University of Edinburgh, UK

⁴Scottish Association for Marine Science, Dunstaffnage Marine Laboratory, Oban, UK

Manuscript published in *Earth and Planetary Science Letters* 294 (2010) 131-142, doi:10.1016/j.epsl.2010.03.021

Abstract

Excess Thorium-230 ($^{230}\text{Th}_{\text{xs}}$) as a constant flux tracer is an essential tool for paleoceanographic studies, but its limitations for flux normalization are still a matter of debate. In regions of rapid sediment accumulation, it has been an open question if $^{230}\text{Th}_{\text{xs}}$ -normalized fluxes are biased by particle sorting effects during sediment redistribution. In order to study the sorting effect of sediment transport on $^{230}\text{Th}_{\text{xs}}$, we analyzed the specific activity of $^{230}\text{Th}_{\text{xs}}$ in different particle size classes of carbonate-rich sediments from the South East Atlantic, and of opal-rich sediments from the Atlantic sector of the Southern Ocean. At both sites, we compare the $^{230}\text{Th}_{\text{xs}}$ distribution in neighboring high vs. low accumulation settings. Two grain-size fractionation methods are explored. We find that the $^{230}\text{Th}_{\text{xs}}$ distribution is strongly grain size dependent, and 50-90 % of the total $^{230}\text{Th}_{\text{xs}}$ inventory is concentrated in fine material smaller than 10 μm , which is preferentially deposited at the high accumulation sites. This leads to an overestimation of the focusing factor Ψ , and consequently to an underestimation of the vertical flux rate at such sites. The distribution of authigenic uranium indicates that fine organic-rich material has also been re-deposited from lateral sources. If the particle sorting effect is considered in the flux calculations, it reduces the estimated extent of sediment focusing. In order to assess the maximum effect of particle sorting on Ψ , we present an extreme scenario, in which we assume a lateral sediment supply of only fine material (<10 μm). In this case, the focusing factor of the opal-rich core would be reduced from $\Psi = 5.9$ to $\Psi_{\text{corrected}} = 3.2$. In a more likely scenario, allowing silt-sized material to be transported, Ψ is reduced from 5.9 to 5.0 if particle sorting is taken into consideration. The bias introduced by particle sorting is most important for strongly focused sediments. Comparing $^{230}\text{Th}_{\text{xs}}$ -normalized mass fluxes biased by sorting effects with uncorrected mass fluxes, we suggest that $^{230}\text{Th}_{\text{xs}}$ -normalization is still a valid tool to correct for lateral sediment redistribution. However, differences in focusing factors between core locations have to be evaluated carefully, taking the grain size distributions into consideration.

2.1 Introduction

2.1.1 Main carrier phases for $^{230}\text{Th}_{\text{xs}}$ in water column and sediment

The accurate knowledge of vertical and lateral particle transport in the ocean is crucial for understanding the modern biogeochemical cycles and for paleoceanographic reconstructions. The naturally occurring radionuclide Thorium-230 (^{230}Th) is considered to be a powerful tracer of marine particle transport, because of its short residence time in the ocean and nearly constant flux to the seafloor [Thomson *et al.*, 1993; Henderson *et al.*, 1999]. ^{230}Th is supplied to seawater uniformly at a rate of $0.0267 \text{ dpm m}^{-3} \text{ a}^{-1}$ from decaying Uranium-234 (^{234}U). However, concentrations of dissolved ^{230}Th in seawater are very low because it becomes rapidly attached to suspended and sinking particles (=excess ^{230}Th , $^{230}\text{Th}_{\text{xs}}$) by the “reversible scavenging” mechanism [Nozaki *et al.*, 1981; Bacon and Anderson, 1982]. This process eventually transports ^{230}Th to the sea floor. Th sorption kinetics have been studied in vitro under well defined experimental conditions [e.g. Guo *et al.*, 2002; Geibert and Usbeck, 2004] but results from in situ measurements (sediment traps or in situ-pumps) are difficult to interpret, leading to an on-going debate about the main carrier phases of adsorbed Th under natural conditions. In general, Th sorption in seawater has been found to be weak on biogenic silica [Chase *et al.*, 2002; Roy-Barman *et al.*, 2005]. Main carrier phases have been identified as lithogenics [Luo and Ku, 1999], carbonates and lithogenics [Chase *et al.*, 2002; Siddall *et al.*, 2005], or Mn oxides [Roy-Barman *et al.*, 2005, 2009]. In the upper water column, findings of ^{234}Th [Santschi *et al.*, 2006] suggest that most Th is transported by organic phases like acid polysaccharides, which are not likely to be transported unmodified to the sea floor.

Carrier phases can be classified by their composition and origin, or by different grain size fractions. As summarized by Rutgers van der Loeff and Geibert [2008], adsorbed Th can change the carrier phase during settling through the water column by numerous processes. Once buried in the sediment, Th carrier phases are affected by early diagenetic processes, and also by lateral redistribution, e.g. in a nepheloid layer [Rutgers van der Loeff *et al.*, 2002]. Scholten *et al.* [1994] suggested restricting the application of $^{230}\text{Th}_{\text{xs}}$ normalized fluxes to those settings where the origin and grain-size dependent composition of focused sediment is known, a suggestion that has so far not been realized. When the $^{230}\text{Th}_{\text{xs}}$ normalization method was established, Bacon [1984] already recommended considering separately the fine and coarse fractions of carbonate sediments. François *et al.* [2004] advise that $^{230}\text{Th}_{\text{xs}}$ normalization should not be applied to the coarse fraction of the sediment as it is much less prone to lateral redistribution. However, to our knowledge, the grain size dependent distribution of ^{230}Th in sediments has been addressed in only three studies [Luo and Ku, 1999; Thomson *et al.*, 1993; Scholten *et al.*, 1994].

2.1.2 $^{230}\text{Th}_{\text{xs}}$ applications, assumptions and uncertainties

Using $^{230}\text{Th}_{\text{xs}}$ in sediments, we are able to distinguish between (a) vertical rain rate, providing the amount of sediment that settled vertically through the water column and (b) syndepositional or postdepositional sediment dislocation by currents, estimated with the focusing factor Ψ that characterizes sediment winnowing ($\Psi < 1$) or focusing ($\Psi > 1$) conditions. The method of $^{230}\text{Th}_{\text{xs}}$ normalization was developed by e.g. Bacon [1984], Suman and Bacon [1989] and François *et al.* [1990]. It was reviewed by Frank *et al.* [1999], Henderson and Anderson [2003] and François *et al.* [2004].

Paleoceanographic studies often target locations of high sediment accumulation in order to achieve high temporal resolution. However, these locations are often strongly affected by lateral sediment redistribution [e.g. Bianchi and McCave, 2000; Ohkouchi *et al.*, 2002] so that the reconstruction of the vertical particle fluxes needs to be corrected by $^{230}\text{Th}_{\text{xs}}$ -normalization. Evidence for strong lateral redistribution has been detected e.g. in sediments from Bermuda Rise [$\Psi = 13.2$; Suman and Bacon, 1989], the Southern Ocean Indian sector [$\Psi = 12.5$; François *et al.*, 1993 and $\Psi = 10.0$; Dezileau *et al.*, 2000], in the Southern Ocean Atlantic sector [$\Psi = 7.7$; Frank *et al.*, 2000a], in the equatorial Pacific [$\Psi = 4$; Marcantonio *et al.*, 2001; $\Psi = 8$; Loubere *et al.*, 2004 and $\Psi = 7.5$; Kienast *et al.*, 2007]. It is still unclear to which extent the corrected fluxes are biased due to particle sorting effects during sediment redistribution. This is an important aspect in recent discussions about the validity of the entire approach, e.g. in the equatorial Pacific [Thomas *et al.*, 2000; Lyle *et al.*, 2005, 2007; François *et al.*, 2007; Broecker, 2008].

The main assumption for applying $^{230}\text{Th}_{\text{xs}}$ normalization and the focusing factor is that redistribution affects the total sediment, i.e. grains of all particle sizes are resuspended, transported and redeposited together. It is further assumed that sediment from the vertical flux and laterally supplied sediments are equal in composition, size distribution and $^{230}\text{Th}_{\text{xs}}$ concentration. In this study, we test the hypothesis that the grain size fractions differ in composition and $^{230}\text{Th}_{\text{xs}}$ activity. A further hypothesis is that the redistribution of particles is variable for different grain sizes and will introduce a sorting effect on $^{230}\text{Th}_{\text{xs}}$ inventories in sediments. For this purpose, we will (a) present data of $^{230}\text{Th}_{\text{xs}}$ distribution by sediment particle class and identify the main carrier phase, taking into consideration the effect of lithology (carbonate-rich vs. opal-rich), (b) compare $^{230}\text{Th}_{\text{xs}}$ inventories of rapidly and slowly accumulated sediments (“twin cores”) and (c) calculate the maximum bias on the focusing factor introduced by the particle sorting effect.

2.2 Materials and Methods

2.2.1 Sample selection

To study the influence of sediment redistribution on the $^{230}\text{Th}_{\text{xs}}$ -signal, inventories of $^{230}\text{Th}_{\text{xs}}$ from neighboring sites, characterized by contrasting accumulation conditions, were

compared. Therefore, two sediment cores (“twin cores”) were chosen being in close vicinity to each other and similar in water depth. In addition, the stratigraphy needed to be well constrained. We selected a twin core location fulfilling all requirements located in the Southern Ocean (PS1768-8 and PS1769-1). Because of its high content of biogenic silica this sediment is from hereon referred to as the “siliceous sediment”. A second set of twin cores is located in the SE Atlantic Ocean (GeoB1027-2 and GeoB1028-4). We refer to it as “carbonate sediment” due to high content of CaCO_3 . In the following, the two locations of the twin cores are described briefly.

Table 2.1: Position and sedimentology of the studied sediment samples. Shading indicates the core sites under slowly accumulating conditions.

core ID	latitude °S	longitude °E	waterdepth [m]	coredepth [cm]	age [ka]	DBD [g cm ⁻³]	TOC [%]	CaCO ₃ [%]	opal [%]
GeoB1027-2	-19.6558	9.1377	2668	13-16	3.1	0.76	0.64 ^a	83 ^a	n.a.
GeoB1028-4	-20.0993	9.1777	2215	16-19	4.8	0.80	0.28 ^b	93 ^b	0.5 ^b
PS1768-8	-52.5930	4.4760	3299	166-169	16	0.82 ^c	0.47 ^c (1.03) ^e	0.9 ^c	55
PS1769-1	-52.6125	4.4580	3269	14-16	16	0.85 ^d	0.21 ^d (0.53) ^e	0.6 ^d	60

(a) and (b) from Müller [2003a, b].

(c) and (d) unpublished data [personal communication G. Kühn] averaged over depth intervals 1.60-1.71 m and 0.1-0.2 m, respectively.

(e) TOC analyzed on size fraction <20 μm

2.2.1.1 Carbonate sediment

Two giant box corers, GeoB1027-2 and GeoB1028-4 were recovered at approximately 20°S, 9°E from the Walvis Ridge, South East Atlantic in the Benguela upwelling area with a lateral distance of 49 km between core sites. GeoB1027-2 was taken in 2668 m water depth, where an echosounder survey indicated focusing of surface sediment layers. In contrast, site GeoB1028-4 was collected from a depth 453 m shallower, and less affected by focusing. The sediment of both core sites consists of foraminiferal sand and carbonaceous mud. Near surface samples were taken from GeoB1027-2 at 13-16 cm (3.1 ka) and from GeoB1028-4 at 16-19 cm (4.8 ka, **Table 2.1**).

2.2.1.2 Siliceous sediment

The second study area is located in the Southern Ocean, currently south of the Antarctic Polar Front and north of Bouvet Island in the permanently sea-ice-free Antarctic Zone. The gravity cores PS1768-8 and PS1769-1 were recovered at 52.6°S and 4.5°E with a lateral distance of 2.5 km, in water depths of 3300 m and 3270 m, respectively. The Parasound survey (**Figure 1.4**) revealed twofold higher sedimentation rates at site PS1768-8 than at the 30 m shallower site PS1769-1. The sediment consisted of alternating layers of diatomaceous mud and ash-bearing diatomaceous mud with few calcareous microfossils [*Gersonde and Hempel, 1990*]. Age control of sediment core PS1768-8 was established by radiocarbon dating and diatom stratigraphy. This core has been studied extensively [e.g. *Diekmann et al., 2003; Nürnberg et al., 1997; Zielinski et al., 1998*]. *Frank et al.* [1996] reported for this core site during Holocene and LGM a focusing factor of 4.5-6 and vertical rain rates of 1-4 g cm⁻² ka⁻¹. Sediment core PS1769-1 has been less extensively analyzed, and the stratigraphy was obtained by correlation of the magnetic susceptibility record with that of the parallel core PS1768-8 (**Figure 1.5**). Samples were taken from core depths 1.66-1.69 m (PS1768-8) and 0.14-0.16 m (PS1769-1) with an interpolated age of 16 ka (**Table 2.1**).

2.2.2 Grain size fractionation

In the following section we present two methods of sediment fractionation by sieving and settling in (a) purified water with ultrasonication and (b) natural seawater without ultrasonication. In most previous studies for grain size-specific metal analysis the water used for wet sieving was discarded afterwards [e.g. *Ackermann et al., 1983; Barbanti and Bothner, 1993; Koopmann and Prange, 1991*]. *Förstner* [2004] pointed out that generally wet sieving does not alter metal concentrations. However, the potential leakage of U and Th from solids to supernatant during the processing must be taken into account, which was one important consideration in this study.

2.2.2.1 Grain size fractionation in purified water

Samples were not dried prior to grain size fractionation in order to avoid artifacts by particle aggregation. The dry net weight was calculated using moisture content data determined separately. For desalination, samples were suspended in purified water (>15 MΩ, Elix 5, Millipore Corporation) (weight:volume 1:5) and agitated for two minutes, then centrifuged and decanted. This “washing” procedure was repeated three times for leaching the sea salt ions from the sediment because particles smaller than 10-20 μm are prone to be coagulated by cations [*Köster, 1964; McCave et al., 1995*]. For disaggregation, the samples were ultrasonicated. Chemical dispersants were not applied as these may interact with the particles’ active surface

layer and may affect Th adsorption. Samples were wet-sieved subsequently with three nylon sieves (125 μm , 63 μm , 20 μm) using purified water (“pureW”) for 10 min each. The particle suspension that passed the <20 μm sieve was collected in cylinders for further fractionation into classes <2 μm and 2-20 μm based on the settling velocity principle. The terminal fall velocity of particles in an aqueous fluid was determined according to Stokes law [descriptions e.g. in Köster, 1964 and Syvitski *et al.*, 1991] assuming the particle density to be equal to the density of quartz (2.65 g cm^{-3}). The resulting grain sizes are quartz-equivalent spherical sedimentation diameters (ESSD). After a certain settling time, the fine fraction (ESSD: <2 μm) remaining in suspension was siphoned off, while the coarser fraction (ESSD: 2-20 μm) settled out from suspension to the bottom of the settling tube and was again resuspended in purified water. This procedure was repeated 10-20 times until the supernatant fluid achieved a low turbidity. Due to the repeated decantations the <2 μm -fraction was recovered in a volume of 10 to 30 L of water. As flocculation reagent, a CaCl_2 -solution was added for extracting all particles from the water. The flocculated particles were allowed to settle down for four days, and then supernatant was decanted and stored separately in a canister.

The coarse fractions (>20 μm) of the siliceous samples (PS1768 and PS1769) consisted of a mixture of biogenic opal particles and lithogenic particles that are distinctly different in densities (diatoms: ~1.1 g cm^{-3} reported for different diatom species by *van Ierland and Peperzak*, 1984; quartz: 2.65 g cm^{-3} , *Klein et al.*, 1985), which influence their hydrodynamic properties and hence their sinking velocity in a natural marine system. Therefore, a further separation by settling was performed. The three sieve fractions 20-63 μm , 63-125 μm and >125 μm were split into slowly settling and fast settling fractions. Three settling velocities were specified: the maximum terminal velocity, $V_{\tau\text{-max}}$ (fast sinking particles), the minimum terminal velocity $V_{\tau\text{-min}}$ (slowly sinking particles) and the cut-off velocity V_c . $V_{\tau\text{-max}}$ was estimated assuming the average density of quartz (2.65 g cm^{-3}). $V_{\tau\text{-min}}$ was determined empirically by measuring settling times of the slowest particles. V_c is the intermediate velocity between $V_{\tau\text{-max}}$ and $V_{\tau\text{-min}}$ that was chosen to siphon off the slowly settling fraction after the fast fraction settled to the bottom. This separation was repeated for each fraction 15-20 times until the supernatant fluid appeared clear.

The carbonate samples (GeoB1027 and GeoB1028) displayed homogeneous particle densities because this sediment was mainly composed of carbonaceous microfossils. For this reason the above described separation of slowly and fast settling was not applied to these samples.

2.2.2.2 Grain size fractionation in natural seawater

As we wanted to infer information about the transport of adsorbed particulate Th in seawater, we applied a second fractionation method with modified pretreatment and natural seawater as sieving fluid. The seawater technique should simulate “near-natural” conditions.

Natural seawater (“seaW”) was filtered through polycarbonate-filters (pore size 1 μm) before sieving. The samples were suspended in seawater and agitated for 2 minutes. The sieve and settle process was as described in section 2.2.2.1, but omitting the desalination and ultrasonication steps. The separation into the classes $<2\ \mu\text{m}$ and $2\text{-}20\ \mu\text{m}$ was not possible, as the smallest particles flocculated in seawater. Therefore the size class $<20\ \mu\text{m}$ was split into $<10\ \mu\text{m}$ and $10\text{-}20\ \mu\text{m}$ by settling as described in 2.2.2.1.

2.2.2.3 Processing of supernatants

In order to minimize the loss of Th and U by desorption effects, processing time was kept as short as possible, and small water volumes were used. However, assuming a leaching of U and Th due to desorption and dissolution effects, we collected the supernatant fluid (10-30 L per sample) in canisters for further processing. First the supernatant was filtered through a polycarbonate-filter (1 μm) in order to remove any remaining particulate Th. *Moore and Hunter* [1985] reported that 90-95 % of particulate Th suspended in seawater is filtered by a 1.2 μm -filter. The filter was fully digested and analyzed for Th and U isotopes following the same protocol for sediment analysis (section 2.2.3). The results of particulate Th and U on filters were not reported separately. Instead, they were included in the smallest fraction ($<2\ \mu\text{m}$ or $<10\ \mu\text{m}$). The filtrated supernatant fluid was then acidified to pH 2-3 by addition of HNO_3 (subboiling distilled). A solution of iron chloride (FeCl_3 in HCl , $50\ \text{mg mL}^{-1}$) was added together with the spikes ^{229}Th and ^{236}U . After 24 hours of equilibration, the pH was readjusted to pH 8 to 9 by adding NH_3 (suprapur) for the co-precipitation with $\text{Fe}(\text{OH})_3$ [*Rutgers van der Loeff and Moore*, 1999]. The $\text{Fe}(\text{OH})_3$ -precipitate was re-dissolved in HNO_3 , and Fe, Th and U were separated by ion exchange columns following the same protocol as described for the sediment samples (section 2.2.3).

2.2.2.4 Procedural blanks

Procedural blanks have been determined for both fractionation methods for comparison with the supernatants' Th and U contents for detecting any potential loss or uptake of Th and U that occurred during the fractionation procedures. Two blanks were performed with purified water (8 L each), and two blanks with seawater (5 L and 22 L). The procedural blanks accounted for 0.01-0.08 % (^{230}Th), 0.01-0.15 % (^{232}Th), 0.01-0.27 % (^{238}U in pureW), and 70-200% (^{238}U in seaW) of the concentrations found in sediment samples.

2.2.3 Analysis of U and Th isotopes

Th and U isotopes were analyzed on freeze-dried samples (5-50 mg) by isotope dilution, i.e. adding spikes of ^{229}Th (9 pg) and ^{236}U (800 pg) as internal standards. Samples and spikes were weighed into Teflon vials and fully dissolved in HNO_3 (3 mL, concentrated, subboiling distilled), HCl (2 mL, 30 %, suprapur) and HF (0.5 mL, 40 %, suprapur) by heating to 225°C for 2 h in a pressure-assisted microwave digestion system (CEM MARSXpress). After sample digestion, the acid was fumed off until dry by gentle heating in the microwave evaporation system (CEM XpressVap). The samples were then re-dissolved in diluted HNO_3 (5 mL, 1 M, subboiling distilled) and heated to 150°C for 15 min. Iron chloride (100 μL) for precipitation was added. The $\text{Fe}(\text{OH})_3$ -precipitates of sediment samples and supernatant samples were re-dissolved in HNO_3 (3 mL, 3 M), and Fe, Th and U were separated by ion exchange with UTEVA resin columns. Prior to separation, an $\text{Al}(\text{NO}_3)_3$ solution (150 μL , 1 M) was added to avoid unfavorable matrix interactions with, e.g., phosphate [Horwitz *et al.*, 1993]. The columns were conditioned with three column volumes (cv) HNO_3 (3 M), then loaded with the samples and rinsed with HNO_3 (3 cv, 3 M) for eluting Fe. Th was eluted with HCl (1 cv, 9 M and 2 cv, 5 M, suprapur) followed by elution of U with HCl (3 cv, 0.02 M). The eluates of U and Th were collected in Teflon beakers, evaporated, and re-dissolved in HNO_3 twice. U and Th fractions were diluted in 5 mL HNO_3 (1 M) and analyzed by Inductively Coupled Plasma-Sector Field Mass Spectrometry (ICP-SFMS, Element2, Thermo Scientific) with a desolvation system (Apex Q, ESI). For details of machine settings see Martínez-García *et al.* [2009]. Within each batch of 24 samples, 2 replicates of the certified reference material (CRM) *UREM 11* and 2 procedural blanks were processed. The recommended value for the Uranium concentration in *UREM 11* is 58.9 ± 0.5 ppm (1 σ) [Hansen and Ring, 1983]. From this value, we deduced the concentrations of the isotopes ^{238}U (58.5 ± 0.5 ppm) and ^{230}Th (957 ± 8 pg g^{-1}). The external reproducibility from replicate analyses ($n = 23$) was within 3.8 % for ^{238}U (60.4 ± 2.3 ppm) and 5.0 % for ^{230}Th (959 ± 48 pg g^{-1}). The mean values in procedural blanks ($n = 21$) were 253 $\text{pg }^{238}\text{U}$ and 0.024 $\text{pg }^{230}\text{Th}$ accounting for ~ 0.02 % and ~ 0.6 % of the samples, respectively. The results of Th and U specific activities in grain size fractions are given in dpm g^{-1} (disintegration per minute per gram of size fractionated particles).

2.2.4 Characterization of grain size fractions

Sediment fractions (seaW-method) of the samples GeoB1027-2 and PS1769-1 were examined in more detail by scanning electron microscopy (SEM), and their specific surface area (SSA) was studied together with the grain size distribution (GSD) in order to further describe the result of particle separation. For the SEM study, sediment fractions were fixed on a sample holder, coated with gold and viewed with the SEM *XL30 Esem* (Philips) at 10.0 kV.

The SSA was determined by gas adsorption analysis on a Quantachrome *Nova 2200*.

The sediment samples were degassed and heated (110°C for 2h) to remove surface adsorbed water. After evacuation, the sediment was subjected to five partial pressures of N₂ gas (purity 99.996 %) and the surface area was calculated using the BET-theory [Brunauer *et al.*, 1938] according to ISO 9277.

Prior to the measurement of GSD, the dry sediment fractions were soaked in deionized water over night, sodium pyrophosphate (Na₄P₂O₇) was added, and the suspension was heated until boiling. We refrained from the removal of organic matter, carbonate and opal, as these components are assumed to be important carriers of particulate Th and U. The GSDs were determined with the *LS 13320 Laser Diffraction Particle Size Analyzer* (Beckman Coulter) in demineralized and degassed water.

The chemical composition (biogenic opal and some major elements) has been determined on the sediment fractions (seaW) of the samples PS1768-8 and PS1769-1. The determination of opal followed the description of Müller and Schneider [1993] where opal was extracted with NaOH (1 M) at 85°C, and dissolved silica was continuously analyzed by molybdate-blue spectrophotometry. The elements Mg, Al, K, Ca, Mn, Fe, Rb, and Cs has been analyzed on the samples after full acid digestion (see description for microwave digestion, section 2.2.3) using the ICP-SF-MS Element2 (Thermo Scientific). Calibrations were done with certified standard solutions and external reproducibility was monitored using the NIST standard reference material 2702 (inorganics in marine sediment).

2.2.5 ²³⁰Th_{xs} normalization and focusing factor

For particle flux studies, only the unsupported ²³⁰Th deriving from scavenging (excess ²³⁰Th) is of interest. For calculation of excess ²³⁰Th activity, any ²³⁰Th supported by detrital or authigenic U needs to be subtracted. The excess ²³⁰Th activity then needs to be decay corrected (half-life 75,380 years) to get the initial activity of excess ²³⁰Th at the time of deposition (in the following referred to as ²³⁰Th_{xs}). ²³⁰Th_{xs} is calculated following the descriptions of François *et al.* [2004] and Henderson and Anderson [2003]. Briefly, the activity of ²³⁰Th_{detrital} in lithogenic material (in secular equilibrium with ²³⁸U_{detrital}), and the activity of ²³⁰Th_{authigen} derived from authigenic ²³⁴U must be subtracted from the measured ²³⁰Th activity. The activity of ²³⁸U_{detrital} is inferred from the activity ratio ²³⁸U/²³²Th that has been suggested to be on average 0.6±0.1 for the Atlantic basin. The activity of ²³⁰Th_{authigen} is estimated from authigenic ²³⁸U (= ²³⁸U_{total} - ²³⁸U_{detrital}), multiplied by 1.14 (activity ratio of ²³⁴U/²³⁸U in seawater), calculating the ²³⁰Th production since the time of deposition. These calculations are based on assumptions for bulk samples and may be problematic for grain size separated samples, because size fractionation may produce a U/Th fractionation due to lithogenic minerals of different size classes. Especially the detrital ²³⁸U/²³²Th ratio could deviate significantly from the average value 0.6±0.1.

Following the assumption that ²³⁰Th in seawater is completely scavenged and buried

at the seafloor, $^{230}\text{Th}_{\text{xs}}$ specific activity in sediment is inversely related to the vertical flux of particles. According to *Suman and Bacon* [1989], the $^{230}\text{Th}_{\text{xs}}$ normalized sediment flux F_V is the vertical flux of any sediment constituent i , given by its ratio to the decay-corrected $^{230}\text{Th}_{\text{xs}}$. F_V is calculated by equation (2.1):

$$F_V = \beta_{230} \times z \times f_i / [^{230}\text{Th}_{\text{xs}}], \quad (2.1)$$

where β_{230} is the annual production of ^{230}Th in the seawater [$0.0267 \text{ dpm m}^{-3} \text{ yr}^{-1}$], z is the water depth [m], f_i is the weight fraction of component i , and $[^{230}\text{Th}_{\text{xs}}]$ is the specific activity of ^{230}Th [dpm g^{-1}] in the sediment at the time of deposition in excess of ^{234}U .

The focusing factor Ψ is given by the inventory of $^{230}\text{Th}_{\text{xs}}$ in the sediment section divided by the ^{230}Th production in seawater:

$$\Psi = [^{230}\text{Th}_{\text{xs}}] \times \rho \times (s_1 - s_2) \times 10 / \beta_{230} \times z \times (t_1 - t_2), \quad (2.2)$$

where ρ is the mean dry bulk density [g cm^{-3}], s_1 and s_2 are the sediment depths [cm], and t_1 and t_2 are the corresponding ages [ka].

2.3 Results

2.3.1 Recoveries of sediment, U and Th

The recoveries of sediment after the fractionation process range between 81 % and 100 % (**Table 2.2**). Recoveries of Th and U isotopes are 82-106 % and 59-123 %, respectively. The error propagation by summation of all grain size specific activities of a sediment sample yields errors of up to 12 %, so that recoveries between 88 % and 112 % are generally regarded to be

Table 2.2: Recovery and loss through the fractionation process. The recovery of sediment, Th and U after sieving and settling and the leaching loss of Th and U to the supernatant are given in % relative to initial bulk values. Shading indicates the core sites under slowly accumulating conditions. *NA* = not data.

core ID	method	recovery [%]				loss to supernatant [%]		
		sediment after fractionation	^{230}Th	^{232}Th	^{238}U	^{230}Th	^{232}Th	^{238}U
GeoB1027-2	pureW	93	104	106	94	0.3	0.6	20.7
GeoB1027-2	seaW	100	94	95	<i>NA</i>	0.8	0.5	<i>NA</i>
GeoB1028-4	pureW	94	99	100	59	0.3	0.5	17.1
GeoB1028-4	seaW	99	92	92	<i>NA</i>	1	0.7	<i>NA</i>
PS1768-8	pureW	81	87	82	96	3.1	1.7	36.6
PS1768-8	seaW	93	87	87	75	2.4	1.7	12.6
PS1769-1	pureW	86	86	85	100	1.1	0.6	8.6
PS1769-1	seaW	93	90	90	123	2.4	1.6	28.3

within the propagated error. Recoveries lower than 88 % are probably due to loss of material. In contrast the high U recovery of sample PS1769-1 (seaW, 123 %) could be possibly a result of U uptake from the natural seawater during fractionation processing. However, by comparing the U content in the procedural blanks with that in the supernatants, an enrichment of U in the supernatant has been detected that indicates an U loss from the sediment by leaching (28 % of total sediment U is leached, **Table 2.2**). This discrepancy in sample PS1769-1 between high recovery of U and loss to supernatant remains an unexplained inconsistency. Leaching losses of ^{230}Th and ^{232}Th are low (0.3-3.9 % and 0.5-2.2 %, respectively). Due to the rather high losses of U to the processing water, the $^{230}\text{Th}_{\text{xs}}$ data of each grain size fraction may be undercorrected.

Table 2.3: Contribution of Th and U isotopes by each grain size class in percentage of the total inventory. Shading indicates the core sites under slowly accumulating conditions. Analytical uncertainty is given as $\pm 2\sigma$.

		$^{230}\text{Th}_{\text{xs}}$ [%]							
size [μm]	method	GeoB1027	2 σ	GeoB1028	2 σ	PS1768	2 σ	PS1769	2 σ
<2	pureW	53.1	3.8	55.2	5.0	88.7	6.2	79.9	5.7
2-20	pureW	22.8	1.4	11.7	0.7	9.3	0.6	15.3	1.0
20-63	pureW	11.6	0.7	6.3	0.4	1.3	0.1	2.7	0.2
63-125	pureW	6.8	0.4	9.8	0.6	0.3	0.0	0.5	0.1
>125	pureW	5.6	0.4	16.9	1.0	0.4	0.1	1.5	0.1
<10	seaW	54.0	3.9	50.2	3.6	88.9	6.4	88.4	6.7
10-20	seaW	5.9	0.4	2.9	0.2	1.4	0.1	1.1	0.1
20-63	seaW	11.0	0.7	7.6	0.5	7.7	0.7	7.2	0.6
63-125	seaW	10.5	0.6	11.5	0.7	1.4	0.1	1.6	0.2
>125	seaW	18.6	1.1	27.8	1.7	0.6	0.1	1.7	0.2
		^{238}U [%]							
<2	pureW	57.7	2.2	26.0	1.0	72.6	2.8	64.1	2.4
2-20	pureW	18.6	0.7	18.6	0.7	22.5	0.9	28.2	1.1
20-63	pureW	10.4	0.4	8.9	0.3	4.1	0.2	5.6	0.3
63-125	pureW	6.8	0.3	15.4	0.6	0.4	0.0	0.8	0.0
>125	pureW	6.5	0.2	31.1	1.2	0.4	0.0	1.4	0.1
<10	seaW	47.8	1.8	35.8	1.4	89.1	3.6	85.5	3.4
10-20	seaW	4.7	0.2	2.2	0.1	1.1	0.0	1.1	0.0
20-63	seaW	11.3	0.4	7.7	0.3	8.0	0.4	10.2	0.6
63-125	seaW	12.1	0.5	12.8	0.5	1.4	0.1	1.7	0.1
>125	seaW	24.0	1.0	41.4	1.6	0.4	0.0	1.5	0.1
		^{232}Th [%]							
<2	pureW	59.1	3.7	59.4	3.1	69.2	4.6	67.1	4.5
2-20	pureW	27.7	0.9	17.4	0.5	26.5	0.9	25.1	0.9
20-63	pureW	5.8	0.2	3.9	0.1	2.4	0.1	3.9	0.2
63-125	pureW	3.6	0.1	6.2	0.2	1.1	0.1	1.2	0.1
>125	pureW	3.9	0.1	13.1	0.4	0.9	0.0	2.7	0.1
<10	seaW	66.2	3.7	58.3	2.6	88.8	4.0	86.9	4.8
10-20	seaW	6.1	0.2	3.3	0.1	2.7	0.1	2.0	0.1
20-63	seaW	6.8	0.2	4.9	0.2	6.5	0.3	6.7	0.3
63-125	seaW	6.6	0.2	8.1	0.3	1.1	0.1	1.8	0.1
>125	seaW	14.2	0.4	25.4	0.8	0.9	0.1	2.6	0.1

Assuming that U leaching only affects the authigenic U (U_{auth}), and regarding the relatively young age of the samples, the contribution from decaying $^{234}\text{U}_{\text{auth}}$ to supported ^{230}Th is rather low. When the dissolved $^{234}\text{U}_{\text{auth}}$ fraction is included in ^{230}Th correction, $^{230}\text{Th}_{\text{xs}}$ results are reduced insignificantly by 0.02-0.45 % (carbonate fractions), 0.001-0.41 % (siliceous fractions $>20\ \mu\text{m}$) and 0.03-2.53 % (siliceous fractions $<20\ \mu\text{m}$). However, it is not possible to allocate the amount of dissolved U in the supernatant to any of the individual grain size fractions.

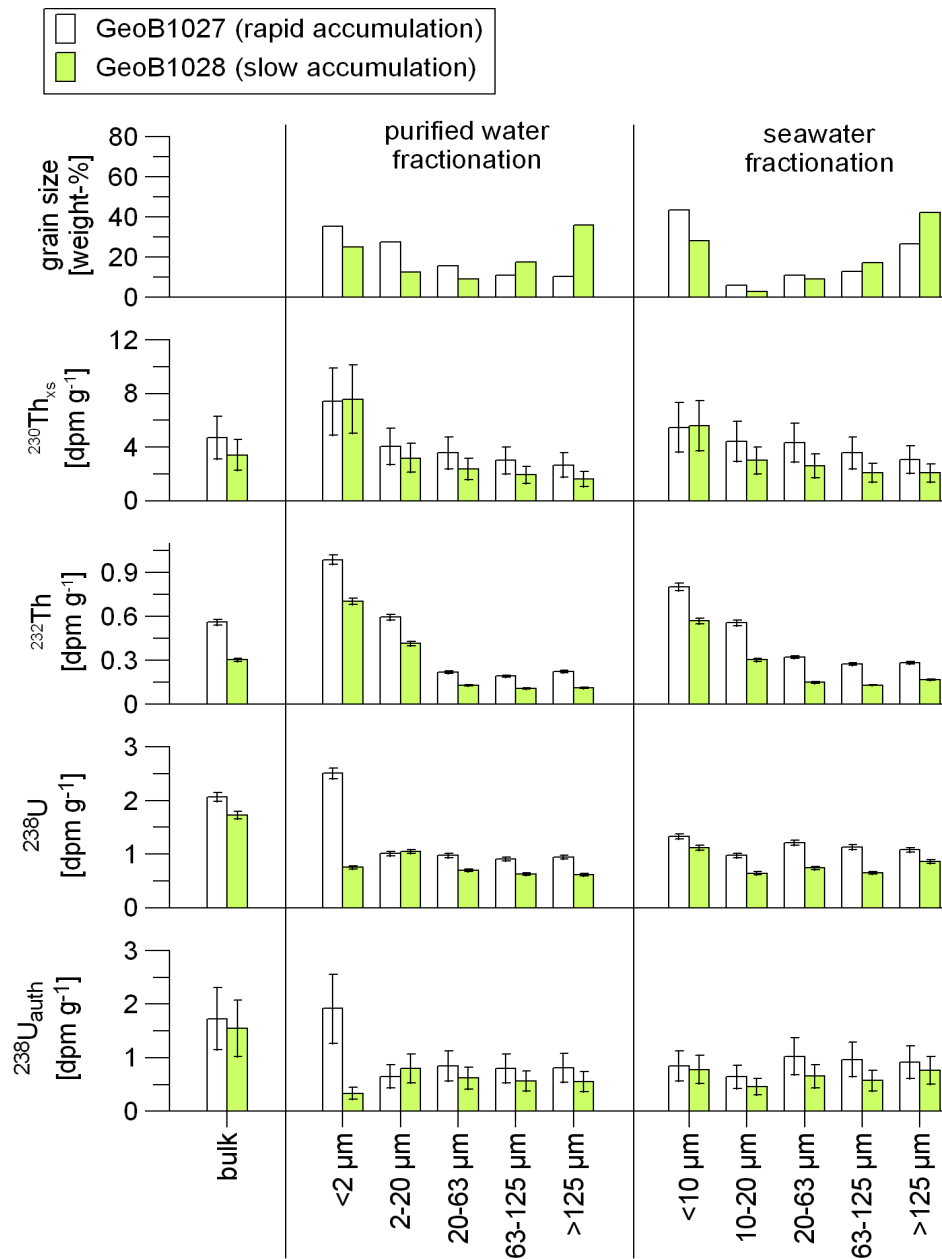


Figure 2.1: Distribution of Th and U isotopes by grain size classes of the carbonate sediment at sites of rapid accumulation (GeoB1027-2, white bars) and slow accumulation (GeoB1028-4, colored bars). The results of two fractionation techniques are shown (purified water with ultrasonication and natural seawater without ultrasonication, error bars indicate analytical uncertainty of $\pm 2\sigma$).

Thus, the approximate errors introduced by U dissolution are included in the propagated errors calculated for the $^{230}\text{Th}_{\text{xs}}$ activity in each of the grain-size sediment fractions.

2.3.2 Fractionations with seawater versus purified water

The seawater fractionation produces grain size spectra that are overall coarser than the purified water fractionation (Figure 2.1 and Figure 2.2). For example, at GeoB1027, the fraction $<63\ \mu\text{m}$

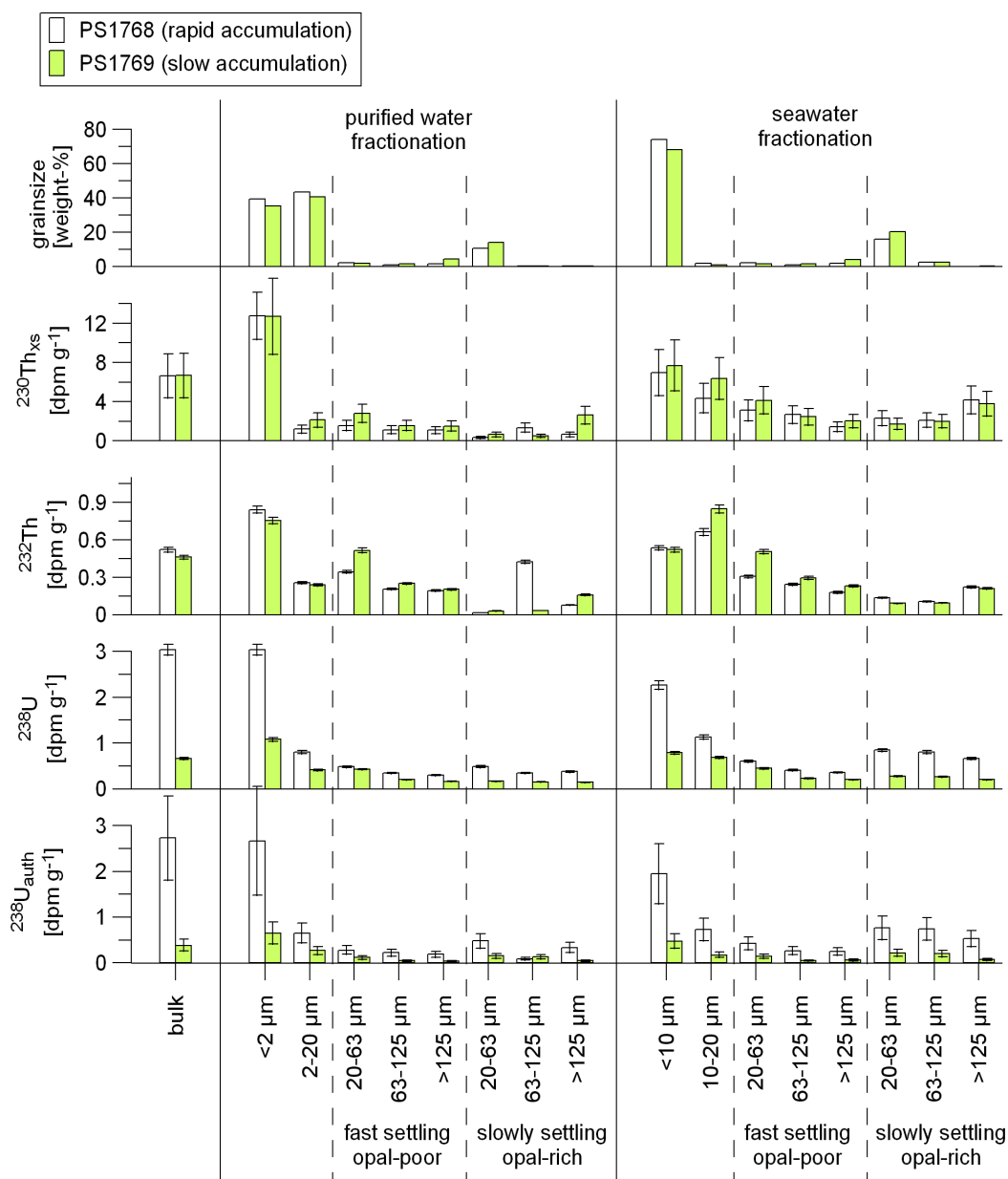


Figure 2.2: Distribution of Th and U isotopes by grain size classes of the siliceous sediment at sites of rapid accumulation (PS1768-8, white bars) and slow accumulation (PS1769-1, colored bars). The grain size classes 20-63 μm , 63-125 μm , and >125 μm are separated into slowly settling (opal-rich) and fast settling (lithogenic-rich) particle classes. The results of two fractionation techniques are shown (purified water with ultrasonication and natural seawater without ultrasonication, error bars indicate analytical uncertainty of $\pm 2\ \sigma$).

accounts for 60 % of the total sample when sieved with the seaW-method, but 79 % using the pureW-method. Virtually all size classes $>20\ \mu\text{m}$ contain higher specific activities of $^{230}\text{Th}_{\text{xs}}$, ^{232}Th and ^{238}U in the seaW-fractionated samples compared with the pureW-fractionation. The small particles $<20\ \mu\text{m}$ contribute higher portions of $^{230}\text{Th}_{\text{xs}}$, ^{232}Th , and ^{238}U to the bulk sediment's inventory when fractionated with pureW (**Table 2.3**).

2.3.3 Distribution of fine sediment, Th and U at rapid versus slow accumulation sites

The isotopic composition of the carbonate sediment is dominated by the smallest particle class $<2\ \mu\text{m}$. This class accounts for 35-40 weight-% of the total sediment and it holds roughly 50-60 % of the total sediment's Th and 30-60 % of the total sediment's U (**Table 2.3**). The rapidly accumulated sediment (GeoB1027) is finer in grain size distribution. In contrast, the slowly accumulating sediment (GeoB1028) contains a much higher percentage of sand-sized particles $>125\ \mu\text{m}$ (36-42 %). This leads to a remarkably high contribution to total Th (13-25 %) and total U (31-41 %) by the coarsest fraction at GeoB1028. The twin cores display identical $^{230}\text{Th}_{\text{xs}}$ activities within the smallest particles ($<2\ \mu\text{m}$ and $<10\ \mu\text{m}$, **Figure 2.1**). This is not the case for all particle classes coarser than $2\ \mu\text{m}$ ($10\ \mu\text{m}$), as they all display slightly but insignificantly higher $^{230}\text{Th}_{\text{xs}}$ activities at the rapidly accumulated core (GeoB1027).

The isotopic composition of the siliceous sediment is controlled by the smallest particle class $<2\ \mu\text{m}$, accounting for 40 weight-% of the total sediment, 60-70 % of total ^{238}U , 70 % of total ^{232}Th and 80-90 % of total $^{230}\text{Th}_{\text{xs}}$ (**Table 2.3**). The deposition of fine particles $<20\ \mu\text{m}$ is

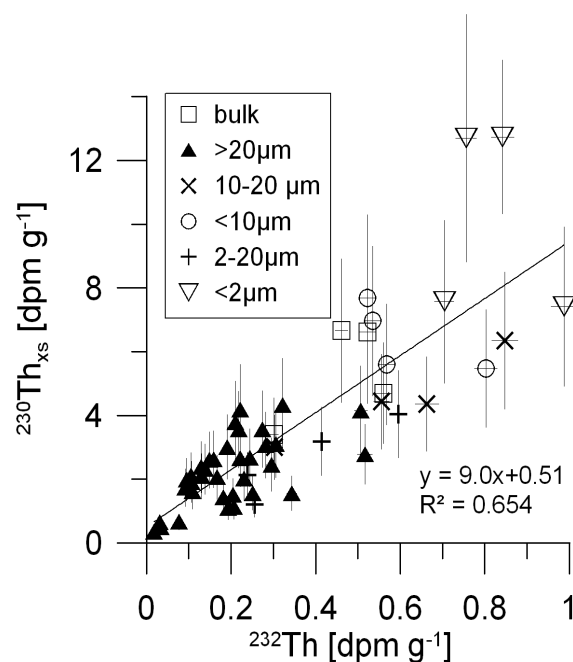


Figure 2.3: Scatter plot of $^{230}\text{Th}_{\text{xs}}$ and ^{232}Th activities in all analyzed grain size fractions of siliceous and carbonate samples.

Table 2.4: Characterization of the particle fractions obtained by sieving and settling. The analyses of specific surface area and grain size and the SEM imaging have been performed on the size fractions of GeoB1027 and PS1769. Biogenic opal has been analyzed on fractions of the opal-rich sediment (for more opal data see **Table A-1** in the appendix). “f” and “s” mean fast settling and slowly settling, respectively. *NA* = not analyzed.

	specific surface area [m ² g ⁻¹]	mean grain size [μm]	biogenic opal [%]	particle composition (minor components are in parantheses)
GeoB1027-2				
bulk	9.2	29.3	<i>NA</i>	
<2μm	29.1	2.3	<i>NA</i>	clay + coccoliths
2-20μm	5.7	6.4	<i>NA</i>	coccoliths + foraminifera fragments
20-63μm	5.2	33.7	<i>NA</i>	foraminifera and foram. fragments
63-125μm	4.3	79.6	<i>NA</i>	foraminifera
>125μm	4.3	204.1	<i>NA</i>	foraminifera
PS1769-1				
bulk	19.2	22.3	60	
<2μm	56.5	2.6	61	clay + diatom fragments
2-20μm	13.0	10.9	80	diatom fragments
f 20-63μm	2.7	41.4	17	rock fragments (+ radiolarians + diatoms)
f 63-125μm	1.6	87.0	5	rock fragments + radiolarians
f >125μm	3.3	418.1	4	rock fragments + radiolarians
s 20-63μm	11.2	30.4	82	diatoms
s 63-125μm	9.5	70.4	79	diatoms
s >125μm	<i>NA</i>	154.2	<i>NA</i>	diatoms (+ radiolarians)

slightly higher at the rapidly accumulated core site (PS1768), and therefore it contributes more to the Th and U inventory than at the slowly accumulated core site (PS1769). The twin cores display identical ²³⁰Th_{xs} activities within the smallest particles (<2 μm and <10 μm; **Figure 2.2**). The coarser particles (classes 10-20 μm and fast sinking >20 μm) are slightly but insignificantly higher in ²³⁰Th_{xs} at the slow accumulation site (PS1769). ²³⁸U activities in siliceous and carbonate sediments (**Figure 2.1** and **Figure 2.2**) reveal a regular distribution pattern for all grain sizes at both accumulation settings. The smaller the particles, the higher the U activities are, but with an overall lower level of U activity in the slowly accumulated sediment.

In the siliceous sediment, all fractions >20 μm play a minor role as carrier for ²³⁰Th_{xs}, ²³²Th, and ²³⁸U (**Figure 2.2; Table 2.3**). In contrast, ²³⁰Th_{xs}, ²³²Th, and ²³⁸U in the carbonate sediment are more uniformly distributed between fine and coarse particles (**Figure 2.1; Table 2.3**), revealing a lower grain size effect than in the siliceous sediment, i.e., carbonate sand and coarse silt play an important role for Th and U inventories in carbonate sediments.

The scatter diagram (**Figure 2.3**) shows ²³⁰Th_{xs} and ²³²Th data from both carbonate and siliceous sediment fractions. On a linear regression line (R² = 0.654), larger particles (>20 μm) form a group of low Th values and small particles (<10 μm and <2 μm) are located at the opposite end, at high Th values.

2.3.4 Characterization of sediment fractions

The size fractionation of sediments results in a differentiation of components. Each grain size class is composed of biogenic and lithogenic components with different physical properties (specific surface area and mean grain size), as reported for the samples GeoB1027-2 and PS1769-1 in **Table 2.4**. Chemical properties (biogenic opal content and elemental composition) are reported for the samples PS1768-8 and PS1769-1 in **Table A-1** in the appendix. The finest particle classes ($<20\ \mu\text{m}$) of carbonate sediment contain clay and coccoliths with a mean grain size of $2\text{-}6\ \mu\text{m}$ and a specific surface area (SSA) of $6\text{-}29\ \text{m}^2\ \text{g}^{-1}$. The coarser carbonate fractions ($>20\ \mu\text{m}$) mainly consist of foraminifera and their fragments ($34\text{-}204\ \mu\text{m}$, $4\text{-}5\ \text{m}^2\ \text{g}^{-1}$ see also **Plate A-1** in the appendix). The finest fractions ($<20\ \mu\text{m}$) of the siliceous sediment consist of clay minerals and diatom fragments ($3\text{-}11\ \mu\text{m}$, $13\text{-}57\ \text{m}^2\ \text{g}^{-1}$, $59\text{-}80\%$ biogenic opal). All coarser fast sinking particle fractions ($>20\ \mu\text{m}$) consist of a mixture of lithogenic particles and radiolarian frustules (**Figure 2.4a**, $41\text{-}418\ \mu\text{m}$, $2\text{-}3\ \text{m}^2\ \text{g}^{-1}$, $3\text{-}17\%$ biogenic opal). Diatom shells and their fragments are the main component of the slowly sinking particle fractions (**Figure 2.4b**, $30\text{-}154\ \mu\text{m}$, $10\text{-}11\ \text{m}^2\ \text{g}^{-1}$, $75\text{-}82\%$ biogenic opal). Diatoms shells are also present among the fast settling particles.

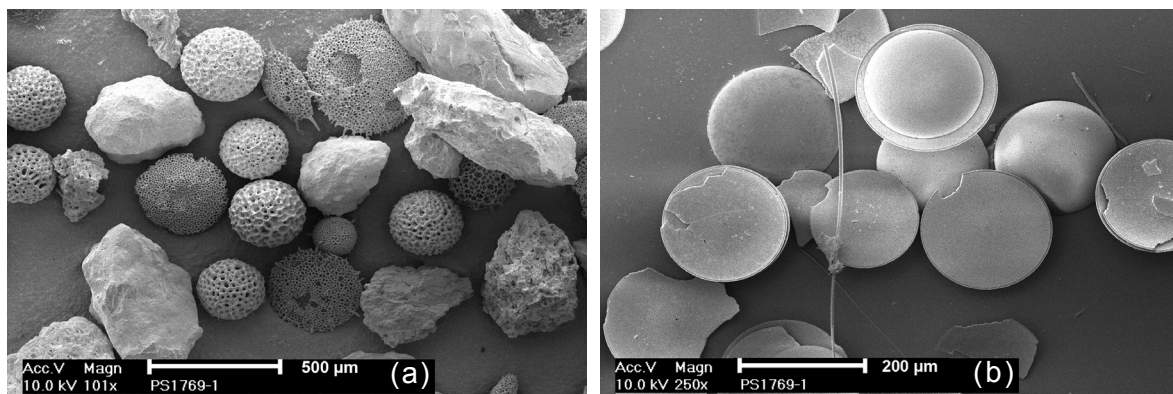


Figure 2.4a and 2.4b: SEM photographs of the largest grain size fraction ($>125\ \mu\text{m}$) of PS1769-1. This sediment sample was separated into (a) a fast settling particle class containing rock fragments and radiolarians and (b) a slowly settling particle class containing mainly diatoms. For additional photographs see **Plate A-1** in the appendix.

2.3.5 Th and U isotopes related to surface area, grain size and elemental composition

To test the relation between the SSA and mean grain size described in 2.3.4 with the distribution of $^{230}\text{Th}_{\text{xs}}$, ^{232}Th and $^{238}\text{U}_{\text{auth}}$ as shown for the fractionated samples GeoB1027-2 and PS1769-1 in **Figure 2.5**, Spearman's rho statistic was used to estimate a rank-based measure of association (correlation r and level of significance p). Spearman's rho is a non-parametric test which is considered to be appropriate for our data as they are small in sample size and do not come from a bivariate normal distribution [Siegel 2001]. The specific surface

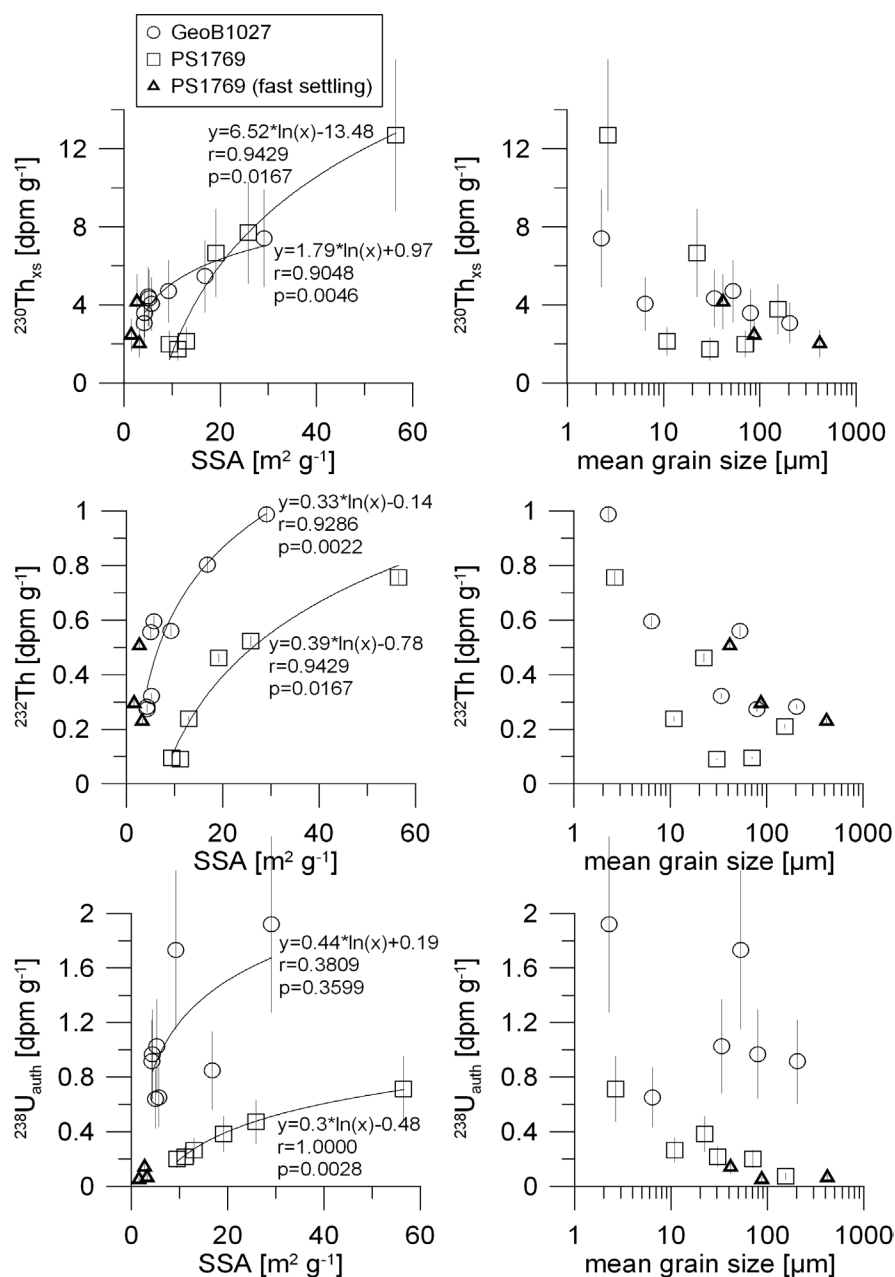


Figure 2.5: Scatter plot of the specific surface area (SSA) and the mean grain size with $^{230}\text{Th}_{\text{xs}}$, ^{232}Th and $^{238}\text{U}_{\text{auth}}$ for the size fractions (seawater fractionation) of the samples GeoB1027-2 and PS1769-1. The isotopes show inverse correlations with mean grain sizes and positive correlations with SSA. A logarithmic function fits best to the SSA – Th/U correlation.

area of the carbonate sample is correlated significantly with $^{230}\text{Th}_{\text{xs}}$ ($r=0.905$ $p \leq 0.01$) and ^{232}Th ($r=0.929$ $p \leq 0.01$). $^{238}\text{U}_{\text{auth}}$ is not correlated ($r=0.381$ $p > 0.05$). The SSA of the siliceous sample is correlated with $^{230}\text{Th}_{\text{xs}}$ ($r=0.943$ $p \leq 0.05$), ^{232}Th ($r=0.943$ $p \leq 0.05$), and $^{238}\text{U}_{\text{auth}}$ ($r=1.000$ $p \leq 0.01$) only when the fast settling particles are excluded. The best fit of the regression lines is achieved by logarithmic equations. Correlations between mean grain size and the isotopes are apparent but less pronounced. Positive correlations appear between $^{230}\text{Th}_{\text{xs}}$ and the two alkali metals Rb and Cs. Other elements do not correlate with $^{230}\text{Th}_{\text{xs}}$ (Figure A-1 in the appendix).

2.4 Discussion

2.4.1 Grain size distributions

The choice of fractionation techniques affects the grain size fractions. Grain size spectra obtained by pure W -fractionation are finer than by sea W -fractionation, probably because (a) in seawater, the particles are prone to flocculation and not suspended as individual grains, (b) clay that sticks to large particles could be detached during ultrasonication in the pure W -suspension, or (c) suspension in pure W and ultrasonication may partially dissolve or break large particles into fragments.

Both twin core locations show a preferential deposition of fine material at the more rapidly accumulated core, confirming the assumption of particle sorting by lateral sediment transport. The sediments of the Southern Ocean locations are fine-grained (74 % in the $<10 \mu\text{m}$ class) and probably deposited as aggregates, because particles $<10 \mu\text{m}$ behave cohesively [McCave and Hall, 2006]. Most of the particulate material is carried vertically downward by aggregates that settle faster than it would be expected for individual particles. Ziervogel and Forster [2005] show that pelagic diatoms potentially increase the rate of particle aggregation, and that diatom bearing aggregates of in vitro experiments (140-200 μm) reach 52-104 m d^{-1} . Mean sinking rates are calculated from sediment trap deployments to be 157 m d^{-1} in the Southern Ocean [Fischer and Karakas, 2009]. Therefore, the “slowly settling particles”, as classified in this study, may not have settled as isolated grains through the water column and settling velocities ($\sim 26 \text{m d}^{-1}$, mean size 154 μm) may underestimate velocities found under natural conditions.

The carbonate sediment of the Walvis Ridge locations is less fine grained (28-43 % in the $<10 \mu\text{m}$ class) than the siliceous twin core sediments. The variations in grain size distributions and carbonate concentrations between the carbonate twin cores can be explained by differences in deposition of fine material or carbonate dissolution. According to Volbers and Henrich [2002], the carbonate preservation at this depth of Walvis Ridge is good to moderate, but the higher TOC content and the deeper water depth at site GeoB1027 (Table 2.1) may lead to stronger carbonate dissolution and fragmentation of foraminifera shells than at GeoB1028.

2.4.2 $^{230}\text{Th}_{\text{xs}}$ in particle classes

Our hypothesis that particles of the same composition and size from the same water-depth are equilibrated with the same amount of $^{230}\text{Th}_{\text{xs}}$ adsorbed is confirmed for the finest particles, but not for the coarser particles. This finest fraction ($<2 \mu\text{m}$ and $<10 \mu\text{m}$) is the main carrier for $^{230}\text{Th}_{\text{xs}}$, because it has the largest specific surface area, capturing most ^{230}Th . The specific activity of $^{230}\text{Th}_{\text{xs}}$ is inversely related to the grain size. Within the siliceous sediment, the adsorption of $^{230}\text{Th}_{\text{xs}}$ onto the opal-rich fine fractions ($<2 \mu\text{m}$, 61-68 % opal) is very strong compared to the opal-rich coarse fractions ($>20 \mu\text{m}$, 75-82 % opal). We deduce that the lithogenic (clay mineral)

content within the fine fraction is responsible for the strong Th scavenging and that Th has a weak affinity to opal, corroborating the results of *Chase et al.* [2002], *Luo and Ku* [1999] and *Roy-Barman et al.* [2005].

Within coarse fractions ($>2\ \mu\text{m}$ and $>10\ \mu\text{m}$) of the carbonate and siliceous samples, the level of $^{230}\text{Th}_{\text{xs}}$ adsorption is lower, and the twin cores display some unexpected discrepancies in $^{230}\text{Th}_{\text{xs}}$ when comparing results of the corresponding size fractions. Even though differences are statistically insignificant (within $2\ \sigma$ -error), we discuss them as they seem to be a systematic feature. Possible explanations for this unexpected result are: (a) The higher $^{230}\text{Th}_{\text{xs}}$ activities in the rapidly accumulated carbonate sediment may be attributed to the deeper location (453 m deeper) thus receiving higher vertical $^{230}\text{Th}_{\text{xs}}$ fluxes from the water column than the slowly accumulating site. However, after normalizing the $^{230}\text{Th}_{\text{xs}}$ activities of both twin cores to the same water depth (data not shown here), an unexplained discrepancy between both core sites remains. The difference in water depth (30 m) between PS1768 and PS1769 is negligible for the $^{230}\text{Th}_{\text{xs}}$ differences. (b) The samples of GeoB1027-2 and GeoB1028-4 differ in their (interpolated) age by 1.7 ka (**Table 2.1**). The conditions of sedimentation (water masses, current speed, and sediment supply) may not have been constant during this time period, so that the two samples are potentially not directly comparable concerning their $^{230}\text{Th}_{\text{xs}}$ activities. In the siliceous twin cores, the age differences should be of minor importance as the samples are from the same (interpolated) age. (c) The differences in Th and U leaching during sieve and settling could potentially be a further reason for the observed $^{230}\text{Th}_{\text{xs}}$ differences. During the pureW fractionation Th and U leaching from sample PS1768 is 3-4 times stronger than from sample PS1769 (**Table 2.2**). On the other hand all other fractionations are very similar concerning Th and U leaching, arguing against the leaching scenario.

Summarizing the $^{230}\text{Th}_{\text{xs}}$ distribution in the grain size classes, we find that the finest material ($<2\ \mu\text{m}$) contains 50-90 % of the total sediment's $^{230}\text{Th}_{\text{xs}}$ inventory. This fraction is preferentially deposited at the rapid accumulation sites, and therefore contributes more to the $^{230}\text{Th}_{\text{xs}}$ inventory than at the slow accumulation sites. Similar results are reported from North Atlantic sediments by *Scholten et al.* [1994], who find ~90 % of $^{230}\text{Th}_{\text{xs}}$ in the grain size class $<6.3\ \mu\text{m}$, and by *Thomson et al.* [1993] who find 3-fold higher concentrations of $^{230}\text{Th}_{\text{xs}}$ in the fine fraction ($<5\ \mu\text{m}$) than in the coarse fraction ($>400\ \mu\text{m}$).

2.4.3 U in particle classes

Elevated U concentrations can be due to the formation of authigenic U (U_{auth}) under chemically reducing conditions, induced by the high flux of organic carbon. As already reported by *Anderson et al.* [1998] for several sediment cores in the South Atlantic near 52°S , sediment focusing enhanced the accumulation rates of U_{auth} during Holocene and the LGM. The preferential deposition of small and slowly sinking particles may increase the local flux of organic

matter relative to the vertical organic matter flux from surface waters [Anderson *et al.*, 1998; Beaulieu, 2002; Mollenhauer *et al.*, 2006]. Especially unconsolidated organic-rich aggregates at the sediment-water-interface are prone to resuspension at low critical shear velocities (e.g. 0.4-0.8 cm s^{-1} for diatom derived detritus; Beaulieu, 2003). At both twin core locations, the concentration of total organic matter is more than twice as high at the rapid accumulation site (**Table 2.1**), probably enhancing the precipitation of U_{auth} . At the carbonate twin cores, the difference in U_{auth} in bulk samples is relatively small (2.3 ppm and 2.1 ppm, respectively). The portion of the total U that is authigenic ranges from 84 % to 90 % (bulk) and from 44 % to 90 % (grain size fractions, **Table A-2** in the appendix). In contrast, the twin cores at the siliceous location differ by a factor of ~ 7 (3.7 ppm and 0.5 ppm, respectively). The difference of U_{auth} between the twin cores is particularly pronounced in the smallest $< 2 \mu\text{m}$ fractions (**Figure 2.1** and **Figure 2.2**). The portion of the total U that is authigenic at the rapid accumulation site is 90 % (bulk) and 26-92 % (grain size fractions), and at the slow accumulation site it is 58 % (bulk) and 22-89 % (grain size fractions). Although the sediment cores are in close proximity, they exhibit contrasting concentrations of U_{auth} , indicating that organic carbon accumulation in this case is the result of sediment redistribution rather than export production.

2.4.4 Th and U related to the specific surface area

The observed distribution of $^{230}\text{Th}_{\text{xs}}$ corroborate the general hypothesis that ^{230}Th adsorption onto particles depends on grain size and specific surface area (SSA, **Figure 2.5**). Surprisingly, however, the fast sinking particles do not fit on the logarithmic regression line, revealing a relatively high $^{230}\text{Th}_{\text{xs}}$ concentration relative to their surface area. This could be due to differences in elemental composition (see **Table A-1** and **Figure A-1** in the appendix), which may enhance or reduce the particle's affinity for ^{230}Th adsorption.

The correlation of ^{232}Th with the SSA (**Figure 2.5**) can be attributed to lithogenic (clay mineral) particles rich in ^{232}Th , which generally reside in smaller particle size classes with higher SSA. This would indicate the preferential affinity of $^{230}\text{Th}_{\text{xs}}$ to lithogenic material, which is further supported by the linear correlation between $^{230}\text{Th}_{\text{xs}}$ and ^{232}Th (**Figure 2.3**).

2.4.5 Focusing factor and $^{230}\text{Th}_{\text{xs}}$ normalization corrected for particle sorting

The bulk focusing factor is calculated for PS1768 (12-24 ka) and PS1769 (16-24 ka) to be $\Psi = 5.9$ and 3.2, respectively. This means that mass accumulation is largely controlled by lateral sediment flux, and it is twice faster at PS1768 than at PS1769. In the following section, we calculate to which extent particle sorting could potentially bias the focusing factor and $^{230}\text{Th}_{\text{xs}}$ normalized fluxes of the studied samples. The conventional focusing factor (Ψ) is calculated for a core section between two dated core depths and based on the $^{230}\text{Th}_{\text{xs}}$ inventory averaged over

this core depth [François et al. 2004]. In the present study, the focusing factor that is corrected for the particle sorting effect (Ψ_c) is derived from only one single sample depth, representing the whole core section, as no further size-fractionated $^{230}\text{Th}_{\text{xs}}$ data is available.

Our assumption for particle sorting correction is that the lateral sediment flux is controlled by preferential transport of fine material. The vertical particle flux consequently must have been coarser in grain size distribution than measured in the bulk sample. As grain size distributions of the vertical and lateral fluxes are unknown, we need to postulate a certain grain size distribution with predefined portions of fine and coarse particles within one of the fluxes. From this we are able to calculate the grain size weighted $^{230}\text{Th}_{\text{xs}}$ within the lateral (or vertical) sediment flux. In the appendix it is shown how the fluxes can be calculated for any choice of grain size distribution in the lateral (vertical) flux. If we make the simplifying assumption that the lateral flux consists only of small particles, the problem reduces to the situation that the excess ^{230}Th sedimentation is exclusively supplied by small advected particles, which can be expressed with equation 2.3

$$x = \frac{T_m}{T_k} \left(1 - \frac{1}{\Psi} \right) \quad (2.3)$$

where x is the portion of the lateral sediment flux related to the sedimentation rate, Ψ is the focusing factor measured, T_m is the bulk $^{230}\text{Th}_{\text{xs}}$ activity [dpm g⁻¹] in the sediment, T_k is the $^{230}\text{Th}_{\text{xs}}$ activity [dpm g⁻¹] in the small particle fraction. With x we are able to calculate the grain size corrected Ψ_c :

$$\Psi_c = \frac{1}{1-x} = \frac{1}{1 - \frac{T_m}{T_k} \left(1 - \frac{1}{\Psi} \right)} \quad (2.4)$$

According to the corrected focusing factor Ψ_c the preserved vertical mass flux F_V [g cm⁻² ka⁻¹] needs to be corrected (F_{Vc}):

$$F_{Vc} = F_V \frac{\Psi}{\Psi_c} \quad (2.5)$$

As an alternative, for the calculation of x the vertical $^{230}\text{Th}_{\text{xs}}$ flux can be assumed to be carried by the large particles and a fraction of the small ones calculated to match the water column derived ^{230}Th production. In this case the lateral sediment flux consists of only small particles which transport the difference between the total accumulated $^{230}\text{Th}_{\text{xs}}$ and the water column derived $^{230}\text{Th}_{\text{xs}}$. This is a special case of the derivation given in the appendix and yields the same solution.

The calculations are performed with grain size and $^{230}\text{Th}_{\text{xs}}$ data sets of both methods (pureW and seaW) and results are equivalent within a range of 0.1-5.5 %. In most cases the data

from pure \mathcal{W} -fractionated samples produce a stronger bias than the sea \mathcal{W} -fractionations. The following discussion refers only to data from the sea \mathcal{W} method (**Table 2.5**), which is expected to better match natural conditions. With the simplifying assumption that the lateral flux consists of only “small particles” we calculate three scenarios of Ψ_{C} with “small particles” defined as (a) $<125 \mu\text{m}$, (b) $<63 \mu\text{m}$, and (c) $<10 \mu\text{m}$. For example, if the lateral flux at core site PS1768-8 ($\Psi = 5.9$) is assumed to be limited to particles $<125 \mu\text{m}$, x equals 0.82, i.e. a mixing ratio of 82 % lateral flux with 18 % vertical flux is required, resulting in $\Psi_{\text{C}} = 5.5$. If the lateral flux is assumed to be limited to particles $<63 \mu\text{m}$ the calculation would yield $x = 0.8$ and $\Psi_{\text{C}} = 5.0$. A scenario of lateral flux of particles $<10 \mu\text{m}$ ($x = 0.69$) results in $\Psi_{\text{C}} = 3.2$. This means that the actual degree of focusing is overestimated accordingly due to particle sorting effects. As a consequence higher vertical mass flux rates than estimated using the classical bulk ^{230}Th correction method are required in order to balance lateral fluxes composed primarily of smaller grains. This effect becomes stronger with smaller predominant grain size of laterally supplied material. In case of particles $<10 \mu\text{m}$ at PS1768 and PS1769, the vertical fluxes F_{V} would increase with respect to those estimated using the bulk $^{230}\text{Th}_{\text{xs}}$ method from 1.7 to 3.1 $\text{g cm}^{-2} \text{ka}^{-1}$ and from 1.4 to 2.1 $\text{g cm}^{-2} \text{ka}^{-1}$, respectively (**Table 2.5**).

Table 2.5: Estimation of grain size sorting effects on focusing factor (Ψ) and $^{230}\text{Th}_{\text{xs}}$ normalized vertical flux (F_{V}). Ψ and F_{V} are corrected for selective depositions of grain sizes $<125 \mu\text{m}$, $<63 \mu\text{m}$ and $<10 \mu\text{m}$ (seawater fractionation). In contrast the mass accumulation rate (MAR) show the uncorrected sediment flux to the seafloor.

	Ψ_{C}				$F_{\text{VC}} [\text{g cm}^{-2} \text{ka}^{-1}]$				MAR [$\text{g cm}^{-2} \text{ka}^{-1}$]
	corrected for the deposition of				corrected for the deposition of				
	bulk	$<125\mu\text{m}$	$<63\mu\text{m}$	$<10\mu\text{m}$	bulk	$<125\mu\text{m}$	$<63\mu\text{m}$	$<10\mu\text{m}$	
GeoB1027-2	2.3	2	1.9	1.8	1.5	1.7	1.8	1.9	3.4
GeoB1028-4	1.8	1.5	1.4	1.3	1.7	2.1	2.2	2.4	3.0
PS1768-8	5.9	5.5	5	3.2	1.7	1.8	2	3.1	10.1
PS1769-1	3.2	3	2.8	2.1	1.4	1.5	1.6	2.1	4.4

It is likely that sand-sized particles $>63 \mu\text{m}$ quickly fall out of suspension [*McCave and Gross, 1991*], while fine material $<63 \mu\text{m}$ is transported over longer distances. A current driven sorting of particles smaller than $2 \mu\text{m}$ is unlikely, because particles $<7-11 \mu\text{m}$ behave cohesively, are transported as flocs, and are not subject to sorting effects [*McCave et al., 1995*]. A selective deposition of only fines $<10 \mu\text{m}$ should be considered as a maximum sorting effect that is likely to occur only under regimes dominated by weak bottom currents. Strong bottom current regimes as prevailing in the Antarctic circumpolar current region are more likely to transport also coarser particles. Therefore we consider selective deposition of particle classes $<63 \mu\text{m}$ as the more likely

scenarios for the locations of this study.

Isotopes of Th and U are not equally distributed within particle classes and therefore the sorting effect bears the potential to induce a decoupling of Th and U isotopic records. However, in the scenarios $\Psi_{<10\mu\text{m}}$ and $\Psi_{<63\mu\text{m}}$, the isotopic decoupling is negligible or not evident: e.g. in the case of PS1768, the lateral flux accounts for 83 % of total deposited ^{230}Th , 81-83 % of total deposited ^{238}U , and 83-88 % of total deposited ^{232}Th .

2.5 Conclusions

2.5.1 Technique of sediment fractionation

The comparison of two fractionation methods reveals that the choice of sample pretreatment and fractionation fluid affects the distributions of grain sizes, Th and U. Generally, the seaW-technique has the disadvantages that (a) small grain sizes cannot be separated properly due to the flocculation effect and (b) that complex interactions between the natural seawater matrix (e.g. with high U content) and the suspended particles lead to experimental conditions that are difficult to reproduce. The pureW-technique turns out to be more reproducible, but it potentially affects the particles by dissolution and/or comminution. As a consequence for future experiments, we suggest to use a gentle fractionation method with artificial seawater (free of Th and U) and to monitor Th and U in the supernatant, because leaching and/or uptake of Th and U during fractionation could introduce an error in calculating grain size fractionated $^{230}\text{Th}_{\text{xs}}$.

2.5.2 $^{230}\text{Th}_{\text{xs}}$ in different grain-size and lithologic classes

The main carrier for the sedimentary $^{230}\text{Th}_{\text{xs}}$ -signal is the fine sediment fraction, whereas coarse particles carry a much lower $^{230}\text{Th}_{\text{xs}}$ activity. This general distribution pattern is observed at all locations. However, in the siliceous sediment, the affinity of $^{230}\text{Th}_{\text{xs}}$ to fine and lithogenic-rich material is more pronounced than in the carbonate sediment. The coarse carbonate fractions (mainly foraminifera) carry a relatively large $^{230}\text{Th}_{\text{xs}}$ signal. In contrast, the biogenic opal content does not significantly affect the $^{230}\text{Th}_{\text{xs}}$ concentrations. Some coarse particle fractions reveal differences between the twin cores, which cannot be readily explained. The identical $^{230}\text{Th}_{\text{xs}}$ specific activities within the finest sediment fractions of the twin cores suggests that redistributed sediment particles must have the same source, and that the distance of redistribution cannot have been very large, supporting the $^{230}\text{Th}_{\text{xs}}$ -based approach to correct for sediment redistribution. The fine material is preferentially deposited at the rapidly accumulated locations potentially influencing the $^{230}\text{Th}_{\text{xs}}$ inventory.

2.5.3 Implications for $^{230}\text{Th}_{\text{xs}}$ as constant flux tracer

Our study clearly illustrates that particle sorting during lateral transport has an effect on $^{230}\text{Th}_{\text{xs}}$ inventories of bulk sediments. A systematically higher $^{230}\text{Th}_{\text{xs}}$ concentration is found in the fine grain size fractions. As a result, $^{230}\text{Th}_{\text{xs}}$ inventories of focused sediments are biased towards the contribution of fine-grained sediments, which results generally in overestimating the effect of focusing and underestimating the actual vertical particle fluxes in focused sediments. In general, we can state that the smaller the particles and the higher the clay mineral content within the laterally transported sediment with respect to the vertical component, the stronger is the grain size bias on the focusing factor. Strongest grain size bias would accordingly occur in those regimes dominated by weak bottom currents, where the finest grain size fractions are preferentially deposited. At locations of very high focusing factors as e.g. in the equatorial Pacific, we suppose against the background of our data, that $^{230}\text{Th}_{\text{xs}}$ accumulation in sediments is controlled by processes of sedimentology [i.e. winnowing/focusing, cf. *Kienast et al.*, 2007, *Kusch et al.*, 2010, *Loubere et al.*, 2004, *Marcantonio et al.*, 2001, *Siddall et al.*, 2008] rather than by an increased scavenging efficiency [cf. *Broecker*, 2008, *Lyle et al.*, 2005, *Thomas et al.*, 2000]. Consequently we expect high focusing factors to be lower and the vertical sediment fluxes to be higher after applying a grain size correction.

As illustrated for the core PS1768-8, the $^{230}\text{Th}_{\text{xs}}$ normalized vertical flux rate is higher after grain size correction ($F_{\text{VC}} = 3.1 \text{ g cm}^{-2} \text{ ka}^{-1}$ at maximum). However, the error introduced by using $^{230}\text{Th}_{\text{xs}}$ normalization is low compared to a sediment flux rate that has not been $^{230}\text{Th}_{\text{xs}}$ normalized (MAR = $10.1 \text{ g cm}^{-2} \text{ ka}^{-1}$). Thus, the normalization procedure is still a considerable improvement compared to the uncorrected fluxes. This leads us to conclude that $^{230}\text{Th}_{\text{xs}}$ normalization is still the method of choice to unravel strong lateral sediment dislocation events.

Chapter 3

The origin of focused marine sediments: an exploration of local vs. remote sediment sources from grain size data, $^{230}\text{Th}_{\text{xs}}$ and clay mineralogy

Sven Kretschmer^{1, 2}, Walter Geibert^{4, 5}, Dave Heslop^{2, 3}, Gerhard Kuhn¹,
Inka Meyer^{2, 3}, Michiel M. Rutgers van der Loeff¹, Gesine Mollenhauer^{1, 2}

¹ Alfred-Wegener-Institut für Polar- und Meeresforschung, Bremerhaven, Germany

² Fachbereich Geowissenschaften, Universität Bremen, Germany

³ MARUM – Zentrum für Marine Umweltwissenschaften der Universität Bremen, Germany

⁴ School of GeoSciences, University of Edinburgh, Edinburgh, UK

⁵ Scottish Association for Marine Science, Dunstaffnage Marine Laboratory, Oban, UK

Manuscript to be submitted to *Paleoceanography*.

Abstract

Focused sedimentation is an important issue in the deep-sea research, as the primary vertical particle flux, which is of major interest for paleoceanographers, is diluted by the lateral particle advection at focusing locations. The constant flux proxy excess Thorium-230 ($^{230}\text{Th}_{\text{xs}}$) is an important tool for the identification of lateral sediment transport as it allows quantifying vertical and lateral fluxes. The origin of laterally advected material, however, must be determined by other proxies (e.g. clay minerals) and the origin of the accumulated $^{230}\text{Th}_{\text{xs}}$ -signal remains an open question. This study, therefore, centers on the processes and origin of $^{230}\text{Th}_{\text{xs}}$ -focusing in the Eastern Atlantic Sector of the Southern Ocean. Decomposition of grain size distributions by principal component analysis suggests the existence of a fine-grained (<300 μm) endmember which is attributed to being laterally transported. The grain size sorting effect induced by the deposition of this fine-grained endmember at our study site causes a minor biasing of $^{230}\text{Th}_{\text{xs}}$ -normalized vertical flux rates, which is considered to be negligible. A modeling of bulk $^{230}\text{Th}_{\text{xs}}$ data over the past 140,000 years show that the temporal change in the $^{230}\text{Th}_{\text{xs}}$ -signal is largely a function of the intensity of clay accumulation. The exploration of a clay mineral data set (published elsewhere) reveals a close association between chlorite and $^{230}\text{Th}_{\text{xs}}$ deposition. This suggests the $^{230}\text{Th}_{\text{xs}}$ -signal to derive from distant sources upstream of our study site.

3.1 Introduction

It has been observed that the intensity of sediment redistribution is related to glacial-interglacial cycles [Marcantonio *et al.*, 1996; 2001; Higgins *et al.*, 2002]. Systematically higher sediment focusing intensity during glacial stages have been reported for several locations (e.g. in the Central Equatorial Pacific by Marcantonio *et al.* [2001]; in the East Atlantic sector of the Southern Ocean by Frank *et al.* [1999]; in the Indian sector of the Southern Ocean by Dezileau *et al.* [2000]; with a notable exception at the Weddell Sea Continental Margin reported by Frank *et al.* [1995]). A climate induced change in bottom current regimes related to the ocean circulation is usually thought to be the main driving force for the changes in redistribution pattern. However, higher sediment focusing intensity cannot be attributed immediately to higher or lower bottom flow speed only. Sediment redistribution is a function of current strength along the transport pathway from the source to the deposition area. The sources of the sediment supply determine the total amount available for redistribution. Here, we investigate the relative importance of potential factors controlling focusing variability over glacial-interglacial cycles, and we investigate to what extent focusing can be determined from physical and mineralogical information about the sediment.

3.1.1 Glacial-interglacial variation in current velocities

In the case of current strength, Egbert *et al.* [2004] showed in a modeling study that during the Last Glacial Maximum (LGM) tidal dissipation was higher than today and a large fraction of tidal energy scattered into internal tides to the deep ocean due to the lower sea level. Internal tides can intermittently increase the residual flow speed over the threshold for particle motion [Turnewitsch *et al.*, 2008; Peine *et al.*, 2009]. The importance of intermittent maximum flow speed (“benthic storm”) for the formation of bottom nepheloid layers (BNL) has been shown by several authors [Hollister and McCave, 1984; Dickson and McCave, 1986; Gross *et al.*, 1988]. Semiquantitative information on mean flow speed of paleo-bottom currents can be inferred from sedimentary grain size distributions. Those paleo-flow speed records, however, give contrasting results for different regions of the Southern Ocean.

A glacial decline in bottom water vigor reconstructed from grain size distributions has been reported for the northern Weddell Sea [Pudsey *et al.*, 1988; Pudsey, 1992], and for the southern Cape Basin [Kuhn and Diekmann, 2002]. This contrasts with the invigoration of glacial bottom currents as reported for the Antarctic Circumpolar Current (ACC) in the Scotia Sea [Pudsey and Howe, 1998; Howe and Pudsey, 1999] or the increase in flow velocity of Antarctic Bottom Water (AABW) in the Vema Channel during the last two interglacial-glacial-transitions [Ledbetter, 1986]. In addition, the reconstruction of temperature and salinity of surface waters during the LGM based on oxygen isotopes indicates that the glacial production of Antarctic Bottom Water was slightly higher than the modern one [Duplessy *et al.*, 1996]. Our study area

is located in a region (East Atlantic sector of the Southern Ocean) which is believed to have stronger bottom currents during the last glacial period.

3.1.2 Variations in sediment sources

Sediment sources for the abyssal plains comprise the vertically derived material (ice-rafted detritus, dust, biogenic material) and the laterally advected material. Uncertainties exist on the mass proportions of ice-rafted detritus and dust input to the Atlantic section of the Southern Ocean abyssal plains [Nielsen *et al.*, 2007; Pugh *et al.*, 2009]. Ice-rafting is the most important transport mechanism for sand and gravel to the pelagic sea, whereas bottom currents are the main carrier for high proportions of fine-grained sediment compounds [Diekmann and Kubn, 1999]. At our study site, the laterally advected material has been traced by clay mineralogy to originate from distant areas upstream [Patagonia and Antarctic Peninsula, Petschick *et al.*, 1996; Diekmann *et al.*, 1996]. The sediment input may be larger during glacial stages with low sea level, because less sediment is deposited on the shelf. Grobe and Mackensen [1992] explain the higher sediment fluxes during glacial stages with the “bulldozing effect” of shelf grounded ice sheets that trigger turbidity currents to the deep-sea. However, due to sluggish bottom water production at the Antarctic continental margin, less silt could be carried in suspension. More sand and silt has been deposited at the base of the continental slope during the last glacial maximum, rather than being entrained in the BNL [Pudsey, 1992].

3.1.3 Variations in sediment and ^{230}Th focusing

For paleoceanographic studies it is crucial to quantify the lateral sediment input that dilutes the primary vertical signal in order to reconstruct the oceanic paleo-productivity or other paleo-environmental parameters as accurately as possible. The variability of ^{230}Th accumulation is assumed to be a function of sediment focusing. The ^{230}Th -normalization method allows to calculate the vertical particle fluxes and to discriminate them from the advected material so that “preserved vertical rain rates” [François *et al.*, 2004] can be derived, providing information about export paleo-productivity. However, due to heterogeneous distribution of ^{230}Th concentrations in different sediment fractions, particle sorting induced by bottom currents and subsequent deposition of fine material could potentially lead to a biasing in calculation of the preserved vertical rain rates [Kretschmer *et al.*, 2010; chapter 2 in this work]. If the sediment supply from Patagonia and West Antarctica was higher during glacial stages (bulldozing effect) and benthic storms were stronger or more frequent (tidal forcing) this could account for higher particle concentrations in deep and bottom waters and higher sediment fluxes to remote depositional areas. This scenario would explain the glacial increase in sediment and ^{230}Th redistribution. If we take into account the residual bottom flow being more sluggish in the source areas during the

glacial (less Antarctic Bottom Water production in the Weddell Sea), the coarser particles would settle out from the BNL quickly while the transport within the BNL and the mass delivery to the abyssal plains would entrain mainly fine particles. Fine particles have the potential to carry a higher ^{230}Th specific activity due to their higher surface to volume ratio than coarser particles [Kretschmer *et al.*, 2010]. An increased redistribution of fine particles during the glacial, therefore, could result in an enhanced redistribution of particulate ^{230}Th .

3.1.4 Aims of the study

With the aim of understanding the mechanism of past sediment redistribution, this study investigates to what extent the particle size (i.e. bottom current velocity), and the sources of sediment control the sedimentary ^{230}Th accumulation. The study includes the following steps:

Influence on ^{230}Th accumulation by the bottom current velocity.

1. By hindcast modeling of bulk ^{230}Th using a set of constant grain size specific ^{230}Th activities, we test to what extent the bulk $^{230}\text{Th}_{\text{xs}}$ signal is a function of the grain size distribution.
2. By employing a particle size correction, we test to what extent the ^{230}Th focusing factor is sensitive to the selective deposition of fine particles. For the meaningful evaluation of particle size sorting, the maximum particle size that has been laterally advected is deduced from
 - the comparison of grain size distributions of two neighboring sediment cores, and
 - the decomposition of grain size distributions using a two end-member model.

Influence on ^{230}Th accumulation by the sources of sediment.

3. The source and pathway of advected ^{230}Th is deduced from a combined interpretation of ^{230}Th and clay mineralogy.

3.2 Materials and Methods

3.2.1 Study area

The study area is located in the eastern Atlantic sector of the Southern Ocean, south of the Antarctic Polar Front within the Antarctic Zone close to Bouvet Island. In this region the sedimentation is controlled by the Antarctic Circumpolar Current (ACC) with its Circumpolar Deep Water (CDW) extending to the ocean bottom [Gersonde *et al.*, 1999].

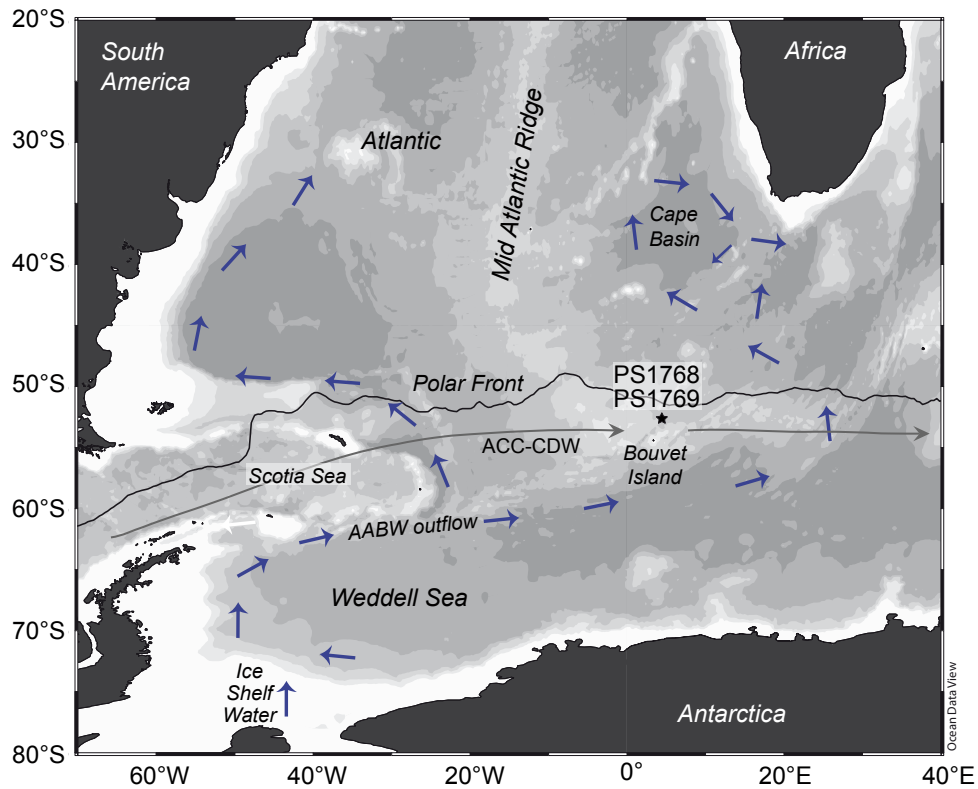


Figure 3.1: The Atlantic Southern Ocean with locations of sediment cores PS1768-8 and PS1769-1 North East of Bouvet Island. Short arrows indicate the flow pattern of Antarctic Bottom Water (AABW) [Modified from Diekmann *et al.*, 2003]. The eastward flowing Antarctic Circumpolar Current (ACC) with its circumpolar deep water (CDW) extends to the seafloor at the core locations [Gersonde *et al.*, 1999].

3.2.2 Sediment core location and sample selection

The gravity cores PS1768-8 and PS1769-1 were recovered north of Bouvet Island at 52.5930°S, 4.4760°E from 3299 m water depth and at 52.6125°S, 4.4580°E from 3269 m water depth, respectively (**Figure 3.1**) during Polarstern cruise ANT-VIII/3. The sediment composition is dominated by alternating layers of diatomaceous mud and diatomaceous ooze with ice-rafted detritus [Gersonde and Hempel, 1990]. Despite their proximity (a lateral separation of 2.5 km, “twin cores”), the cores reveal contrasting mass accumulation rates (MAR). At PS1768-8 the mass accumulation rate during the Last Glacial Maximum (LGM) to marine isotope stage (MIS) 3 is twice that of PS1769-1. This disparity is assumed to result from lateral sediment transport by bottom currents. The age model of core PS1768-8 is constrained by radiocarbon dating and diatom stratigraphy [Frank *et al.*, 1996]. Age control for core PS1769-1 is obtained by correlating the magnetic susceptibility record to that of the parallel core (**Figure 1.5**). Grain size specific ^{230}Th was determined on three samples from PS1768-8 (from 13 ka, 16 ka, and 24 ka) and on two samples from PS1769-1 (from 16 ka and 24 ka). Results on grain size fractionated $^{230}\text{Th}_{\text{xs}}$ from the 16 ka-samples have been previously published by Kretschmer *et al.* [2010]. The

grain size distribution by sieve analysis was performed on the entire core PS1768-8 using the same mesh size as for the grain size fractionation. Additional grain size distributions have been measured by laser diffraction analysis on small core sections (16 to 49 ka) of both cores in order to get more detailed information on grain size during the last interglacial-glacial cycle. Additionally, bulk ^{230}Th data from the core PS1768-8 (5-13 ka and 52-142 ka) are taken from *Frank et al.* [2000a, b].

3.2.3 Grain-size analysis

In order to gain detailed information on the terrigenous granulometry over the last glacial-interglacial cycle a laser diffraction particle sizing has been performed in samples from the past ~49 ka (section 3.2.3.1). In addition to this measurement, another granulometric analysis has been performed (section 3.2.3.2) in order to provide the distribution of the size classes clay, silt, and sand over the past ~140 ka. Those two methods are not comparable, as they measure different properties of the grains. This second analysis was done in the same way (sieve and settle) and with the same grain size limits (2 μm and 63 μm) as done for the grain size fractionation (section 2.4), thus providing comparable information on size classes.

3.2.3.1 Laser diffraction analysis

Grain size distributions have been measured on the terrigenous component (free of organic matter, carbonate, and opal) from both sediment cores between 16 and 49 ka by laser diffraction. A general overview on principles of laser diffraction and sample preparation is provided by e.g. *Blott et al.* [2004] and *Beuselinck et al.* [1998]. Prior to the measurement of the grain size distribution the laser diffraction, the biogenic compounds are removed from the sediment by chemical leaching. The first step is the removal of organic carbon. H_2O (25 mL demineralized) and H_2O_2 (10 mL 35 %) are added to the sediment sample (about 0.5 g dry weight) and boiled until the reaction stops. In a second step, the suspension is filled up to 100 mL, HCl (10 mL, 10 %) is added and boiled for one minute for removing CaCO_3 . To remove the HCl from the sample, the suspension is filled up with demineralized H_2O to 1000 mL. The supernatant is decanted to ~100 mL after 24 h. This is repeated a second time. Removal of biogenic silica is achieved by adding 6 g NaOH-pellets to the 100 mL suspension and boiling for 10 min. To remove the NaOH from the sample, again the suspension is diluted with H_2O by filling up and decanting twice. To keep the particles well dispersed during the measurement, sodiumpyrophosphate (300 mg, $\text{Na}_4\text{P}_2\text{O}_7 \times 10\text{H}_2\text{O}$) is added to the 100 mL suspension and boiled shortly. Measurement is performed in demineralized and degassed water on the *LS 200 Laser Diffraction Particle Size Analyzer* (Beckman Coulter) with a lower detection limit of 0.4 μm . Results are given in volume-percentage (vol-%). Additionally to the laser diffraction analysis, a sieving and settling analysis has been performed as described in the next section.

3.2.3.2 Sieving and settling analysis

The sieve and settling analysis has been performed on the organic- and carbonate-free samples of the entire sediment cores PS1768-8 and PS1769-1. For the granulometric characterization of silt and clay, sub-samples were washed through a 63 μm mesh for grain size separation of sand and gravel from silt and clay. The fine fraction was treated with 3 % hydrogen peroxide solution and 10 % acetic acid for disaggregation and the removal of organic carbon and carbonate. Silt and clay then was separated at 2 μm in settling tubes [Kuhn and Diekmann, 2002]. This method of granulometry is consistent to that of the next section (3.2.4 Grain size fractionation) where the same grain size intervals (<2 μm , 2-63 μm , >63 μm) are applied.

3.2.4 Grain size fractionation

The fractionation procedure and the resulting sediment fractions are described in detail by Kretschmer *et al.* [2010]. Sediment samples are separated into particle size-classes by sieving through nylon sieves using natural seawater. The resulting particle size-classes 20-63, 63-125 and >125 μm are further fractionated by their density in water into “slowly settling particles” and “fast settling particles”. The particle class <20 μm is further fractionated by settling through purified water into clay-sized particles <2 μm and fine silt particles 2-20 μm . A high concentration of biogenic opal (mainly diatoms, 75-86 wt-%) is the main characteristic of the slowly settling particles. Also the fine silt (2-20 μm) and the clay-sized (<2 μm) particle fractions contain high amounts of opal (mainly diatom fragments, 54-80 wt-% and 41-68 wt-%, respectively). In contrast, the fast settling particles with lower opal content (1-17 wt-%) contain mainly ice-rafted rock fragments, mixed with radiolarians and few diatoms.

Grain size fractions obtained by sieving and settling are analyzed on the laser diffraction analyzer in order to check for the quality of size fractionation. In this case, the chemical leaching is skipped to obtain the full spectrum of sizes, including the sizes of biogenic opal, a major component of the samples. Before the measurement, the dry sediment fractions are soaked in demineralized water over night, sodium pyrophosphate is added, and the suspension is boiled shortly and then measured on the same laser analyzer as mentioned above.

3.2.5 Th and U analysis

Th and U isotopes are analyzed on freeze-dried sediment samples by isotope dilution by Inductively Coupled Plasma-Sector Field-Mass Spectrometry (ICP-SF-MS). The method is described in detail by Kretschmer *et al.* [2010]. Sediment samples (5-50 mg) together with spikes ^{229}Th (9 pg) and ^{236}U (800 pg) are weighed into Teflon vials and fully dissolved in concentrated acid (HNO_3 , HCl , HF) by a pressure-assisted microwave digestion system. Uranium and thorium in the dissolved samples are iron ($\text{Fe}(\text{OH})_3$) co-precipitated and re-dissolved in HNO_3 .

Uranium and thorium are separated by ion chromatography with UTEVA resin columns. The separated uranium and thorium fractions are finally diluted in 5 mL HNO₃ and analyzed by ICP-MS (Element2, Thermo Scientific) with a desolvation system (Apex Q, ESI). For details of machine settings see *Martínez-García et al.* [2009]. The external reproducibility from replicate analyses of certified reference material *UREM 11* [*Hansen and Ring*, 1983] is within 3.8 % for ²³⁸U and 5.0 % for ²³⁰Th. Results are given in dpm g⁻¹ (disintegration per minute per gram of size fractionated particles).

3.2.6 Excess ²³⁰Th and focusing factor

Only unsupported ²³⁰Th deriving from scavenging (=excess ²³⁰Th or ²³⁰Th_{xs}) is of interest. ²³⁰Th_{xs} is calculated after *François et al.* [2004] and described here briefly. Any ²³⁰Th supported by lithogenic or authigenic uranium needs to be subtracted from the measured ²³⁰Th. The activity of lithogenic ²³⁰Th in secular equilibrium with lithogenic ²³⁸U, is derived from the activity ratio ²³⁸U/²³²Th that has been suggested to be on average 0.6±0.1 for the Atlantic basin [*Henderson and Anderson*, 2003]. The activity of authigenic ²³⁰Th is estimated from authigenic ²³⁸U (= total ²³⁸U minus lithogenic ²³⁸U), multiplied by 1.14 (activity ratio of ²³⁴U/²³⁸U in seawater), calculating the ²³⁰Th production since the time of deposition. The excess ²³⁰Th activity needs to be decay corrected (half-life 75,380 years) to obtain the initial activity at the time of deposition (= ²³⁰Th_{xs}(0), hereafter written as ²³⁰Th_{xs}).

These calculations are based on assumptions for bulk samples and may be problematic for grain size separated samples, because size fractionation may produce a U/Th fractionation due to lithogenic minerals of different size classes. Especially the lithogenic ²³⁸U/²³²Th activity ratio could deviate significantly from the average value 0.6±0.1.

The focusing factor Ψ is given by the inventory of ²³⁰Th_{xs} in the sediment section divided by the ²³⁰Th production in seawater:

$$\Psi = T_{bulk} \times \rho \times (s_1 - s_2) \times 10 / \beta_{230} \times z \times (t_1 - t_2), \quad (3.1)$$

where T_{bulk} is the bulk ²³⁰Th_{xs} activity [dpm g⁻¹] in the sediment, ρ is the mean dry bulk density [g cm⁻³], s_1 and s_2 are the sediment depths [cm], t_1 and t_2 are the corresponding ages [ka], β_{230} is the annual production of ²³⁰Th in the seawater [0.0267 dpm m⁻³ a⁻¹], and z is the water depth [m]. Assuming a particle size sorting, we can apply a grain size correction for Ψ using the grain size specific ²³⁰Th_{xs} activities. The derivation of the equation for a grain size corrected focusing factor Ψ_c is described by *Kretschmer et al.* [2010] and is included in the appendix of this work. The assumption for particle sorting is that the lateral sediment flux comprises fine material only. Ψ_c is then calculated as:

$$\Psi_c = \frac{1}{1 - \frac{T_{bulk}}{T_f} \left(1 - \frac{1}{\Psi}\right)} \quad (3.2)$$

where Ψ is the focusing factor measured, T_{bulk} is the bulk $^{230}\text{Th}_{xs}$ activity [dpm g⁻¹] in the sediment and T_f is the $^{230}\text{Th}_{xs}$ activity [dpm g⁻¹] in the fine particle fraction. The preserved vertical flux of particles is calculated according to *Suman and Bacon* [1989], where the $^{230}\text{Th}_{xs}$ normalized sediment flux F_V is the vertical flux of any sediment constituent f_i , given by its ratio to the decay-corrected sedimentary $^{230}\text{Th}_{xs}$ (T_{bulk}):

$$F_V = \beta_{230} \times z \times f_i / T_{bulk} \quad (3.3)$$

According to the corrected focusing factor, Ψ_c , the preserved vertical mass flux, F_V [g cm⁻² ka⁻¹], needs to be corrected (F_{VC}) as well:

$$F_{VC} = F_V \times \Psi / \Psi_c \quad (3.4)$$

3.3 Results

3.3.1 Grain size fractionation

The particle size fractions were obtained from five sediment samples (3 samples from PS1768-8 at 13, 16, and 24 ka, and 2 samples from PS1769-1 at 16, and 24 ka). Results are reported in **Table 3.1**. The results of the two 16 ka samples have been previously published by *Kretschmer et al.* [2010]. Note that the fractionation was done without the removal of biogenic opal, resulting in variable amounts of biogenic opal. For instance, the clay fraction contains 41-68 % biogenic opal. The fine silt and the slowly settling particles contain 54-86 %, whereas the particles of the corresponding fast settling size classes contain 1-17 % opal.

Clay and fine silt (<20 μm) are the dominant fractions accounting for more than 50 % (**Table 3.1**). The slowly accumulating core site (PS1769-1) receives less clay and fine silt than the rapidly accumulating one (PS1768-8). In turn, the fast settling sand fractions (>63 μm) have higher concentrations at PS1769-1 (2-17 %) than at PS1768-8 (1-7 %). Mass accumulation rates (uncorrected for focusing) are two times higher at PS1768-8 than at PS1769-1. Consequently, the flux of fine material (<63 μm) to the rapid accumulation site is more than double of that of the slow accumulation site (e.g. clay flux rate at 24 ka: 2.0 and 0.8 g cm⁻² ka⁻¹, respectively).

Figure 3.2 displays the measurement by laser diffraction analysis that was performed on each particle size fraction for monitoring the quality of particle separation. Separation of

coarse silt (20-63 μm), fine sand (63-125 μm) and coarse sand (125-2000 μm) appears to be effective, because peaks are narrow and within the corresponding sieve interval. However, the peaks of coarse silt and fine sand appear to be shifted to sizes slightly coarser than expected. Separation by settling into fine silt (2-20 μm) and clay (<2 μm) produces wide, overlapping size spectra. Also these size spectra are shifted to a size that is coarser than one would expect from

Table 3.1: Comparison of fluxes and specific activities of $^{230}\text{Th}_{\text{xs}}$ at different times (13, 16, and 24 ka BP) in sediment cores PS1768-8 (rapidly accumulated) and PS1769-1 (slowly accumulated). The 16 ka-data are cited from *Kretschmer et al.* [2010]. *NA* = not analyzed. Shading highlights the slowly accumulated sediment core.

size fraction [μm]	settling velocity	weight-% of total sample		mass flux [$\text{g cm}^{-2} \text{ka}^{-1}$]		$^{230}\text{Th}_{\text{xs}}$ [dpm g^{-1}]		$^{230}\text{Th}_{\text{xs}}$ flux [$\text{dpm cm}^{-2} \text{ka}^{-1}$]	
		1768	1769	1768	1769	1768	1769	1768	1769
13 ka BP									
bulk				8.4	<i>NA</i>	3.3	<i>NA</i>	27.8	<i>NA</i>
< 2		23.8	<i>NA</i>	2	<i>NA</i>	10.8	<i>NA</i>	21.7	<i>NA</i>
2-20		45.4	<i>NA</i>	3.8	<i>NA</i>	1.6	<i>NA</i>	6.3	<i>NA</i>
20-63	slowly	20	<i>NA</i>	1.7	<i>NA</i>	1.4	<i>NA</i>	2.3	<i>NA</i>
63-125	slowly	3	<i>NA</i>	0.3	<i>NA</i>	1.3	<i>NA</i>	0.3	<i>NA</i>
>125	slowly	0.2	<i>NA</i>	0	<i>NA</i>	1.6	<i>NA</i>	0	<i>NA</i>
20-63	fast	4.2	<i>NA</i>	0.4	<i>NA</i>	2.2	<i>NA</i>	0.8	<i>NA</i>
63-125	fast	2.1	<i>NA</i>	0.2	<i>NA</i>	2	<i>NA</i>	0.4	<i>NA</i>
>125	fast	1.3	<i>NA</i>	0.1	<i>NA</i>	1.5	<i>NA</i>	0.2	<i>NA</i>
16 ka BP									
bulk				8.5	4.3	6.6	6.7	56.5	29
< 2		39.6	35.5	3.4	1.5	12.7	12.7	43	19.6
2-20		43.6	40.6	3.7	1.8	1.2	2.1	4.5	3.8
20-63	slowly	10.8	14.1	0.9	0.6	0.4	0.7	0.3	0.4
63-125	slowly	0.6	0.6	0.1	0	1.4	0.5	0.1	0
>125	slowly	0.2	0.6	0	0	0.7	2.6	0	0.1
20-63	fast	2.4	2.1	0.2	0.1	1.6	2.8	0.3	0.3
63-125	fast	1	1.8	0.1	0.1	1.1	1.6	0.1	0.1
>125	fast	1.8	4.6	0.2	0.2	1.1	1.5	0.2	0.3
24 ka BP									
bulk				5.6	3.1	6.7	5.7	37.4	17.4
< 2		34.8	25.5	2	0.8	16.3	14	31.8	11
2-20		37.4	31.3	2.1	1	2.5	3.2	5.2	3.1
20-63	slowly	11.2	6.9	0.6	0.2	1.2	1.9	0.8	0.4
63-125	slowly	2.6	1.4	0.1	0	1.2	2	0.2	0.1
>125	slowly	0.8	0.3	0	0	0.8	1.2	0	0
20-63	fast	4	9	0.2	0.3	1.6	0.8	0.4	0.2
63-125	fast	2.6	8.7	0.1	0.3	1.1	0.7	0.2	0.2
>125	fast	6.5	17	0.4	0.5	0.6	0.6	0.2	0.3

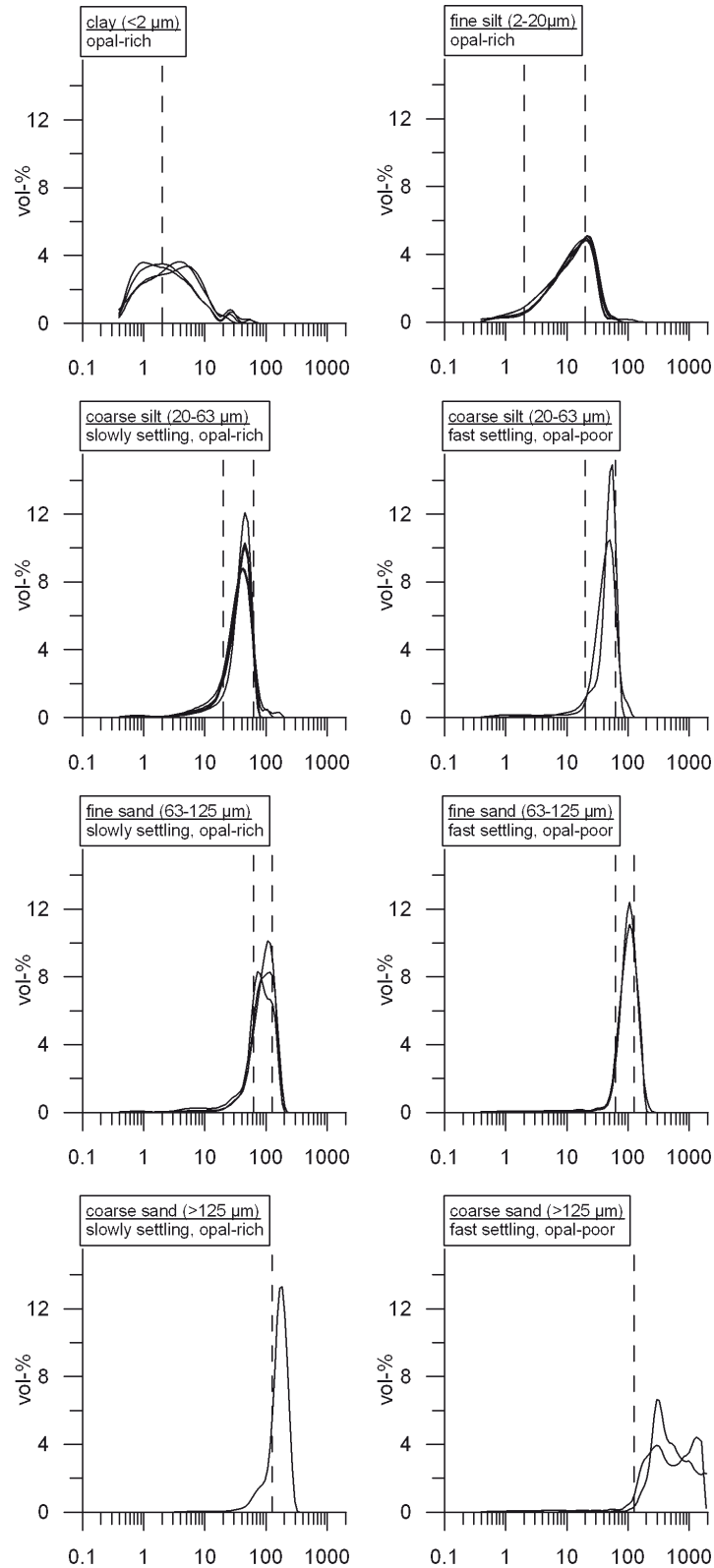


Figure 3.2: Each particle fraction separated by sieving and settling was measured by laser diffraction spectrophotometry. The vertical dashed lines indicate the size intervals employed to obtain the particle fractions. The diagrams contain multiple overlying grain size spectra, because fractions of five sediment samples were processed. Note that the “clay fraction” contains 41-68 % biogenic opal in addition to the clay minerals.

the calculation after Stokes law based on densities of quartz (2.65 g cm^{-3}). As biogenic opal has a lower density (2.3 g cm^{-3}) than quartz, coarser light grains add to the size spectra of fine silt and clay fraction.

3.3.2 Grain size fractionated $^{230}\text{Th}_{\text{xs}}$

The size fractionated sediment samples from 13 and 24 ka reveal $^{230}\text{Th}_{\text{xs}}$ distribution patterns similar to the 16 ka-samples reported by *Kretschmer et al.* [2010], (**Figure 3.3**). The $^{230}\text{Th}_{\text{xs}}$ specific activities are 2-3 fold higher within the clay fraction ($10.7\text{-}16.2 \text{ dpm g}^{-1}$) than in the bulk sediment ($3.0\text{-}6.7 \text{ dpm g}^{-1}$). The $^{230}\text{Th}_{\text{xs}}$ activities in larger particles ($>2 \mu\text{m}$) range

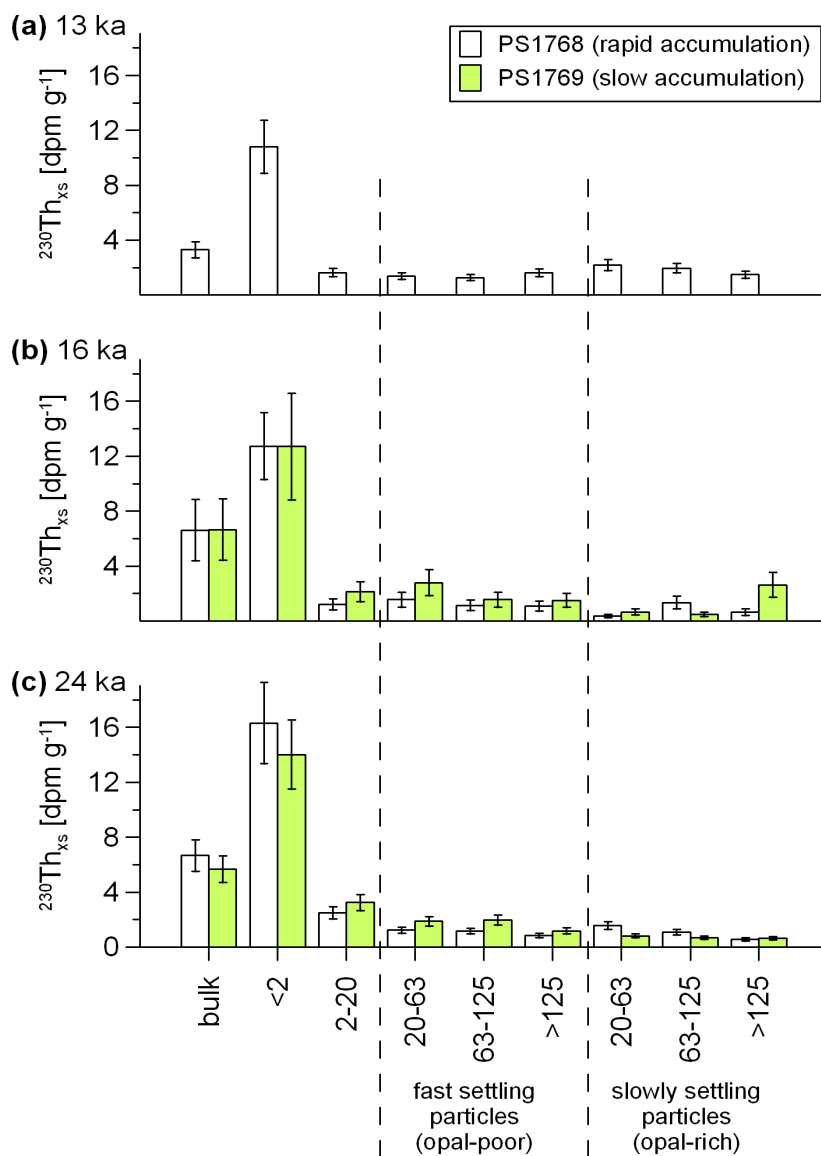


Figure 3.3: $^{230}\text{Th}_{\text{xs}}$ specific activities in bulk samples and size fractions of the rapid accumulation core PS1768-8 (white bars) and the slow accumulation core PS1769-1 (colored bars). Samples are from 13 ka (a), 16 ka (b), and 24 ka (c). From PS1769-1 the 13 ka-sample was not available. $^{230}\text{Th}_{\text{xs}}$ data on the 16 ka sample (b) are from *Kretschmer et al.* (2010). Error bars represent the analytical uncertainty of 1σ .

within a small amplitude (0.4-3.2 dpm g⁻¹) and are lower than in bulk sediment and clay. Average values for ²³⁰Th_{xs} specific activities in clay, silt and sand are listed in **Table 3.2**. The coarse particles of both twin cores contribute only negligible amounts to the total ²³⁰Th_{xs} flux rates (**Table 3.1**). Clay is the major carrier of ²³⁰Th_{xs}. It contributes 66 % to the ²³⁰Th_{xs} flux at the slow accumulation site (PS1769-1), and 75-86 % at the rapid accumulation site (PS1768-8). PS1768-8 receives double to threefold the ²³⁰Th_{xs} flux of PS1769-1. ²³⁰Th_{xs} fluxes are highest during the deglacial and lower during LGM and Holocene. Also fine silt (2-20 μm) contributes a remarkable amount to the ²³⁰Th_{xs} flux. In summary, the bulk ²³⁰Th_{xs} specific activity is controlled by the mixing ratio between the ²³⁰Th_{xs}-rich clay flux and the low ²³⁰Th_{xs} activity of the coarser particles.

Table 3.2: Minima, maxima and average specific activities of ²³⁰Th_{xs} [dpm g⁻¹] per size class as calculated from five size fractionated sediment samples. The average values are assumed to be the same for the whole sediment cores and are used for the size correction of the focusing factor.

	>63 μm	2-63 μm	<2 μm
minimum	0.5	0.3	10.7
maximum	2.6	3.2	16.2
average	1.2	1.7	13.3
standard deviation	0.4	0.6	1.4

3.3.3 Grain size distributions

The proportion of clay, silt, and sand (**Table 3.3**) strongly depends on the technique of granulometry (sections 3.2.3.1 and 3.2.3.2). The laser diffraction analysis (hereafter shortly laser analysis or LDA) results in larger proportion of sand relative to the sieve analysis (SA). In contrast, the clay fraction from the laser analysis is 0.5 to 0.8 times lower than from the settling analysis. Irrespective of their differences, both methods point to a selective grain size deposition that is finer under rapid accumulation (PS1768-8) than at the slowly accumulating site (PS1769-1). The mean grain sizes (LDA, **Table 3.3**) are 27-182 μm (PS1768-8) and 54-204 μm (PS1769-1). **Figure 3.4** provides a more detailed view in the differences of size distributions of the terrigenous component between the twin cores. The size distributions of the twin cores (left panel) and their relative differences (right panel) calculated by subtracting the size distribution of PS1769-1 from PS1768-8 are shown. The fast accumulating site reveals pronounced excess deposition in fines (indicated by the black shaded area for values >0). This excess deposition can be distinguished into two groups, first, “excess mud” (i.e. PS1768-8 has higher proportions in the size range <66 μm than PS1769-1, with mean sizes of “excess mud” of 3-11 μm), and second, “excess silt” (i.e. PS1768-8 has higher proportion in the size range <140 μm, with mean sizes of “excess silt” of 25-47 μm).

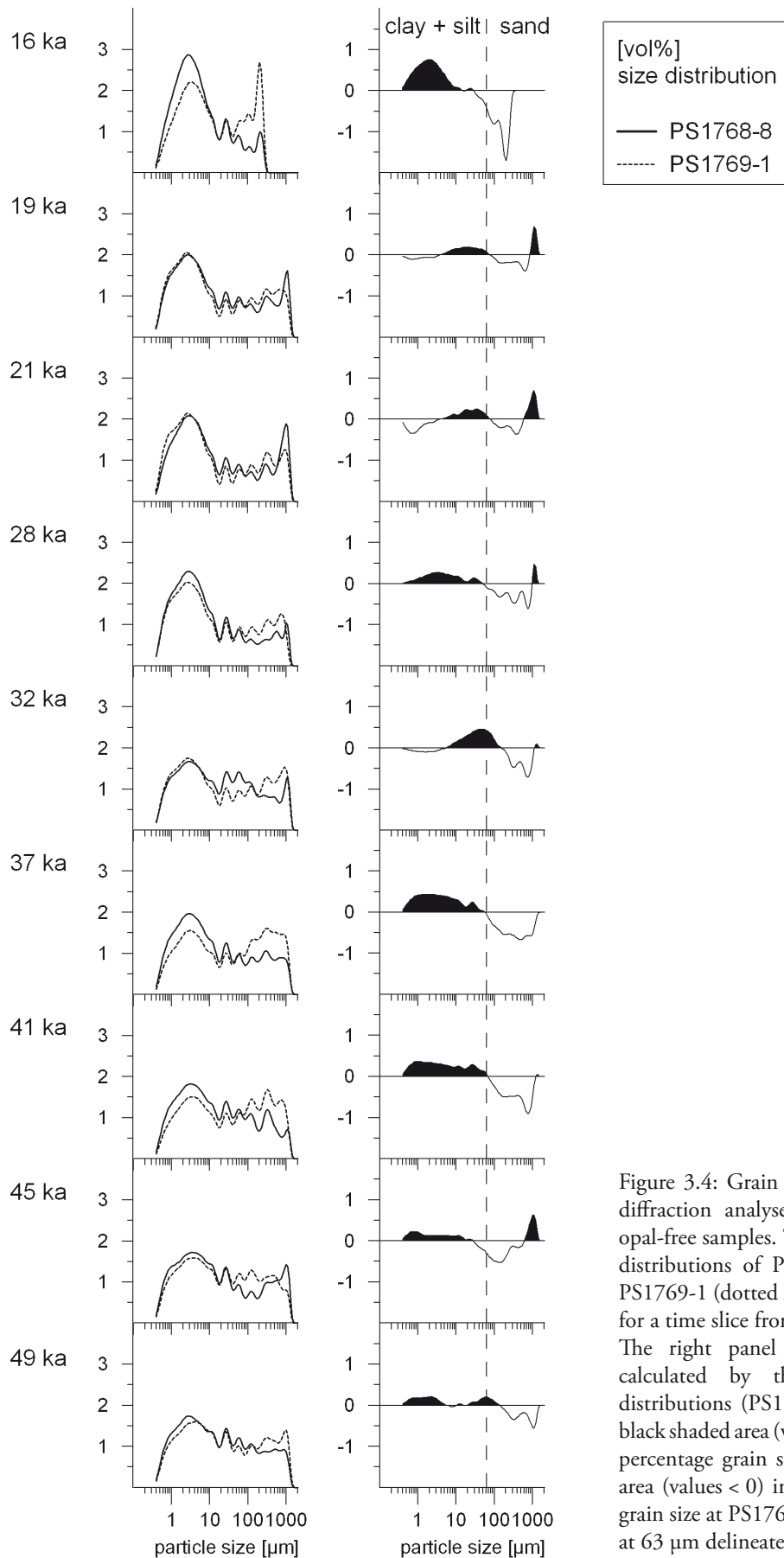


Figure 3.4: Grain size distributions by laser diffraction analyses on carbonate-free and opal-free samples. The left panel displays size distributions of PS1768-8 (solid line) and PS1769-1 (dotted line) in volume percentage for a time slice from 16 to 49 ka.

The right panel displays the differences calculated by the subtraction of size distributions (PS1768 minus PS1769). The black shaded area (values > 0) indicates higher percentage grain size at PS1768. The white area (values < 0) indicates higher percentage grain size at PS1769. The vertical dashed line at 63 μm delineates mud from sand.

Table 3.3: Grain size distributions measured by laser diffraction spectrophotometry and sieve/settle-analysis between 14 and 49 ka BP in the twin cores PS1768-8 (rapid accumulation) and PS1769-1 (slow accumulation). *NA*: no data. Shading highlights the slowly accumulated sediment core.

age [ka]	core	mean [μm]	laser grain size (terrigenous fraction)				sieve/settle grain size (terrigenous + opal)			
			sand	silt	clay	silt/clay	sand	silt	clay	silt/clay
			[vol-%]				[wt-%]			
14	PS1768-8	33.9	15.5	64.7	19.8	3.3	5.8	58.6	35.6	1.6
	PS1769-1	<i>NA</i>	<i>NA</i>	<i>NA</i>	<i>NA</i>	<i>NA</i>	<i>NA</i>	<i>NA</i>	<i>NA</i>	<i>NA</i>
16	PS1768-8	26.7	11.9	64.1	24.0	2.7	5.7	49.5	44.9	1.1
	PS1769-1	53.9	27.5	56.3	16.2	3.5	12.7	59.5	27.8	2.1
19	PS1768-8	165.6	30.4	49.1	20.5	2.4	17.5	45.0	37.4	1.2
	PS1769-1	154.4	32.6	45.6	21.8	2.1	15.8	51.0	33.2	1.5
21	PS1768-8	182.8	30.6	50.2	19.2	2.6	11.9	50.9	37.2	1.4
	PS1769-1	153.8	30.9	46.3	22.9	2.0	15.3	54.4	30.3	1.8
24	PS1768-8	<i>NA</i>	<i>NA</i>	<i>NA</i>	<i>NA</i>	<i>NA</i>	15.8	50.6	33.6	1.5
	PS1769-1	157.3	37.6	47.8	14.6	3.3	13.0	57.5	29.5	1.9
28	PS1768-8	114.2	22.8	54.0	23.2	2.3	10.4	52.8	36.7	1.4
	PS1769-1	136.2	30.5	48.0	21.5	2.2	14.0	57.2	28.8	2.0
32	PS1768-8	149.0	32.7	50.0	17.3	2.9	15.0	55.8	29.2	1.9
	PS1769-1	188.9	37.7	43.9	18.4	2.4	14.0	57.2	28.8	2.0
37	PS1768-8	131.3	29.0	51.7	19.3	2.7	12.9	56.3	30.8	1.8
	PS1769-1	204.0	44.5	41.5	13.9	3.0	15.6	61.9	22.5	2.8
41	PS1768-8	120.5	29.4	52.8	17.8	3.0	16.1	54.6	29.3	1.9
	PS1769-1	189.4	43.5	43.4	13.1	3.3	17.0	59.4	23.6	2.5
45	PS1768-8	168.3	30.8	51.0	18.3	2.8	22.1	52.0	25.9	2.0
	PS1769-1	146.1	35.4	49.0	15.5	3.2	13.4	62.0	24.7	2.5
49	PS1768-8	132.4	30.6	51.7	17.6	2.9	15.5	56.4	28.1	2.0
	PS1769-1	177.8	36.0	48.9	15.1	3.2	14.0	60.5	25.5	2.4

3.4 Discussion

3.4.1 $^{230}\text{Th}_{\text{xs}}$ modeling based on particle size

If sedimentary $^{230}\text{Th}_{\text{xs}}$ was largely controlled by grain size, the “prediction” of $^{230}\text{Th}_{\text{xs}}$ based on the measured grain size distributions should be possible. We test this approach by assuming that the grain size specific $^{230}\text{Th}_{\text{xs}}$ was constant and the distribution of clay, silt, and sand was the variable parameter during the past 140 ka. Based on the measurements of size fractionated $^{230}\text{Th}_{\text{xs}}$ (**Figure 3.3**), we assume average specific activities of $^{230}\text{Th}_{\text{xs}}$ for size classes

<2 μm , 2-63 μm and >63 μm (Table 3.2) as to be the same for the past 140 ka. A stronger redistribution of sediments by stronger bottom currents is not expected to change their specific ^{230}Th contents. If, in addition to this effect, there is a higher input of sediments from shallow sources this would be expected to reduce their specific ^{230}Th contents [François *et al.*, 2004], thus our assumption would be invalid. If this dilution from shallow sources is not a major effect and if our assumption is valid, consequently, only the variability of grain size distributions

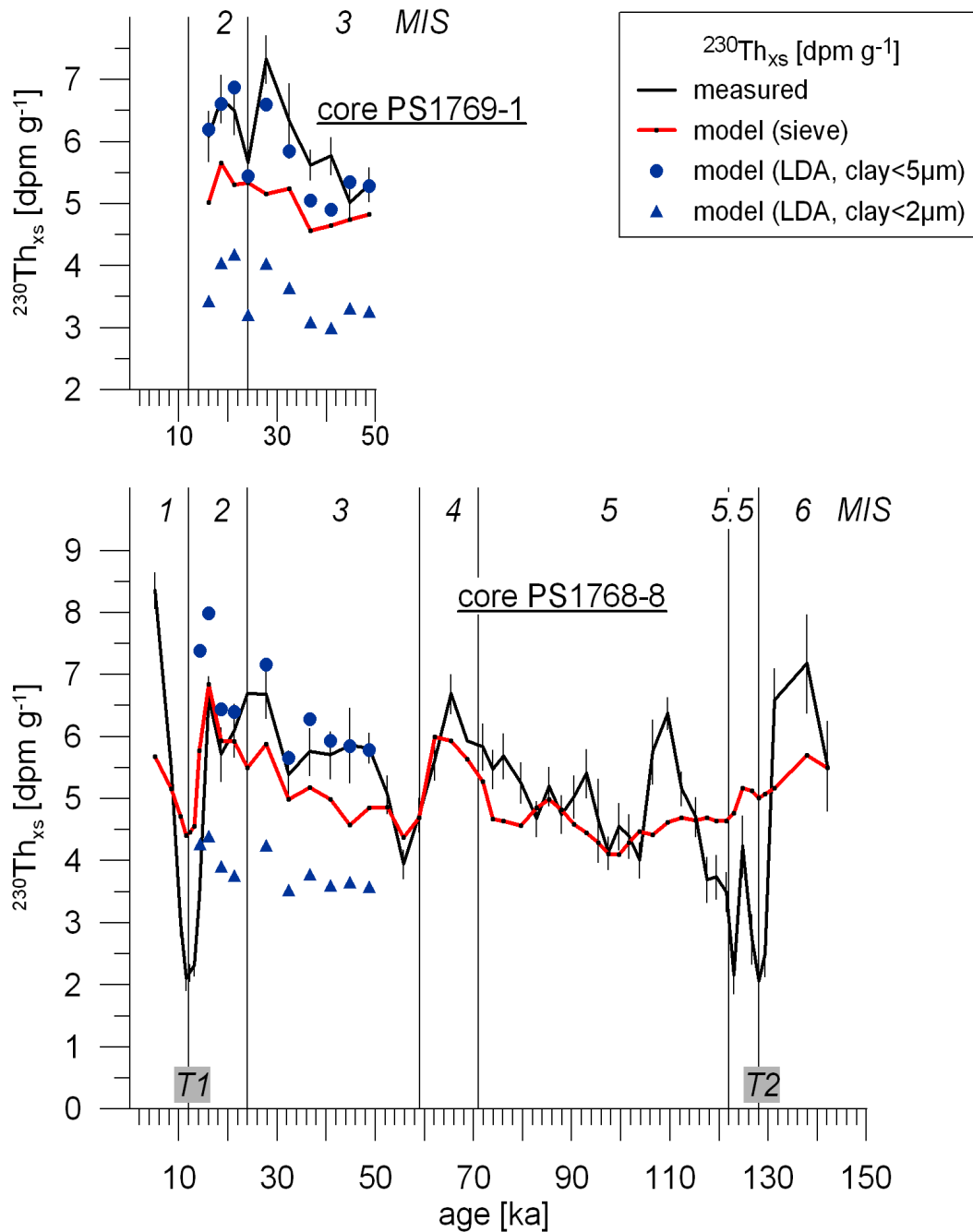


Figure 3.5: Modeling the bulk $^{230}\text{Th}_{\text{xs}}$ specific activities based on particle size data. Average $^{230}\text{Th}_{\text{xs}}$ specific activities are assumed to be constant for the past 140 ka, so that the variability of $^{230}\text{Th}_{\text{xs}}$ is a function of the grain size distribution

would account for the variability of $^{230}\text{Th}_{\text{xs}}$. The average $^{230}\text{Th}_{\text{xs}}$ specific activities multiplied with the corresponding percentage size distribution gives the “predicted” bulk $^{230}\text{Th}_{\text{xs}}$ value. For this calculation we use both grain size class distributions measured by the two grain size quantification methods, LDA and SA. **Figure 3.5** shows that the excursions of the measured $^{230}\text{Th}_{\text{xs}}$ values (black line, own data from 14 to 49 ka extended by the data set of *Frank et al.* [2000a, b]) are reasonably delineated by the model values (red line, based on sieve/settle analysis) between 5 and 100 ka. From 100 to 140 ka a strong mismatch between the curves is observed. Remarkably low $^{230}\text{Th}_{\text{xs}}$ values measured at termination 2, MIS 5.5, and termination 1 are not reproduced by the model values. This mismatch indicates that our assumption of constant ^{230}Th activities may be invalid (i.e. a change of sediment source may have occurred) at those particular points of time.

The calculation based on the laser grain sizes (LDA, blue symbols in **Figure 3.5**) looks different. Applying the standard size limit for clay (2 μm), the model $^{230}\text{Th}_{\text{xs}}$ values (triangles, **Figure 3.5**) are significantly too low, because the clay content is substantially lower by the laser analysis (**Figure 3.2, Table 3.3**). The LDA underestimates the clay content because the platy-shaped clay minerals appear larger by the forward-scattering laser than implied by the respective settling diameter [*Konert and Vandenberghe, 1997*]. An adjustment of the size limit for clay to 5 μm leads to model output values (circles, **Figure 3.5**) that fit quite well with the measured values. Late Holocene values were not predicted due to missing grain size data. In fact, this hindcasting approach reveals that the bulk $^{230}\text{Th}_{\text{xs}}$ specific activities can be explained by the particle size distribution being a controlling factor over a particular time slice. Therefore, if $^{230}\text{Th}_{\text{xs}}$ accumulation in sediments was controlled by the deposition of fine particles, a particle sorting due to the preferential deposition of fine material could lead to an overestimation of the sediment focusing factor that is calculated on the basis of $^{230}\text{Th}_{\text{xs}}$ inventories. To what extent this grain size biasing may occur is described in the following section 3.4.2. The hindcasting approach further indicates that changing parameters apart from the grain size variations control $^{230}\text{Th}_{\text{xs}}$ accumulation at the two last terminations and during MIS 5.3 - 5.5. This point is further discussed in section 3.4.3.

3.4.2 Focusing factor

The focusing factors calculated for the twin cores ($\Psi = 2.1\text{-}5.8$, **Table 3.4**) indicate a sediment supply from a lateral source. The amount of laterally advected sediment is about double for the rapid accumulation site (PS1768-8) than for the slow one (PS1769-1). This contrast in sediment deposition is thought to be caused by differences in the bottom water flow speed that is modulated by the local topography. However, if the $^{230}\text{Th}_{\text{xs}}$ signal is a function of grain size as shown in the previous section, the disparity in the focusing factors between the twin cores may be a reflection of different grain size distributions rather than different amounts

of sediment deposition. The lateral advection of particles by bottom currents could induce a particle size sorting by selective deposition according to the particle size and density and to the bottom water flow speed [McCave, 2005]. A preferential deposition of fine material may result in biasing the focusing factor Ψ , which may be corrected for as proposed by Kretschmer et al. [2010]. For a meaningful grain size correction of the focusing factor at our study site, however, the paleo-bottom flow speed or the grain size fraction that has been laterally transported should

Table 3.4: Focusing factors Ψ and vertical rain rates calculated using bulk $^{230}\text{Th}_{\text{xs}}$ values and grain size corrected $^{230}\text{Th}_{\text{xs}}$ values following the assumption that the deposition of lateral advected material comprises only particles smaller than 300 μm . DBD: dry bulk density; LSR: linear sedimentation rate; MAR: marine accumulation rate; T_{bulk} and T_f : $^{230}\text{Th}_{\text{xs}}$ in bulk sample and fine particle fraction, respectively; P_f : fine particles <300 μm ; Ψ and Ψ_c : focusing factor (bulk and corrected); F_V and F_{Vc} : preserved vertical rain rate (bulk and corrected); NA = not

depth [cm]	age [ka]	DBD [g cm ⁻³]	LSR [cm ka ⁻¹]	MAR	bulk analysis			corrected for particles <300 μm			
					T_{bulk} [dpm g ⁻¹]	Ψ [g cm ⁻² ka ⁻¹]	F_V	P_f [%]	T_f [dpm g ⁻¹]	Ψ_c	F_{Vc} [g cm ⁻² ka ⁻¹]
sediment core PS1768-8											
142	14 ^a										
147		0.78	10.4	8.6	3.41	5.8	2.6	0.99	3.41	4.4	3.4
167		0.82			7.05		1.2	0.99	7.05		1.6
168		0.82			6.63		1.3	0.99	6.63		1.7
194		0.88			5.72		1.5	0.84	6.59		2.0
219		0.82			6.10		1.4	0.82	7.17		1.9
244	24 ^a	0.87	6.4	5.6	6.67	3.8	1.3	<i>NA</i>	<i>NA</i>	2.9	1.7
268		0.86			6.69		1.3	0.88	7.40		1.7
292		0.88			5.39		1.6	0.86	6.06		2.1
319		0.84			5.76		1.5	0.87	6.46		2.0
343		0.85			5.71		1.5	0.88	6.31		2.0
369		0.84			5.86		1.5	0.83	6.84		2.0
393		0.91			5.82		1.5	0.87	6.52		2.0
469	59 ^a										
sediment core PS1769-1											
12	16 ^b	0.85	5.1	4.4	6.09	3.2	1.4	0.84	7.01	2.6	1.8
22		0.85			6.70		1.3	0.84	7.78		1.6
35		0.85			6.50		1.3	0.84	7.52		1.7
53	24 ^b	0.88	3.5	3.1	5.66	2.1	1.5	0.84	6.51	1.8	1.8
62		0.89			7.33		1.2	0.85	8.41		1.4
69		0.89			6.34		1.4	0.8	7.60		1.6
87		0.88			5.63		1.6	0.78	6.87		1.8
97		0.87			5.77		1.5	0.8	6.93		1.8
112		0.89			5.02		1.7	0.85	5.69		2.0
128		0.89			5.31		1.6	0.82	6.22		1.9
175	59 ^b										

be known. Therefore, in the next two sections we attempt to determine criteria to attribute certain size fractions to the lateral advection. This will provide information about the particle size fraction that contributes most to the $^{230}\text{Th}_{\text{xs}}$ focusing at the studied sites. Further, the size correction will show if the focusing factor and the $^{230}\text{Th}_{\text{xs}}$ -normalization method are sensitive towards this grain size effect.

3.4.2.1 Differences in particle size distributions between the sites

By comparing the particle size distributions of the twin cores, we attempt to discriminate and characterize the particular size fraction of sediment which has been laterally advected and preferentially deposited to the site PS1768-8. The size differences between sites of fast accumulation (PS1768-8) and slow accumulation (PS1769-1) shown in the diagrams of **Figure 3.4** are thought to derive from processes linked to the lateral mass transport by bottom currents. Generally, all grain sizes may derive from both transport modes (vertical and lateral), but the coarse sand ($>600\ \mu\text{m}$), however, is assumed to derive from ice-rafted primary glacial detritus supplied vertically to our study sites, only. Particularly distinctive is the comparison between the deglacial period (16 ka) and the LGM (19 and 21 ka). “Excess mud” situations ($<30\ \mu\text{m}$, mean size = $3\ \mu\text{m}$) indicate a relatively sluggish flow speed during deglacial time at location PS1768-8, whereas “excess silt” ($4\text{--}73\ \mu\text{m}$, mean size = $26\text{--}29\ \mu\text{m}$) points to a more vigorous flow at location PS1768-8 during the last glacial period. The change in the focusing factor between MIS 3 and MIS 2 is not clearly reflected by the grain size distributions. Because of this quite heterogeneous pattern, it is hardly possible to identify one typical particle size fraction that accounts for the advective transport throughout the entire time period. One conclusion that can be drawn for site PS1768-8 (**Figure 3.4**) is that particles that have been advected in suspension from a lateral source probably were not larger than $140\ \mu\text{m}$. The lower threshold for a maximum size of advected particles would be $\sim 30\ \mu\text{m}$. Another more statistical approach based on decomposition of grain size distributions is presented in the following section.

3.4.2.2 Endmember model approach

Within this study we consider the laterally and vertically transported material, i.e. a two component system. Therefore, a simple two endmember mixing model was applied to the laser diffraction grain size data (i.e. the grain size of lithogenic material cleaned from opal, carbonate and organic material) to provide insights concerning the covariance between grain size and bulk $^{230}\text{Th}_{\text{xs}}$ specific activities. The endmember model (EMM) involved first centering the grain size data in order that the mean value of each measured size interval was zero. The first principal component of the centered data was then determined via singular value decomposition [Press *et al.*, 1992]. To represent the end-members along the mixing line, the two most extreme

samples along the length of the first principal component were found. The relative proportions with which these two endmember samples would then have to be mixed together in order to recreate the grain size distributions of the remaining samples was found by constrained least-squares [Sturm, 1999]. Using this approach, the two endmember mixing model can explain ~90 % of the variability in our grain size data set.

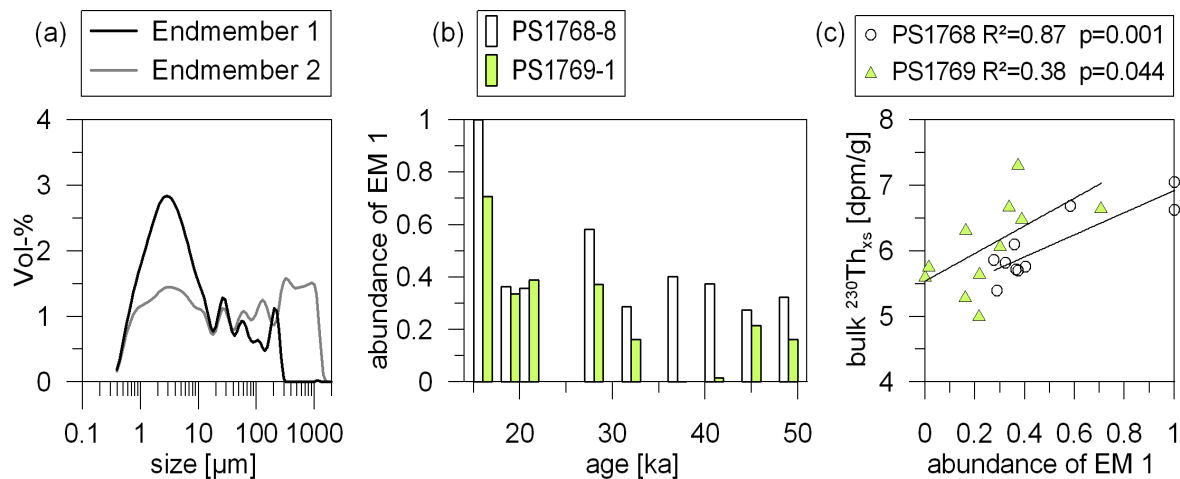


Figure 3.6: The decomposition of a set of grain size distributions into two endmembers by a principal component analysis. (a) The two-endmember-model suggests the existence of a fine component (EM 1) and a coarse component (EM 2). (b) The relative abundance of the fine endmember (EM 1) in both sediment cores plotted against the age. (c) The relative abundance of the fine endmember (EM 1) and the bulk $^{230}\text{Th}_{\text{xs}}$ activities show a positive correlation that is significant at the 95% confident-level.

The two-endmember-model suggests the existence of one coarse endmember (EM 2 with 41 % sand and 59 % mud, **Figure 3.6a**) which is distributed over the entire size spectrum (mean size = 187 μm). EM 2 is attributed to the vertical particle flux which comprises mainly the ice-rafted detritus with typically unsorted particle size distributions [Diekmann and Kuhn, 1999 and references therein]. Also the input of aeolian dust contributes to the vertical particle flux and therefore to the EM 2, which, however, is believed to account for a minor fraction in this area [Martínez-García *et al.*, 2009]. The fine endmember (EM 1 with 11 % sand and 89 % mud, **Figure 3.6a**) comprises the size range smaller than 300 μm , which is thought to reflect the sediment fraction that was advected by bottom currents. Contrary to EM 2, EM 1 is very strongly skewed with a median at 4 μm and a mean size at 25 μm . The relative abundance of EM 1 is highest during the deglacial (**Figure 3.6b**). Mostly, the rapid accumulation site PS1768-8 receives a much higher contribution of EM 1 than the slow accumulation site PS1769-1. A remarkable exception is the Last Glacial Maximum, where EM 1 has the same

abundance for both sites. The relative abundance of EM 1 correlates positively with the bulk $^{230}\text{Th}_{\text{xs}}$ specific activities (**Figure 3.6c**). Based on the distribution of EM 1, the lateral sediment advection potentially affects all particles smaller than 300 μm . The motion of sand particles with a grain diameter of 300 μm requires a minimum friction velocity of $\sim 1.4 \text{ cm s}^{-1}$ [= threshold for quartz density material in water at 20°C; *Miller et al.*, 1977]. That corresponds to a flow velocity at 100 cm above the bed of $\sim 43 \text{ cm s}^{-1}$. Maximum bottom flow velocities of up to more than 40 cm s^{-1} have been reported for different regions of the modern ocean and has been termed “benthic storms” as they intermittently occur as maximum flow speed events [e.g. *Hollister and McCave*, 1984]. Sand particles (i.e. $>63 \mu\text{m}$) account for 11 % of EM 1 and are believed to be mostly moved in traction or saltation as part of the bedload [*Gorsline*, 1984]. 83 % of EM 1 is smaller than 30 μm . This size fraction has been most likely deposited from suspension, as the minimum shear velocity for the transport in suspension is 0.8 cm s^{-1} for a grain diameter of 30 μm [*McCave*, 1984]. Assuming modern flow conditions, with near bottom currents at mean speeds of $\sim 1\text{-}15 \text{ cm s}^{-1}$ as measured for the Northern Weddell Sea [*Pudsey*, 1992; *Barber and Crane*, 1995; *Fahrbach et al.*, 2001], the major amount of the size spectrum of EM 1 could have been transported in suspension.

This two-endmember-model certainly oversimplifies the complexity of the sedimentary processes, but it is an approach to better describe the sediment focusing at the study sites. It further supports the idea that mainly fine material is focused which leads to a grain size bias of the focusing factor. Therefore, we are now able to apply a grain size correction to the $^{230}\text{Th}_{\text{xs}}$ focusing factor. An inconsistency in our data set, however, is important mentioning: The laser diffraction analysis has been made on the lithogenic material (i.e. after removal of carbonate, opal, and organic matter), as the lithogenic component is thought to be the principal carrier of $^{230}\text{Th}_{\text{xs}}$. On the other hand, the particle size specific $^{230}\text{Th}_{\text{xs}}$ analysis was performed on the complete sediment sample including the biogenic components, in order to prevent the alteration of the adsorbed $^{230}\text{Th}_{\text{xs}}$ -signal that is likely to happen by a chemical leaching of biogenic components. As it was shown that the fraction of biogenic opal (slowly settling particle fractions) only accounts for few percent of the total $^{230}\text{Th}_{\text{xs}}$ inventory (cf. **Table 3.1** and **Figure 3.3**), this inconsistency between both methods is believed as to be a negligible uncertainty for the following calculation.

3.4.2.3 The particle size corrected focusing factor

By the decomposition of the grain size distributions we know that lateral transport supplies mainly fine particles probably not larger than 140 to 300 μm . In the following the size threshold 300 μm is employed for the grain size correction of the focusing factors of the sediment cores PS1768-8 and PS1769-1 for the time slice 14 to 49 ka. The main assumption for this grain size correction is that the accumulation of particles $>300 \mu\text{m}$ is considered to equal the vertical flux whereas the accumulation of particles $<300 \mu\text{m}$ is a mixture of vertical flux and

lateral advection. This grain size correction is applied in the same way as proposed by *Kretschmer et al.* [2010] with the only difference that we apply the method on such sediment samples where grain size specific $^{230}\text{Th}_{\text{xs}}$ data are not available, but only bulk $^{230}\text{Th}_{\text{xs}}$ data. Based on the $^{230}\text{Th}_{\text{xs}}$ model approach (**Figure 3.5**), we are confident that we can assume the grain size specific $^{230}\text{Th}_{\text{xs}}$ to be constant during this period of time. That means the grain size specific $^{230}\text{Th}_{\text{xs}}$ data based on few size fractionated samples (as reported in **Table 3.2** and **Figure 3.3**) can be projected to the bulk samples of an extended core segment. Therefore, we assume certain grain size specific $^{230}\text{Th}_{\text{xs}}$ activities for the coarse and the fine size fractions of all samples between 14 and 49 ka. An average $^{230}\text{Th}_{\text{xs}}$ specific activity of 1.2 dpm g^{-1} is assumed for the coarse grain size class $>300 \mu\text{m}$. The corresponding fine size fraction $<300 \mu\text{m}$ contain a $^{230}\text{Th}_{\text{xs}}$ specific activity (T_{fine}) that is calculated according to:

$$T_{\text{fine}} = [T_{\text{bulk}} - (T_{\text{coarse}} \times P_{\text{coarse}})] / P_{\text{fine}}, \quad (3.5)$$

where T_{bulk} and T_{coarse} are the $^{230}\text{Th}_{\text{xs}}$ activities [dpm g^{-1}] in the bulk sample and the coarse size fraction, respectively, P_{coarse} and P_{fine} are the coarse and the fine particles [%], respectively. By inserting the calculated T_{fine} into equation 3.2 (section 3.2.6) the grain size corrected focusing

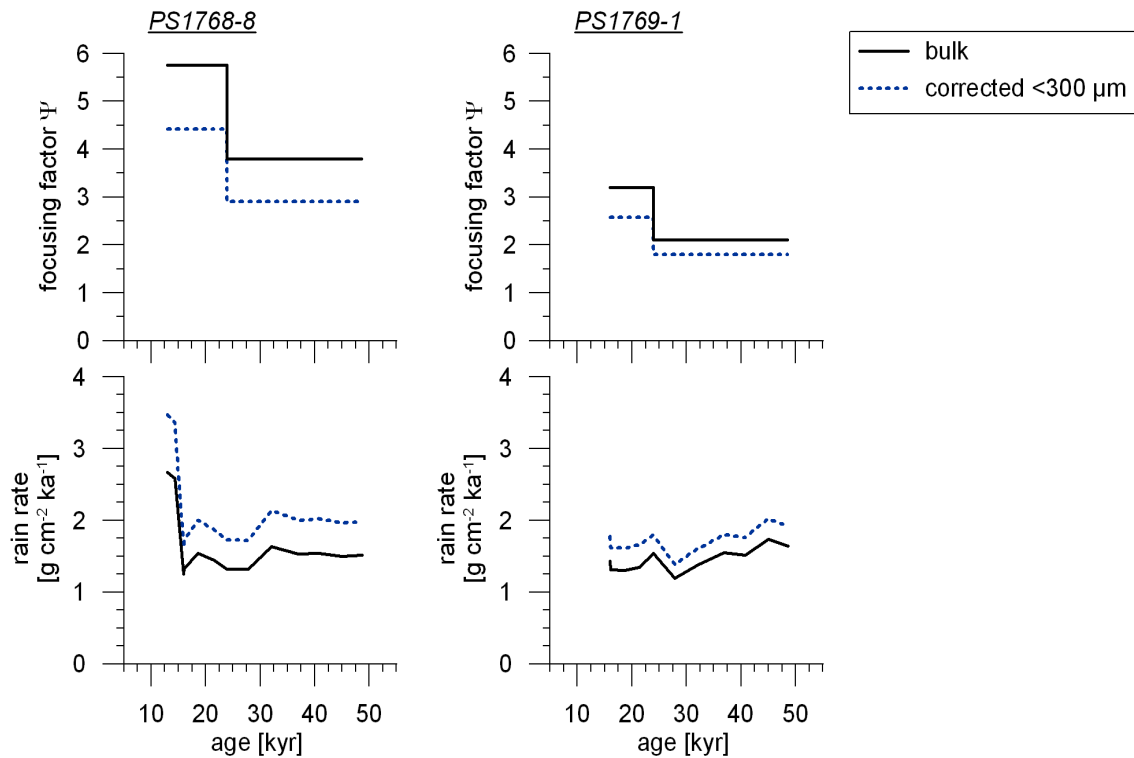


Figure 3.7: Grain size corrections on the focusing factor and the preserved vertical rain rates for the sediment cores PS1768-8 and PS1769-1. For the particle size correction it is assumed that the lateral sediment transport entrains particles of maximum $300 \mu\text{m}$ size.

factor Ψ_C is calculated (Table 3.4, Figure 3.7). The grain size data correct the focusing factor towards lower Ψ values and correspondingly the vertical rain rates towards higher values. The corrections are in a similar range for both twin cores. Focusing factors are reduced through grain size correction by 0.76-0.86 ($\Psi_C = 1.8-4.4$). The grain size corrected vertical rain rates increase by a factor of 1.16-1.31 ($1.4-3.5 \text{ g cm}^{-2} \text{ ka}^{-1}$, Figure 3.7). The higher size corrected vertical rain rates implies that the past export productivity was higher than indicated by non-corrected (i.e. traditionally bulk- ^{230}Th corrected) rain rates. However, even after the grain size correction the rain rate appears to be within the lower range of values (1 to $6 \text{ g cm}^{-2} \text{ ka}^{-1}$), that have been reported for the Atlantic Southern Ocean for the past 140 ka [e.g. Kumar *et al.*, 1993; Frank *et al.*, 1996]. Therefore, the grain size correction of vertical fluxes is not expected to induce a significantly changed interpretation of past ocean primary productivity at the sites studied.

In summary, few grain size specific $^{230}\text{Th}_{\text{xs}}$ data may be extrapolated to an extended core section where bulk $^{230}\text{Th}_{\text{xs}}$ and grain size data are available. This may provide important information about a biasing of the focusing factor by the grain size sorting effect. However, at our study sites small biasing is observed without implication for the paleoceanographic interpretation.

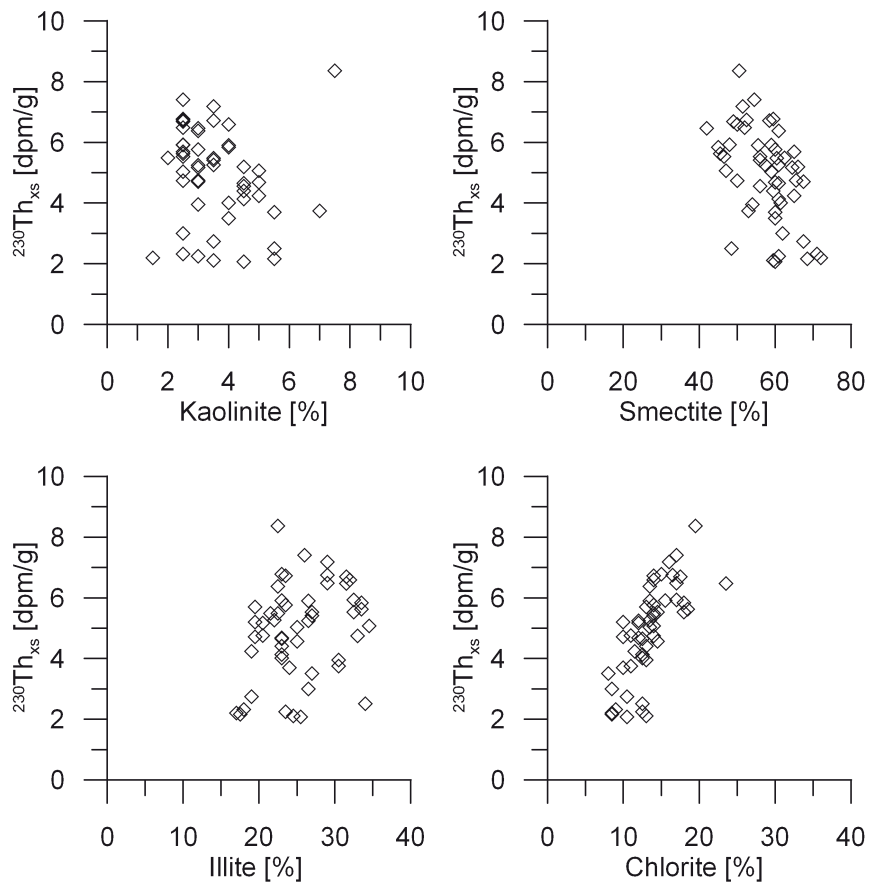


Figure 3.8: Correlation of clay mineral content with bulk $^{230}\text{Th}_{\text{xs}}$ specific activity [clay mineral data from Diekmann *et al.*, 1996, $^{230}\text{Th}_{\text{xs}}$ data from Frank *et al.*, 2000a, b].

3.4.3 The origin of advected clay minerals

Clay accounts for up to 86 % of the sedimentary $^{230}\text{Th}_{\text{xs}}$ inventory. The temporal $^{230}\text{Th}_{\text{xs}}$ variability, however, cannot be explained by the clay concentration alone, as indicated by the model approach in section 3.4.1. The mineralogical composition of the clay fraction could

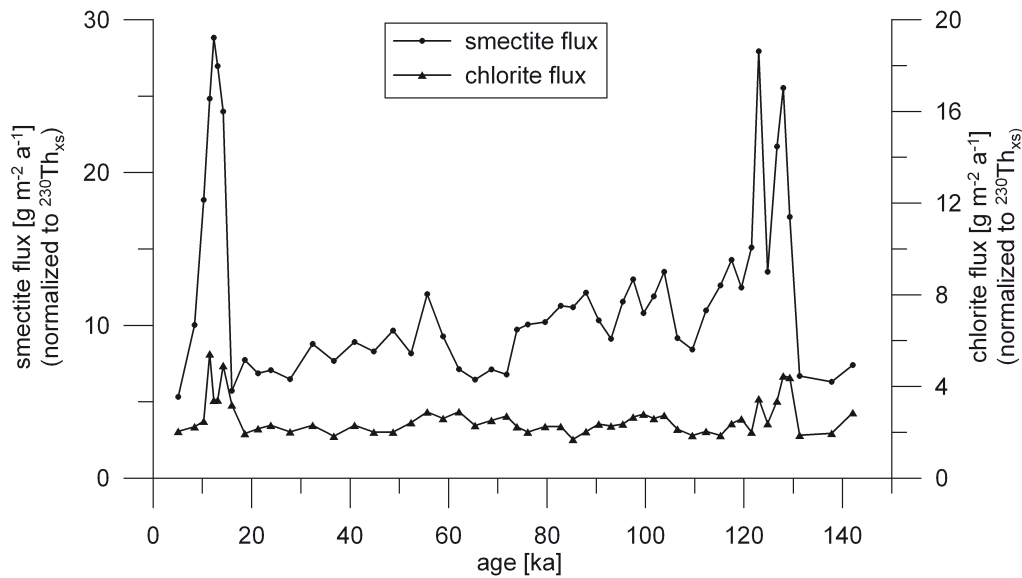


Figure 3.9: $^{230}\text{Th}_{\text{xs}}$ -normalized fluxes of the clay minerals smectite and chlorite at site PS1768-8 [data from *Diekmann et al.*, 1996; *Frank et al.*, 2000a, b].

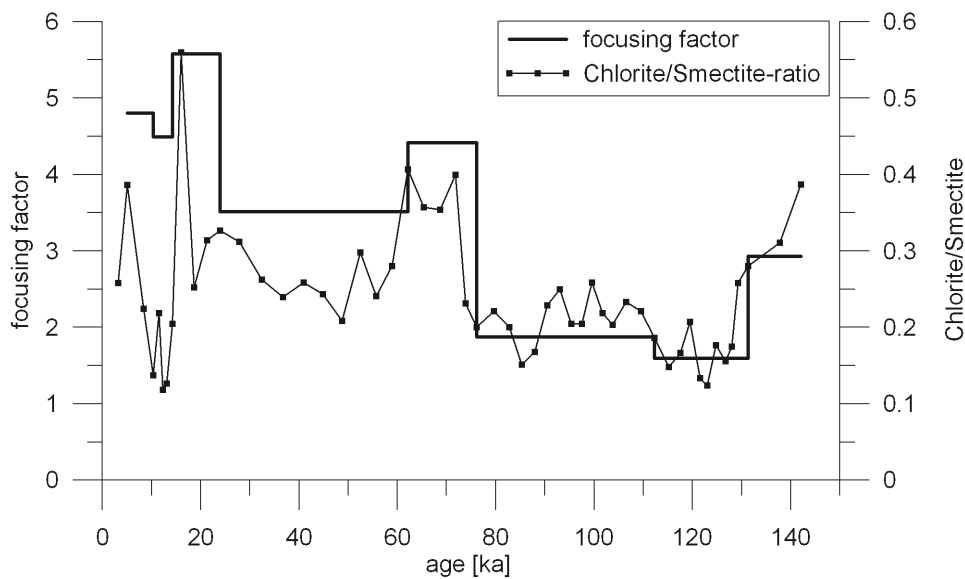


Figure 3.10: The focusing factor (based on bulk $^{230}\text{Th}_{\text{xs}}$ i.e. non-grainsize-corrected) and the chlorite/smectite-ratio at site PS1768-8 over the past 140 ka. [data from *Diekmann et al.*, 1996; *Frank et al.*, 2000a, b].

possibly provide more information about the controlling mechanism. Therefore, a published data set on clay mineralogy from core PS1768-8 [Diekmann and Petschick, 1996; Diekmann *et al.*, 1996] is explored in combination with the bulk $^{230}\text{Th}_{\text{xs}}$ data set. It is striking that the chlorite concentration shows a downcore variation similar to that of $^{230}\text{Th}_{\text{xs}}$. **Figure 3.8** displays the positive correlation between both parameters. Chlorite traces terrigenous glaciogenic material originating from Patagonia or the Antarctic Peninsula. The spatial distribution in Holocene surface sediments points to a source in the Pacific sector of the Southern Ocean [Petschick *et al.*, 1996]. In contrast, the high smectite concentrations are ascribed to local, non-continental origin derived from submarine weathering of basaltic rocks in a proximal area (Bouvet Island) [Petschick *et al.*, 1996]. The interpretation of the smectite signal being of local origin is further supported by the recent work of Middag *et al.* [accepted] who found increased dissolved Mn signals in the water column indicating a hydrothermal activity at the Bouvet triple junction just upstream of our study site. Smectite comprises the largest fraction (40-75 %) of clay in this core. It shows an inverse correlation to $^{230}\text{Th}_{\text{xs}}$ probably due to the dilution effect with chlorite which accounts for only 7-24 % of the clay.

During the long distance transport from the Drake Passage to the site of its final deposition the chlorite could accumulate $^{230}\text{Th}_{\text{xs}}$ because it was bathed by the eastward flowing ^{230}Th -enriched ACC. During the past 130 ka, half of the dissolved ^{230}Th of the Weddell Sea has been exported and incorporated into the ACC where $\frac{3}{4}$ of the advected ^{230}Th is scavenged by particles [Walter *et al.*, 2000]. Therefore, the covariance between chlorite and $^{230}\text{Th}_{\text{xs}}$ is thought to reflect similar source areas rather than a chemical affinity between both tracers. During the last two terminations and MIS 5.5 the $^{230}\text{Th}_{\text{xs}}$ minima (**Figure 3.5**) are accompanied by maxima in $^{230}\text{Th}_{\text{xs}}$ -normalized flux rates of chlorite and smectite (**Figure 3.9**) and a discrepancy between predicted and measured bulk $^{230}\text{Th}_{\text{xs}}$ values (**Figure 3.5**). The three observations made for the last two terminations (clay flux at its maximum, $^{230}\text{Th}_{\text{xs}}$ -concentration at its minimum, and the mismatch of the modeled bulk- $^{230}\text{Th}_{\text{xs}}$ -values) point to a changed source of sediment during the terminations deriving from shallower water depth and containing a lower $^{230}\text{Th}_{\text{xs}}$ -signal, as it was predicted by François *et al.* [2004]. A relatively strong dilution by the enhanced vertical particle flux due to higher primary production during those periods [Frank *et al.*, 1996] may further add to the discrepancy between modeled and measured $^{230}\text{Th}_{\text{xs}}$ -values. A further interesting clue is given by the chlorite/smectite ratio that closely follows the trend of the not-grainsize-corrected focusing factor (**Figure 3.10**, based on own $^{230}\text{Th}_{\text{xs}}$ data extended by data from Frank *et al.* [2000a, b]). Both parameters represent a ratio of an advected signal versus a local autochthonous signal. Thus, higher ratios (advected/local) during glacial stages 2, 4 and 6 may be interpreted as a strengthening of the ACC. It is an important result of this study that obviously the $^{230}\text{Th}_{\text{xs}}$ deposition resembles the flux of one particular clay mineral rather than the total clay flux.

3.5 Conclusions

3.5.1 ^{230}Th focusing

In the studied sediment samples the majority of sedimentary $^{230}\text{Th}_{\text{xs}}$ is adsorbed to clay and the flux of clay to the sediment finally determines the $^{230}\text{Th}_{\text{xs}}$ inventory and thus the focusing factor. Over a certain time interval (MIS 5.2 to LGM) the variability of bulk $^{230}\text{Th}_{\text{xs}}$ activities is a function of the variability of grain size distribution, i.e. it mainly can be explained by the concentration of clay varying through time. According to our data, the grain size specific $^{230}\text{Th}_{\text{xs}}$ activities can be assumed to be relatively constant throughout this time interval. Therefore, a limited number of grain-size specific ^{230}Th measurements can be used to infer a grain size biasing of focusing factors, if detailed grain-size information is available. The correlation of bulk $^{230}\text{Th}_{\text{xs}}$ with chlorite contents of the clay fraction illustrates that the source and composition of the advected material is the strongest control on $^{230}\text{Th}_{\text{xs}}$ activities and that the relative contribution of long-distance inputs changes over time.

3.5.2 Sediment redistribution

By decomposition of grain size distributions, we infer a maximum particle size of 140-300 μm advected to the study sites by bottom currents. Accordingly, the focusing factor is grain size corrected for the laterally transported size fraction smaller than 300 μm . Under certain assumptions based on the observations made in this study, the grain size correction of focusing factors is extrapolated to an extended sediment core section (14-49 ka). This provides important information about a grain size biasing of the focusing factor. However, at our study sites a minor biasing is observed without implication for the paleoceanographic interpretation.

The data from granulometry and a two-endmember model support the idea of changing flow fields that are modulated on a small scale with slower speeds at the site of high accumulation rates (PS1768-8) allowing the deposition of higher amounts of the fine endmember compared with the site of slow accumulation. That means the small scale topography causes a spatial disparity of the focusing factors between the twin cores. An exception is the LGM where the deposition of the fine endmember was identical at both core sites. This coincides with maxima in the focusing factor and the chlorite-smectite-ratio as well as with the highest $^{230}\text{Th}_{\text{xs}}$ concentration in the clay fraction. The temporal variability of sediment redistribution at our study site is controlled by the ocean wide current regime. During glacial stages 2, 4, and 6 a change of the current regime possibly related to an invigoration of the ACC leads to higher input of chlorite (from remote sources) and thus a dilution of smectite (from proximal sources) that is well reflected by the ^{230}Th data. The role of clay minerals for ^{230}Th transport needs to be further investigated in order to obtain a better understanding of transport pathways, and a more realistic estimate of sediment redistribution. The latter is of general concern also for other regions of high sediment focusing e.g. the Eastern Equatorial Pacific.

Chapter 4

Contributions from size fraction-specific $^{230}\text{Th}_{\text{xs}}$ data towards understanding of sediment redistribution processes in the Panama Basin

Gesine Mollenhauer^{1,2}, Sven Kretschmer^{1,2}, Stephanie Kusch^{1,2},
Michiel M. Rutgers van der Loeff¹, Alan C. Mix³

¹ Alfred-Wegener-Institut für Polar- und Meeresforschung, Bremerhaven, Germany

² Fachbereich Geowissenschaften, Universität Bremen, Germany

³ College of Ocean and Atmospheric Sciences, Oregon State University, Corvallis, Oregon, USA

Manuscript to be submitted to *Earth and Planetary Science Letters*.

Abstract

Despite considerable efforts in the recent years, the sedimentation processes in the Eastern Equatorial Pacific, namely the Panama Basin, remain the subject of uncertainty. In particular, the occurrence of lateral sediment redistribution as suggested by constant flux proxies like Thorium-230 excess ($^{230}\text{Th}_{\text{xs}}$) is the subject of much debate. $^{230}\text{Th}_{\text{xs}}$ measurements performed on bulk samples imply strong sediment focusing, particularly during the glacial, while sediment mass accumulation rates imply changes in productivity. Arguments have been put forward suggesting that the assumptions behind the $^{230}\text{Th}_{\text{xs}}$ method may not be entirely valid. One of the aspects to be considered is the affinity of $^{230}\text{Th}_{\text{xs}}$ for certain particle size classes, which in turn affect their respective susceptibility for resuspension and lateral transport.

Using samples from sediment cores Y69-71P and ME0005-24JC from the SW Panama Basin, we examined the $^{230}\text{Th}_{\text{xs}}$ distribution in individual sediment grain size fractions of selected radiocarbon-dated horizons in both cores. We found higher $^{230}\text{Th}_{\text{xs}}$ activities in the smaller grain size fractions than in coarse silt and sand sized material. Size-class specific $^{230}\text{Th}_{\text{xs}}$ data can be used to calculate sediment focusing factors corrected for size-selective particle transport. Our results suggest that both strong lateral sediment focusing and increased vertical fluxes contributed to increased mass accumulation rates during the glacials. Our data are consistent with scavenging of fine-grained ^{230}Th -rich particles suspended in deep nepheloid layers by larger sinking particles related originating in the upper water column.

4.1 Introduction

In the recent literature, a controversial debate has evolved about the occurrence and extent of lateral sediment redistribution in the Equatorial Pacific and the resulting implications for the interpretation of palaeoclimate records obtained from sediments of the region. Several authors using constant flux tracers like $^{230}\text{Th}_{\text{xs}}$ and ^3He observe evidence for substantial sediment redistribution and focusing at sites of deposition in the region [Marcantonio *et al.*, 2001; Loubere *et al.*, 2004; Kienast *et al.*, 2007]. The proxies employed by these authors rely on the fact that for these radionuclides the rate of production (^{230}Th) and extraterrestrial flux (^3He) are well-known and constant. Therefore the vertical flux of these radionuclides per unit time is assumed to be known and can be used for normalization of sediment accumulation rates. Based on sedimentary inventories of ^{230}Th , sediment focusing factors can be calculated as a measure of the sediment laterally supplied to the respective site [François *et al.*, 2004]. Another group of authors doubt the occurrence of very strong sediment redistribution in the Equatorial Pacific based on geophysical data and sediment core comparison [Lyle *et al.*, 2005], or because the very widespread occurrence of constant-flux tracer evidence for sediment focusing across all depth scales and horizontal scales >1000 km, in particular during the last glacial, would imply movement of extremely large amounts of sediment, which appears unlikely without significant climatically driven changes in circulation [Paytan *et al.*, 2004].

Much of the discussion arising from the contrasting views regarding the occurrence and extent of sediment redistribution in the Eastern Equatorial Pacific (EEP), i.e., the Panama Basin, centred around the question whether vertical flux of sediment is best estimated using mass accumulation rates or by applying constant flux proxies [François *et al.*, 2004; Lyle *et al.*, 2005; 2007; François *et al.*, 2007]. Some concerns regarding the applicability of the $^{230}\text{Th}_{\text{xs}}$ method and the validity of the assumptions inherent to it were raised. One of the suggestions made was that other processes than vertical particle settling, e.g., enhanced scavenging of ^{230}Th in areas of high particle flux (“particle flux effect”), control the accumulation of radionuclides in sediments of the EEP [Paytan *et al.*, 2004; Broecker *et al.*, 2008]. A modelling study, however, showed that the particle flux effect is too small to explain the observed high focusing factors in the equatorial Pacific [Siddall *et al.*, 2008]. The authors pointed out that preferential removal of ^{230}Th from the water column by small particles could potentially explain increased ^{230}Th inventories. If ^{230}Th is preferentially bound to the fine fraction, particle sorting effects during transport could result in strongly enhanced ^{230}Th inventories at a given site without a strong horizontal flux of bulk sediment [Lyle *et al.*, 2005].

When using bulk sediment $^{230}\text{Th}_{\text{xs}}$ concentrations for the calculation of vertical fluxes and, by estimating focusing factors, lateral contributions, one of the main assumptions requires homogenous distribution of $^{230}\text{Th}_{\text{xs}}$ concentrations within the sediment or lateral transport of all sediment constituents, i.e., without sorting. This assumption contrasts with the findings of

weak adsorption on biogenic silica [Chase *et al.*, 2002; Roy-Barman *et al.*, 2005], and preferential adsorption on lithogenics, carbonates, and Mn oxides [Luo and Ku, 1999; Chase *et al.*, 2002; Roy-Barman *et al.*, 2005; 2009; Siddall *et al.*, 2005]. In a recent study investigating grain size effects on ^{230}Th inventories, the fine sediment fraction was indeed found to be the main carrier of ^{230}Th both in carbonate-rich and siliceous sediments [Kretschmer *et al.*, 2010]. Heterogeneous distribution of $^{230}\text{Th}_{\text{xs}}$ in different particle size classes likely reflects their individual composition. Consequently, hydrodynamic particle sorting during lateral transport is expected to have a strong effect on calculated focusing factors and normalized vertical flux estimates. Kretschmer *et al.* [2010] recommend making a grain-size correction to account for these effects.

Here we present new $^{230}\text{Th}_{\text{xs}}$ data on bulk sediments and grain-size classes from two cores in the EEP for which extremely high focusing factors have been reported [Kienast *et al.*, 2007]. We demonstrate that if grain-size effects during ^{230}Th adsorption on sinking particles and hydrodynamic sorting during lateral transport are taken into account, corrected focusing factors are substantially reduced relative to those based on bulk measurements. However, our data still imply the occurrence of strong lateral advection.

4.2 Study Area

The Panama Basin is located in the EEP off the coast of Central America and NW Southern America. The Basin is bordered by the submerged volcanic Cocos and Carnegie Ridges which join at the Galapagos Platform. The region is of particular interest for studies investigating past changes in primary productivity and carbon export since it is underlying the equatorial divergence upwelling region, a region of high primary production important for the global carbon cycle. Today, euphotic zone productivity above the Southern Panama Basin amounts to $\sim 600 \text{ mg C m}^{-2} \text{ day}^{-1}$, while in the Central Panama Basin productivity is $\sim 300\text{-}400 \text{ mg C m}^{-2} \text{ day}^{-1}$. The highest productivity is observed along the coastal regions amounting to up to $\sim 1000 \text{ mg C m}^{-2} \text{ day}^{-1}$ [Moore Jr. *et al.*, 1973; Behrenfeld and Falkowski, 1997]. The regional productivity pattern is not directly reflected in the accumulation pattern of sediments, which is additionally controlled by pre- and post-depositional processes most likely including lateral transport and dissolution, while dilution by terrigenous sediments is only important in the nearshore areas [Moore Jr. *et al.*, 1973]. Seasonal vertical mass fluxes reported from sediment traps in the NW and N Panama Basin vary from $20 \text{ mg m}^{-2} \text{ day}^{-1}$ to $1690 \text{ mg m}^{-2} \text{ day}^{-1}$ in mid-water depths ($<1000 \text{ m}$) and from $40 \text{ mg m}^{-2} \text{ day}^{-1}$ to $880 \text{ mg m}^{-2} \text{ day}^{-1}$ in deep-water depths ($>3000 \text{ m}$) [Honjo, 1982; Asper *et al.*, 1992]. Generally, the flux is largely dominated by carbonate in both the mid-water depth (32-94 %) and the deep-water depth (15-62 %), while lithogenic particles (mid-water depth 2-14 %) become proportionally more important in the deep-water depth (25-45 %). Organic C flux accounts for 1-12 % and 3-7 % of the total flux in mid-water and deep-water depths, respectively [Honjo, 1982].

Bottom currents, which are a potential source for laterally supplied particulate matter, originate in the Peru Basin and enter the Panama Basin through the Ecuador Trench. They disperse north- and westward off northern Ecuador and penetrate into the SW Panama Basin south of the Malpelo Ridge where they spread to the north and the south [Laird, 1971; Lonsdale, 1977]. In addition, episodic spillover across the central saddle of the Carnegie Ridge between 85° and 86°W may contribute to lateral particle flux [Lonsdale, 1977].

4.3 Materials and Methods

For our study of grain size effects on $^{230}\text{Th}_{\text{xs}}$ inventories in the EEP, two sediment cores from the southern Panama Basin were selected. Deep-sea sediment core ME0005A-24JC (hereafter: ME24JC) was retrieved during R/V *Melville* cruise ME0005A in 2000 (0°00.3'N, 86°27.8'W, 2941 m water depth). Neighbouring core Y69-71P (0°06'N, 86°29'W, 2740 m water depth) was taken in 1969 on board R/V *Yaquina* during cruise YALOC69. Both core locations are situated north of the Carnegie Ridge in an area of abyssal hills, which is part of a narrow east-west trending trough. Y69-71P was collected mid-slope, while ME24JC was taken within an adjacent but separate abyssal valley about 10 km south of Y69-71P. Previously reported focusing factors for ME24JC are 4.9 for the Holocene and 5.5 for the glacial, while values for Y69-71P are 2.5 and 3.6, respectively [Kienast *et al.*, 2007].

$^{230}\text{Th}_{\text{xs}}$ specific activities were analyzed on bulk sediments and particle size classes from six sediment samples. From each of the two sediment cores we selected three sampling depths corresponding to calibrated radiocarbon ages of approximately 3 ka, 9 ka and 18 ka BP (Table 4.1). The techniques applied for grain size fractionation, isotope analyses, and correction of focusing factors are described in detail by Kretschmer *et al.* [2010]. For the analyses, only samples that have previously been extracted with organic solvents to obtain total lipid extracts *cf.* Kusch *et al.* [2010] were available. Therefore we chose to perform grain-size separations using purified water. Of each sample about 0.6 to 1.9 g dried and solvent-extracted sediment was suspended in purified water, agitated for two minutes and ultrasonicated. Subsequently, samples were wet-sieved using nylon sieves (125 μm , 63 μm , 20 μm) and purified water for about 20 min each. Additional separations were performed on both 18 ka-samples, in which the clay fraction (<2 μm) was separated from the fine silt fraction (2-20 μm) by sinking velocity in water using the Stokes settling diameter. These separations, however, resulted in poor sediment recovery (see Results and Table 4.1). After sieving and settling, the grain size fractions (<2 μm , <20 μm or 2-20 μm , 20-63 μm , 63-125 μm and >125 μm) were freeze dried. Analyses of Th and U isotopes by isotope dilution were performed on 50 mg dry sediment material (bulk sediment and size classes). After spike addition (^{229}Th and ^{236}U), samples were fully acid digested with a microwave assisted system. Samples were purified by iron co-precipitation and separation of Th and U was achieved by column chromatography (UTEVA resin). Isotopes of Th and U were measured by isotope dilution using ICP-SF-MS (Inductively Coupled Plasma-Sector Field-Mass

Spectrometry, Element2, Thermo Scientific). For particle flux studies, the unsupported fraction of ^{230}Th (excess ^{230}Th , or $^{230}\text{Th}_{\text{xs}}$) is of interest. The calculations followed the descriptions of *François et al.* [2004] and *Henderson and Anderson* [2003]. The detrital and the authigenic ^{230}Th were subtracted from the total ^{230}Th . Detrital and authigenic components were estimated using the lithogenic activity ratio $^{238}\text{U}/^{232}\text{Th}$ that has been suggested to be on average 0.7 ± 0.1 for the Pacific basin. The $^{230}\text{Th}_{\text{xs}}$ activity was decay corrected (half-life 75,380 years) to yield the initial activity of $^{230}\text{Th}_{\text{xs}}$ at the time of deposition.

4.4 Results

4.4.1 Grain size

Sediment recoveries after sieving were good (96 %) for the Holocene samples (3 ka and 9 ka). The two glacial samples (18 ka) were poorly recovered (47 and 52 %; **Table 4.1**), but repeat sieving of both glacial samples without ultrasonic pre-treatment resulted in better recoveries (85 %). The sieved grain size class distributions of both core sites compare well (**Figure 4.1**). Size distributions in all samples from ME24JC and Y69-71P are dominated by the $<20 \mu\text{m}$ grain size class (45-70 % and 55-67 %, respectively). The contribution of the “mud” size spectrum ($<63 \mu\text{m}$) amounts to between 67-80 % (ME24JC) and 72-78 % (Y69-71P). The sand sized particle classes ($63\text{-}125 \mu\text{m}$ and $>125 \mu\text{m}$) contribute 18-33 %.

4.4.2 Excess ^{230}Th

Recoveries of $^{230}\text{Th}_{\text{xs}}$ were calculated as the summed $^{230}\text{Th}_{\text{xs}}$ concentrations weighted by size class contribution divided by bulk values. Good recovery (99-100 %) was observed for the 3 ka-samples of both cores (**Table 4.1**). $^{230}\text{Th}_{\text{xs}}$ recoveries were 83 % for both 9 ka-samples and 111 % (135 %) and 116 % (143 %) for the 18 ka-samples of Y69-71P and ME24JC, respectively. Notably, sediment recoveries were low (between 47 % and 85 %) for these latter samples. We suspect that a loss of sediment material during the fractionation process could be due to dissolution of carbonate particles during ultrasonication and sieving/settling with purified water. If carbonate particles were dissolved (i.e. removed and excluded from the ^{230}Th analyses), any $^{230}\text{Th}_{\text{xs}}$ on the carbonate would be released and re-adsorbed on the residual material resulting in higher concentrations of the residual material and recoveries $>100 \%$.

Bulk $^{230}\text{Th}_{\text{xs}}$ values compare within 1σ with published data by *Kienast et al.* [2007] (**Figure 4.2**), assuming similar uncertainty levels for the published data as determined for our analyses. The assumption of similar measurement precision is reasonable as *Kienast et al.* [2007] used equivalent techniques for the determination of radionuclide concentrations. The observed good agreement between data confirms results of *Mollenhauer et al.* [2006], who showed that ^{230}Th concentrations in solvent-extracted sediments are comparable to those in untreated dried

Table 4.1: Recoveries of sediment and $^{230}\text{Th}_{\text{xs}}$ after sediment fractionation, calculated as the sum of the grain size fractions in % of the bulk sediment. Bulk and grain size specific $^{230}\text{Th}_{\text{xs}}$ activities [dpm g^{-1}] are reported with analytical uncertainty of 1σ . The glacial samples of both sediment cores were size fractionated without ultrasonication (a) and with ultrasonic treatment and separation of the clay (<2 μm) fraction (b).

sample depth [cm]	age [ka]	sediment recovery [%]	$^{230}\text{Th}_{\text{xs}}$ recovery [%]	$^{230}\text{Th}_{\text{xs}}$ [dpm g^{-1}]						
				bulk	>125 μm	63-125 μm	20-63 μm	<20 μm	2-20 μm	<2 μm
11-18	3240 \pm 25	96	99	7.33 \pm 0.37	2.08 \pm 0.11	4.87 \pm 0.24	7.29 \pm 0.37	8.48 \pm 0.62		
51-56	9705 \pm 60	96	83	5.19 \pm 0.26	1.75 \pm 0.10	3.38 \pm 0.18	5.66 \pm 0.29	4.78 \pm 0.34		
183-188 (a)	17690 \pm 140	85	111	6.25 \pm 0.32	1.94 \pm 0.15	5.68 \pm 0.39	7.03 \pm 0.45	8.34 \pm 0.49		
183-188 (b)	17690 \pm 140	52	135		1.95 \pm 0.10	3.37 \pm 0.17	6.93 \pm 0.35		6.37 \pm 0.33	17.65 \pm 0.90
15-20	3255 \pm 30	96	100	8.09 \pm 0.42	2.08 \pm 0.11	5.11 \pm 0.26	7.52 \pm 0.43	9.59 \pm 0.79		
76-81	9040 \pm 40	96	83	6.27 \pm 0.32	1.80 \pm 0.09	4.28 \pm 0.21	6.49 \pm 0.32	5.69 \pm 0.41		
345-350 (a)	18050 \pm 65	85	116	5.82 \pm 0.30	2.47 \pm 0.27	5.87 \pm 0.58	7.11 \pm 0.65	8.39 \pm 0.71		
345-350 (b)	18050 \pm 65	47	143		1.79 \pm 0.09	4.72 \pm 0.24	7.15 \pm 0.36		5.94 \pm 0.30	16.31 \pm 0.82

material. The two core sites show similar patterns of $^{230}\text{Th}_{\text{xs}}$ distribution by core depths and grain size classes (**Figure 4.1**). Differences between the core sites were insignificant (smaller than 1σ error). As a general pattern for Holocene and glacial samples of both sediment cores, we observe that larger grain sizes contain lower specific $^{230}\text{Th}_{\text{xs}}$ activities. The corresponding size fractions of the 3 ka- and the 18 ka-samples are quite similar in $^{230}\text{Th}_{\text{xs}}$, while the 9 ka-sample contains slightly less $^{230}\text{Th}_{\text{xs}}$ throughout all size fractions.

4.4.3 Vertical sediment flux and focusing factors

We used published foraminiferal (*N. dutertei*) radiocarbon ages and sediment dry bulk densities [Loubere et al., 2004; Kienast et al., 2007; Kusch et al., 2010] for the calculations of authigenic ^{230}Th , decay corrections and focusing factors. Focusing factors Ψ , linear sedimentation rates (LSR), mass accumulation rates (MAR), and preserved vertical fluxes (F_v) were calculated

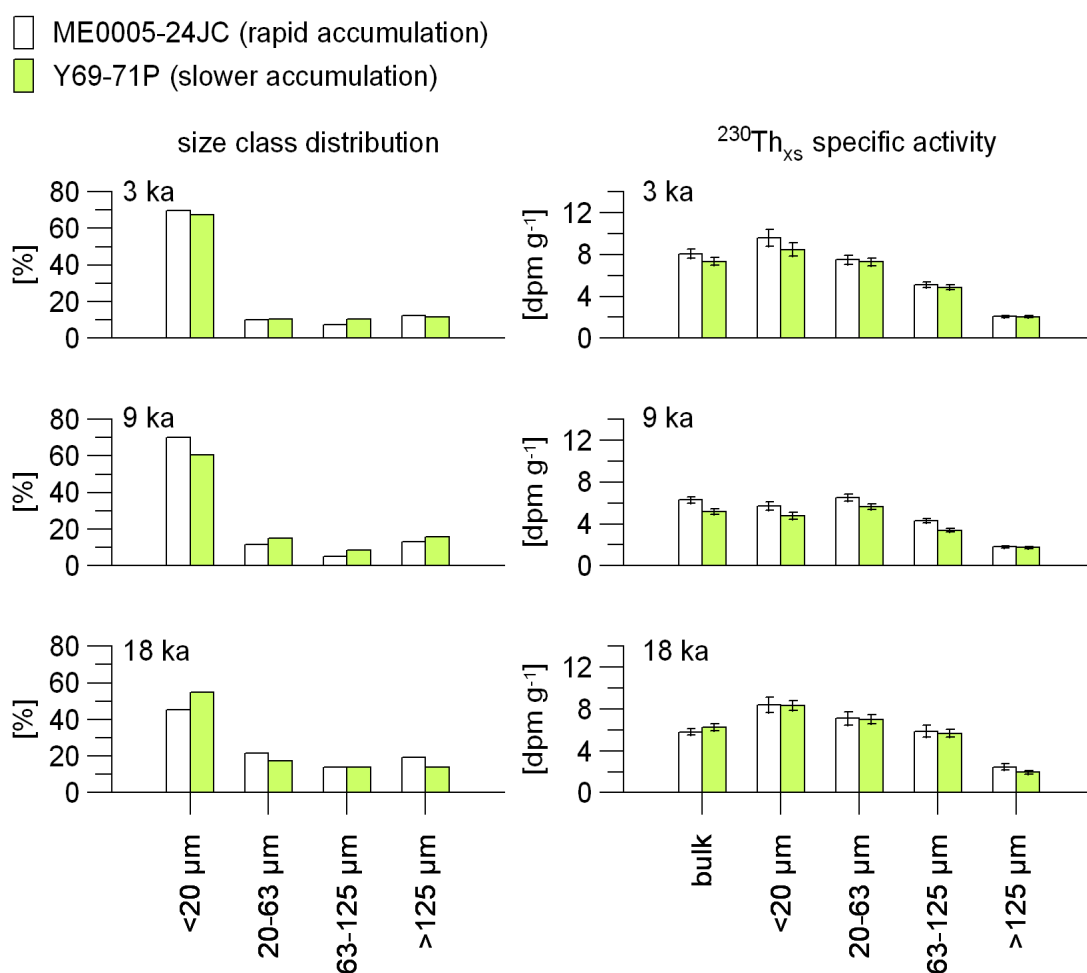


Figure 4.1: Sediment contribution by size class [%] and $^{230}\text{Th}_{\text{xs}}$ specific activity of individual size class [dpm g⁻¹] in two sediment cores at three different ages (3 ka, 9 ka, and 18 ka). White bars represent the more rapidly accumulated sediment core (ME24JC) and colored bars represent the less rapidly accumulated sediment core (Y69-71P). Error bars denote 1σ-level of analytical uncertainty.

for three overlapping age intervals of approximately 2-9 ka, 3-18 ka, and 9-25 ka using $^{230}\text{Th}_{\text{xs}}$ concentrations obtained for bulk samples averaged over three samples within the respective intervals (**Table 4.2**). While our results are in general agreement with the published values [Loubere *et al.*, 2004; Kienast *et al.*, 2007], differences in the absolute values of Ψ result from the definition of core-intervals over which constant $^{230}\text{Th}_{\text{xs}}$ activities are assumed and focusing factors are calculated. These age intervals were chosen such that they each contain one sample depth in which grain-size specific $^{230}\text{Th}_{\text{xs}}$ data were measured.

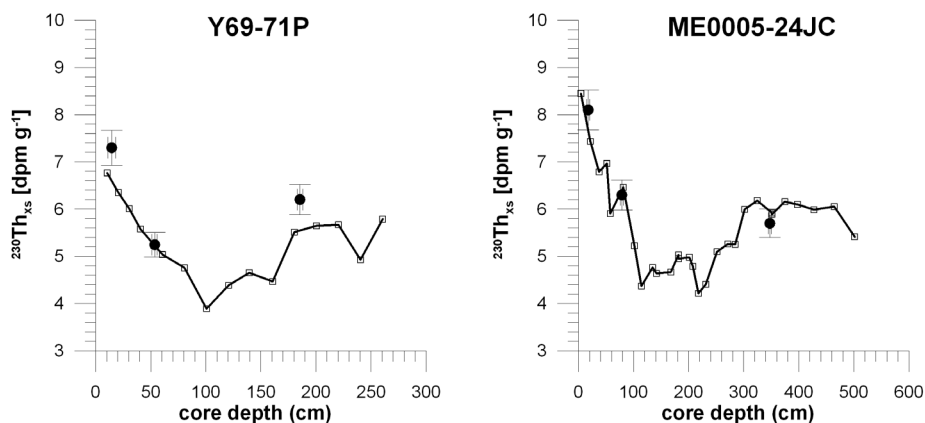


Figure 4.2: Comparison of published (open squares; Kienast *et al.*, 2007) and new (solid dots; this study) bulk sediment $^{230}\text{Th}_{\text{xs}}$ concentrations. Error bars denote 1σ uncertainty levels. Measurements performed in this study were done on solvent-extracted sediment residues. If uncertainty levels for published values are assumed to be similar to ours, all $^{230}\text{Th}_{\text{xs}}$ concentrations agree within 1σ analytical uncertainty.

4.5 Discussion

4.5.1 Grain size class distribution and class-specific ^{230}Th activities

Grain-size spectra at both core locations are dominated by particles of the fine fraction $<20\ \mu\text{m}$ in all core depths, accounting for 61-70 % in the 3 ka and 9 ka samples and for 42-46 % in the 18 ka-samples. In these carbonate rich sediments (50-60 % carbonate; Kienast *et al.*, 2007; Loubere *et al.*, 2004), a substantial contribution of sand-sized foraminiferal shells and sand- to silt-sized shell fragments would be expected. However, the sediments in the Panama Basin are less carbonate-rich than the Walvis Ridge sediments (83-93 % carbonate) studied by Kretschmer *et al.* [2010], which in their study are considered to be representative of a carbonate-dominated end member, and where slightly more coarse-grained particles were found (38-63 % $<20\ \mu\text{m}$).

In contrast, the silica-rich end member sediment (55-60 % opal) in the study by *Kretschmer et al.* [2010] was found to be very strongly dominated by fine-fraction material (76-83 % <20 μm). The grain-size distribution observed in our study therefore represents an intermediate case in accordance with its bulk geochemical composition with mean carbonate and opal contents at ME24JC of 55 % and 16 %, respectively [*Kienast et al.*, 2007].

As expected, highest particle-class specific $^{230}\text{Th}_{\text{xs}}$ activities were found in the fine-fraction particle class (<20 μm and <2 μm) and lowest values in the coarse particles (**Figure 4.1** and **Table 4.1**). However, the spectra show a more homogenous distribution of $^{230}\text{Th}_{\text{xs}}$ across grain-size classes than observed by *Kretschmer et al.* [2010] for both the carbonate-rich and silica-rich sediments. Taking into account the proposed highest affinity of ^{230}Th for adsorption on lithogenic particles, carbonates, and perhaps on metal oxides together with the low affinity to opal [*Luo and Ku*, 1999; *Chase et al.*, 2002; *Roy-Barman et al.*, 2005] we would expect a stronger preference for smaller grain size classes than observed in our Panama Basin sediments. Our observations might therefore indicate that grain size class separations did not effectively separate grains of different mineralogy, i.e., that $^{230}\text{Th}_{\text{xs}}$ -enriched particles like clays are, for instance, contained within chambers of foraminifera.

In the 3 ka and 9 ka time slice samples, site ME24JC shows higher contributions of fine-grained (<20 μm) particles than the shallower site Y69-71P (**Figure 4.1**). More fine particles would be expected at a site with higher deposition of laterally advected material. Thus this observation supports the interpretation of the bulk focusing factors implying that more intense focusing occurs at the deeper site. However, while higher sediment focusing at ME24JC than at Y69-71P is also reconstructed for the 18 ka time slice, the grain-size distribution shows a decreased contribution of the <20 μm fraction at both sites, with lower values at ME24JC, while the contribution of the slightly coarser silt sized spectrum (20-63 μm) is higher. This is not considered to be an artifact of lower sediment recovery for the 18 ka samples, as the coarsening is also observed for the 9 ka samples, where sediment recovery was equal to the 3 ka samples. A higher contribution of coarser silt may indicate the occurrence of stronger bottom currents during the glacial [*McCave et al.*, 1995], again affecting the deeper site more strongly than the shallower site. On the other hand, a coarser size spectrum together with slightly elevated carbonate contents in the 9 ka and 18 ka samples compared with the 3 ka samples could indicate better preservation of carbonate shells of silt and sand size during the glacial and early Holocene, which is in accordance with previous findings of better glacial carbonate preservation [*Loubere et al.*, 2004]. Which of the two processes, stronger currents advecting coarser particles, or better carbonate preservation during glacial to early Holocene times, is responsible for the observed coarser grain size spectra cannot be resolved here.

In general, our data are in good agreement with the expected effect of hydrodynamic sorting of sediment particles during transport supplying predominantly finer grains with higher

specific $^{230}\text{Th}_{\text{xs}}$ activities to locations of strong sediment focusing. Our observation of higher $^{230}\text{Th}_{\text{xs}}$ activities in the finer grain-size classes (activities on particles $<2\ \mu\text{m}$ of 18 ka samples are 2.8 times higher than in the respective bulk sediment; **Table 4.1**), which would be expected to be enriched in suspended, laterally transported particles relative to vertically settling particles, confirms previous results indicating that ^{230}Th concentrations in suspended particles were 1.5 to 3 times higher than in sinking particles [Anderson *et al.*, 1983b].

Table 4.2: Focusing factor Ψ and vertical mass flux F_v and their corresponding grain size corrected values Ψ_c and F_{vc} . For calculating the focusing factors, data of bulk $^{230}\text{Th}_{\text{xs}}$, dry bulk density (DBD) and radiocarbon ages were taken from sources as indicated in the table. Analytical uncertainties are given as 1σ .

depth interval [cm]	age interval [ka]	LSR [cm ka ⁻¹]	MAR [g cm ⁻² ka ⁻¹]	Ψ	Ψ_c	F_v [g cm ⁻² ka ⁻¹]	F_{vc} [g cm ⁻² ka ⁻¹]	data sources
sediment core Y69-71P								
10.5 – 56	2.7 - 9.7	6.5	3.1	2.7 ±0.1	2.2 ±0.2	1.0 ±0.05	1.2 ±0.1	a, b, c, d
11 – 188	3.2 - 17.7	12	5.7	4.9 ±0.2	3.3 ±0.3	1.4 ±0.07	2.1 ±0.2	a, c, d
51 – 200.5	9.7 - 23.9	10	5.0	3.9 ±0.2	2.1 ±0.3	1.2 ±0.06	2.2 ±0.3	a, b, c, d
sediment core ME-0005-24JC								
4.5 – 81	2.0 - 9.0	11	5.2	5.0 ±0.3	3.3 ±0.4	1.0 ±0.05	1.5 ±0.2	a, b, d
15 – 350	3.3 - 18.1	22	10.9	9.3 ±0.5	5.0 ±0.5	1.3 ±0.06	2.3 ±0.3	a, b, d
76 – 374.5	9.0 - 25.2	18	8.8	6.8 ±0.3	3.4 ±0.5	1.3 ±0.07	2.7 ±0.4	a, b

- (a) $^{230}\text{Th}_{\text{xs}}$ data from this study
 (b) $^{230}\text{Th}_{\text{xs}}$ data and ^{14}C age from Kienast *et al.* 2007
 (c) dry bulk density from Loubere *et al.* 2004
 (d) ^{14}C age from Kusch *et al.* 2010

4.5.2 Grain-size correction of focusing factors

In order to assess whether focusing factors as published by Kienast *et al.* [2007] represent an accurate estimate of lateral sediment supply we performed a grain-size correction. Using our grain size-class specific $^{230}\text{Th}_{\text{xs}}$ activities, we calculated “corrected focusing factors” as suggested by Kretschmer *et al.* [2010] and compared them with focusing factors determined according to François *et al.* [2004]. For this calculation, the simplifying assumption was made that the lateral sediment flux transports only “small” particles (“small” was defined here as $<63\ \mu\text{m}$). This assumption requires that the vertical particle flux must have been coarser in grain size distribution than measured in the bulk sediment. Corrected vertical flux values can also be determined (**Table 4.2**).

Uncorrected focusing factors (Ψ) imply that throughout the three age intervals, sediment accumulation is faster and sediment focusing is stronger at ME-0005-24JC than at Y69-71P by a factor of about 1.7 to 1.9. At both core sites sediment focusing is lower during the Holocene interval (5.0 and 2.7 respectively) and highest during the deglacial interval (9.3 and 4.9 respectively). The corrected focusing factors (Ψ_c) are lower than the corresponding Ψ values (**Figure 4.3**). If only fine particles $<63 \mu\text{m}$ with a high specific $^{230}\text{Th}_{\text{xs}}$ activity were supplied by lateral transport, less material is required from a lateral source in order to balance the $^{230}\text{Th}_{\text{xs}}$ inventory observed at a given location. The higher the focusing factor, the stronger is the grain size correction. At ME24JC, Ψ_c are lower than the bulk Ψ (Ψ_c/Ψ ratios of 0.50 to 0.66), and the corrected Ψ_c at Y69-71P correspond to 0.54 to 0.82 times Ψ . As a result the corrected focusing factors range from 2.1 to 3.3 at Y69-71P and from 3.3 to 5.0 at ME-0005-24JC. However, the general observation of increased lateral sediment supply during the glacial and deglacial remains valid even when considering only corrected focusing factors (**Figure 4.3a, b**).

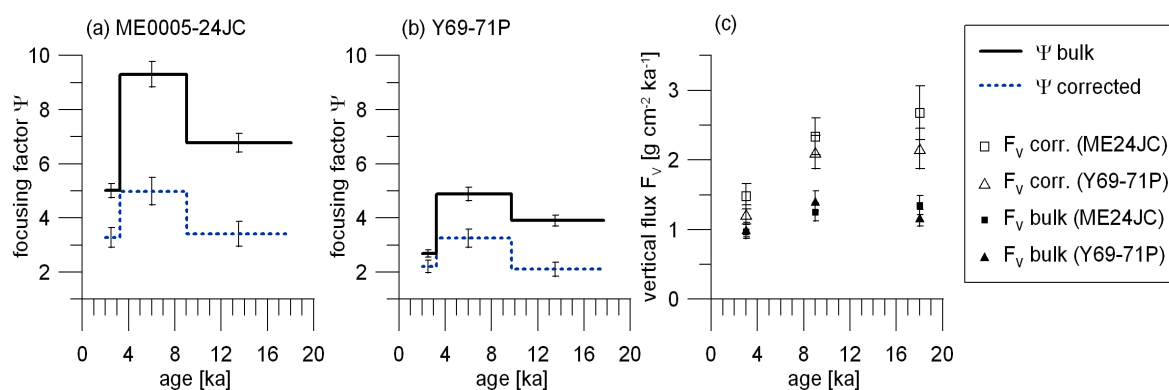


Figure 4.3: Bulk and corrected focusing factors and vertical flux values for the three time intervals assuming that only fine fraction material $<63 \mu\text{m}$ is laterally transported to the core sites. Error bars indicate 1 σ analytical uncertainty including propagated errors of all input parameters ($^{230}\text{Th}_{\text{xs}}$, ^{14}C age, dry bulk density).

Correspondingly, the $^{230}\text{Th}_{\text{xs}}$ normalized vertical fluxes F_v (1.0-1.4 gm²ka⁻¹) are higher after grain size corrections (1.2-2.7 g m⁻² ka⁻¹, **Table 4.2**). While vertical fluxes calculated using the traditional approach as described, e.g., by *François et al.* [2004] do not differ strongly between Holocene, deglacial and glacial core sections, the corrected values suggest significantly increased vertical flux occurred during the deglacial and particularly in the glacial (**Figure 4.3c**). However, in spite of the close proximity of the two core sites, the corrected F_v values indicate higher vertical fluxes at the deeper site ME24JC than at the shallower location of Y69-71P,

while the uncorrected values are very similar. The latter observation was used as one of several lines of evidence to demonstrate the validity of the constant flux proxy [François *et al.*, 2007]. Considering the uncertainty in all input values for the corrected F_v calculation, the differences between the core sites are not statistically significant (**Figure 4.3c**). Additional uncertainty in the corrected flux values is introduced by possible differences in local current regimes at the two core locations resulting from the local topography, which likely lead to different grain size spectra of the advected sediment proportion. Since these differences cannot be accurately assessed, we assumed identical grain size spectra of the advected sediment proportion at both sites.

4.5.3 Implications for lateral transport and productivity in the Panama Basin

Grain-size spectra and $^{230}\text{Th}_{\text{xs}}$ inventories of both cores together with considerations regarding the potential strength of a “particle flux effect” argue strongly in favour of the occurrence of lateral sediment supply in the Panama Basin. Molecular radiocarbon ages of alkenones obtained from the same samples as used for this study, however, show no age differences to co-occurring planktic foraminifera [Kusch *et al.*, 2010]. One possible explanation for this observation is that laterally supplied material is re-distributed syndepositionally shortly after its formation, i.e., within time periods equivalent to the uncertainty ranges of radiocarbon dating, typically a few decades. These estimated timescales of transport refer to fine-fraction material, in which the organic biomarkers reside, and which is more susceptible to transport. Incidentally, these estimated timescales are similar to the mean residence time of ^{230}Th in the water column [Anderson *et al.*, 1983b]. If transport really occurs within several decades, ^{230}Th would equilibrate with suspended particles. Elevated ^{230}Th concentrations in fine-fraction material must therefore be explained as the result of preferential adsorption of ^{230}Th on the particles types contained in suspended and transported material. This effect of preferential adsorption could be either caused by mineralogy or by the large specific surface area of the small-grained suspended particles. For the following discussion it is irrelevant whether it is a mineralogical or a grain-size effect.

Sediment trap studies in the northern Panama Basin revealed that lithogenic flux was higher in deeper than in shallower traps [Honjo *et al.*, 1982]. This increase was attributed to clay eroded from nearby topographic highs, which was primarily transported horizontally until scavenged by organic-rich particles originating from a plankton bloom [Honjo, 1982; Honjo *et al.*, 1982]. The occurrence of benthic nepheloid layers of substantial thickness (up to 400 m) consisting of resuspended particles of approximately 1 μm diameter, i.e., within the clay size range, is also known for other regions in the EEP [Baker and Feely, 1978]. Since we found that small-grained particles are the major carrier of ^{230}Th with highest $^{230}\text{Th}_{\text{xs}}$ activities in the clay fraction of the 18 ka samples (**Table 4.1**), the processes controlling their resuspension and lateral transport and final burial in sediments might hold the key to explaining ^{230}Th inventories in marine sediments. The observed agreement in estimated timescales of lateral transport

affecting (coccolithophorid-derived) marine organic matter and average residence time of ^{230}Th in seawater may thus be purely coincidental. However, the above described process by which plankton-derived organic matter becomes aggregated with ^{230}Th -rich fine-grained suspended material (e.g., clays) scavenged from the water column explains a common deposition as well as the observed lack in radiocarbon age offset between the marine biomarkers alkenones and co-occurring coarse-grained foraminifera [Kusch *et al.*, 2010]. The formation of aggregates with high enough settling velocity to be collected in sediment traps or to ultimately reach the seafloor and become buried has also been suggested to explain the observed seasonal variation on radionuclide fluxes (e.g., ^{230}Th) in sediment traps [Bacon *et al.*, 1985]. Those aggregates may be subject to lateral transport and focusing at locations where current regimes and topography are amenable to deposition of easily eroded particles. Asper *et al.* [1992] furthermore describe the occurrence of fluffy and presumably organic-rich aggregates that are easily resuspended from the seafloor and, like the clays, scavenged from the water column by rapidly sinking denser aggregates. Areas of high vertical flux may thus become areas, where not only large amounts of vertically supplied material are deposited at but at the same time a strong contribution of laterally supplied, resuspended material is incorporated in the sediments. Similarly, times of elevated vertical fluxes related to increased productivity would be associated with more efficient scavenging of resuspended fluffy aggregates and ^{230}Th -rich small-grained particles resulting in high accumulation rates and elevated sediment inventories. A process coupling higher particle fluxes with changes in circulation, which would presumably change the extent and intensity of resuspension of fine-grained ^{230}Th -rich particles, was suggested as a possible explanation for the Panama Basin controversy [Paytan *et al.*, 2004]. Our proposed scenario would satisfy these requirements. The scavenging process suggested by several authors to be responsible for elevated radionuclide inventories [Paytan *et al.*, 2004; Broecker, 2008] would in this scenario not involve dissolved ^{230}Th ions but rather suspended fine-grained (clay) particles strongly enriched in ^{230}Th by a factor of 2.8 to 3 [Table 4.1; Anderson *et al.*, 1983b].

If the described process is really responsible for ^{230}Th distribution in sediments, it has important implications for reconstructing paleoproductivity in the Panama Basin. Our corrected vertical fluxes are higher for the 9 ka and 18 ka time slices than for the late Holocene time slice at 3 ka. The earlier time slices are at the same time characterized by very high ^{230}Th -inventories suggesting high amounts of lateral contribution to the sediments. High vertical fluxes and elevated radionuclide inventories would in our scenario be coupled by the process of clay-scavenging. Due to the preferential adsorption of ^{230}Th on clays, however, the total amount of laterally supplied sediment would be much smaller than implied by bulk focusing factors resolving partly the controversy discussed in the literature.

4.6 Conclusions

The occurrence of strongly increased glacial sediment accumulation rates observed in the Panama Basin has been explained either by elevated vertical flux rates implying increased productivity, or by strong sediment focusing. Both views have been controversially discussed in the literature. Our study of $^{230}\text{Th}_{\text{xs}}$ activities in different grain size classes in sediments deposited at 3 ka, 9 ka, and 18 ka taken from two Panama Basin sediment cores confirmed previous findings that the distribution of the particle reactive radionuclide is heterogeneous between size classes, likely reflecting different affinities of ^{230}Th to grains of different mineralogical composition and different specific surface area. Taking into account that during transport, particles are sorted according to their hydrodynamic properties, the heterogeneous distribution allows calculating corrected sediment focusing factors, which are smaller by 18-50 % than previously reported values based on bulk sediment $^{230}\text{Th}_{\text{xs}}$ activities with strongest reductions during the glacial. However, increased sediment focusing would still be inferred for glacial and deglacial times relative to the 3 ka time slice. Likewise, vertical flux rates derived from the same calculation appear to be slightly elevated during the glacial and deglacial period. Highest specific $^{230}\text{Th}_{\text{xs}}$ activities on clay sized particles explain elevated $^{230}\text{Th}_{\text{xs}}$ inventories during times of higher vertical sediment fluxes when considering their hydrodynamic properties: small-grained particles are known to be readily resuspended, form nepheloid layers in the water column and are redeposited involving a particle scavenging process caused by sinking organic matter. In summary, our data partially support both scenarios suggested for the Panama Basin.

Chapter 5

Fractionation of ^{230}Th , ^{231}Pa , and ^{10}Be induced by particle size and composition within an opal-rich sediment of the Atlantic Southern Ocean

Sven Kretschmer^{1, 2}, Walter Geibert^{3, 4}, Michiel M. Rutgers van der Loeff¹,
Christoph Schnabel⁵, Sheng Xu⁵, Gesine Mollenhauer^{1, 2}

¹ Alfred-Wegener-Institut für Polar- und Meeresforschung, Bremerhaven, Germany

² Fachbereich Geowissenschaften, Universität Bremen, Germany

³ School of GeoSciences, University of Edinburgh, UK

⁴ Scottish Association for Marine Science, Dunstaffnage Marine Laboratory, Oban, UK

⁵ Scottish Universities Environmental Research Centre, East Kilbride, UK

Manuscript submitted to *Geochimica et Cosmochimica Acta* (September 7th 2010).

Abstract

The particle reactive radionuclides ^{231}Pa , ^{230}Th and ^{10}Be recorded in deep sea sediments have been used for tracing past marine particle fluxes. Here, we investigate the influence of oceanic particle composition on the element adsorption in order to improve our understanding of sedimentary isotope records. We present new data on particle size specific ^{231}Pa and, for the first time, particle size specific ^{10}Be concentrations. An additional separation step, based on settling velocities, led to the isolation of a very opal-rich phase. We find that opal-rich particles contain the highest ^{231}Pa and ^{10}Be concentrations, and higher $^{231}\text{Pa}/^{230}\text{Th}$ and $^{10}\text{Be}/^{230}\text{Th}$ isotope ratios than opal-poor particles. The fractionation relative to ^{230}Th induced by the adsorption to opal-rich particles is more pronounced for ^{231}Pa than for ^{10}Be . We conclude that bulk $^{231}\text{Pa}/^{230}\text{Th}$ in Southern Ocean sediments is most suitable as a proxy for past opal fluxes. The comparison between two neighboring cores with rapid and slow accumulation rates reveals that these isotope ratios are not influenced by the intensity of sediment focusing (i.e. sorting) at these two study sites. The study of compound-specific $^{231}\text{Pa}/^{230}\text{Th}$ and $^{10}\text{Be}/^{230}\text{Th}$, as conducted here, allows a more detailed picture of the origin of the isotopic signatures.

5.1 Introduction

Since the beginning of radionuclide analysis in the marine realm, the natural radionuclides ^{231}Pa , ^{230}Th , and ^{10}Be have been applied as tracers by a large number of particle flux studies. The main characteristic of these particle flux tracers is their particle reactivity. Their distinct affinities to different kinds of particles are subject to ongoing discussions because differences in element adsorption complicate the interpretation of radionuclide distributions. This paper contributes new data to the discussion about the role of particle composition.

The production rates of dissolved ^{230}Th and ^{231}Pa in seawater (daughter nuclides of seawater-dissolved ^{234}U and ^{235}U , respectively) are known [e.g. *Cochran, 1992*], whereas the deposition rate of cosmogenic ^{10}Be on Earth in the geological past is subject to ongoing investigation [*Christl et al., 2010*]. Removal of dissolved elements from the water column by adsorption to particles (scavenging) is very efficient for Th, leading to a short residence time of 20-40 a [*Anderson et al., 1983b*]. In contrast, the less particle reactive Pa and Be (residence times 50-100 a and 500-1000 a, respectively) are advected from regions of lower particle flux to those of higher particle flux where scavenging efficiency and thus the radionuclide flux to sediments is enhanced [boundary scavenging, *Anderson et al., 1990*]. As the ratios of particulate $^{231}\text{Pa}/^{230}\text{Th}$ and $^{10}\text{Be}/^{230}\text{Th}$ correlate positively with the intensity of particle flux [*Yang et al., 1986; Lao et al., 1993*], they have been applied as export productivity proxies [*Kumar et al., 1993; Anderson et al., 1998; Pichat et al., 2004*]. However, in the Southern Ocean the ^{231}Pa scavenging is mainly controlled by the opal flux and cannot be explained by the ocean margin effect [*Rutgers van der Loeff and Berger, 1993; Walter et al., 1997*]. Therefore in most recent studies, the application of $^{231}\text{Pa}/^{230}\text{Th}$ was restricted to reconstructing past changes of opal fluxes [*Bradtmilller et al., 2007; 2009; Anderson et al., 2009*], rather than total mass fluxes. Another proxy application uses the sedimentary $^{231}\text{Pa}/^{230}\text{Th}$ for reconstruction of the past overturning circulation due to its sensitivity to the oceanic hydrography [*Yu et al., 1996; McManus et al., 2004; Guihou et al., 2010; Negre et al., accepted*]. The latter application needs to be carried out carefully, considering the sensitivity of $^{231}\text{Pa}/^{230}\text{Th}$ to particle composition, which has the potential to overprint the hydrographic scavenging effect [*Lippold et al., 2009*]. It also relies on the assumption that sediment redistribution does not affect $^{231}\text{Pa}_{\text{xs}}/^{230}\text{Th}_{\text{xs}}$ ratios, which we can test as part of this study.

For further proxy development, various studies have investigated the scavenging and fractionation of ^{231}Pa , ^{230}Th , and ^{10}Be with respect to particle phases. These include field observations of geographical variability [e.g. *Walter et al., 1997*], scavenging experiments under controlled laboratory conditions [e.g. *Geibert and Usbeck, 2004*], correlations between radionuclides and sediment phases in surface sediments [e.g. *Lao et al., 1992*] or sediment cores [e.g. *Henken-Mellies et al., 1990*], studies on the partitioning between dissolved and particulate form in the water column by collecting suspended or settling particles [e.g. *Chase et al., 2002*],

component specific radionuclide analysis by physical or chemical isolation of particle fractions from sediments [e.g. *Bourles et al.*, 1989b; *Luo and Ku*, 1999; *Lal et al.*, 2006], and finally modeling studies [e.g. *Dutay et al.*, 2009]. In summary, these studies mostly conform to the view that biogenic opal strongly scavenges Pa and Be, lithogenic particles strongly scavenge Th and Be, whereas carbonate is a strong scavenger for Th only.

Generally, data on oceanic ^{231}Pa and ^{10}Be are still scarce and beyond that, contrasting results led to discussions about their interpretation [*Luo and Ku*, 1999; 2004a, b *Chase et al.*, 2002; *Chase and Anderson*, 2004]. However, the further development of $^{231}\text{Pa}/^{230}\text{Th}$ and $^{10}\text{Be}/^{230}\text{Th}$ as quantitative proxies needs more investigation of the chemical reactivity of these radionuclides with respect to the different oceanic particle compositions. Our data contribute to this discussion. The methods of sediment phase separation are challenging, because physical separation leads to incomplete isolation of sediment phases [cf. *Luo and Ku*, 1999], whereas selective leaching of sediment phases risks biasing due to desorption/adsorption kinetics of reactive nuclides from one phase to another [cf. *Robinson et al.*, 2008]. For this study, we decided to physically separate particles into small size intervals by sieving, and additionally by settling velocity. By a gentle treatment with natural seawater, the artificial chemical and physical influence on radionuclide distribution is reduced to a minimum. Advantageous to the interpretation of our results is that the two deglacial (16 ka) sediment samples from the Southern Ocean are composed of only two phases (opal and lithogenic). Carbonate particles contribute a negligibly small amount (<1 weight-%).

As a result of the three controlling parameters, i.e., oceanic hydrography, scavenging residence times, and chemical composition of oceanic particles, the opal-rich sediments of the Southern Ocean act as a sink for ^{231}Pa and ^{10}Be . Opal-rich sediments appear to be particularly susceptible to resuspension, which makes redistribution by strong abyssal bottom currents especially important in the opal-belt of the Antarctic Circumpolar Current (ACC) [*Geibert et al.*, 2005]. $^{231}\text{Pa}/^{230}\text{Th}$ and $^{10}\text{Be}/^{230}\text{Th}$ ratios are commonly assumed to be insensitive to sediment focusing. So far this assumption has not yet been proved. Focusing and winnowing occur under the influence of variable abyssal current velocities. Therefore laterally transported sediment particles may be subject to a particle sorting according to particle size and hydrodynamic behavior [*McCave et al.*, 1995]. If distinct particle types with high and low tracer concentrations are isolated from each other, this may potentially change the particulate $^{231}\text{Pa}/^{230}\text{Th}$ and $^{10}\text{Be}/^{230}\text{Th}$ ratios in sediments after re-deposition. In order to obtain more information about the influence of accumulation rates on the sedimentary radionuclide signal, we compare two sediment samples from two neighboring sediment cores (“twin cores”), previously described by *Kretschmer et al.* [2010], that differ in their sedimentation rates solely because of local differences in focusing intensity.

5.2 Materials and Methods

5.2.1 Sediment core location

Two neighboring sediment cores located in the Southern Ocean opal belt, Atlantic sector south of the Antarctic Polar front (APF), equal in water depth, but different in sedimentation rates were selected for comparison. These two gravity cores (PS1768-8 and PS1769-1) were recovered during Polarstern cruise ANT-VIII/3 at 52.5930°S, 4.4760°E, 3299 m water depth and at 52.6125°S, 4.4580°E, 3269 m water depth, respectively. The sediment composition is dominated by diatomaceous mud and ice rafted debris [Gersonde and Hempel, 1990]. Despite the only 2.5 km lateral distance between the twin cores, they reveal contrasting accumulation rates. The sediment deposition during the last deglacial at core site PS1768-8 (mass accumulation rate, MAR = 10.1 g cm⁻² ka⁻¹, focusing factor $\Psi = 5.9$; Frank *et al.*, 1996) is twice as high as at core site PS1769-1 (MAR = 4.4 g cm⁻² ka⁻¹, focusing factor $\Psi = 3.2$; Kretschmer *et al.*, 2010), which is assumed to result from lateral sediment transport by bottom currents. The age model of core PS1768-8 is constrained by a combination of oxygen isotope stratigraphy, siliceous microfossil biofluctuation stratigraphy and radiocarbon dating [Frank *et al.*, 1996]. Age control for core PS1769-1 was obtained by correlating the magnetic susceptibility record to that of the parallel core (**Figure 1.5**). Each of the twin cores was sampled at one core depth (PS1768-8 at core depth 166-169 cm; PS1769-1 at core depth 14-16 cm) representing the last deglacial period (16 ka).

5.2.2 Grain size fractionation

The two sediment samples were separated into particle size-classes by sieving through nylon sieves using natural seawater. The resulting particle size-classes 20-63, 63-125 and >125 μm were further fractionated by their density in seawater into “slowly settling particles” and “fast settling particles”. The particle class <20 μm was further fractionated by settling through purified water into clay-sized particles <2 μm and fine silt particles 2-20 μm . A high concentration of biogenic opal (mainly diatom tests, 75-82 wt-%) is the main characteristic of the slowly settling particles. Also the fine silt (2-20 μm) and the clay-sized (<2 μm) particle fractions contain high amounts of opal (mainly fragments of diatom tests, 76-80 wt-% respectively 61-68 wt-%). In contrast, the fast settling particles with lower opal content (3-17 wt-%) contain mainly ice rafted rock fragments, mixed with radiolarians and few diatoms. The fractionation procedure and all further measurements that have been applied to the particle size fractions (analyses of biogenic opal, specific surface area, and element concentrations) are reported by Kretschmer *et al.* [2010].

5.2.3 Radioisotope analyses

The analyses of ^{231}Pa , ^{230}Th , and ^{10}Be were performed in the laboratories of the Marine Geochemistry department, Alfred-Wegener-Institute, Bremerhaven, Germany and the NERC Cosmogenic Isotope Analysis Facility (CIAF) and AMS laboratory, both at the Scottish Universities Environmental Research Center (SUERC), East Kilbride, UK. These laboratories participated in the GEOTRACES inter-calibration program for ^{231}Pa , ^{230}Th and ^{10}Be [Henderson *et al.*, 2007]. All data on ^{231}Pa ($T_{1/2}=32.5$ ka), ^{230}Th ($T_{1/2}=75.4$ ka), and ^{10}Be ($T_{1/2}=1.5$ Ma) reported in this manuscript are decay-corrected for the time of deposition.

5.2.3.1 ^{231}Pa sample preparation and ICP-MS

For the isotope dilution analysis by Inductively Coupled Plasma-Sector Field-Mass Spectrometry (ICP-SF-MS) the samples were spiked with ^{229}Th , ^{233}Pa and ^{236}U . The protactinium spike ^{233}Pa was produced from a ^{237}Np solution by separating ^{233}Pa from its progenitor by chromatography on a silica gel column. The spikes ^{229}Th , ^{233}Pa and ^{236}U were calibrated against the reference standard material *UREM 11*, an uranium ore. The consensus value for the uranium concentration in *UREM 11* is 58.9 ± 0.5 ppm [Hansen and Ring, 1983]. From this value, we deduced the concentrations of ^{238}U (58.48 ± 0.50 ppm), ^{234}U (3.16 ± 0.03 ng g $^{-1}$) and ^{235}U (418.8 ± 3.6 ng g $^{-1}$). Assuming secular equilibrium, we calculated the concentrations of the respective daughter nuclides ^{230}Th (957.3 ± 8.2 pg g $^{-1}$) and ^{231}Pa (19.16 ± 0.16 pg g $^{-1}$).

Samples (10-100 mg) and spikes (0.7 pg ^{233}Pa , 9 pg ^{229}Th , and 800 pg ^{236}U) were weighed into Teflon vials and fully dissolved in HCl, HNO $_3$, and HF by microwave-assisted digestion. Samples were evaporated to dryness, re-dissolved, and co-precipitated with Fe(OH) $_3$. Separation of Pa, Th and U was achieved by ion exchange chromatography with two different exchange resins (Eichrom UTEVA and BioRad AG 1-X8). The UTEVA columns were conditioned with three column volumes (cv) HNO $_3$ (3M), then loaded with the samples and rinsed with HNO $_3$ (3 cv, 3 M). Th was eluted with HCl (1 cv, 9 M and 2 cv, 5 M suprapur) followed by elution of Pa and U with 3 cv HCl (0.02 M) + HF (0.02 M suprapur). The eluates were collected and evaporated in Teflon beakers. The Th fraction was re-dissolved in HNO $_3$ and as the last step diluted to 5 mL HNO $_3$ (1 M). The Pa-U fraction was re-dissolved in HCl (9 M). The AG 1-X8 columns were conditioned with HCl (9 M) and loaded with the Pa-U fraction. The first rinsing (3 cv HCl 9 M) cleaned the column from any remaining Th and was discarded. Subsequently it was collected for Pa (3 cv HCl 9 M + HF 0.14 M) and for U (5 cv HCl 0.5 M). The separated Pa and U fractions were evaporated and re-dissolved in HNO $_3$ twice, and finally diluted to 5 mL HNO $_3$ (1 M).

Isotopes of Pa, Th and U were analyzed by isotope dilution using ICP-SF-MS (Element2, Thermo Scientific). Samples were injected into the plasma by a desolvation system (Apex Q, ESI). During the injection of the Pa fraction, Th hydride ($^{232}\text{ThH}^+$) formation may contribute

to the mass 233. This was reduced to a minimum by optimizing the sample and Argon gas flow rates and the plasma temperature. In addition, the ^{232}Th peak tailing contributes to the masses 233 and 231. The regular external measurement of a ^{232}Th standard solution allowed the assessment of these analytical effects. The contribution to masses 231 and 233 by $^{232}\text{ThH}^+$ and ^{232}Th peak tailing was corrected by measuring the ^{232}Th in each Pa sample. The instrument mass bias was assessed externally by bracketing samples with a uranium standard solution. Further corrections accounted for ^{233}U bleeding (traced by ^{236}U) and procedural blanks. Procedural blanks (including spike contribution) were equivalent to 0.8-3 % (^{231}Pa) and 0.6 % (^{230}Th) of the samples.

Only the unsupported fraction of ^{231}Pa (excess $^{231}\text{Pa} = ^{231}\text{Pa}_{\text{xs}}$) and ^{230}Th (excess $^{230}\text{Th} = ^{230}\text{Th}_{\text{xs}}$) derived from scavenging is of interest. Therefore ^{231}Pa and ^{230}Th specific activities were corrected for the fraction of ^{231}Pa and ^{230}Th that is supported by lithogenic and authigenic uranium [Henderson and Anderson, 2003].

5.2.3.2 ^{10}Be sample preparation and AMS

^{10}Be was analyzed on 12 sediment samples ($2 \times$ bulk + $10 \times$ fractions) and four seawater samples. The size classes $<2 \mu\text{m}$ and $2\text{-}20 \mu\text{m}$ were not analyzed and the two size classes $63\text{-}125 \mu\text{m}$ and $>125 \mu\text{m}$ of each sample were combined into one size class $>63 \mu\text{m}$. About 340 mg Be carrier (3 wt-% HNO_3 , $1.127 \text{ mg Be g}^{-1}$) was added to the sediment samples ($\sim 100 \text{ mg}$) prior to the microwave-assisted full acid digestion. After sample digestion, the acid was fumed off until dryness and samples were re-dissolved in HCl (3 mL, 6 M) twice. The four acidified (pH 2-3) seawater samples ($2 \times$ supernatant, $2 \times$ procedural blank, 11-15 L each) were prepared for ^{10}Be measurement by adding 2 mL solution of iron chloride (FeCl_3 in HCl, 50 mg mL^{-1}) and 340 mg Be carrier (3 wt-% HNO_3 , $1.127 \text{ mg Be g}^{-1}$). After 24 h of equilibration aqueous ammonia was added until pH 10 was reached and Be was co-precipitated with $\text{Fe}(\text{OH})_3$ and $\text{Mg}(\text{OH})_2$. The supernatant was siphoned off and the precipitate was re-dissolved in HCl. After three times of co-precipitations the sample volume was $\sim 30 \text{ mL}$. It was further reduced to $\sim 3 \text{ mL}$ by evaporation on hotplates.

Samples (in HCl, 3 mL, 6 M) were loaded on basic anion exchange resin (Merck, Dowex 1-X8, 2 mL), eluted with HCl (3 cv, 6 M), and immediately collected for Be. Fe is bound to the resin as FeCl_4^- -anion. As the Fe content in the seawater samples was very high due to the $\text{Fe}(\text{OH})_3$ -co-precipitation, each seawater sample was split into two fractions and anion exchange was repeated using a large column (5 mL resin) for each sample split. After anion exchange the sample splits were combined again before the next step.

Samples were converted into sulfate form by adding H_2SO_4 (1 mL 0.5 M, analytical grade) and evaporating to near dryness. H_2O_2 (6 drops 2 wt-%) and H_2SO_4 (2 mL 0.04 M) were added and evaporated two times to a syrupy droplet. The sample was re-dissolved in H_2SO_4 (2 mL

Table 5.1: Sieving recoveries and leaching loss of ^{231}Pa and ^{10}Be after the size fractionation of the sediment samples. The leaching loss is the amount of ^{231}Pa and ^{10}Be that was lost by desorption and/or dissolution during sieving/settling and remained in the supernatant water, expressed as the percentage of the total initial amount. Shading indicates the sediment core site of slower mass accumulation rate.

samples	AMS ID	Sediment sieved [g]	^{231}Pa in sediment [dpm g ⁻¹]	Recovery of ^{231}Pa after sieving [%]	seawater used for sieving [kg]	^{231}Pa in seawater [dpm kg ⁻¹]	amount of ^{231}Pa leached from sediment [dpm]	^{231}Pa lost to supernatant in % of total ^{231}Pa amount [%]
PS1768-8		7.7	0.83	110	22.49	0.00181	0.032	0.5
PS1769-1		7.9	0.8	109	19.10	0.00169	0.025	0.4
blank					21.69	0.00037		
samples	AMS ID	Sediment sieved [g]	^{10}Be in sediment [atoms g ⁻¹]	Recovery of ^{10}Be after sieving [%]	seawater used for sieving [kg]	^{10}Be in seawater [atoms kg ⁻¹]	amount of ^{10}Be leached from sediment [atoms]	^{10}Be lost to supernatant in % of total ^{10}Be amount [%]
PS1768-8	b2692	14.4	2.54E+09	103	11.31	1.88E+07	2.09E+08	0.6
PS1769-1	b2832	18.6	2.24E+09	104	15.40	1.93E+07	2.92E+08	0.7
blank 1	b2693				11.53	3.12E+05		
blank 2	b2694				15.51	2.50E+05		

0.04 M), let stand overnight and centrifuged before loading to the cation exchange columns. The “fast settling” particle fractions were estimated to contain high cation loads (especially Na^+ , Mg^{2+} , Ca^{2+} , Al^{3+} , and TiO^{2+}), so that they were split onto two columns (each 2 mL) in parallel. All other samples were separated on one column. Samples were loaded on a sulfonic acid cation exchange resin (BioRad, AG 50W-X8 Resin, 2 mL, 200-400 mesh) conditioned with 0.2 M H_2SO_4 . Then the TiO^{2+} -containing fraction was eluted from the resin with H_2SO_4 (6 cv 0.5 M), followed by elution of Be^{2+} with HCl (5 cv 1.2 M), and Al^{3+} was removed from the resin with HCl (3 cv 4.5 M).

The Be-fraction was reduced to a small volume (~1 mL) by evaporation and $\text{Be}(\text{OH})_2$ was precipitated at pH 9 by adding an aqueous NH_3 solution (25 wt-%). The precipitate was centrifuged and washed with pH 7 solution (1 mL) three times, dissolved in concentrated HNO_3 (60 μL 70 %, certified) and transferred to quartz crucibles. Samples were dried down on a hotplate, and $\text{Be}(\text{NO}_3)_2$ was partly decomposed by increasing the temperature to above 200°C. For conversion to BeO the samples were heated in a furnace to 900°C.

For the AMS analysis BeO was mixed with Niobium (~4 mg, purity 99.99 %, Alfa Aesar, 325 mesh; mixing ratio BeO/Nb = 1:6 wt/wt) and pressed into a Cu cathode. The $^{10}\text{Be}/^9\text{Be}$ ratios that resulted after carrier addition were measured with the 5 MV accelerator mass spectrometer at SUERC [Freeman *et al.*, 2007]. The measurement is described in detail by Xu *et al.* [2010]. NIST SRM4325 with a $^{10}\text{Be}/^9\text{Be}$ ratio of 3.06×10^{-11} [Middleton *et al.*, 1993] was used for normalization.

5.2.3.3 Recovery and leaching of ^{231}Pa and ^{10}Be during sediment sieving

After the grain size fractionation the supernatant was collected and analyzed together with the procedural blanks for determining the amount of ^{231}Pa and ^{10}Be that was leached from the sediment during processing. Procedural blanks were obtained by performing all fractionation steps (three nylon sieves, settling tubes, acidification, $\text{Fe}(\text{OH})_3$ -co-precipitation) using the same batch of natural seawater that had been used for sediment fractionation. The ^{231}Pa and ^{10}Be in the procedural blank was subtracted from the supernatant amounts (Table 5.1). The difference is assumed to be the amount that was leached from sediment during fractionation. It accounts for 0.4-0.7 % relative to the total amount of the respective bulk sample (Table 5.1).

The isotope recoveries after sediment sieving are calculated by summing up the ^{231}Pa and ^{10}Be concentrations of all particle size fractions and dividing by the concentration of the respective bulk sample. Recoveries of ^{10}Be and $^{231}\text{Pa}_{\text{xs}}$ in sediment fractions sum up to, respectively, 103-104 % and 109-110 % relative to the bulk sample (Table 5.1).

5.3 Results and Discussion

5.3.1 Protactinium

The fast sinking coarse particles $>20 \mu\text{m}$ (opal-poor) are characterized by very low $^{231}\text{Pa}_{\text{xs}}$ specific activities ($0.03\pm 0.01 - 0.19\pm 0.03 \text{ dpm g}^{-1}$, **Figure 5.1**, **Table A-3** in the Appendix), and by $^{231}\text{Pa}_{\text{xs}}/^{230}\text{Th}_{\text{xs}}$ activity ratios ($0.013\pm 0.003 - 0.05\pm 0.01$) lower than the production ratio (0.093). In contrast, the slowly sinking coarse particles $>20 \mu\text{m}$ (opal-rich) and the fine particles $<20 \mu\text{m}$ (opal-rich) reveal high specific activities ($0.46\pm 0.08 - 1.89\pm 0.32 \text{ dpm g}^{-1}$) and their $^{231}\text{Pa}_{\text{xs}}/^{230}\text{Th}_{\text{xs}}$ activity ratios ($0.11\pm 0.03 - 0.54\pm 0.13$) are similar to or higher than the production ratio. The $<2 \mu\text{m}$ -size class is composed of biogenic opal (61-68 %) and a lithogenic fraction, mainly clay minerals. Therefore, the $^{231}\text{Pa}_{\text{xs}}/^{230}\text{Th}_{\text{xs}}$ ratio within this size class results from two contrasting particle types. Assuming that the opal fraction within the $<2 \mu\text{m}$ -size class contain the same $^{231}\text{Pa}_{\text{xs}}/^{230}\text{Th}_{\text{xs}}$ ratio (0.33-0.46) as the opal-rich particle classes (“opal-endmember”), the $^{231}\text{Pa}_{\text{xs}}/^{230}\text{Th}_{\text{xs}}$ ratio is calculated for the “clay mineral-endmember” to be 0.051-0.073. These contrasting ratios within one particle size class point to the strong affinity of Th adsorbing to clay, and Pa adsorbing to opal.

Bulk $^{231}\text{Pa}_{\text{xs}}$ activities ($1.10\pm 0.19 \text{ dpm g}^{-1}$, **Figure 5.1**) are in agreement with $^{231}\text{Pa}_{\text{xs}}$ data from *Frank et al.* [1996] who report for the same sediment core PS1768-8 at similar core depth (156-181 cm) a decay corrected $^{231}\text{Pa}_{\text{xs}}$ activity of $1.37\pm 0.27 \text{ dpm g}^{-1}$ analyzed with alpha spectrometry. Bulk $^{231}\text{Pa}_{\text{xs}}/^{230}\text{Th}_{\text{xs}}$ ratios (0.16 ± 0.04) are within the range of previously published ratios (0.12-0.24) reported for the glacial Southern Ocean on sediment cores just south of the Antarctic polar front (APF) close to our core site by *Kumar et al.*, [1995] and *Anderson et al.* [1998].

5.3.2 Beryllium

The fast sinking coarse particles $>20 \mu\text{m}$ (opal-poor) are characterized by ^{10}Be concentrations ($0.50\pm 0.02 - 0.86\pm 0.03 \times 10^9 \text{ atoms g}^{-1}$, **Figure 5.1**, **Table A-4** in the Appendix) and $^{10}\text{Be}/^{230}\text{Th}_{\text{xs}}$ ratios ($0.21\pm 0.04 - 0.33\pm 0.06 \times 10^9 \text{ atoms dpm}^{-1}$) lower than within all other particle classes. The slowly sinking coarse particles $>20 \mu\text{m}$ (opal-rich) reveal ^{10}Be concentrations ($0.84\pm 0.03 - 1.33\pm 0.04 \times 10^9 \text{ at g}^{-1}$) not much higher than the fast sinking particles, but their $^{10}\text{Be}/^{230}\text{Th}_{\text{xs}}$ ratios ($0.49\pm 0.08 - 0.57\pm 0.10 \times 10^9 \text{ at dpm}^{-1}$) are the highest of all. In contrast, the fine particles $<20 \mu\text{m}$ (opal-rich) carry the highest ^{10}Be concentrations ($3.03\pm 0.09 - 3.11\pm 0.10 \times 10^9 \text{ at g}^{-1}$), but their $^{10}\text{Be}/^{230}\text{Th}_{\text{xs}}$ ratios ($0.39\pm 0.07 - 0.45\pm 0.08 \times 10^9 \text{ at dpm}^{-1}$) are lower than in the slowly sinking classes. $^{10}\text{Be}/^{230}\text{Th}_{\text{xs}}$ ratios in all particle size classes exceed the production ratio in seawater ($0.136-0.170 \times 10^9 \text{ at dpm}^{-1}$).

Within the same core PS1768-8, at similar core depth (156-181 cm), *Frank et al.* [1996] analyzed the ^{10}Be concentration by sediment leaching and report a ^{10}Be concentration of

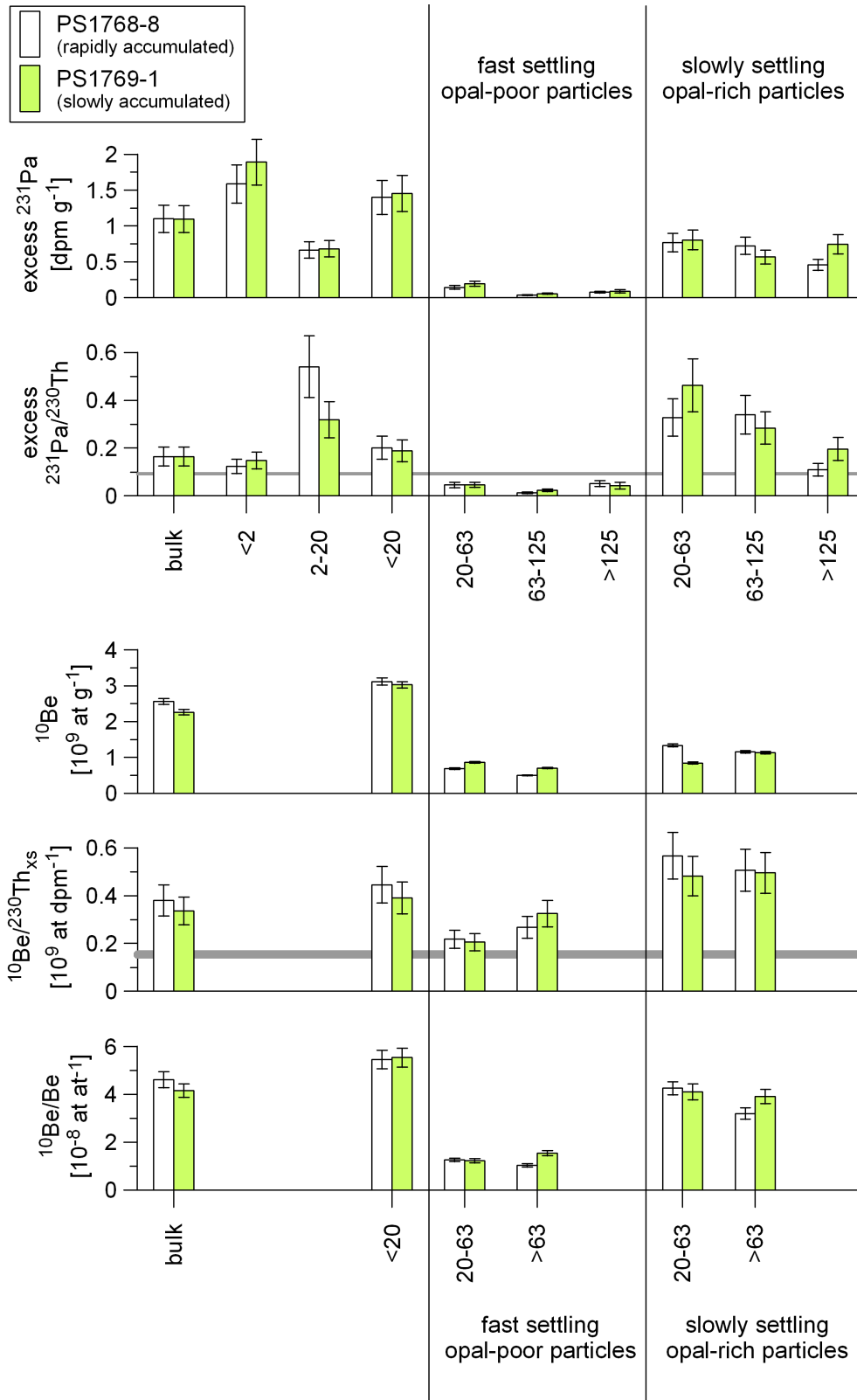


Figure 5.1: Concentrations and isotope ratios of $^{231}\text{Pa}_{\text{xs}}$ and ^{10}Be distributed by particle classes [μm]. The error bars display 1σ . Grey horizontal lines indicate the production ratio of $^{231}\text{Pa}_{\text{xs}}/^{230}\text{Th}_{\text{xs}}$ ($=0.093$) and a range of the production ratio of $^{10}\text{Be}/^{230}\text{Th}_{\text{xs}}$ ($=0.136\text{-}0.170 \times 10^9$ atoms dpm $^{-1}$). This range is based on ^{230}Th production at 3300 m water depth and a global average production of ^{10}Be at about 16 ka BP between 1.2 and 1.5×10^6 atoms cm $^{-2}$ a [derived from *Christl et al.*, 2007 and *Frank et al.*, 1997].

$1.23 \pm 0.04 \times 10^9$ at g^{-1} . This is half the concentration of what we measured by complete acid digestion ($2.5 \pm 0.1 \times 10^9$ at g^{-1}). This higher ^{10}Be signal may partly derive from a lithogenic ^{10}Be source as only $\sim 70\%$ of the total ^{10}Be is of authigenic origin [Bourles *et al.*, 1989b]. In order to distinguish between distinctive ^{10}Be sources we look at the intrinsic $^{10}\text{Be}/\text{Be}$ ratios within the particle fractions. Lal *et al.* [2006] analyzed $^{10}\text{Be}/\text{Be}$ in cleansed opal samples that were separated from sediments from the ODP core 1093 located very close to our core site. The intrinsic $^{10}\text{Be}/\text{Be}$ ratio as reported by these authors for a deglacial opal sample ($4.3 \pm 0.2 \times 10^{-8}$ at at^{-1}) is virtually identical (within error) with the intrinsic $^{10}\text{Be}/\text{Be}$ ratio of our slowly settling opal-rich samples (4.10 ± 0.17 and $4.26 \pm 0.14 \times 10^{-8}$ at at^{-1} , **Figure 5.1**). The authors argue that dissolved trace metals are trapped within the silica structure of diatoms and therefore past metal concentrations in surface waters are recorded by sedimentary opal tests. Following this line of argument, our ^{10}Be concentrations in the slowly settling opal-rich fractions probably reflect an authigenic surface water derived ^{10}Be signal. This interpretation is supported by the observation of ^{10}Be depletion in surface waters of the modern Atlantic ACC which is suggested to result from enhanced scavenging by opal particles in the euphotic zone [Frank *et al.*, 2002]. In contrast, the fine particle fractions ($<20 \mu\text{m}$) of PS1768 and PS1769 reveal a slightly enhanced $^{10}\text{Be}/\text{Be}$ ratio (5.46 and 5.54×10^{-8} at at^{-1} , respectively, **Figure 5.1**). This fine particle fraction consists of two components, the opal (55 % and 58 %, respectively) and the residual component, which is mainly clay and fine silt. If the $^{10}\text{Be}/\text{Be}$ ratio of the “opal-endmember” is known to be 4.3×10^{-8} at at^{-1} as mentioned above, the “clay mineral-endmember” within the two samples (45 % and 42 %, respectively) is calculated to carry a $^{10}\text{Be}/\text{Be}$ ratio of 6.9 and 7.3×10^{-8} at at^{-1} , respectively. This higher ratio points to a source different than that for the opal-rich fractions. Possibly ^{10}Be adsorbed to clay was equilibrated with the water depth at which the clay finally was deposited. However, the ratio is much lower than reported for the modern deep and bottom water of the circumpolar current [$10\text{-}11 \times 10^{-8}$ at at^{-1} ; Kusakabe *et al.*, 1987]. Probably the “clay mineral-endmember” does not reflect an authigenic seawater signal, as it is diluted with a lower $^{10}\text{Be}/\text{Be}$ ratio deriving from aeolian dust that may range from 0.1 to 2×10^{-8} at at^{-1} , as reported for surface soils [Barg *et al.*, 1997]. However, as the absolute ^{10}Be contribution to the deep water by aeolian dust is insignificant [Wang *et al.*, 1996], we assume that aeolian dust contributes only minor amounts of ^{10}Be to the sediment samples of our study site, acting mainly as a diluting agent; dust fluxes of $1\text{-}5 \text{ g m}^{-2} \text{ a}^{-1}$ have been reported from ODP core 1090 [Martínez-García *et al.*, 2009], located in a comparable situation with respect to dust supply. Regarding the modern oceanography, it has been suggested that only an advection of ^{10}Be from the deep Pacific could explain the high ^{10}Be concentrations in the deep water of the Atlantic sector of the Southern Ocean [Frank *et al.*, 2002]. Furthermore, the sedimentary clay mineral assemblage of the Eastern South Atlantic sediments indicates a long distance transport of lithogenic material originating from Patagonia and the Antarctic Peninsula [Diekmann *et al.*,

1996]. Therefore, we can interpret high ^{10}Be concentrations found in the $<20\ \mu\text{m}$ -fraction to be partly derived from the adsorption on clay minerals that are advected by bottom currents from distant sources. Summarizing, particle specific ^{10}Be at our study site is mainly composed of an authigenic surface water signal (carried by biogenic opal) mixed to a variable extent with an advected signal (carried by clay in equilibrium with deep water), diluted to some extent by aeolian dust.

5.3.3 Isotope ratios under sediment focusing conditions

Comparing the rapid with the slow accumulation site (**Figure 5.1**, white and colored bars, respectively) they mostly reveal identical (within 1σ) isotope concentrations and ratios. Systematic differences between both sites are not observable. This result is obvious, because both sites probably receive particles of the same composition that experience the same water masses, owing to their close neighborhood and the same water depth. We conclude that mass accumulation rates and consequently the total fluxes of Pa, Th and Be may differ largely between two sites under contrasting focusing conditions on local scale without affecting their respective isotope concentrations and ratios. However, the source of the advected particles remains unknown. It is possible that fine material is re-suspended at a winnowing site and transported away, while leaving behind the coarser material. To assess the potential size sorting effect on the sediments isotope signal, **Table 5.2** provides the percentage of biogenic opal, $^{230}\text{Th}_{\text{xs}}$, ^{10}Be , and $^{231}\text{Pa}_{\text{xs}}$ contributed by each size class in relation to the total inventories. The class of small particles $<20\ \mu\text{m}$ contributes slightly more to the Th (91 %) and Be (90 %) than to the Pa (88-89 %) inventories. The slowly sinking particles contribute more Pa (11 %) and Be (7-9 %) than Th (5-7 %). In contrast, the fast sinking particles, contribute less Pa (1 %) and Be (1-3 %) than Th (3-4 %). The small and slowly sinking particles are the main contributors to the sediments' isotope inventories and determine the high sedimentary isotope ratios. In contrast, the fast settling particles carry the inverse isotope ratios, but they contribute only a minor fraction. A particle sorting theoretically assumed would only change the sedimentary isotope ratio, if these two contrasting particle types would separate efficiently during particle re-suspension, transport, or re-deposition. Regarding the sedimentary setting occurring at the study site (strong sediment focusing during glacial and interglacial; *Frank et al.*, 1996), this case appears rather unlikely. Therefore, we conclude that variations in fluxes of particulate Th, Be, and Pa by lateral advection have little or no influence on sedimentary isotope ratios in the study area. Sorting was found to have no effect on the isotope ratios at this site. An influence of particle sorting on isotope ratios would only be possible at sites of strong winnowing, such as, e.g., reported for places south of the Subantarctic Front between 46°S and 48°S [*Frank et al.*, 1996].

Table 5.2: Percentage contribution by particle size classes. Each size class contributes a certain fraction to the total flux of opal and particulate $^{230}\text{Th}_{\text{xs}}$, $^{231}\text{Pa}_{\text{xs}}$, and ^{10}Be . Expressed in percentage, comparison between parameters become possible and the potential influence of particle size sorting on isotope ratios can be assessed.

particle size class [μm]	settling velocity	percentage contribution [%] to total inventory				
		wt-% size fraction	opal	$^{230}\text{Th}_{\text{xs}}$	^{10}Be	$^{231}\text{Pa}_{\text{xs}}$
sediment core PS1768-8						
<20		76.4	77.1	90.5	90	88.6
20-63	slowly	14.7	20.3	5.9	7.4	9.3
>63	slowly	2.8	1.9	1.1	1.2	1.6
20-63	fast	2.7	0.5	1.4	0.7	0.3
>63	fast	3.5	0.1	1.1	0.7	0.2
sediment core PS1769-1						
<20		72.5	74.7	90.6	90.4	87.7
20-63	slowly	14.9	21.8	4.2	5.2	10.0
>63	slowly	3.0	2.1	1.0	1.4	1.4
20-63	fast	2.6	0.8	1.8	0.9	0.4
>63	fast	7.0	0.6	2.5	2.0	0.5

5.3.4 Influence of opal content on isotope ratios

$^{231}\text{Pa}_{\text{xs}}$, ^{10}Be , and $^{230}\text{Th}_{\text{xs}}$ concentrations correlate positively with the specific surface area, reflecting the adsorptive binding of all three nuclides to the surfaces of particles (**Figure 5.2a**). The ratios $^{231}\text{Pa}_{\text{xs}}/^{230}\text{Th}_{\text{xs}}$ and $^{10}\text{Be}/^{230}\text{Th}_{\text{xs}}$ are positively correlated with the biogenic opal content of the particles (**Figure 5.2b**) confirming findings of earlier studies [*Taguchi et al.*, 1989; *François et al.*, 1993; *Asmus et al.*, 1999; *Chase et al.*, 2002; *Bradtmiller et al.*, 2009]. In contrast, they show an inverse correlation or no correlation to concentrations of Al or ^{232}Th , respectively (**Figure 5.2b**). Al and ^{232}Th concentrations are thought to trace particles from lithogenic sources. We conclude that the intensity of element adsorption is a function of the surface area of the particle, whereas the ability to fractionate between elements depends on the opal content of the particle.

In order to test whether this fractionation by opal content is stronger for either one of

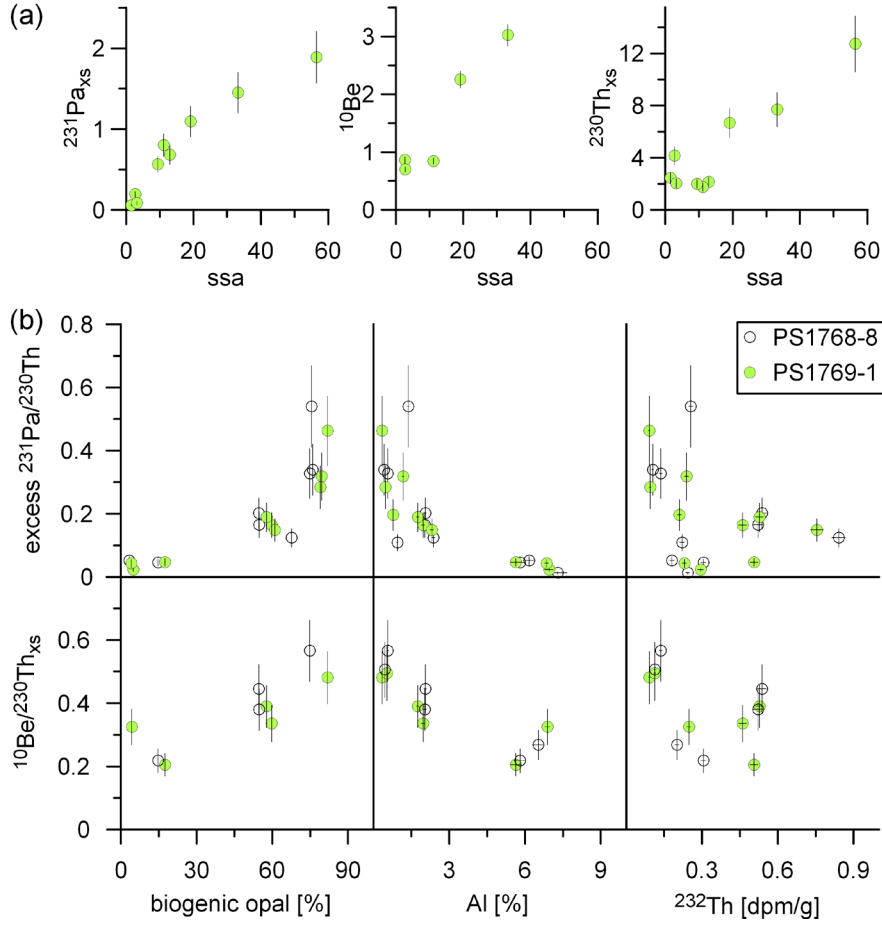


Figure 5.2: (a) $^{231}\text{Pa}_{\text{xs}}$ and $^{230}\text{Th}_{\text{xs}}$ specific activities [dpm g^{-1}] and ^{10}Be concentrations [10^9 at g^{-1}] in particle classes (error bars = analytical uncertainty of 1σ) are plotted against the specific surface area (ssa) [$\text{m}^2 \text{g}^{-1}$] of the particles. (b) $^{231}\text{Pa}_{\text{xs}}/^{230}\text{Th}_{\text{xs}}$ [activity ratio] and $^{10}\text{Be}/^{230}\text{Th}_{\text{xs}}$ [$10^9 \text{ atoms dpm}^{-1}$] in particle classes are plotted against biogenic opal [%], aluminum concentration [%] and ^{232}Th specific activity [dpm g^{-1}] (error bars = analytical uncertainty of 1σ). Data and methods on specific surface area, biogenic opal content and Al concentrations are reported by *Kretschmer et al.* [2010].

the nuclides ^{231}Pa or ^{10}Be , we introduce the distribution ratio D_{Th} as a new parameter. As D_{Th} is a ratio of percentages, the direct comparison between the Pa-Th- and Be-Th-fractionation is possible and independent of units. The percentage (i.e. the fraction:bulk ratio) of the nuclide N (^{231}Pa or ^{10}Be) within a certain particle size class is divided by the percentage of ^{230}Th within the same particle size class (equation 5.1),

$$D(N/\text{Th}) = [N_{\text{fraction}}/N_{\text{bulk}}] / [\text{Th}_{\text{fraction}}/\text{Th}_{\text{bulk}}], \quad (5.1)$$

where N is the concentration of either initial $^{231}\text{Pa}_{\text{xs}}$ or ^{10}Be , and Th is the concentration of initial $^{230}\text{Th}_{\text{xs}}$. Deviation of D_{Th} from 1.0 reflects adsorption intensities of N different from that of Th. $D_{\text{Th}} > 1$ indicates preferential adsorption and $0 < D_{\text{Th}} < 1$ indicates less adsorption of N relative to Th. The D_{Th} ratio is displayed in **Figure 5.3** on a logarithmic scale where bars are sorted from

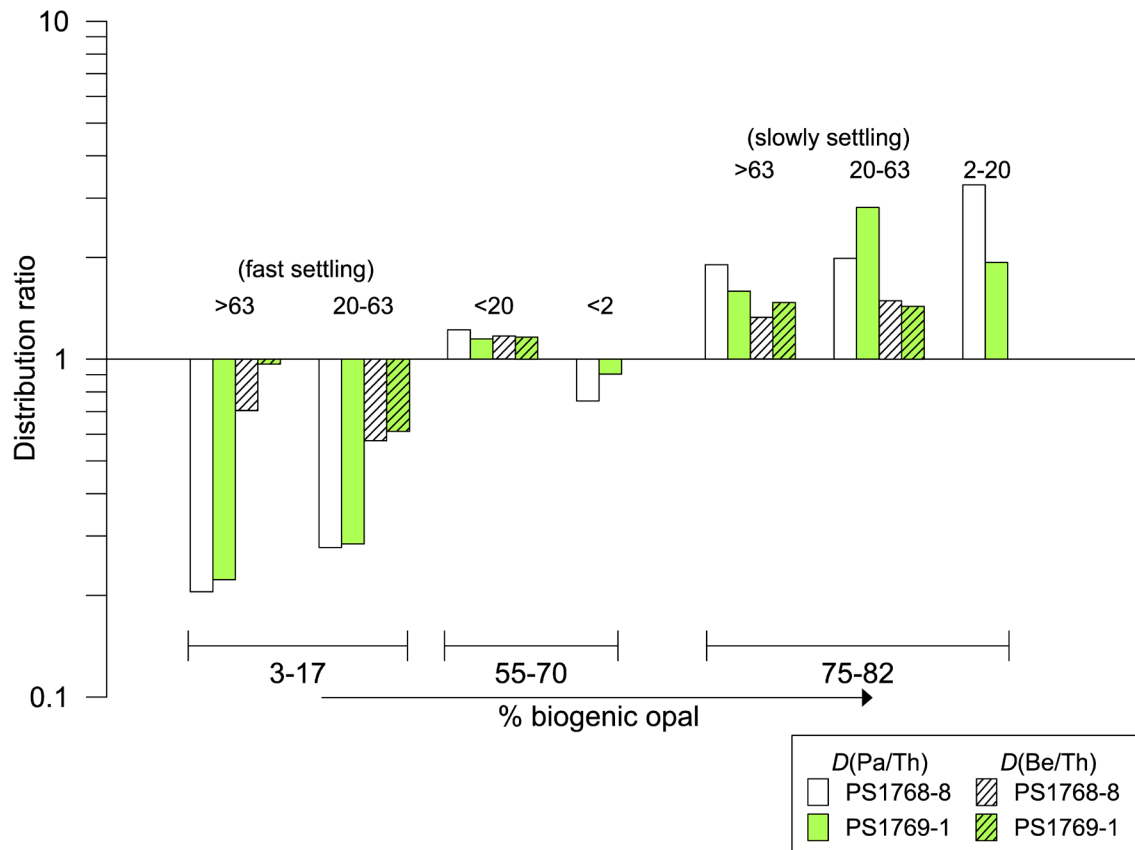


Figure 5.3: The distribution ratio $D(N/Th)$ (see text for definition) is calculated for each particle fraction. Values of D are plotted on a logarithmic scale, where $0 < D < 1$ indicates a fractionation that favors ^{230}Th over the radionuclide N (^{231}Pa or ^{10}Be), and $D > 1$ indicates a fractionation that favors the radionuclide N (^{231}Pa or ^{10}Be) over ^{230}Th . The samples are ordered on the x-axis with increasing biogenic opal content from left to right. Numbers above the bars indicate the particle sizes [μm].

left to right by increasing opal content. As expected, preferential scavenging of Th relative to Pa and Be is found in the opal-poor particles ($D_{Th} = 0.2 - 0.9$), whereas the inverse situation is found within the opal-rich particle classes ($D_{Th} = 1.3 - 3.3$). Within all particle classes, $D(^{10}Be/^{230}Th)$ is closer to unity than $D(^{231}Pa/^{230}Th)$. This leads us to conclude, that the fractionation between ^{230}Th and ^{10}Be is less sensitive to the opal content than the fractionation between ^{230}Th and ^{231}Pa . This is consistent with results of other investigators suggesting that ^{10}Be scavenging is sensitive to both opal and lithogenic particles fluxes [e.g. *Lao et al.*, 1992; *Frank et al.*, 2000a; *Chase et al.*, 2002], whereas opal is the major phase for Pa scavenging [*Chase et al.*, 2002; *Scholten et al.*, 2005].

The size classes $< 2 \mu m$ and $< 20 \mu m$ show $D(^{231}Pa/^{230}Th)$ values close to unity in spite of their high opal concentrations (55-70 %). These particle fractions contain the highest concentrations of both $^{231}Pa_{xs}$ (**Figure 5.1**) and $^{230}Th_{xs}$. Assuming the most extreme case to

explain this observation, all ^{231}Pa could be scavenged by opal particles, and all ^{230}Th could be scavenged by clay minerals. The relative contribution of the individual particle types to total ^{231}Pa and ^{230}Th , however, cannot be fully resolved here and must be addressed in further investigations.

Our data support the view of *Frank et al.* [2000a] who conclude from observations on the same sediment core (PS1768-8) that the ^{10}Be flux rate is not a suitable tracer for biogenic particle flux in the Southern Ocean. Owing to its sensitivity to both lithogenic particle flux and biogenic opal flux ^{10}Be should be used as tracer for total particle fluxes and its application should be restricted to situations when oceanic particle composition does not change significantly over time. In contrast, the exclusive affinity to opal makes $^{231}\text{Pa}_{\text{xs}}$ a unique tracer for opal fluxes into the Southern Ocean sediments, as recently shown by *Anderson et al.* [2009] and *Bradtmiller et al.* [2009].

5.4 Conclusions

Many studies have applied the $^{231}\text{Pa}_{\text{xs}}/^{230}\text{Th}_{\text{xs}}$ and $^{10}\text{Be}/^{230}\text{Th}_{\text{xs}}$ ratios for paleoceanographic reconstructions on sediments deposited under rapid accumulation, making the assumption that isotope ratios are not influenced by accumulation rate and sediment transport. Our results confirm this assumption, because concentrations and ratios appear to be insensitive to the strong focusing at the Southern Ocean study site. Based on our data, elemental fractionation physically induced by particle size sorting appears unlikely under the sediment focusing conditions of our study site, but a definite conclusion cannot be drawn as we do not have data from a corresponding winnowing site.

The particle specific intrinsic $^{10}\text{Be}/\text{Be}$ ratios reveal that the opal-rich particles reflect a seawater derived ^{10}Be signal, whereas maximum ^{10}Be concentrations and $^{10}\text{Be}/\text{Be}$ ratios within the fine particles $<20\ \mu\text{m}$ point to another ^{10}Be source, possibly adsorbed to clay and advected by bottom currents.

Within various studies the biogenic opal was suggested to be the major influencing factor for $^{231}\text{Pa}_{\text{xs}}$ and ^{10}Be scavenging in the water column. Our data show that $^{231}\text{Pa}_{\text{xs}}$ and ^{10}Be remain strongly associated to the opal-rich particles even after burial in the sediment. The fractionation from $^{230}\text{Th}_{\text{xs}}$ by opal-rich particles is more pronounced for $^{231}\text{Pa}_{\text{xs}}$ than for ^{10}Be . In congruence with previous studies we can conclude that opal fluxes in sediments are better recorded by $^{231}\text{Pa}_{\text{xs}}$ than by ^{10}Be . At locations where opal and lithogenic fluxes are predominant, ^{10}Be could be used for tracing the total particle fluxes.

The compound-specific information about $^{231}\text{Pa}_{\text{xs}}/^{230}\text{Th}_{\text{xs}}$ and $^{10}\text{Be}/^{230}\text{Th}_{\text{xs}}$, which we determined here, showed the potential to trace the origin of an isotopic signature better than the previously accessible bulk isotope ratios. This allows to a certain extent to discriminate between signals of remote origin, and local signals from surface waters.

Chapter 6

Conclusions and Perspectives

Grain size and component specific isotope analyses reveal that the association of $^{230}\text{Th}_{\text{xs}}$ with sediment particles is heterogeneously distributed among the distinct particles types. $^{230}\text{Th}_{\text{xs}}$ is preferentially associated with the smallest particles (including clay minerals), less strongly with the silt- to sand-sized carbonate particles, and lowest concentrations have been found in the silt- to sand-sized biogenic opal and ice-rafted particles. Therefore, in sediments where biogenic opal is the main component (the Southern Ocean study site), $^{230}\text{Th}_{\text{xs}}$ is strongly concentrated within the clay size class. In contrast, the size specific distribution of ^{230}Th is found to be less pronounced at locations where carbonate is the dominant phase (Panama Basin, Walvis Ridge).

Owing to the grain size dependent distribution, the application of $^{230}\text{Th}_{\text{xs}}$ as a constant flux proxy is likely to be biased by grain size sorting during the particle transport by bottom currents. Information on size-specific $^{230}\text{Th}_{\text{xs}}$ allows correcting for the hypothetically assumed grain size biasing. Generally, at sites of strong sediment focusing, these size corrections lead to lower focusing factors and higher vertical flux rates than those based on bulk $^{230}\text{Th}_{\text{xs}}$ measurements. The grain size correction applied to the Panama Basin sediments suggests that the vertical flux rate during the Last Glacial Maximum may have been significantly higher than based on the bulk $^{230}\text{Th}_{\text{xs}}$ data, and also it may have been significantly higher than during the Holocene. However, the procedure of grain size correction itself remains speculative as long as we are unable to precisely determine the grain size fraction that has experienced lateral transport. Detailed information on the sedimentology at the Southern Ocean study site suggests a maximum particle size of 140 to 300 μm for lateral transport. Based on this grain size information, the resulting grain size corrections of the focusing factors and vertical flux rates are insignificant for this study site. This grain size-biasing in flux calculations introduced by using $^{230}\text{Th}_{\text{xs}}$ -normalized fluxes is low compared to sediment flux rates that have not been $^{230}\text{Th}_{\text{xs}}$ -normalized. Therefore, despite the error introduced to $^{230}\text{Th}_{\text{xs}}$ inventories by particle sorting, the $^{230}\text{Th}_{\text{xs}}$ -approach as constant flux proxy is still regarded as a valuable method for unraveling sediment redistribution.

Generally, it is recommended for future investigations to extend the data set of component specific ^{230}Th analyses. First of all, this study provides a relatively small data set and therefore, it should be tested by further similar analyses if the results and conclusions made in this study are reproducible for other marine sediment types and at other locations. A larger data set on component-specific $^{230}\text{Th}_{\text{xs}}$ combined with detailed grain size analyses by laser diffraction will help to characterize the controlling mechanisms (intensity of currents, changes in the source areas of sediment supply) on sediment redistribution and $^{230}\text{Th}_{\text{xs}}$ distribution. Such an investigation will help in understanding the mechanisms of sediment focusing and lateral particle transport, and will give insight into the past ocean circulation.

The relationship between clay and $^{230}\text{Th}_{\text{xs}}$ implies that the source and composition of advected material is the strongest control on $^{230}\text{Th}_{\text{xs}}$ accumulation. The flux and deposition of clay controls the $^{230}\text{Th}_{\text{xs}}$ inventory at the site of interest. For the Southern Ocean study site, this study reveals that the clay mineral ratio (chlorite/smectite) closely resembles the $^{230}\text{Th}_{\text{xs}}$ -focusing factor. As chlorite and smectite have contrasting source areas (distant versus local source), the $^{230}\text{Th}_{\text{xs}}$ -focusing factor is interpreted being a function of the climate induced change in ocean circulation. The observation for the Southern Ocean study site gives reason to a new explanation of the high focusing factors found in the Panama Basin sediments. There, resuspended $^{230}\text{Th}_{\text{xs}}$ -rich clays are scavenged from the benthic nepheloid layer by sinking organic particles, explaining high $^{230}\text{Th}_{\text{xs}}$ deposition during times of high biological production i.e. higher vertical particle fluxes. As a future perspective, a combined approach of clay mineral analyses and size/component specific $^{230}\text{Th}_{\text{xs}}$ analyses is expected to bear great potential for tracing transport pathways of $^{230}\text{Th}_{\text{xs}}$. In the case of the Panama Basin sediments this would be of highest interest. This approach, either by indirect methods (correlation statistics) or direct measurement (component specific $^{230}\text{Th}_{\text{xs}}$ analysis on isolated clay minerals) could ultimately determine the origin of the high $^{230}\text{Th}_{\text{xs}}$ signal in the Panama Basin sediments.

Inventories of deep-sea sediment components vary substantially even between proximate locations. The comparison of twin cores revealed higher authigenic uranium concentrations at sites of stronger sediment focusing. This may result from either a selective deposition of organic matter or variations in the preservation of organic carbon during early diagenesis, processes that make authigenic uranium not suitable for reconstructing the past variations in biological ocean productivity. As an alternative, isotope ratios such as $^{231}\text{Pa}_{\text{xs}}/^{230}\text{Th}_{\text{xs}}$ and $^{10}\text{Be}/^{230}\text{Th}_{\text{xs}}$ are insensitive to early diagenesis, and therefore, are more reliable in tracing past export productivity. This study supports the use of those isotope ratios, because it is shown that after burial the isotopes remain associated with the particle phases which scavenged them from the water column. A strong association of ^{231}Pa and ^{10}Be with opal-rich particles is opposed to the strong affinity of ^{230}Th to adsorb onto lithogenic particles. Further, the isotope ratios $^{231}\text{Pa}/^{230}\text{Th}$ and $^{10}\text{Be}/^{230}\text{Th}$ are found to be insensitive to the intensity of sediment focusing. This remains to be tested for winnowing locations.

Size and component specific isotope ratios have the potential to trace the origin of an isotopic signature better than bulk isotope ratios. For instance, ratios in opal may better reflect the surface water derived isotope signals, whereas clay minerals may better reflect deep water signals advected from remote origins. This observation raises the question if the reversible scavenging model holds true for the biogenic opal particles. If particle reactive trace elements are incorporated into opal by entrapment during the biogenic SiO_2 -formation this trace element

fraction is potentially not subject to a reversible adsorption/desorption-process. Isotope ratios in opal tests may reflect the surface water conditions during the growth of diatoms rather than the kinetic equilibrium with the deep water shortly before deposition, or may be the result of a mixture of both sources. Improved methods of particle separation and the purification of sediment phases combined with advanced analytical techniques would substantially improve our understanding in this field. This study showed that isolation of particle classes needs to be carefully carried out in order to not affect the fraction of isotopes that is adsorbed on the particle surfaces. In the case of biogenic SiO_2 , an advanced purification method is required that minimizes the artificial effect of the fractionation procedure on the adsorbed isotopes. In combination with a subsequent measurement on a laser ablation-multicollector-ICP-MS it is expected that $^{231}\text{Pa}_{\text{xs}}/^{230}\text{Th}_{\text{xs}}$ -analyses on cleansed opal samples would help to better constrain the origin of the sedimentary $^{231}\text{Pa}_{\text{xs}}/^{230}\text{Th}_{\text{xs}}$ signal. A detailed understanding of the $^{231}\text{Pa}_{\text{xs}}/^{230}\text{Th}_{\text{xs}}$ signal related to opal particles could hold the potential for a quantitative calibration of $^{231}\text{Pa}_{\text{xs}}/^{230}\text{Th}_{\text{xs}}$ as a proxy for past opal fluxes, which in turn would give insight into the past biological production in oceans of the high latitudes, where opal production forms the major contribution to the biogenic sediment.

References

- Ackermann, F., H. Bergmann, and U. Schleichert (1983), Monitoring of heavy metals in coastal and estuarine sediments - a question of grain-size: <20 μm versus >60 μm , *Environmental Technology*, 4(7), 317 - 328.
- Anderson, R. F., M. P. Bacon, and P. G. Brewer (1983a), Removal of ^{230}Th and ^{231}Pa at ocean margins, *Earth and Planetary Science Letters*, 66, 73-90.
- Anderson, R. F., M. P. Bacon, and P. G. Brewer (1983b), Removal of ^{230}Th and ^{231}Pa from the open ocean, *Earth and Planetary Science Letters*, 62(1), 7-23.
- Anderson, R. F., Y. Lao, W. S. Broecker, S. E. Trumbore, H. J. Hofmann, and W. Wölfli (1990), Boundary Scavenging in the Pacific Ocean - A Comparison of ^{10}Be and ^{231}Pa , *Earth and Planetary Science Letters*, 96(3-4), 287-304.
- Anderson, R. F., N. Kumar, R. A. Mortlock, P. N. Froelich, P. Kubik, B. Dittrich-Hannen, and M. Suter (1998), Late-Quaternary changes in productivity of the Southern Ocean, *Journal of Marine Systems*, 17(1-4), 497-514.
- Anderson, R. F., Z. Chase, M. Q. Fleisher, and J. Sachs (2002), The Southern Ocean's biological pump during the Last Glacial Maximum, *Deep Sea Research Part II: Topical Studies in Oceanography*, 49(9-10), 1909-1938.
- Anderson, R. F. (2004), Chemical Tracers of Particle Transport, in *Treatise on Geochemistry*, edited by H. Holland, D. and K. Turekian, K. , pp. 247-273, *The Oceans and Marine Geochemistry*, series edited by H. Elderfield, Pergamon, Oxford.
- Anderson, R. F., S. Ali, L. I. Bradtmiller, S. H. H. Nielsen, M. Q. Fleisher, B. E. Anderson, and L. H. Burckle (2009), Wind-Driven Upwelling in the Southern Ocean and the Deglacial Rise in Atmospheric CO_2 , *Science*, 323(5920), 1443-1448, doi: 10.1126/science.1167441.
- Asmus, T., M. Frank, C. Koschmieder, N. Frank, R. Gersonde, G. Kuhn, and A. Mangini (1999), Variations of biogenic particle flux in the southern Atlantic section of the Subantarctic Zone during the late Quaternary: Evidence from sedimentary $^{231}\text{Pa}_{\text{ex}}$ and $^{230}\text{Th}_{\text{ex}}$, *Marine Geology*, 159(1-4), 63-78.
- Asper, V. L., S. Honjo, and T. H. Orst (1992), Distribution and transport of marine snow aggregates in the Panama Basin, *Deep Sea Research*, 39(6), 939-952.
- Bacon, M. P., and R. F. Anderson (1982), Distribution of Thorium Isotopes between Dissolved and Particulate Forms in the Deep-Sea, *Journal of Geophysical Research-Oceans and Atmospheres*, 87(NC3), 2045-2056.
- Bacon, M. P. (1984), Glacial to Interglacial Changes in Carbonate and Clay Sedimentation in the Atlantic-Ocean Estimated from Th-230 Measurements, *Isotope Geoscience*, 2(2), 97-111.
- Bacon, M. P., C.-A. Huh, A. P. Fleer, and W. G. Deuser (1985), Seasonality in the flux of natural radionuclides and plutonium in the deep Sargasso Sea, *Deep Sea Research Part A. Oceanographic Research Papers*, 32(3), 273-286.
- Baker, E. T., and R. A. Feely (1978), Chemistry of Oceanic Particulate Matter and Sediments: Implications for Bottom Sediment Resuspension, *Science*, 200(4341), 533-535, doi: 10.1126/science.200.4341.533.
- Barbanti, A., and M. H. Bothner (1993), A procedure for partitioning bulk sediments into distinct grain-size fractions for geochemical analysis, *Environmental Geology*, 21(1), 3-13.

- Barber, M., and D. Crane (1995), Current Flow in the North-West Weddell Sea, *Antarctic Science*, 7(1), 39-50.
- Barg, E., D. Lal, M. J. Pavich, M. W. Caffee, and J. R. Southon (1997), Beryllium geochemistry in soils: evaluation of $^{10}\text{Be}/^9\text{Be}$ ratios in authigenic minerals as a basis for age models, *Chemical Geology*, 140(3-4), 237-258.
- Beaulieu, S. E. (2002), Accumulation and fate of phytodetritus on the sea floor, in *Oceanography and Marine Biology, Vol 40*, edited, pp. 171-232, *Oceanography and Marine Biology*, series edited, Taylor & Francis Ltd, London.
- Beaulieu, S. E. (2003), Resuspension of phytodetritus from the sea floor: A laboratory flume study, *Limnology and Oceanography*, 48, 1235-1244.
- Beer, J., A. Blinov, G. Bonani, R. C. Finkel, H. J. Hofmann, B. Lehmann, H. Oeschger, A. Sigg, J. Schwander, T. Staffelbach, B. Stauffer, M. Suter, and W. Wotfli (1990), Use of ^{10}Be in polar ice to trace the 11-year cycle of solar activity, *Nature*, 347(6289), 164-166.
- Behrenfeld, M. J., and P. G. Falkowski (1997), Photosynthetic rates derived from satellite-based chlorophyll concentration, *Limnology and Oceanography*, 42(1), 1-20.
- Beuselinck, L., G. Govers, J. Poesen, G. Degraer, and L. Froyen (1998), Grain-size analysis by laser diffractometry: comparison with the sieve-pipette method, *CATENA*, 32(3-4), 193-208.
- Bianchi, G. G., and I. N. McCave (2000), Hydrography and sedimentation under the deep western boundary current on Björn and Gardar Drifts, Iceland Basin, *Marine Geology*, 165(1-4), 137-169.
- Biscaye, P. E., and S. L. Eitrem (1977), Suspended particulate loads and transports in the nepheloid layer of the abyssal Atlantic Ocean, *Marine Geology*, 23(1-2), 155-172.
- Blott, S. J., D. J. Croft, K. Pye, S. E. Saye, and H. E. Wilson (2004), Particle size analysis by laser diffraction, *Geological Society, London, Special Publications*, 232(1), 63-73, doi: 10.1144/gsl.sp.2004.232.01.08.
- Bourdon, B., S. P. Turner, G. M. Henderson, and C. C. Lundstrom (2003), Introduction to U-series Geochemistry, in *Uranium-Series Geochemistry*, edited by B. Bourdon, G. M. Henderson, C. C. Lundstrom and S. P. Turner, pp. 1-21, *Reviews in Mineralogy & Geochemistry*, series edited by J. J. Rosso and P. H. Ribbe, Mineralogical Society of America, Washington.
- Bourles, D. L., G. Klinkhammer, A. C. Campbell, C. I. Measures, E. T. Brown, and J. M. Edmond (1989a), Beryllium in marine pore waters: geochemical and geochronological implications, *Nature*, 341(6244), 731-733.
- Bourles, D. L., G. M. Raisbeck, and F. Yiou (1989b), ^{10}Be and ^9Be in marine sediments and their potential for dating, *Geochimica Et Cosmochimica Acta*, 53(2), 443-452.
- Boyle, E. A. (1992), Cadmium and delta13C Paleochemical Ocean Distributions During the Stage 2 Glacial Maximum, *Annual Review of Earth and Planetary Sciences*, 20(1), 245-287, doi: doi:10.1146/annurev.earth.20.050192.001333.
- Bradt Miller, L. I., R. F. Anderson, M. Q. Fleisher, and L. H. Burckle (2007), Opal burial in the equatorial Atlantic Ocean over the last 30 ka: Implications for glacial-interglacial changes in the ocean silicon cycle, *Paleoceanography*, 22(4), PA4216.
- Bradt Miller, L. I., R. F. Anderson, M. Q. Fleisher, and L. H. Burckle (2009), Comparing glacial and Holocene opal fluxes in the Pacific sector of the Southern Ocean, *Paleoceanography*, 24(2), PA2214.
- Broecker, W. (2008), Excess sediment ^{230}Th : Transport along the sea floor or enhanced water column scavenging?, *Global Biogeochemical Cycles*, 22.

- Broecker, W., E. Clark, and S. Barker (2008), Near constancy of the Pacific Ocean surface to mid-depth radiocarbon-age difference over the last 20 kyr, *Earth and Planetary Science Letters*, 274, 322-326.
- Brunauer, S., P. H. Emmett, and E. Teller (1938), Adsorption of Gases in Multimolecular Layers, *Journal of the American Chemical Society*, 60(2), 309-319.
- Chase, Z., R. F. Anderson, and M. Q. Fleisher (2001), Evidence from Authigenic Uranium for Increased Productivity of the Glacial Subantarctic Ocean, *Paleoceanography*, 16(5), 468-478.
- Chase, Z., R. F. Anderson, M. Q. Fleisher, and P. W. Kubik (2002), The influence of particle composition and particle flux on scavenging of Th, Pa and Be in the ocean, *Earth and Planetary Science Letters*, 204(1-2), 215-229.
- Chase, Z., R. F. Anderson, M. Q. Fleisher, and P. W. Kubik (2003), Scavenging of ^{230}Th , ^{231}Pa and ^{10}Be in the Southern Ocean (SW Pacific sector): the importance of particle flux, particle composition and advection *Deep Sea Research Part II: Topical Studies in Oceanography*, 50(3-4), 739-768.
- Chase, Z., and R. F. Anderson (2004), Comment on "On the importance of opal, carbonate, and lithogenic clays in scavenging and fractionating ^{230}Th , ^{231}Pa and ^{10}Be in the ocean" by S. Luo and T.-L. Ku, *Earth and Planetary Science Letters*, 220(1-2), 213-222.
- Chase, Z. (2008), Sediment Signatures of U- and Th-Series Nuclides and their Application as Paleoceanographic Tracers, in *U-Th Series Nuclides in Aquatic Systems*, edited by S. Krishnaswami and J. K. Cochran, pp. 383-416, *Radioactivity in the Environment*, series edited by M. Baxter, Elsevier.
- Christl, M., A. Mangini, and P. W. Kubik (2007), Highly resolved Beryllium-10 record from ODP Site 1089 - A global signal?, *Earth and Planetary Science Letters*, 257(1-2), 245-258.
- Christl, M., J. Lippold, F. Steinhilber, F. Bernsdorff, and A. Mangini (2010), Reconstruction of global ^{10}Be production over the past 250 ka from highly accumulating Atlantic drift sediments, *Quaternary Science Reviews*, 29(19-20), 2663-2672.
- Cochran, J. K. (1992), The oceanic chemistry of the uranium and thorium series nuclides., in *Uranium-series disequilibrium; Applications to earth, marine, and environmental sciences*, edited by M. Ivanovich and R. S. Harmon, pp. 334-395, series edited.
- Dezileau, L., G. Bareille, J. L. Reyss, and F. Lemoine (2000), Evidence for strong sediment redistribution by bottom currents along the southeast Indian ridge, *Deep Sea Research Part I: Oceanographic Research Papers*, 47, 1899-1936.
- Dickson, R. R., and I. N. McCave (1986), Nepheloid layers on the continental slope west of Porcupine Bank, *Deep Sea Research Part A. Oceanographic Research Papers*, 33(6), 791-818.
- Diekmann, B., and R. Petschick (1996), Clay mineralogy of sediment core PS1768-8, PANGAEA, <http://doi.pangaea.de/10.1594/PANGAEA.51425>
- Diekmann, B., R. Petschick, F. X. Gingele, D. K. Fütterer, A. Abelmann, U. Brathauer, R. Gersonde, and A. Mackensen (1996), Clay mineral fluctuations in Late Quaternary sediments of the southeastern South Atlantic: Implications for past changes of deep water advection, in *South Atlantic - Present and Past Circulation*, edited by G. Wefer, W. H. Berger, G. Siedler and D. J. Webb, pp. 621-644, series edited, Springer-Verlag Berlin, Berlin.
- Diekmann, B., and G. Kuhn (1999), Provenance and dispersal of glacial-marine surface sediments in the Weddell Sea and adjoining areas, Antarctica: ice-rafting versus current transport, *Marine Geology*, 158(1-4), 209-231.

- Diekmann, B., D. Fütterer, H. Grobe, C.-D. Hillenbrand, G. Kuhn, K. Michels, R. Petschick, and M. Pirrung (2003), Terrigenous sediment supply in the polar to temperate South Atlantic: Land-ocean links of environmental changes during the late quaternary, in *The South Atlantic in the Late Quaternary. Reconstructions of Material Budgets and Current Systems.*, edited by G. Wefer, S. Mulitza and V. Ratmeyer, pp. 375-399, series edited, Springer, Berlin.
- Duplessy, J. C., L. Labeyrie, M. Paterne, S. Hovine, T. Fichefet, J. Duprat, and M. Labracherie (1996), High latitude deep water sources during the last glacial maximum and the intensity of the global oceanic circulation, in *South Atlantic - Present and Past Circulation*, edited by G. Wefer, W. H. Berger, G. Siedler and D. J. Webb, pp. 445-460, series edited, Springer-Verlag Berlin, Berlin 33.
- Dutay, J. C., F. Lacan, M. Roy-Barman, and L. Bopp (2009), Influence of particle size and type on ^{231}Pa and ^{230}Th simulation with a global coupled biogeochemical-ocean general circulation model: A first approach, *Geochemistry Geophysics Geosystems*, 10, Q01011, doi: 10.1029/2008GC002291.
- Egbert, G. D., R. D. Ray, and B. G. Bills (2004), Numerical modeling of the global semidiurnal tide in the present day and in the last glacial maximum, *J. Geophys. Res.*, 109(C3), C03003.
- Eglinton, T. I., B. C. Benitez-Nelson, A. Pearson, A. P. McNichol, J. E. Bauer, and E. R. M. Druffel (1997), Variability in Radiocarbon Ages of Individual Organic Compounds from Marine Sediments, *Science*, 277(5327), 796-799, doi: 10.1126/science.277.5327.796.
- Fahrbach, E., S. Harms, G. Rohardt, M. Schröder, and R. A. Woodgate (2001), Flow of bottom water in the northwestern Weddell Sea, *J. Geophys. Res.*, 106.
- Finkel, R., S. Krishnaswami, and D. L. Clark (1977), ^{10}Be in Arctic Ocean sediments, *Earth and Planetary Science Letters*, 35(2), 199-204.
- Fischer, G., and G. Karakas (2009), Sinking rates and ballast composition of particles in the Atlantic Ocean: implications for the organic carbon fluxes to the deep ocean, *Biogeosciences*, 6(1), 85-102.
- Förstner, U. (2004), Traceability of sediment analysis, *TrAC Trends in Analytical Chemistry*, 23(3), 217-236.
- François, R., M. A. Altabet, E.-F. Yu, D. M. Sigman, M. P. Bacon, M. Frank, G. Bohrmann, G. Bareille, and L. D. Labeyrie (1997), Contribution of Southern Ocean surface-water stratification to low atmospheric CO_2 concentrations during the last glacial period, *Nature*, 389(6654), 929-935.
- François, R., M. P. Bacon, and D. O. Suman (1990), Thorium-230 Profiling in Deep-Sea Sediments: High-Resolution Records of Flux and Dissolution of Carbonate in the Equatorial Atlantic During the Last 24,000 Years, *Paleoceanography*, 5(5), 761-787.
- François, R., M. P. Bacon, M. A. Altabet, and L. D. Labeyrie (1993), Glacial/Interglacial Changes in Sediment Rain Rate in the SW Indian Sector of Subantarctic Waters as Recorded by ^{230}Th , ^{231}Pa , U, and $\delta^{15}\text{N}$, *Paleoceanography*, 8(5), 611-629.
- François, R., M. Frank, M. M. Rutgers van der Loeff, and M. P. Bacon (2004), ^{230}Th normalization: An essential tool for interpreting sedimentary fluxes during the late Quaternary *Paleoceanography*, 19, doi:10.1029/2003PA000939.
- François, R., M. Frank, M. Rutgers van der Loeff, M. P. Bacon, W. Geibert, S. Kienast, R. F. Anderson, L. Bradtmiller, Z. Chase, G. Henderson, F. Marcantonio, and S. E. Allen (2007), Comment on "Do geochemical estimates of sediment focusing pass the sediment test in the equatorial Pacific?" by M. Lyle et al, *Paleoceanography*, 22.

- Frank, M., A. Eisenhauer, W. J. Bonn, P. Walter, H. Grobe, P. W. Kubik, B. Dittrich-Hannen, and A. Mangini (1995), Sediment redistribution versus paleoproductivity change: Weddell Sea margin sediment stratigraphy and biogenic particle flux of the last 250,000 years deduced from $^{230}\text{Th}_{\text{ex}}$, ^{10}Be and biogenic barium profiles, *Earth and Planetary Science Letters*, 136(3-4), 559-573.
- Frank, M., A. Mangini, R. Gersonde, M. Rutgers van der Loeff, and G. Kuhn (1996), Late Quaternary sediment dating and quantification of lateral sediment redistribution applying $^{230}\text{Th}_{\text{ex}}$: a study from the eastern Atlantic sector of the Southern Ocean, *Geologische Rundschau*, 85(3), 554-566.
- Frank, M., B. Schwarz, S. Baumann, P. W. Kubik, M. Suter, and A. Mangini (1997), A 200 kyr record of cosmogenic radionuclide production rate and geomagnetic field intensity from ^{10}Be in globally stacked deep-sea sediments, *Earth and Planetary Science Letters*, 149(1-4), 121-129.
- Frank, M., R. Gersonde, and A. Mangini (1999), Sediment Redistribution, $^{230}\text{Th}_{\text{ex}}$ -Normalization and Implications for the Reconstruction of Particle Flux and Export Paleoproductivity, in *Use of Proxies in Paleoceanography: Examples from the South Atlantic*, edited by F. G. and G. Wefer, pp. 409-426, series edited, Springer, Berlin Heidelberg.
- Frank, M. (2000), Comparison of cosmogenic radionuclide production and geomagnetic field intensity over the last 200 000 years, *Phil. Trans R. Soc. Lond. A*, 358(1768), 1089-1107.
- Frank, M., R. Gersonde, M. Rutgers van der Loeff, G. Bohrmann, C. C. Nürnberg, P. Kubik, M. Suter, and A. Mangini (2000a), Similar glacial and interglacial export bioproductivity in the Atlantic sector of the Southern Ocean: Multiproxy evidence and implications for glacial atmospheric CO_2 , *Paleoceanography*, 15(6), 642-658.
- Frank, M., R. Gersonde, M. Rutgers van der Loeff, G. Bohrmann, C. C. Nürnberg, P. Kubik, M. Suter, and A. Mangini (2000b), Radionuclids in sediment core PS1768-8, PANGAEA, <http://doi.pangaea.de/10.1594/PANGAEA.57487>
- Frank, M., M. M. Rutgers van der Loeff, P. W. Kubik, and A. Mangini (2002), Quasi-conservative behaviour of ^{10}Be in deep waters of the Weddell Sea and the Atlantic sector of the Antarctic Circumpolar Current, *Earth and Planetary Science Letters*, 201(1), 171-186.
- Frank, M., J. Backman, M. Jakobsson, K. Moran, M. O'Regan, J. King, B. A. Haley, P. W. Kubik, and D. Garbe-Schönberg (2008), Beryllium isotopes in central Arctic Ocean sediments over the past 12.3 million years: Stratigraphic and paleoclimatic implications, *Paleoceanography*, 23(1), PA1S02.
- Freeman, S., P. Bishop, C. Bryant, G. Cook, D. Dougans, T. Ertunc, A. Fallick, R. Ganeshram, C. Maden, P. Naysmith, C. Schnabel, M. Scott, M. Summerfield, and S. Xu (2007), The SUERC AMS laboratory after 3 years, *Nuclear Instruments and Methods in Physics Research Section B: Beam Interactions with Materials and Atoms*, 259(1), 66-70.
- Freudenthal, T., S. Neuer, H. Meggers, R. Davenport, and G. Wefer (2001), Influence of lateral particle advection and organic matter degradation on sediment accumulation and stable nitrogen isotope ratios along a productivity gradient in the Canary Islands region, *Marine Geology*, 177(1-2), 93-109.
- Gardner, W. D., J. B. Southard, and C. D. Hollister (1985), Sedimentation, resuspension and chemistry of particles in the northwest Atlantic, *Marine Geology*, 65(3-4), 199-242.
- Geibert, W., and R. Usbeck (2004), Adsorption of thorium and protactinium onto different particle types: experimental findings, *Geochimica Et Cosmochimica Acta*, 68(7), 1489-1501.

- Geibert, W., M. M. Rutgers van der Loeff, R. Usbeck, R. Gersonde, G. Kuhn, and J. Seeberg-Elverfeldt (2005), Quantifying the opal belt in the Atlantic and southeast Pacific sector of the Southern Ocean by means of ^{230}Th normalization, *Global Biogeochemical Cycles*, 19(4), GB4001, doi: doi: 10.1029/2005GB002465.
- Geibert, W. (2008), Charts of the ^{238}U , ^{235}U , ^{232}Th , and ^{241}Am Decay Series with Principal Modes of Decay, their Intensities and Energies, in *U-Th Series Nuclides in Aquatic Systems*, edited by S. Krishnaswami and J. K. Cochran, pp. 417-423, *Radioactivity in the Environment*, series edited by M. Baxter, Elsevier.
- Gersonde, R., and G. Hempel (1990), Die Expedition ANTARKTIS-VIII/3 und VIII/4 mit FS "Polarstern" 1989, *Berichte zur Polarforschung*, 74, 173 pp.
- Gersonde, R., D. A. Hodell, P. Blum, and e. al. (1999), Proceedings ODP, Initial Reports, 177 [Online]. available from World Wide Web: <http://www-odp.tamu.edu/publications/177_IR/177TOC.HTM> [cited 2010-08-08].
- Goel, P. S. (1969), Production Rate of ^{10}Be from Oxygen Spallation, *Nature*, 223(5212), 1263-1264.
- Gorsline, D. S. (1984), A review of fine-grained sediment origins, characteristics, transport and deposition, in *Fine-grained Sediments: Deep-Water Processes and Facies*, edited by D. A. V. Stow and D. J. W. Piper, pp. 17-34, series edited, Blackwell Scientific Publications, Oxford.
- Grobe, H., and A. Mackensen (1992), Late Quaternary climatic cycles as recorded in sediments from the Antarctic continental margin, in *Antarctic Research Series*, edited by J. P. Kennett and D. Warnke, pp. 349-376, *The Antarctic Paleoenvironment: a perspective on Global Change*, series edited.
- Gross, T. F., A. J. Williams, and A. R. M. Newell (1988), A deep-sea sediment transport storm, *Nature*, 331, 518-521, doi: doi:10.1038/331518a0.
- Guihou, A., S. Pichat, S. Nave, A. Govin, L. Labeyrie, E. Michel, and C. Waelbroeck (2010), Late slowdown of the Atlantic Meridional Overturning Circulation during the Last Glacial Inception: New constraints from sedimentary ($^{231}\text{Pa}/^{230}\text{Th}$), *Earth and Planetary Science Letters*, 289(3-4), 520-529.
- Guo, L. D., M. Chen, and C. Gueguen (2002), Control of Pa/Th ratio by particulate chemical composition in the ocean, *Geophysical Research Letters*, 29(20), doi: 10.1029/2002GL015666, doi: doi: 10.1029/2002GL015666.
- Hansen, R. G., and E. J. Ring (1983), *The Preparation and Certification of a Uranium reference material*, 8 pp., Council for Mineral Technology, Randburg, South Africa.
- Henderson, G. M., C. Heinze, R. F. Anderson, and A. M. E. Winguth (1999), Global distribution of the ^{230}Th flux to ocean sediments constrained by GCM modelling, *Deep Sea Research Part I: Oceanographic Research Papers*, 46(11), 1861-1893.
- Henderson, G. M., and R. F. Anderson (2003), The U-series toolbox for paleoceanography, in *Uranium-Series Geochemistry*, edited by B. Bourdon, G. M. Henderson, C. C. Lundstrom and S. P. Turner, pp. 493-531, *Reviews in Mineralogy & Geochemistry*, series edited by J. J. Rosso and P. H. Ribbe, Mineralogical Society of America, Washington.
- Henderson, G. M., R. F. Anderson, J. Adkins, P. Andersson, E. A. Boyle, G. Cutter, H. de Baar, A. Eisenhauer, M. Frank, R. Francois, K. Orians, T. Gamo, C. German, W. Jenkins, J. Moffett, C. Jeandel, T. Jickells, S. Krishnaswami, D. Mackey, C. I. Measures, J. K. Moore, A. Oschlies, R. Pollard, M. R. D. van der Loeff, R. Schlitzer, M. Sharma, K. von Damm, J. Zhang, and P. Masque (2007), GEOTRACES - An international study of the global marine biogeochemical cycles of trace elements and their isotopes, *Chemie Der Erde-Geochemistry*, 67(2), 85-131.

- Henken-Mellies, W. U., J. Beer, F. Heller, K. J. Hsü, C. Shen, G. Bonani, H. J. Hofmann, M. Suter, and W. Wölfli (1990), ^{10}Be and ^9Be in South Atlantic DSDP Site 519: Relation to geomagnetic reversals and to sediment composition, *Earth and Planetary Science Letters*, 98(3-4), 267-276.
- Higgins, S. M., R. F. Anderson, F. Marcantonio, P. Schlosser, and M. Stute (2002), Sediment focusing creates 100-ka cycles in interplanetary dust accumulation on the Ontong Java Plateau, *Earth and Planetary Science Letters*, 203(1), 383-397.
- Hollister, C. D., and I. N. McCave (1984), Sedimentation under deep-sea storms, *Nature*, 309, 220-225, doi: 10.1038/309220a0.
- Holmes, M. E., C. Eichner, U. Struck, and G. Wefer (1999), Reconstruction of Surface Ocean Nitrate Utilization Using Stable Nitrogen Isotopes in Sinking Particles and Sediments, in *Use of Proxies in Paleoceanography: Examples from the South Atlantic*, edited by G. Fischer and G. Wefer, pp. 447-468, series edited, Springer, Berlin Heidelberg.
- Honjo, S. (1982), Seasonality and interaction of biogenic and lithogenic particulate flux at the Panama Basin, *Science*, 218, 883-884.
- Honjo, S., D. W. Spencer, and J. W. Farrington (1982), Deep advective transport of lithogenic particles in Panama Basin, *Science*, 216, 516-518.
- Horwitz, E. P., R. Chiarizia, M. L. Dietz, H. Diamond, and D. M. Nelson (1993), Separation and preconcentration of actinides from acidic media by extraction chromatography, *Analytica Chimica Acta*, 281(2), 361-372.
- Howe, J. A., and C. J. Pudsey (1999), Antarctic circumpolar deep water: A Quaternary paleoflow record from the northern Scotia Sea, South Atlantic ocean, *Journal of Sedimentary Research*, 69(4), 847-861.
- ISO9277 Determination of the specific surface area of solids by gas adsorption - BET method.
- Kienast, S. S., M. Kienast, A. C. Mix, S. E. Calvert, and R. François (2007), Thorium-230 normalized particle flux and sediment focusing in the Panama Basin region during the last 30,000 years, *Paleoceanography*, 22.
- Klein, C., J. D. Dana, and C. S. Hurlbut (1985), *Manual of mineralogy (after James D. Dana)*, Wiley, New York.
- Knox, F., and M. B. McElroy (1984), Changes in Atmospheric CO_2 : Influence of the Marine Biota at High Latitude, *Journal of Geophysical Research*, 89(D3), 4629-4637.
- Kohfeld, K. E., R. F. Anderson, and J. Lynch-Stieglitz (2000), Carbon Isotopic Disequilibrium in Polar Planktonic Foraminifera and Its Impact on Modern and Last Glacial Maximum Reconstructions, *Paleoceanography*, 15(1), 53-64.
- Konert, M., and J. Vandenberghe (1997), Comparison of laser grain size analysis with pipette and sieve analysis: A solution for the underestimation of the clay fraction, *Sedimentology*, 44(3), 523-535.
- Koopmann, C., and A. Prange (1991), Multielement determination in sediments from the German Wadden Sea--investigations on sample preparation techniques, *Spectrochimica Acta Part B: Atomic Spectroscopy*, 46(10), 1395-1402.
- Köster, E. (1964), *Granulometrische und morphometrische Meßmethoden an Mineralkörnern, Steinen und sonstigen Stoffen*, 336 pp., Ferdinand Enke Verlag, Stuttgart.
- Kretschmer, S., W. Geibert, M. M. Rutgers van der Loeff, and G. Mollenhauer (2010), Grain size effects on $^{230}\text{Th}_{\text{xs}}$ inventories in opal-rich and carbonate-rich marine sediments, *Earth and Planetary Science Letters*, 294(1-2), 131-142.

- Ku, T. L., M. Kusakabe, C. I. Measures, J. R. Southon, G. Cusimano, J. S. Vogel, D. E. Nelson, and S. Nakaya (1990), Beryllium isotope distribution in the western North Atlantic: a comparison to the Pacific, *Deep Sea Research Part A. Oceanographic Research Papers*, 37(5), 795-808.
- Kuhn, G., and B. Diekmann (2002), Late Quaternary variability of ocean circulation in the southeastern South Atlantic inferred from the terrigenous sediment record of a drift deposit in the southern Cape Basin (ODP Site 1089), *Palaeogeography, Palaeoclimatology, Palaeoecology*, 182(3-4), 287-303.
- Kumar, N., R. Gwiazda, R. F. Anderson, and P. N. Froelich (1993), $^{231}\text{Pa}/^{230}\text{Th}$ ratios in sediments as a proxy for past changes in Southern Ocean productivity, *Nature*, 362(6415), 45-48.
- Kumar, N., R. F. Anderson, R. A. Mortlock, P. N. Froelich, P. Kubik, B. Dittrich-Hannen, and M. Suter (1995), Increased biological productivity and export production in the glacial Southern Ocean, *Nature*, 378(6558), 675-680.
- Kusakabe, M., T. L. Ku, J. Vogel, J. R. Southon, D. E. Nelson, and G. Richards (1982), ^{10}Be profiles in seawater, *Nature*, 299(5885), 712-714.
- Kusakabe, M., T. L. Ku, J. R. Southon, J. S. Vogel, D. E. Nelson, C. I. Measures, and Y. Nozaki (1987), Distribution of ^{10}Be and ^9Be in the Pacific Ocean, *Earth and Planetary Science Letters*, 82(3-4), 231-240.
- Kusch, S., T. I. Eglinton, A. C. Mix, and G. Mollenhauer (2010), Timescales of lateral sediment transport in the Panama Basin as revealed by radiocarbon ages of alkenones, total organic carbon and foraminifera, *Earth and Planetary Science Letters*, 290(3-4), 340-350.
- Laird, N. P. (1971), Panama Basin deep water - properties and circulation, *Journal of Marine Research*, 29(226-234).
- Lal, D., C. Charles, L. Vacher, J. N. Goswami, A. J. T. Jull, L. McHargue, and R. C. Finkel (2006), Paleo-ocean chemistry records in marine opal: Implications for fluxes of trace elements, cosmogenic nuclides (^{10}Be and ^{26}Al), and biological productivity, *Geochimica Et Cosmochimica Acta*, 70(13), 3275-3289.
- Langmuir, D., and J. S. Herman (1980), The mobility of thorium in natural waters at low temperatures, *Geochimica Et Cosmochimica Acta*, 44(11), 1753-1766.
- Lao, Y., R. F. Anderson, W. S. Broecker, S. E. Trumbore, H. J. Hofmann, and W. Wölfli (1992), Transport and burial rates of ^{10}Be and ^{231}Pa in the Pacific Ocean during the Holocene period, *Earth and Planetary Science Letters*, 113(1-2), 173-189.
- Lao, Y., R. F. Anderson, W. S. Broecker, H. J. Hofmann, and W. Wölfli (1993), Particulate fluxes of ^{230}Th , ^{231}Pa , and ^{10}Be in the northeastern Pacific Ocean, *Geochimica Et Cosmochimica Acta*, 57(1), 205-217.
- Ledbetter, M. T. (1986), A Late Pleistocene time-series of bottom-current speed in the Vema Channel, *Palaeogeography, Palaeoclimatology, Palaeoecology*, 53(1), 97-105.
- Lippold, J., J. Grützner, D. Winter, Y. Lahaye, A. Mangini, and M. Christl (2009), Do sedimentary $^{231}\text{Pa}/^{230}\text{Th}$ from the Bermuda Rise monitor past Atlantic Meridional Overturning Circulation?, *Geophysical Research Letters*, 36, L12601, doi: 10.1029/2009GL038068
- Lonsdale, P. (1977), Inflow of bottom water to the Panama Basin, *Deep Sea Research*, 24(12), 1065-1094, doi: 10.1016/0146-6291(77)90514-8.
- Loubere, P., F. Mekik, R. Francois, and S. Pichat (2004), Export fluxes of calcite in the eastern equatorial Pacific from the Last Glacial Maximum to present, *Paleoceanography*, 19.
- Luo, S., and T.-L. Ku (1999), Oceanic $^{231}\text{Pa}/^{230}\text{Th}$ ratio influenced by particle composition and remineralization, *Earth and Planetary Science Letters*, 167(3-4), 183-195.

- Luo, S., and T.-L. Ku (2003), Constraints on deep-water formation from the oceanic distributions of ^{10}Be , *J. Geophys. Res.*, *108*(C5), 3137.
- Luo, S., and T.-L. Ku (2004a), On the importance of opal, carbonate, and lithogenic clays in scavenging and fractionating ^{230}Th , ^{231}Pa and ^{10}Be in the ocean, *Earth and Planetary Science Letters*, *220*(1-2), 201-211.
- Luo, S., and T.-L. Ku (2004b), Reply to Comment on “On the importance of opal, carbonate, and lithogenic clays in scavenging and fractionating ^{230}Th , ^{231}Pa and ^{10}Be in the ocean”, *Earth and Planetary Science Letters*, *220*(1-2), 223-229.
- Lyle, M., N. Mitchell, N. Pisias, A. Mix, J. I. Martinez, and A. Paytan (2005), Do geochemical estimates of sediment focusing pass the sediment test in the equatorial Pacific?, *Paleoceanography*, *20*, PA1005, doi:10.1029/2004PA001019.
- Lyle, M., N. Pisias, A. Paytan, J. I. Martinez, and A. Mix (2007), Reply to comment by R. Francois et al. on “Do geochemical estimates of sediment focusing pass the sediment test in the equatorial Pacific?": Further explorations of ^{230}Th normalization, *Paleoceanography*, *22*.
- Marcantonio, F., R. F. Anderson, M. Stute, N. Kumar, P. Schlosser, and A. Mix (1996), Extraterrestrial ^3He as a tracer of marine sediment transport and accumulation, *Nature*, *383*(6602), 705-707.
- Marcantonio, F., R. F. Anderson, S. M. Higgins, M. Stute, P. Schlosser, and P. Kubik (2001), Sediment focusing in the central equatorial Pacific ocean *Paleoceanography*, *16*(3), 260-267.
- Marcantonio, F., D. J. Thomas, S. Woodard, D. McGee, and G. Winckler (2009), Extraterrestrial ^3He in Paleocene sediments from Shatsky Rise: Constraints on sedimentation rate variability, *Earth and Planetary Science Letters*, *287*(1-2), 24-30.
- Martínez-García, A., A. Rosell-Melé, W. Geibert, R. Gersonde, P. Masqué, V. Gaspari, and C. Barbante (2009), Links between iron supply, marine productivity, sea surface temperature, and CO_2 over the last 1.1 Ma, *Paleoceanography*, *24*, PA1207, doi: 10.1029/2008PA001657.
- McCave, I. N. (1984), Erosion, transport and deposition of fine-grained marine sediments, in *Fine-grained Sediments: Deep-Water Processes and Facies*, edited by D. A. V. Stow and D. J. W. Piper, pp. 35-69, series edited, Blackwell Scientific Publications, Oxford.
- McCave, I. N. (1986), Local and global aspects of the bottom nepheloid layers in the world ocean, *Netherlands Journal of Sea Research*, *20*(2-3), 167-181.
- McCave, I. N., and T. F. Gross (1991), In-situ measurements of particle settling velocity in the deep sea, *Marine Geology*, *99*(3-4), 403-411.
- McCave, I. N., B. Manighetti, and S. G. Robinson (1995), Sortable Silt and Fine Sediment Size/Composition Slicing: Parameters for Palaeocurrent Speed and Palaeoceanography, *Paleoceanography*, *10*.
- McCave, I. N. (2002), PALEOCLIMATE: A Poisoned Chalice?, *Science*, *298*(5596), 1186-1187, doi: 10.1126/science.1076960.
- McCave, I. N. (2005), Deposition from Suspension, in *Encyclopedia of Geology*, edited by R. C. Selley, L. R. M. Cocks and M. J. Malone, pp. 8-17, *Sedimentary Processes*, series edited, Elsevier, Oxford.
- McCave, I. N., and I. R. Hall (2006), Size sorting in marine muds: Processes, pitfalls, and prospects for paleoflow-speed proxies, *Geochem. Geophys. Geosyst.*, *7*, doi: Q10N05, doi:10.1029/2006GC001284.

- McGee, D., F. Marcantonio, J. F. McManus, and G. Winckler, The response of excess ^{230}Th and extraterrestrial ^3He to sediment redistribution at the Blake Ridge, western North Atlantic, *Earth and Planetary Science Letters*, In Press.
- McManus, J. F., R. Francois, J. M. Gherardi, L. D. Keigwin, and S. Brown-Leger (2004), Collapse and rapid resumption of Atlantic meridional circulation linked to deglacial climate changes, *Nature*, 428(6985), 834-837.
- Middag, R., H. J. W. de Baar, P. Laan, P. Cai, and J. C. van Ooijen, Dissolved Manganese in the Atlantic Sector of the Southern Ocean, *Deep Sea Research* (accepted).
- Middleton, R., L. Brown, B. Dezfouly-Arjomandy, and J. Klein (1993), On ^{10}Be standards and the half-life of ^{10}Be , *Nuclear Instruments and Methods in Physics Research Section B: Beam Interactions with Materials and Atoms*, 82(3), 399-403.
- Miller, M. C., I. N. McCave, and P. D. Komar (1977), Threshold of sediment motion under unidirectional currents, *Sedimentology*, 24(4), 507-527.
- Mollenhauer, G., T. I. Eglinton, N. Ohkouchi, R. R. Schneider, P. J. Müller, P. M. Grootes, and J. Rullkötter (2003), Asynchronous alkenone and foraminifera records from the Benguela Upwelling System, *Geochimica Et Cosmochimica Acta*, 67(12), 2157-2171.
- Mollenhauer, G., M. Kienast, F. Lamy, H. Meggers, R. Schneider, J. Hayes, and T. I. Eglinton (2005), An evaluation of ^{14}C age relationships between co-occurring foraminifera, alkenones, and total organic carbon in continental margin sediments, *Paleoceanography*, 20, 1-12.
- Mollenhauer, G., J. F. McManus, A. Benthien, P. J. Müller, and T. I. Eglinton (2006), Rapid lateral particle transport in the Argentine Basin: Molecular ^{14}C and $^{230}\text{Th}_{\text{xs}}$ evidence *Deep Sea Research Part I: Oceanographic Research Papers*, 53(7), 1224-1243.
- Mollenhauer, G., and T. I. Eglinton (2007), Diagenetic and sedimentological controls on the composition of organic matter preserved in California Borderland Basin sediments, *Limnology and Oceanography*, 52(2), 558-576.
- Monaghan, M. C., S. Krishnaswami, and K. K. Turekian (1986), The global-average production rate of ^{10}Be , *Earth and Planetary Science Letters*, 76(3-4), 279-287.
- Moore Jr., T. C., G. R. Heath, and L. D. Kowsmann (1973), Biogenic sediments of the Panama Basin, *Journal of Geology*, 81, 458-472.
- Moore, R. M., and K. A. Hunter (1985), Thorium adsorption in the ocean: reversibility and distribution amongst particle sizes, *Geochimica Et Cosmochimica Acta*, 49(11), 2253-2257.
- Moore, R. M., and G. E. Millward (1988), The kinetics of reversible Th reactions with marine particles, *Geochimica Et Cosmochimica Acta*, 52(1), 113-118.
- Morris, J. D., J. Gosse, S. Brachfeld, and F. Tera (2002), Cosmogenic Be-10 and the Solid Earth: Studies in Geomagnetism, Subduction Zone Processes, and Active Tectonics, in *Beryllium: Mineralogy, Petrology, and Geochemistry*, edited by E. S. Grew, pp. 207-270, *Reviews in Mineralogy and Geochemistry*, series edited by P. H. Ribbe, Mineralogical Society of America, Washington.
- Müller, P. J., and R. Schneider (1993), An automated leaching method for the determination of opal in sediments and particulate matter, *Deep Sea Research Part I: Oceanographic Research Papers*, 40(3), 425-444.
- Müller, P. J. (2003a), Bulk elemental composition of sediment core GeoB1028-4, PANGAEA, <http://doi.pangaea.de/10.1594/PANGAEA.132799>
- Müller, P. J. (2003b), Carbonate and carbon content of sediment core GeoB1027-2, PANGAEA, <http://doi.pangaea.de/10.1594/PANGAEA.96367>

- Negre, C., R. Zahn, A. L. Thomas, P. Masqué, G. M. Henderson, G. Martínez-Méndez, I. R. Hall, and J. L. Mas, Reversed Atlantic deep water flow during the Last Glacial Maximum, *Nature* (accepted).
- Nielsen, S. H. H., D. A. Hodell, G. Kamenov, T. Guilderson, and M. R. Perfit (2007), Origin and significance of ice-rafted detritus in the Atlantic sector of the Southern Ocean, *Geochim. Geophys. Geosyst.*, 8(12), Q12005.
- Niven, S. E. H., and R. M. Moore (1993), Thorium sorption in seawater suspensions of aluminium oxide particles, *Geochimica Et Cosmochimica Acta*, 57(10), 2169-2179.
- Nozaki, Y., Y. Horibe, and H. Tsubota (1981), The water column distributions of thorium isotopes in the western North Pacific, *Earth and Planetary Science Letters*, 54(2), 203-216.
- Nürnberg, C. C., G. Bohrmann, M. Schlüter, and M. Frank (1997), Barium Accumulation in the Atlantic Sector of the Southern Ocean: Results From 190,000-Year Records, *Paleoceanography*, 12, 594-603.
- Ohkouchi, N., T. I. Eglinton, L. D. Keigwin, and J. M. Hayes (2002), Spatial and Temporal Offsets Between Proxy Records in a Sediment Drift, *Science*, 298(5596), 1224-1227, doi: 10.1126/science.1075287.
- Patterson, D. B., K. A. Farley, and B. Schmitz (1998), Preservation of extraterrestrial ^3He in 480-Ma-old marine limestones, *Earth and Planetary Science Letters*, 163(1-4), 315-325.
- Paytan, A., M. Lyle, A. Mix, and Z. Chase (2004), Climatically driven changes in oceanic processes throughout the equatorial Pacific, *Paleoceanography*, 19, PA4017, doi: doi:4010.1029/2004PA001024.
- Paytan, A., and E. M. Griffith (2007), Marine barite: Recorder of variations in ocean export productivity, *Deep Sea Research Part II: Topical Studies in Oceanography*, 54(5-7), 687-705.
- Pearson, A., A. P. McNichol, B. C. Benitez-Nelson, J. M. Hayes, and T. I. Eglinton (2001), Origins of lipid biomarkers in Santa Monica Basin surface sediment: a case study using compound-specific $\Delta^{14}\text{C}$ analysis, *Geochimica Et Cosmochimica Acta*, 65(18), 3123-3137.
- Peine, F., R. Turnewitsch, C. Mohn, T. Reichelt, B. Springer, and M. Kaufmann (2009), The importance of tides for sediment dynamics in the deep sea--Evidence from the particulate-matter tracer ^{234}Th in deep-sea environments with different tidal forcing, *Deep Sea Research Part I: Oceanographic Research Papers*, 56(7), 1182-1202.
- Petschick, R., G. Kuhn, and F. Gingele (1996), Clay mineral distribution in surface sediments of the South Atlantic: sources, transport, and relation to oceanography, *Marine Geology*, 130(3-4), 203-229.
- Pichat, S., K. W. W. Sims, R. François, J. F. McManus, S. Brown Leger, and F. Albarède (2004), Lower export production during glacial periods in the equatorial Pacific derived from $(^{231}\text{Pa}/^{230}\text{Th})_{\text{xs}}$ measurements in deep-sea sediments, *Paleoceanography*, 19(4), PA4023.
- Press, W. H., B. P. Flannery, S. A. Teukolsky, and W. T. Vetterling (1992), *Numerical Recipes in FORTRAN 77: The Art of Scientific Computing, Second Edition*, second ed., 992 pp., University Press, Cambridge.
- Pudsey, C. J., P. F. Barker, and N. Hamilton (1988), Weddell Sea abyssal sediments a record of Antarctic Bottom Water Flow, *Marine Geology*, 81(1-4), 289-314.
- Pudsey, C. J. (1992), Late quaternary changes in Antarctic bottom water velocity inferred from sediment grain size in the northern Weddell Sea, *Marine Geology*, 107(1-2), 9-10.

- Pudsey, C. J., and J. A. Howe (1998), Quaternary history of the Antarctic Circumpolar Current: evidence from the Scotia Sea, *Marine Geology*, 148(1-2), 83-112.
- Pugh, R. S., I. N. McCave, C. D. Hillenbrand, and G. Kuhn (2009), Circum-Antarctic age modelling of Quaternary marine cores under the Antarctic Circumpolar Current: Ice-core dust-magnetic correlation, *Earth and Planetary Science Letters*, 284(1-2), 113-123.
- Raisbeck, G. M., F. Yiou, M. Fruneau, M. Lieuvin, and J. M. Loiseaux (1978), Measurement of ^{10}Be in 1,000- and 5,000-year-old Antarctic ice, *Nature*, 275(5682), 731-733.
- Raisbeck, G. M., F. Yiou, M. Fruneau, J. M. Loiseaux, M. Lieuvin, and J. C. Ravel (1981a), Cosmogenic $^{10}\text{Be}/^7\text{Be}$ as a probe of atmospheric transport processes, *Geophysical Research Letters*, 8(9), 1015-1018.
- Raisbeck, G. M., F. Yiou, M. Fruneau, J. M. Loiseaux, M. Lieuvin, J. C. Ravel, and C. Lorius (1981b), Cosmogenic ^{10}Be concentrations in Antarctic ice during the past 30,000 years, *Nature*, 292(5826), 825-826.
- Ransom, B., K. F. Shea, P. J. Burkett, R. H. Bennett, and R. Baerwald (1998), Comparison of pelagic and nepheloid layer marine snow: implications for carbon cycling, *Marine Geology*, 150(1-4), 39-50.
- Robinson, L. F., N. S. Belshaw, and G. M. Henderson (2004), U and Th concentrations and isotope ratios in modern carbonates and waters from the Bahamas, *Geochimica Et Cosmochimica Acta*, 68(8), 1777-1789.
- Robinson, L. F., T. L. Noble, and J. F. McManus (2008), Measurement of adsorbed and total $^{232}\text{Th}/^{230}\text{Th}$ ratios from marine sediments, *Chemical Geology*, 252(3-4), 169-179.
- Roy-Barman, M., C. Jeandel, M. Souhaut, M. Rutgers van der Loeff, I. Voege, N. Leblond, and R. Freydier (2005), The influence of particle composition on thorium scavenging in the NE Atlantic ocean (POMME experiment), *Earth and Planetary Science Letters*, 240(3-4), 681-693.
- Roy-Barman, M., C. Lemaître, S. Ayrault, C. Jeandel, M. Souhaut, and J. C. Miquel (2009), The influence of particle composition on Thorium scavenging in the Mediterranean Sea, *Earth and Planetary Science Letters*, 286(3-4), 526-534.
- Rutgers van der Loeff, M. M., and G. W. Berger (1993), Scavenging of ^{230}Th and ^{231}Pa near the antarctic polar front in the South Atlantic, *Deep Sea Research Part I: Oceanographic Research Papers*, 40(2), 339-357.
- Rutgers van der Loeff, M. M., and W. S. Moore (1999), Determination of natural radioactive tracers, in *Methods of Seawater Analysis*, edited by K. Grasshoff, K. Kremling and M. Ehrhardt, pp. 365-397, series edited, Wiley-VCH, Weinheim.
- Rutgers van der Loeff, M. M., R. Meyer, B. Rudels, and E. Rachor (2002), Resuspension and particle transport in the benthic nepheloid layer in and near Fram Strait in relation to faunal abundances and ^{234}Th depletion, *Deep Sea Research Part I: Oceanographic Research Papers*, 49(11), 1941-1958.
- Rutgers van der Loeff, M. M., and W. Geibert (2008), U- and Th-Series Nuclides as Tracers of Particle Dynamics, Scavenging and Biogeochemical Cycles in the Oceans, in *U-Th Series Nuclides in Aquatic Systems*, edited by S. Krishnaswami and K. J. Cochran, pp. 227-268, *Radioactivity in the Environment*, series edited by M. Baxter, Elsevier.
- Santschi, P. H., J. W. Murray, M. Baskaran, C. R. Benitez-Nelson, L. D. Guo, C. C. Hung, C. Lamborg, S. B. Moran, U. Passow, and M. Roy-Barman (2006), Thorium speciation in seawater, *Marine Chemistry*, 100(3-4), 250-268.
- Sarmiento, J. L., and J. R. Toggweiler (1984), A New Model for the Role of the Oceans in Determining Atmospheric pCO_2 , *Nature*, 308(5960), 621-624.

- Sayles, F. L., W. R. Martin, Z. Chase, and R. F. Anderson (2001), Benthic remineralization and burial of biogenic SiO₂, CaCO₃, organic carbon, and detrital material in the Southern Ocean along a transect at 170° West, *Deep Sea Research Part II: Topical Studies in Oceanography*, 48(19-20), 4323-4383.
- Schlüter, M., M. M. Rutgers van der Loeff, O. Holby, and G. Kuhn (1998), Silica cycle in surface sediments of the South Atlantic, *Deep Sea Research Part I: Oceanographic Research Papers*, 45(7), 1085-1109.
- Scholten, J. C., R. Botz, H. Paetsch, and P. Stoffers (1994), ²³⁰Th_{ex} flux into Norwegian-Greenland Sea sediments: Evidence for lateral sediment transport during the past 300,000 years, *Earth and Planetary Science Letters*, 121(1-2), 111-124.
- Scholten, J. C., J. Fietzke, S. Vogler, M. M. Rutgers van der Loeff, A. Mangini, W. Koeve, J. Waniek, P. Stoffers, A. N. Antia, and J. Kuss (2001), Trapping efficiencies of sediment traps from the deep Eastern North Atlantic: the ²³⁰Th calibration *Deep-Sea Research II*, 48, 2383-2408.
- Scholten, J. C., J. Fietzke, A. Mangini, P. Stoffers, T. Rixen, B. Gaye-Haake, T. Blanz, V. Ramaswamy, F. Sirocko, H. Schulz, and V. Ittekkot (2005), Radionuclide fluxes in the Arabian Sea: the role of particle composition, *Earth and Planetary Science Letters*, 230(3-4), 319-337.
- Siddall, M., G. M. Henderson, N. R. Edwards, M. Frank, S. A. Müller, T. F. Stocker, and F. Joos (2005), ²³¹Pa / ²³⁰Th fractionation by ocean transport, biogenic particle flux and particle type, *Earth and Planetary Science Letters*, 237(1-2), 135-155.
- Siddall, M., R. F. Anderson, G. Winckler, G. M. Henderson, L. I. Bradtmiller, D. McGee, A. Franzese, T. F. Stocker, and S. A. Müller (2008), Modeling the particle flux effect on distribution of ²³⁰Th in the equatorial Pacific, *Paleoceanography*, 23, doi: PA2208, doi:10.1029/2007PA001556.
- Siegel, S. (2001), *Nichtparametrische Statistische Methoden.*, 5. unveränd. Aufl. ed., Verlag Dietmar Klotz GmbH, Eschborn bei Frankfurt a.M.
- Sturm, J. F. (1999), Using SeDuMi 1.02, a MATLAB toolbox for optimization over symmetric cones, *Optim. Method Softw.*, 11, 625-653.
- Suman, D. O., and M. P. Bacon (1989), Variations in Holocene sedimentation in the North American Basin determined from ²³⁰Th measurements, *Deep Sea Research Part A. Oceanographic Research Papers*, 36(6), 869-878.
- Syvitski, J. P. M., K. W. Asprey, and D. A. Clattenburg (1991), Principles, design, and calibration of settling tubes, in *Principles, methods, and application of particle size analysis*, edited by J. P. M. Syvitski, pp. 45-63, series edited, Cambridge University Press, Cambridge.
- Taguchi, K., K. Harada, and S. Tsunogai (1989), Particulate removal of ²³⁰Th and ²³¹Pa in the biologically productive northern North Pacific, *Earth and Planetary Science Letters*, 93(2), 223-232.
- Thomas, E., K. K. Turekian, and K. Y. Wei (2000), Productivity Control of Fine Particle Transport to Equatorial Pacific Sediment, *Global Biogeochem. Cycles*, 14, 945-955.
- Thomsen, L., and T. C. E. van Weering (1998), Spatial and temporal variability of particulate matter in the benthic boundary layer at the N.W. European Continental Margin (Goban Spur), *Progress In Oceanography*, 42(1-4), 61-76.
- Thomsen, L., and G. Gust (2000), Sediment erosion thresholds and characteristics of resuspended aggregates on the western European continental margin, *Deep Sea Research Part I: Oceanographic Research Papers*, 47(10), 1881-1897.

- Thomson, J., S. Colley, R. Anderson, G. T. Cook, A. B. MacKenzie, and D. D. Harkness (1993), Holocene Sediment Fluxes in the Northeast Atlantic from $^{230}\text{Th}_{\text{excess}}$ and Radiocarbon Measurements, *Paleoceanography*, 8(5), 631-650.
- Turnewitsch, R., J.-L. Reyss, J. Nycander, J. J. Waniek, and R. S. Lampitt (2008), Internal tides and sediment dynamics in the deep sea - Evidence from radioactive $^{234}\text{Th}/^{238}\text{U}$ disequilibria, *Deep Sea Research Part I: Oceanographic Research Papers*, 55(12), 1727-1747.
- van Ierland, E. T., and L. Peperzak (1984), Separation of marine seston and density determination of marine diatoms by density gradient centrifugation, *J. Plankton Res.*, 6(1), 29-44, doi: 10.1093/plankt/6.1.29.
- Volbers, A. N. A., and R. Henrich (2002), Present water mass calcium carbonate corrosiveness in the eastern South Atlantic inferred from ultrastructural breakdown of Globigerina bulloides in surface sediments, *Marine Geology*, 186(3-4), 471-486.
- Walter, H. J., M. M. Rutgers van der Loeff, and H. Hoeltzen (1997), Enhanced scavenging of ^{231}Pa relative to ^{230}Th in the South Atlantic south of the Polar Front: Implications for the use of the $^{231}\text{Pa}/^{230}\text{Th}$ ratio as a paleoproductivity proxy, *Earth and Planetary Science Letters*, 149(1-4), 85-100.
- Walter, H. J., M. M. Rutgers van der Loeff, H. Hölzzen, and U. Bathmann (2000), Reduced scavenging of ^{230}Th in the Weddell Sea: implications for paleoceanographic reconstructions in the South Atlantic, *Deep Sea Research Part I: Oceanographic Research Papers*, 47(7), 1369-1387.
- Wang, L., T. L. Ku, S. Luo, J. R. Southon, and M. Kusakabe (1996), ^{26}Al - ^{10}Be systematics in deep-sea sediments, *Geochimica Et Cosmochimica Acta*, 60(1), 109-119.
- Xu, S., A. B. Dougans, S. P. H. T. Freeman, C. Schnabel, and K. M. Wilcken (2010), Improved ^{10}Be and ^{26}Al -AMS with a 5 MV spectrometer, *Nuclear Instruments and Methods in Physics Research Section B: Beam Interactions with Materials and Atoms*, 268(7-8), 736-738.
- Yang, H.-S., Y. Nozaki, H. Sakai, and A. Masuda (1986), The distribution of ^{230}Th and ^{231}Pa in the deep-sea surface sediments of the Pacific Ocean, *Geochimica Et Cosmochimica Acta*, 50(1), 81-89.
- Yu, E.-F., R. Francois, and M. P. Bacon (1996), Similar rates of modern and last-glacial ocean thermohaline circulation inferred from radiochemical data, *Nature*, 379(6567), 689-694.
- Zielinski, U., R. Gersonde, R. Sieger, and D. Fütterer (1998), Quaternary Surface Water Temperature Estimations: Calibration of a Diatom Transfer Function for the Southern Ocean, *Paleoceanography*, 13, 365-383.
- Ziervogel, K., and S. Forster (2005), Aggregation and sinking behaviour of resuspended fluffy layer material, *Continental Shelf Research*, 25(15), 1853-1863.

Appendix

Grain Size Correction of the Focusing Factor

This grain size correction is applied to the focusing factors using the equation A-12 in the Manuscripts I, II, and III. The equation for calculating a grain size corrected focusing factor is derived as following. See Chapter 2 (Manuscript I) for explanation.

Measured composition

i	grain size fraction measured in sediment
T_i	$^{230}\text{Th}_{\text{xs}}$ activity [dpm g^{-1}] in grain size fraction i
T_m	$^{230}\text{Th}_{\text{xs}}$ activity [dpm g^{-1}] in bulk sample
k_m	portion of small particles measured in sediment
Ψ	focusing factor measured

The $^{230}\text{Th}_{\text{xs}}$ activity T in the fraction of small (or large) sized particles is calculated as the sum of the grain size weighted $^{230}\text{Th}_{\text{xs}}$ activities.

$$T = \sum (T_i \times i)$$

We can calculate the variables for the lateral (vertical) composition for any choice of the grain size distribution in the lateral (vertical) flux.

T_{kL}	$^{230}\text{Th}_{\text{xs}}$ activity in small particles in lateral flux
T_{gL}	$^{230}\text{Th}_{\text{xs}}$ activity in large particles in lateral flux
T_{kV}	$^{230}\text{Th}_{\text{xs}}$ activity in small particles in vertical flux
T_{gV}	$^{230}\text{Th}_{\text{xs}}$ activity in large particles in vertical flux
k_L	portion of small particles in the lateral flux

Calculation

x	portion of the lateral flux related to the sedimentation rate
k_V	portion of small particles in vertical flux

With those variables as defined above, there are two unknown variables to be solved by two equations. The first equation describes the composition of small particles by the lateral and the vertical contribution:

$$k_m = x k_L + (1-x) k_V \tag{A-1}$$

so that the vertical contribution of small particles is:

$$k_V = \frac{k_m - x k_L}{1 - x} \quad (\text{A-2})$$

Equation (A-3) is calculating the focusing factor Ψ what is the total Th flux (vertical + lateral) divided by the vertical Th flux:

$$\Psi = \frac{x \left(k_L T_{k_L} + (1 - k_L) T_{g_L} \right) + (1 - x) \left(k_V T_{k_V} + (1 - k_V) T_{g_V} \right)}{(1 - x) \left(k_V T_{k_V} + (1 - k_V) T_{g_V} \right)} \quad (\text{A-3})$$

This can be written as equation (A-4):

$$x \left(k_L T_{k_L} + (1 - k_L) T_{g_L} \right) + (1 - x) \left(k_V T_{k_V} + (1 - k_V) T_{g_V} \right) = \Psi \left((1 - x) \left(k_V T_{k_V} + (1 - k_V) T_{g_V} \right) \right) \quad (\text{A-4})$$

By substitution of k_V with equation (A-2) we obtain equation (A-5):

$$x \left(k_L T_{k_L} + (1 - k_L) T_{g_L} \right) + (k_m - x k_L) (T_{k_V} - T_{g_V}) + T_{g_V} (1 - x) = \Psi \left((k_m - x k_L) (T_{k_V} - T_{g_V}) + T_{g_V} (1 - x) \right) \quad (\text{A-5})$$

Which is simplified and solved for x :

$$x = \frac{(\Psi - 1) \left(k_m (T_{k_V} - T_{g_V}) \right) + T_{g_V}}{k_L T_{k_L} + (1 - k_L) T_{g_L} + (\Psi - 1) \left(k_L (T_{k_V} - T_{g_V}) + T_{g_V} \right)} \quad (\text{A-6})$$

If the portion of fine particles in the lateral flux is 100% we can set:

$$k_L = 1 \quad (\text{A-7})$$

As Th activities in vertical and lateral fluxes are unknown we assume same activities for both fluxes. Than we can write:

$$T_{k_V} = T_{k_L}, \text{ simply } T_k \quad (\text{A-8})$$

and

$$T_{gV} = T_{gL}, \text{ simply } T_g \quad (\text{A-9})$$

With the assumptions (A-7, A-8, A-9) the equation can be simplified written as:

$$x = \frac{(\Psi - 1) \left(k_m T_k + (1 - k_m) T_g \right)}{\Psi T_k} \quad (\text{A-10})$$

This is the same as

$$x = \frac{(\Psi - 1) T_m}{\Psi T_k} = \frac{T_m}{T_k} \left(1 - \frac{1}{\Psi} \right) \quad (\text{A-11})$$

Knowing the portion of lateral flux (x) and vertical flux ($1-x$) we are able to calculate the grain size corrected focusing factor Ψ_c :

$$\Psi_c = \frac{1}{1-x} = \frac{1}{1 - \frac{T_m}{T_k} \left(1 - \frac{1}{\Psi} \right)} \quad (\text{A-12})$$

Table A-1: Opal content and concentrations of major elements in particle fractions of the samples PS1768-8 and PS1769-1. n.a. = not analyzed; sd = standard deviation [%].

fraction. method	size class	settling velocity	biogenic opal	Mg		Al		K		Ca		Fe		Mn		Rb		Cs	
				sd	sd	sd	sd	sd	sd	sd	sd	sd	sd	sd	sd	sd	sd	sd	sd
				[μm]															
				[%]															
				[ppm]															
bulk																			
pureW	<2		55	0.99	1.6	2.03	1.5	0.69	0.7	0.73	1.3	1.36	0.5	0.20	0.4	23.8	1.8	1.80	1.8
pureW	2-20		68	0.72	1.5	2.37	1.5	0.61	2.1	0.33	1.8	1.45	1.2	0.16	0.7	29.8	2.3	2.55	1.7
pureW	20-63	fast	76	0.22	1.6	1.38	1.1	0.41	0.5	0.61	0.6	0.67	0.8	0.11	1.3	9.9	0.7	0.69	1.3
pureW	63-125	fast	n.a.	1.49	2.9	6.33	1.2	0.49	0.6	7.42	0.7	5.12	1.6	1.01	1.3	14.6	0.5	0.70	1.0
pureW	>125	fast	n.a.	1.91	2.8	7.31	1.7	0.61	0.2	7.09	2.2	5.60	1.0	1.11	2.1	12.7	0.8	0.80	0.6
pureW	20-63	slowly	n.a.	2.29	0.2	7.38	1.2	0.48	1.0	8.34	1.3	5.67	2.6	1.12	1.3	10.0	0.4	0.62	0.7
pureW	63-125	slowly	n.a.	0.04	1.7	0.17	0.9	0.10	0.2	0.12	2.2	0.07	0.6	0.02	0.9	1.1	0.8	0.16	0.6
pureW	>125	slowly	n.a.	0.06	1.5	0.21	1.6	0.08	1.8	0.24	1.0	0.14	1.0	0.03	1.0	2.0	0.6	1.11	0.2
seaW	<10	slowly	n.a.	0.19	1.8	0.88	0.9	0.18	1.1	0.72	0.5	0.75	1.0	0.14	1.4	3.9	0.8	0.88	0.6
seaW	10-20		60	0.68	2.8	1.98	0.5	0.95	1.6	0.52	0.9	1.23	0.0	0.14	0.0	23.6	0.4	1.80	1.4
seaW	20-63	fast	n.a.	1.06	0.9	4.97	0.9	0.97	0.9	3.80	0.6	3.90	0.2	0.60	1.6	21.4	0.5	1.21	0.5
seaW	63-125	fast	15	1.34	1.2	5.81	2.0	0.70	2.1	5.25	0.2	4.62	1.1	0.84	3.4	13.6	0.9	0.68	0.6
seaW	>125	fast	n.a.	2.01	1.9	7.30	2.5	0.47	1.8	7.23	3.0	6.01	0.6	1.13	1.1	14.2	0.8	0.69	0.7
seaW	20-63	slowly	3	1.78	0.9	6.17	1.4	0.43	2.4	5.25	0.5	4.87	1.6	0.98	1.0	13.7	1.6	0.82	1.2
seaW	63-125	slowly	75	0.27	1.5	0.57	2.9	0.29	2.7	0.28	0.5	0.39	4.8	0.06	0.7	5.5	1.2	0.45	0.7
seaW	>125	slowly	76	0.16	0.9	0.42	1.4	0.14	1.8	0.23	0.8	0.31	1.3	0.05	3.0	3.9	0.3	0.36	1.0
seaW		slowly	n.a.	0.32	3.7	0.95	1.3	0.21	2.2	1.76	0.1	0.88	0.8	0.16	0.5	7.2	0.4	0.87	0.7
bulk																			
pureW	<2		60	0.95	2.2	1.97	1.7	0.91	1.5	1.13	1.7	1.68	1.7	0.44	1.6	19.5	1.2	1.36	0.4
pureW	2-20		61	0.79	0.2	2.31	1.3	0.58	1.1	0.19	1.1	2.05	0.4	0.33	0.7	29.1	0.6	2.40	2.7
pureW	20-63	fast	80	0.20	1.7	1.17	1.1	0.38	0.5	0.58	1.4	0.63	1.3	0.28	1.2	8.5	0.5	0.52	0.8
pureW	63-125	fast	n.a.	1.45	0.8	5.92	1.2	0.87	2.3	6.04	0.6	4.68	0.9	0.99	2.2	16.2	1.2	0.67	0.7
pureW	>125	fast	n.a.	2.05	2.8	7.47	0.7	0.66	1.7	7.43	0.9	5.98	1.3	1.17	0.7	13.1	1.2	0.67	1.2
pureW	20-63	slowly	n.a.	3.08	1.2	7.31	1.8	0.62	1.4	6.88	0.3	6.26	1.1	1.18	0.2	11.9	0.6	0.59	0.9
pureW	63-125	slowly	n.a.	0.04	1.8	0.21	1.6	0.12	1.5	0.19	1.3	0.12	0.4	0.15	0.7	1.2	0.6	0.11	1.5
pureW	>125	slowly	n.a.	0.06	1.0	0.29	0.6	0.12	0.8	0.27	2.2	0.20	1.4	0.19	1.3	1.7	0.8	0.44	0.3
pureW	<10	slowly	n.a.	0.30	0.7	1.10	1.0	0.25	1.4	1.31	0.9	1.06	1.0	0.28	0.5	5.8	1.3	0.55	1.3
seaW	10-20		59	0.74	1.5	1.71	0.5	0.63	0.3	0.55	2.2	1.47	1.9	0.30	1.3	22.8	0.5	1.59	0.4
seaW	20-63	fast	n.a.	1.10	1.7	4.85	1.2	0.81	0.6	3.74	1.4	3.59	1.8	0.77	0.7	25.1	2.0	1.04	1.1
seaW	63-125	fast	17	1.45	1.5	5.65	1.9	0.60	3.0	5.20	2.5	4.83	0.7	1.01	0.3	17.1	0.7	0.66	0.5
seaW	>125	fast	5	1.93	0.2	6.96	1.2	0.48	0.5	6.90	1.4	5.77	0.0	1.16	0.4	14.5	0.2	0.69	0.8
seaW	20-63	slowly	4	2.06	1.8	6.86	0.5	0.43	1.6	6.10	1.6	6.41	0.7	1.32	0.9	14.1	1.0	0.79	0.8
seaW	63-125	slowly	82	0.22	1.5	0.35	1.3	0.17	1.7	0.17	1.4	0.28	1.7	0.23	0.4	3.5	1.3	0.25	0.3
seaW	>125	slowly	79	0.19	0.5	0.48	0.6	0.14	1.9	0.33	2.2	0.42	0.8	0.36	0.9	3.1	0.2	0.26	0.5
seaW		slowly	n.a.	0.27	0.7	0.78	0.2	0.23	1.2	0.98	1.9	0.94	0.4	0.31	0.3	8.8	0.1	0.75	0.6

Table A-2: Th and U specific activities in particle fractions of the carbonate and the siliceous samples

fraction. method	size class [μm]	size fraction [%]	^{230}Th	^{232}Th	^{234}U	^{235}U	$^{238}\text{U}_{\text{total}}$	$^{238}\text{U}_{\text{auth}}$	$^{234}\text{U}/^{238}\text{U}$	[$\%$]	
			$\pm 2\sigma$	$\pm 2\sigma$	$\pm 2\sigma$	$\pm 2\sigma$	$\pm 2\sigma$	$\pm 2\sigma$	$\pm 2\sigma$		$\pm 2\sigma$
sediment core GeoB1027-2											
bulk			5.0	0.56	2.35	0.095	2.07	1.73	84	1.13	0.06
pureW	<2	35.2	7.9	0.99	2.84	0.11	2.51	1.92	76	1.13	0.06
pureW	2-20	27.5	4.3	0.60	1.12	0.04	1.01	0.65	65	1.11	0.06
pureW	20-63	15.9	3.6	0.22	1.15	0.05	0.98	0.85	87	1.18	0.07
pureW	63-125	11.1	3.1	0.19	1.08	0.04	0.92	0.80	87	1.18	0.06
pureW	>125	10.3	2.7	0.22	1.07	0.04	0.94	0.81	86	1.14	0.06
seaW	<10	43.4	5.8	0.80	1.51	0.06	1.33	0.85	64	1.14	0.06
seaW	10-20	5.9	4.7	0.56	1.10	0.04	0.97	0.64	66	1.13	0.06
seaW	20-63	11.2	4.4	0.32	1.43	0.06	1.22	1.03	84	1.17	0.06
seaW	63-125	12.9	3.7	0.27	1.33	0.05	1.13	0.97	85	1.18	0.06
seaW	>125	26.7	3.2	0.28	1.26	0.05	1.08	0.92	84	1.17	0.07
sediment core GeoB1028-4											
bulk			3.5	0.30	1.98	0.08	1.73	1.55	90	1.14	0.06
pureW	<2	25.0	7.7	0.70	0.84	0.04	0.76	0.33	44	1.11	0.06
pureW	2-20	12.6	3.3	0.41	1.20	0.05	1.05	0.80	76	1.15	0.06
pureW	20-63	9.1	2.4	0.13	0.83	0.03	0.70	0.62	89	1.19	0.07
pureW	63-125	17.5	1.9	0.11	0.74	0.03	0.63	0.56	90	1.18	0.06
pureW	>125	35.9	1.6	0.11	0.73	0.03	0.62	0.55	89	1.18	0.06
seaW	<10	28.3	5.7	0.57	1.29	0.05	1.12	0.78	70	1.15	0.06
seaW	10-20	3.0	3.1	0.30	0.75	0.03	0.64	0.46	72	1.16	0.06
seaW	20-63	9.1	2.6	0.15	0.88	0.03	0.74	0.66	88	1.18	0.06
seaW	63-125	17.3	2.1	0.13	0.77	0.03	0.65	0.57	88	1.18	0.06
seaW	>125	42.3	2.1	0.17	1.00	0.04	0.86	0.76	88	1.17	0.06

Table A-2 (continued): Th and U specific activities in particle fractions of the carbonate and the siliceous samples.

fraction, method	size class settling velocity	size fraction [%]	^{230}Th	$^{230}\text{Th}_{\text{ss}}$	^{232}Th	^{234}U	^{235}U	$^{238}\text{U}_{\text{total}}$	$^{238}\text{U}_{\text{auth}}$	^{238}U	$^{234}\text{U}/^{238}\text{U}$	
			$\pm 2\sigma$	$\pm 2\sigma$	$\pm 2\sigma$	$\pm 2\sigma$	$\pm 2\sigma$	$\pm 2\sigma$	$\pm 2\sigma$	$\pm 2\sigma$	$\pm 2\sigma$	
			[dpm g ⁻¹]									
			sediment core PS1768-8 (166-169 cm)									
bulk			6.5	6.6	0.52	3.40	0.140	3.04	2.73	3.04	90	
pure W	<2	39.6	11.9	12.7	0.84	4.47	0.181	3.04	2.67	3.04	88	
pure W	2-20	43.6	1.3	1.2	0.26	0.90	0.037	0.80	0.65	0.80	81	
pure W	20-63	2.4	1.6	1.6	0.34	0.54	0.022	0.48	0.28	0.48	58	
pure W	63-125	1.0	1.1	1.1	0.21	0.38	0.016	0.35	0.22	0.35	64	
pure W	>125	1.8	1.1	1.1	0.19	0.33	0.014	0.30	0.19	0.30	61	
pure W	20-63	10.8	0.4	0.3	0.02	0.56	0.022	0.48	0.48	0.48	98	
pure W	63-125	0.6	1.4	1.3	0.43	0.35	0.016	0.34	0.09	0.34	26	
pure W	>125	0.2	0.7	0.7	0.08	0.42	0.017	0.38	0.33	0.38	88	
sea W	<10	74.1	6.6	7.0	0.54	2.56	0.104	2.27	1.95	2.27	86	
sea W	10-20	1.8	4.3	4.4	0.66	1.25	0.052	1.13	0.73	1.13	65	
sea W	20-63	2.2	2.9	3.1	0.31	0.68	0.028	0.61	0.42	0.61	70	
sea W	63-125	0.9	2.5	2.7	0.24	0.47	0.019	0.41	0.26	0.41	64	
sea W	>125	1.9	1.4	1.4	0.18	0.41	0.017	0.36	0.25	0.36	70	
sea W	20-63	16.0	2.2	2.3	0.14	0.99	0.039	0.85	0.76	0.85	90	
sea W	63-125	2.7	2.0	2.1	0.11	0.93	0.037	0.80	0.74	0.80	92	
sea W	>125	0.2	3.8	4.2	0.22	0.77	0.030	0.66	0.53	0.66	80	
			sediment core PS1769-1 (14-16cm)									
bulk			6.1	6.7	0.46	0.72	0.030	0.66	0.38	0.66	58	
pure W	<2	35.5	11.5	12.7	0.76	1.19	0.053	1.08	0.65	1.08	60	
pure W	2-20	40.6	2.0	2.1	0.24	0.45	0.019	0.41	0.27	0.41	65	
pure W	20-63	2.1	2.7	2.8	0.52	0.43	0.020	0.43	0.12	0.43	27	
pure W	63-125	1.8	1.5	1.6	0.25	0.20	0.009	0.20	0.05	0.20	25	
pure W	>125	4.6	1.4	1.5	0.20	0.16	0.007	0.16	0.04	0.16	23	
pure W	20-63	14.1	0.6	0.7	0.03	0.19	0.008	0.17	0.15	0.17	89	
pure W	63-125	0.6	0.5	0.5	0.03	0.16	0.007	0.15	0.13	0.15	87	
pure W	>125	0.6	2.4	2.6	0.16	0.14	0.007	0.14	0.05	0.14	33	
sea W	<10	68.1	7.0	7.7	0.52	0.86	0.036	0.79	0.47	0.79	60	
sea W	10-20	1.0	6.0	6.4	0.85	0.72	0.031	0.68	0.17	0.68	25	
sea W	20-63	1.8	3.9	4.2	0.51	0.46	0.021	0.45	0.14	0.45	32	
sea W	63-125	1.6	2.3	2.5	0.30	0.24	0.010	0.23	0.05	0.23	22	
sea W	>125	4.1	1.9	2.0	0.23	0.21	0.009	0.20	0.06	0.20	32	
sea W	20-63	20.3	1.6	1.7	0.09	0.31	0.013	0.27	0.22	0.27	80	
sea W	63-125	2.7	1.8	2.0	0.10	0.29	0.012	0.26	0.20	0.26	78	
sea W	>125	0.5	3.4	3.8	0.21	0.21	0.009	0.20	0.07	0.20	36	

Table A-3: Results on particle size specific excess ^{231}Pa activities and excess $^{231}\text{Pa}/^{230}\text{Th}$, and the distribution ratio $D(\text{Pa}/\text{Th})$ (see text for explanation). All activities are decay corrected to the time of deposition (The error denotes the analytical uncertainty of 1σ).

size class [μm]	settling velocity	$x_s^{231}\text{Pa}$ [dpm g^{-1}]	$x_s^{231}\text{Pa}/^{230}\text{Th}$	$D(\text{Pa}/\text{Th})$
sediment core PS1768-8				
bulk		1.10 \pm 0.19	0.16 \pm 0.04	
<2		1.59 \pm 0.27	0.12 \pm 0.03	0.8
2-20		0.67 \pm 0.11	0.54 \pm 0.13	3.3
<20		1.40 \pm 0.24	0.20 \pm 0.05	1.2
20-63	fast	0.14 \pm 0.03	0.05 \pm 0.01	0.3
63-125	fast	0.03 \pm 0.01	0.01 \pm 0.00	0.1
>125	fast	0.08 \pm 0.01	0.05 \pm 0.01	0.3
>63	fast	0.06 \pm 0.01	0.03 \pm 0.01	0.2
20-63	slowly	0.77 \pm 0.13	0.33 \pm 0.08	2.0
63-125	slowly	0.72 \pm 0.12	0.34 \pm 0.08	2.1
>125	slowly	0.46 \pm 0.08	0.11 \pm 0.03	0.7
>63	slowly	0.71 \pm 0.12	0.31 \pm 0.08	1.9
sediment core PS1769-1				
bulk		1.10 \pm 0.19	0.16 \pm 0.04	
<2		1.89 \pm 0.32	0.15 \pm 0.04	0.9
2-20		0.68 \pm 0.11	0.32 \pm 0.08	1.9
<20		1.45 \pm 0.25	0.19 \pm 0.05	1.1
20-63	fast	0.19 \pm 0.03	0.05 \pm 0.01	0.3
63-125	fast	0.06 \pm 0.01	0.02 \pm 0.01	0.1
>125	fast	0.09 \pm 0.02	0.04 \pm 0.01	0.3
>63	fast	0.08 \pm 0.02	0.04 \pm 0.01	0.2
20-63	slowly	0.81 \pm 0.14	0.46 \pm 0.11	2.8
63-125	slowly	0.57 \pm 0.10	0.28 \pm 0.07	1.7
>125	slowly	0.74 \pm 0.13	0.20 \pm 0.05	1.2
>63	slowly	0.60 \pm 0.10	0.26 \pm 0.06	1.6

Table A-4: Results on particle size specific ^{10}Be concentrations, $^{10}\text{Be}/^{230}\text{Th}_{\text{xs}}$, intrinsic $^{10}\text{Be}/\text{Be}$ and the distribution ratio $D(\text{Be}/\text{Th})$ (see text for explanation). All ^{10}Be concentrations are decay corrected to the time of deposition. (The error denotes the analytical uncertainty of 1σ).

AMS ID	size class [μm]	settling velocity	^{10}Be [10^9 at g^{-1}]	$^{10}\text{Be}/\text{Be}$ [10^{-8} at at^{-1}]	$^{10}\text{Be}/^{230}\text{Th}_{\text{xs}}$ [10^9 at dpm^{-1}]	$D(\text{Be}/\text{Th})$
sediment core PS1768-8						
b2690	bulk		2.56 ± 0.08	4.61 ± 0.17	0.38 ± 0.07	
b2688	<20		3.11 ± 0.10	5.46 ± 0.19	0.45 ± 0.08	1.2
b2655	20-63	fast	0.69 ± 0.02	1.26 ± 0.04	0.22 ± 0.04	0.6
b2659	>63	fast	0.50 ± 0.02	1.04 ± 0.03	0.27 ± 0.05	0.7
b2689	20-63	slowly	1.33 ± 0.04	4.26 ± 0.14	0.57 ± 0.10	1.5
b2658	>63	slowly	1.15 ± 0.04	3.20 ± 0.12	0.51 ± 0.09	1.3
sediment core PS1769-1						
b2660	bulk		2.26 ± 0.07	4.16 ± 0.14	0.34 ± 0.06	
b2661	<20		3.03 ± 0.09	5.54 ± 0.20	0.39 ± 0.07	1.2
b2663	20-63	fast	0.86 ± 0.03	1.23 ± 0.04	0.21 ± 0.04	0.6
b2664	>63	fast	0.70 ± 0.02	1.55 ± 0.05	0.33 ± 0.06	1
b2662	20-63	slowly	0.84 ± 0.03	4.10 ± 0.17	0.49 ± 0.08	1.4
b2665	>63	slowly	1.14 ± 0.03	3.91 ± 0.15	0.50 ± 0.08	1.5

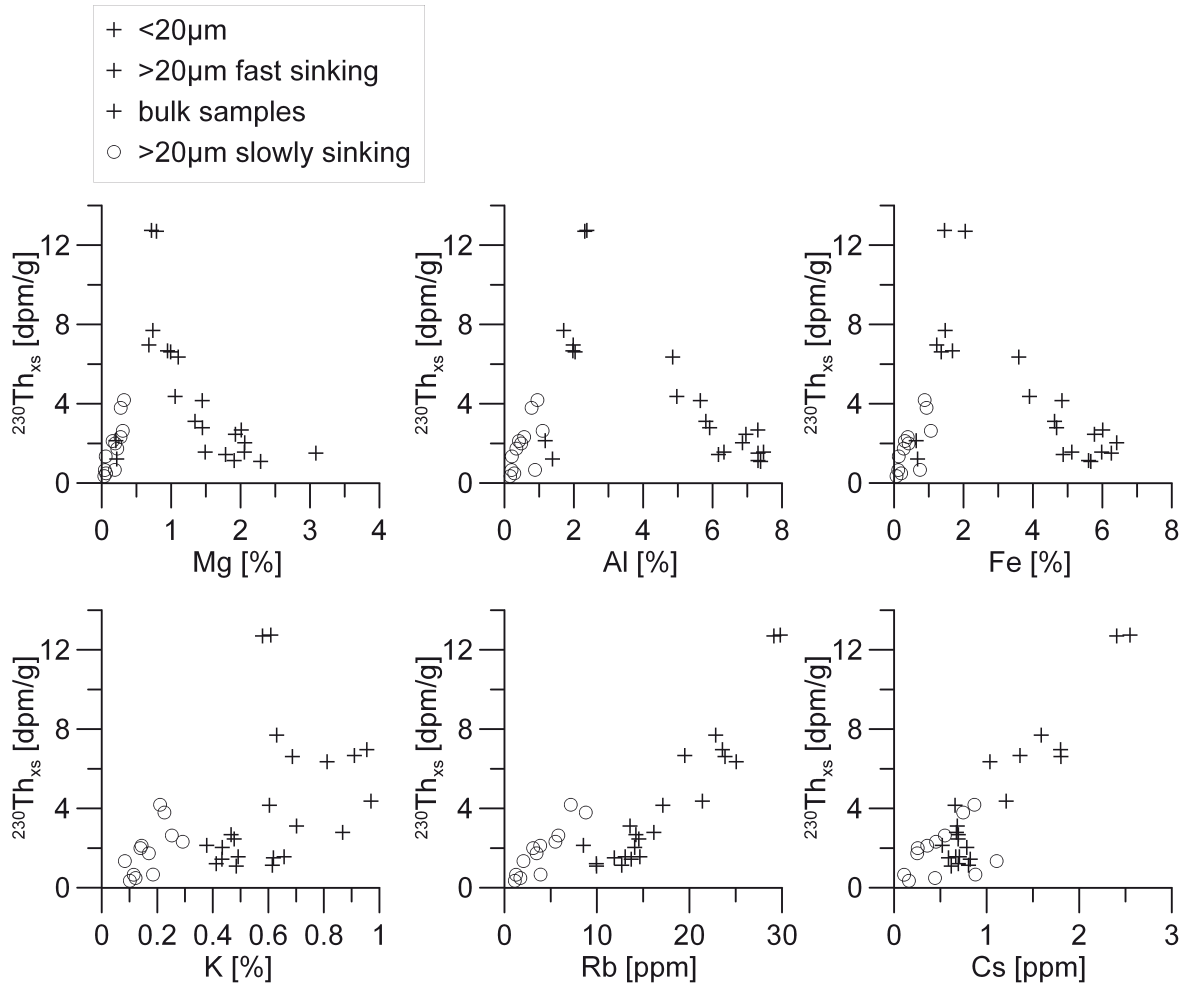


Figure A-1: Scatter plot of $^{230}\text{Th}_{\text{xs}}$ specific activities against different element concentrations within the sediment fractions of the samples from cores PS1768-8 and PS1769-1. The particle class >math>>20\mu\text{m}</math> (slowly sinking) is depicted as a circle (o) and all other particle classes are depicted as a cross (+). Only Rb and Cs show positive correlations with $^{230}\text{Th}_{\text{xs}}$.

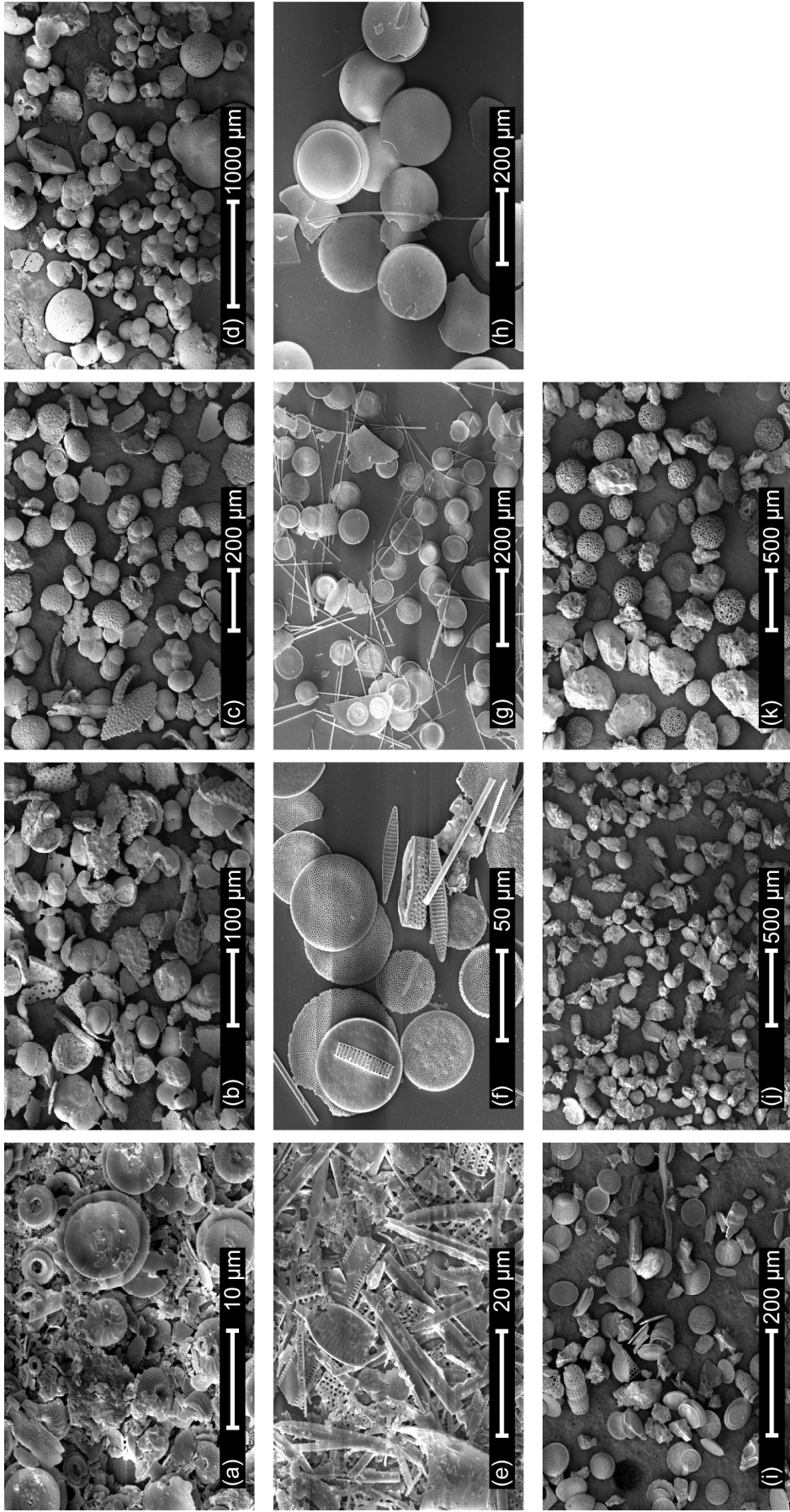


Plate A-1: Scanning electron microscope photographs of sediment particle fractions.
 Size fractions of Geob1027-2: (a) $< 20 \mu\text{m}$; (b) 20-63 μm ; (c) 63-125 μm ; (d) $> 125 \mu\text{m}$
 Size fractions of PS1769-1: (e) $< 20 \mu\text{m}$; (f) 20-63 μm slowly settling; (g) 63-125 μm slowly settling; (h) $> 125 \mu\text{m}$ slowly settling;
 (i) 20-63 μm fast settling; (j) 63-125 μm fast settling; (k) $> 125 \mu\text{m}$ fast settling

Danksagung

Vorliegende Arbeit ist ein Teilprojekt der Arbeitsgruppe *Helmholtz Universities Young Investigators Group* mit dem Titel *Applications of compound-specific radiocarbon analysis for the study of sedimentation processes and carbon cycling in marine sediments* unter der Leitung von Gesine Mollenhauer und wurde aus den Mitteln dieser Gruppe finanziert.

Für die Betreuung meiner Arbeit bedanke ich mich herzlich bei Gesine Mollenhauer. Während der vergangenen vier Jahre habe ich ihre stetige Unterstützung erfahren. Das Vertrauen in mich, sowie ihre Hilfsbereitschaft, ihr Optimismus und Verständnis haben mich während meiner Doktorarbeiten begleitet. Bei der wissenschaftlichen Arbeit hat sie mir Freiheit gelassen und mich gefördert. Walter Geibert gebührt mein Dank, da er mir stetig mit Motivation und Kritik eine große Stütze war, zu Beginn im Labor und später beim Verfassen der Arbeit. Dank seines unermüdlichen Lesens und seiner fachkundigen Korrekturen der zahllosen Vorabversionen und durch die anregenden Diskussionen mit ihm haben die Manuskripte dieser Arbeit erheblich an Qualität gewonnen. Bei Michiel Rutgers van der Loeff bedanke ich mich für die fruchtbaren Diskussionen und für seine Denkanstöße, die ich während des Verfassens meiner Arbeit erfahren habe. Seine kritische Durchsicht aller Manuskripte, das Aufzeigen von Denkfehlern im Argumentationsaufbau, sowie die Hilfestellung bei Rechenproblemen haben einen wesentlichen Teil zu dieser Arbeit beigetragen.

Mein Dank gilt allen Kollegen der Marinen Geochemie am AWI. Insbesondere Michael Schlüter danke ich für die Übernahme des Zweitgutachtens. Ingrid Stimac, Sonja Ebert, Robert Karandi und Hendrik Grotheer haben durch ihre tatkräftige Hilfe wesentlich zum Gelingen der Laborarbeit beigetragen. Ich freue mich, dass ich mit Celia Venchiarutti zeitweise das Büro, das Reinraumlabor und die Nutzung des ICP-MS teilen durfte. Durch den Austausch von Erfahrungen und die Diskussionen mit ihr über die Methoden zur Protactinium-Analyse konnte ich meine eigene Arbeit und Methodik im Labor verbessern. Bei Jana Friedrich möchte ich mich herzlich für das schnelle Korrekturlesen bedanken.

Ebenfalls habe ich Unterstützung durch die Kollegen der Marinen Geologie am AWI erfahren. Rainer Gersonde hat mir Sedimentproben aus der Antarktis bereit gestellt. Gerhard Kuhn sei für das Überlassen von Sedimentologie-Datensätzen gedankt. Durch die Hilfe von Ute Bock und Rita Fröhlking konnte ich Aufnahmen am Rasterelektronenmikroskop sowie die Messung von biogenem Opal durchführen.

Danke an die Kollegen der Universität Bremen und des MARUM: Inka Meyer und Jan-Berend Stuuat haben mir in ihrem Labor die Messung von Korngrößenverteilungen ermöglicht. Dave Heslop half mir geholfen, mit dem „Endmember-Modeling“ diese Korngrößenverteilungen zu interpretieren.

Christoph Schnabel und Allan Davidson sei für die gelungene Durchführung unseres gemeinsamen ^{10}Be -Projektes gedankt. Vielen Dank an Autun Purser für die Korrektur meines „awkward english“. Dank Bernhard Diekmann, Hans-Wolfgang Hubberten, Andreas Borchers, Peter Sperlich und Ines Voigt ist unsere gemeinsame Polarstern-Expedition in die Antarktis erfolgreich und in angenehmer Atmosphäre verlaufen. Die Arbeitszeiten im Büro und/oder während Tagungen sind dank Christina Morchner, Janet Rethemeyer, Maria Winterfeld, Stephanie Kusch und Andreas Basse zu keinem Zeitpunkt langweilig geworden.

Zu guter Letzt möchte ich meiner Familie für ihr Wohlwollen und die moralische Unterstützung danken. Mein ganz besonderer Dank gilt Sibila. Sie hat mich mit Liebe und Vertrauen bei meiner Arbeit unterstützt. Ich hoffe, dass ich ihr während der Fertigstellung ihrer eigenen Doktorarbeit eine ebenso zuverlässige Stütze sein werde. An dieser Stelle möchte ich ebenfalls Lucas dankbar erwähnen, denn er zeigt mir täglich auf seine eigene Weise, wie man die Welt ganz ohne Naturwissenschaft neu entdecken kann.

